

# DESIGN, CONTROL AND ANALYSIS OF GRID CONNECTED PV SYSTEM

*by*  
**Hemant Saxena**

Submitted  
In fulfilment of the requirements for the award of degree of  
DOCTOR OF PHILOSOPHY



Department of Electrical Engineering  
Delhi Technological University  
Delhi-110042, India

DELHI TECHNOLOGICAL UNIVERSITY, DELHI, 2021  
ALL RIGHTS RESERVED

30 July 2021



# Certificate

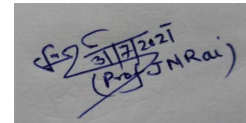
This is to certify that the thesis entitled “**Design, Control and Analysis of Grid Connected PV System**” being submitted by **Mr. Hemant Saxena** for the award of degree of **Doctor of Philosophy** in the Department of Electrical Engineering, Delhi Technological University, Delhi, is the record of students own work carried out by him under our supervision. The contents of this research work have not been submitted in part or fully to any other Institute or University for the award of any degree.

Date: 31 July 2021



**Prof. Alka Singh**

Department of Electrical Engineering  
Delhi Technological University  
Delhi-110042, India



**Prof. Jitendra Nath Rai**

Department of Electrical Engineering  
Delhi Technological University  
Delhi-110042, India

# Acknowledgments

I would like to express my deep and sincere gratitude to my supervisors **Prof. Alka Singh** and **Prof. Jitendra Nath Rai** for their valuable guidance and continuous monitoring of my research work. It was great honor for me to pursue my research work under their supervisions. Prof. Alka Singh has been the motivating and inspiring factor behind my research work. It's her vigor and hunger to perform in adverse situation, which has inspired me to thrive for excellence. Continuous monitoring by Prof. Jitendra Nath Rai, valuable guidance and input has always been a driving force to complete my research work. It is a life time experience to work under both of my supervisors and humbly acknowledge lifetime gratitude to them .

I would like to express my thanks to **Prof. Uma Nangia, HOD (EE)** for her kind support.

I would also like to convey my sincere gratitude to **Dr. Ram Bhagat**, Associate Professor, DTU, who has taught me the relevant course work. I would like to thank the SRC members mainly **Prof. Majid Jamil**, who has given me valuable guidance and advice to improve quality of my research work. I am extremely grateful to **Prof. S. T. Nagrajan, Prof. Madhusudan Singh, Prof. Pragati Kumar, Prof. D. R. Bhaskar** for their valuable assistance and support. I am extremely thankful to staff members of Power System Lab **Ashok, Ajendra Singh and Komal Singh** for providing me immense facility and assistance to carry out my research work. I would like to thank other office staffs, Central library and Computer Centre staff members, for their valuable co-operation and support.

I would like my sincere thanks to **Dr. Prakash Chittora** and **Dr. Manoj Badoni**,

who have guided me to develop hardware at initial level of my research work. I am extremely grateful to my research group and friends **Rajat Raj Singh, Rajat Kesarwani, Allu Bhargava, Amarendra Pandey, Ajishek Raj, Suryakant Shukla, Astitva Kumar, Pallavi Verma, Ashutosh Trivedi, Ambrish Devanshu, and Imran Ahmed Quadri** for their valuable assistance, co-operation and great source of learning.

If I get any success today for my research work, the entire credit should go to my mother **Smt. Sushma Devi**, father **Sri Ram Ratan Prasad** and my younger brother **Shashi Ranjan Kumar**.

I deeply convey my gratitude to my wife **Anisha** who has endured me and my long hours spent in the laboratory with patience and encouraged me to carry out my research work. I would like to thank other family members supporting me directly or indirectly to carry out my research work.

Last, but not the least, I thank **Mother Nature** and **Almighty God** for providing me the opportunity for pursuing doctoral studies.

Date: 30 July 2021

Place: Delhi

*Hemant Saxena*

**Hemant Saxena**

Roll No 2K16PHDEE10

# Abstract

Solar photovoltaic (PV) generating system is gaining lot of importance these days. Out of all the renewable energy sources solar PV is most promising because of clean and inexhaustible supply, less maintenance requirement, lower mechanical components involved and can be installed in modular from small-scale to large-scale generating system. The modern distributed grid is connected with different power electronic loads and other types of linear (lagging or leading) loads. These loads may results in poor power factor and produces harmonics to the grid.

In this thesis work, design, control and analysis of grid connected PV system has been presented. It enables the active and reactive compensation to the distribution, load balancing in three-phase and power quality improvement. The proposed system is implemented in both the single-phase and three-phase distribution network. Maximum Power Point Tracking (MPPT) technique has been implemented to extract maximum power from the PV in both single-stage and double-stage grid-connected PV system.

Parameters of the proposed system has been estimated and the prototype of single-phase and three-phase Shunt Active Power Filter (SAPF) have been configured. The proper functioning of the grid-connected PV system require a suitable control algorithm. Conventionally, control algorithms require synchronization technique, fundamental component estimation technique, DC-link voltage controller and the feed-forward term. For the purpose of estimation grid synchronization signal different conventional techniques have been presented and novel advanced techniques have been proposed for both the single-phase and three-phase grid-connected PV system. Phase Locked Loops (PLLs) are widely employed to estimate synchronizing

signal and also have the capability of phase, frequency and the magnitude of the grid voltage signal. These techniques have been tested under different grid voltage conditions such as voltage sag/swell, harmonics, frequency change, phase change and noisy grid. For the single-phase system the conventional algorithms presented are Synchronous Reference Frame Phase Locked Loop (SRF-PLL) , Enhanced Phase Locked Loop (EPLL), Second-Order Generalized Integrator-PLL (SOGI-PLL) have been employed. Further new and advanced technique such combined SOGI-FLL and Reduced Order Generalized Integrator (ROGI) has been proposed which shows the improved performance during the harmonic grid. A fast and robust technique based on adaptive zero-crossing detection has been proposed which shows the precise frequency estimation and faster dynamic response.

For the three-phase system, the simplest unit-template method has been used to generate synchronizing but it works good when the grid voltage has no abnormalities. The conventional three-phase SRF-PLL has been also presented and its poor performance during the harmonic grid and dynamic condition. Further advanced technique have been proposed to improve the performance of PLLs. Improved Adaline PLL has been proposed which has adaptive in nature and improves its dynamic response without compromising the steady-state performance. An adaptive spline based PLL has been proposed for smooth estimation of grid parameters and distortion free synchronizing signals.

Some conventional and advanced techniques have been employed for estimation of fundamental component of the non-linear load current. Further the synchronization techniques and the fundamental estimation technique have been employed in single-phase and three-phase system feeding linear/non-linear load under normal and distorted grid conditions for SAPF system. The PV has been connected in both single-stage and double-stage mode to the DC-link of the Voltage Source Converter (VSC). dSpace 1104 has been used for single-phase grid-connected PV system and dSpace 1202 has been used for three-phase grid-connected PV system for processing the grid parameter signals and to estimate switching pulses for Insulated-Gate

Bipolar Transistor (IGBT) switches of VSC and DC-DC converter. The proposed system and algorithms have been simulated and analysed in MATLAB/Simulink environment. The experimental results validate and fulfils the objectives of the thesis work.

# Contents

<b>Certificate</b>	<b>i</b>
<b>Acknowledgements</b>	<b>iii</b>
<b>Abstract</b>	<b>vi</b>
<b>List of Figures</b>	<b>xxvii</b>
<b>List of Tables</b>	<b>xxix</b>
<b>List of Symbols</b>	<b>xxxii</b>
<b>List of Abbreviations</b>	<b>xxxiii</b>
<b>1 Introduction</b>	<b>1</b>
1.1 General . . . . .	1
1.2 Modern Distribution System and Power Quality . . . . .	3
1.3 State of Art . . . . .	4
1.4 Scope of Work . . . . .	6
1.5 Thesis Structure . . . . .	8
<b>2 Literature Survey</b>	<b>10</b>
2.1 General . . . . .	10
2.2 Literature Survey on PV Modelling and MPPT Techniques . . . . .	10
2.3 Literature Survey on PQ Problems, Impacts and Their Solutions . . . . .	11
2.4 Literature Survey on Synchronization Schemes . . . . .	13

2.5	Literature Survey on Control Algorithms of SAPF . . . . .	15
2.6	Literature Survey on PV Integration to Distribution Grid . . . . .	16
2.7	Identified Research Gap . . . . .	17
2.8	Objectives of Research Work . . . . .	17
2.9	Conclusions . . . . .	18
<b>3</b>	<b>Design and Development of Single-Phase and Three-Phase Grid-Connected PV System</b>	<b>19</b>
3.1	Design and Development of Single-Phase Grid-Connected PV System	19
3.1.1	Calculation of DC-link Reference Voltage . . . . .	22
3.1.2	Design of DC-link Capacitor . . . . .	23
3.1.3	Design of Interfacing Inductor . . . . .	23
3.1.4	Modelling and Design of PV Array . . . . .	24
3.1.4.1	Modelling of PV Module . . . . .	24
3.1.4.2	Design of PV Array . . . . .	28
3.1.5	Design of DC-DC Boost Converter . . . . .	29
3.1.6	Design of Hysteresis Current Controller (HCC) . . . . .	32
3.1.7	Design and Development of Sensor Circuits . . . . .	34
3.1.8	Design of Amplifier Circuit for IGBT Driver . . . . .	35
3.2	Design and Development of Three-Phase Grid-Connected PV System	36
3.2.1	Calculation of DC-link Reference Voltage . . . . .	38
3.2.2	Design of DC-link Capacitor . . . . .	39
3.2.3	Design of Interfacing Inductor . . . . .	39
3.2.4	Design of PV Array . . . . .	40
3.3	Conclusions . . . . .	41
<b>4</b>	<b>Grid Synchronization Techniques</b>	<b>42</b>
4.1	Single-Phase Grid Synchronization Techniques . . . . .	42
4.1.1	Delay based SRF-PLL . . . . .	43
4.1.1.1	Simulation Results . . . . .	44



4.1.1.2	Experimental Results . . . . .	46
4.1.2	Enhanced Phase Locked Loop (EPLL) . . . . .	50
4.1.2.1	Simulation Results . . . . .	53
4.1.2.2	Experimental Results . . . . .	55
4.1.3	Second-Order Generalized Integrator Phase-Locked Loop (SOGI- PLL) . . . . .	58
4.1.3.1	Simulation Results . . . . .	61
4.1.3.2	Experimental Results . . . . .	63
4.1.4	Second-Order Generalized Integrator Frequency Locked Loop (SOGI-FLL) . . . . .	66
4.1.4.1	Simulation Results . . . . .	68
4.1.4.2	Experimental results . . . . .	70
4.1.5	SOGI-FLL and Reduced Order Generalized Integrator (ROGI) based Synchronization Technique . . . . .	72
4.1.5.1	Simulation Results . . . . .	75
4.1.5.2	Experimental Results . . . . .	77
4.1.5.3	Performance Comparison of SOGI-FLL, ROGI and SOGI-FLL-ROGI . . . . .	79
4.1.6	Adaptive Zero-Crossing Detection (AZCD) based Synchro- nization . . . . .	81
4.1.6.1	Zero-Crossing Detector . . . . .	81
4.1.6.2	Frequency Adaptive ZCD . . . . .	82
4.1.6.3	Simulation Results . . . . .	87
4.1.6.4	Experimental Results . . . . .	89
4.1.6.5	Comparison of Single-Phase Synchronization Tech- niques . . . . .	90
4.2	Three-Phase Grid Synchronization Techniques . . . . .	93
4.2.1	Unit Template Estimation . . . . .	93
4.2.1.1	Simulation Results . . . . .	93

4.2.1.2	Experimental Results . . . . .	94
4.2.2	Three-Phase SRF-PLL . . . . .	96
4.2.2.1	Simulation Results . . . . .	97
4.2.2.2	Experimental Results . . . . .	98
4.2.3	Improved Adaline PLL . . . . .	100
4.2.3.1	Mathematical Modelling of Adaline . . . . .	100
4.2.3.2	Estimation of Synchronizing Signals by Improved Adaline based PLL . . . . .	102
4.2.3.3	Simulation Results . . . . .	103
4.2.3.4	Experimental Results . . . . .	105
4.2.3.5	Performance Comparison of Adaline-PLL and IAdaline-PLL . . . . .	107
4.2.4	Spline based PLL . . . . .	109
4.2.4.1	Simulation Results . . . . .	111
4.2.4.2	Experimental Results . . . . .	113
4.3	Conclusions . . . . .	115
<b>5</b>	<b>SAPF Operation under Normal and Polluted Grid</b>	<b>117</b>
5.1	Single-Phase SAPF under Ideal Grid Condition . . . . .	118
5.1.1	SOGI Control with Unit Template Synchronization . . . . .	119
5.1.1.1	Estimation of Reference Current . . . . .	122
5.1.1.2	Simulation Results . . . . .	123
5.1.1.3	Experimental Results . . . . .	125
5.1.2	Cascaded SOGI with Unit-template Synchronization . . . . .	127
5.1.2.1	Simulation Results . . . . .	129
5.1.2.2	Experimental Results . . . . .	130
5.2	Single-Phase SAPF under Polluted Grid Condition . . . . .	133
5.2.1	SOGI Control with Adaptive-ZCD Synchronization Technique	133
5.2.1.1	Estimation of Reference Current and Switching Signals	133
5.2.1.2	Simulation Results . . . . .	134

5.2.1.3	Experimental Results . . . . .	136
5.2.2	SOGI-ROGI for Control and Synchronization . . . . .	139
5.2.2.1	Estimation of Reference Current and Switching Signals	140
5.2.2.2	Simulation Results . . . . .	141
5.2.2.3	Experimental Results . . . . .	145
5.3	Three-Phase SAPF under Ideal and Polluted Grid . . . . .	150
5.3.1	Three-Phase SRF Control with Unit-Template Synchronization	151
5.3.1.1	Fundamental Component Estimation by SRFT Algorithm . . . . .	151
5.3.1.2	Estimation of Loss Component . . . . .	152
5.3.1.3	Generation of Switching Pulses . . . . .	153
5.3.1.4	Simulation Results . . . . .	154
5.3.2	Three-Phase SRF control with SRF-PLL Synchronization Technique . . . . .	158
5.3.2.1	Simulation Results . . . . .	158
5.3.3	Three-Phase SRF Control with Spline-PLL Synchronization Technique . . . . .	162
5.3.3.1	Simulation results . . . . .	162
5.3.3.2	Experimental Results . . . . .	165
5.4	Conclusions . . . . .	166
<b>6</b>	<b>Power Quality Improvement in Single-Phase Grid-Connected PV System</b>	<b>168</b>
6.1	Single-Stage and Double-stage Grid-Connected PV System . . . . .	168
6.1.1	Fundamental Load Component Estimation . . . . .	169
6.1.1.1	Single-Phase SRFT Technique . . . . .	170
6.1.1.2	SOGI-ROGI Technique . . . . .	171
6.1.2	Maximum Power Point Tracking (MPPT) . . . . .	172
6.1.3	Feed-Forward Current Estimation . . . . .	175
6.1.4	Loss Component Estimation . . . . .	176

6.1.5	Generation of Switching Pulses . . . . .	176
6.2	Performance of SRFT Control in a Single-Phase Grid-Connected PV System . . . . .	177
6.2.1	Simulation Performance for Single-Stage Grid-Connected PV System . . . . .	178
6.2.2	Simulation Performance for Double-Stage Grid-Connected PV System . . . . .	182
6.3	Performance of SOGI-ROGI Control in a Single-Phase Grid-Connected PV System . . . . .	186
6.3.1	Simulation Performance for Single-Stage Grid-Connected PV System . . . . .	187
6.3.2	Experimental Performance for Single-Phase Single-Stage Grid- Connected PV System . . . . .	189
6.3.3	Simulation Performance for Double-Stage Grid Connected PV System . . . . .	190
6.4	Conclusions . . . . .	195
<b>7</b>	<b>Power Quality Improvement in Three-Phase Grid-Connected PV System</b>	<b>196</b>
7.1	Three-Phase Single-Stage and Double-Stage SAPF for Grid-Connected PV System . . . . .	196
7.1.1	Fundamental Load Current Component Estimation . . . . .	198
7.1.1.1	Three-Phase SRFT Control Technique . . . . .	198
7.1.1.2	Improved Adaline Control Technique . . . . .	199
7.1.2	Feed-Forward Current Estimation . . . . .	202
7.1.3	Estimation of Switching Pulses for Three-Phase VSC . . . . .	202
7.2	Performance of SRFT Control Algorithm for Three-Phase Grid-Connected PV System . . . . .	204
7.2.1	Simulation Results for Single-Stage Grid-Connected PV System	205
7.2.2	Simulation Results for Double-Stage Grid-Connected PV System	209

7.3	Performance of Improved Adaline Control Algorithm for Three-Phase Grid-Connected PV System . . . . .	213
7.3.1	Simulation Results for Single-Stage Grid-Connected PV System	214
7.3.2	Experimental Results for Single-Stage SAPF Grid-Connected PV System . . . . .	218
7.3.3	Simulation Results for Double-Stage SAPF Grid Connected PV System . . . . .	219
7.4	Conclusions . . . . .	223
<b>8</b>	<b>Conclusions and Future Scope</b>	<b>224</b>
8.1	Conclusions . . . . .	224
8.2	Future Scope . . . . .	227

# List of Figures

3.1	Single-phase SAPF system . . . . .	20
3.2	Single-phase single-stage grid connected PV system . . . . .	20
3.3	Experimental setup for single-phase single-stage grid connected PV system . . . . .	21
3.4	Single-phase double-stage grid connected PV system . . . . .	21
3.5	Practical single diode model of PV cell . . . . .	24
3.6	P-V and I-V curve of PV module (a) $25^{\circ}C$ and at specified irradiance (b) $1000W/m^2$ and at specified temperatures . . . . .	27
3.7	P-V and I-V curve of PV string for single-stage grid-tied PV system at STC (a) $25^{\circ}C$ and at specified irradiance (b) $1000W/m^2$ and at specified temperatures . . . . .	29
3.8	P-V and I-V curve of PV array for double-stage grid-tied PV system at STC (a) $25^{\circ}C$ and at specified irradiance (b) $1000W/m^2$ and at specified temperatures . . . . .	30
3.9	DC-DC boost converter circuit . . . . .	30
3.10	Hysteresis current controller . . . . .	32
3.11	Sensor circuits (a) voltage sensor circuit (b) current sensor circuit (c) practical voltage and current sensors . . . . .	34
3.12	Sensor circuits (a) Amplifier circuit for IGBT driver circuit (b) Prac- tical amplifier for Skyper 32 Pro . . . . .	35
3.13	Three-phase SAPF system . . . . .	36
3.14	Three-phase single-stage grid-tied PV system . . . . .	37

3.15	Experimental setup for three-phase grid tied PV system . . . . .	37
3.16	Three-phase double-stage grid-tied PV system . . . . .	38
4.1	Structure of single-phase SRF-LL . . . . .	43
4.2	Simulation performance of single-phase SRF-PLL under voltage sag of 0.3pu and polluted grid . . . . .	45
4.3	Simulation performance of single-phase SRF-PLL under frequency shift of +2Hz and noisy grid . . . . .	46
4.4	Simulation performance of single-phase SRF-PLL under phase-shift of $\pi/2$ and 20% DC-offset . . . . .	47
4.5	Experimental performance of single-phase SRF-PLL under (a) voltage sag of 20% (b) polluted grid (THD 18.0%) . . . . .	47
4.6	Experimental performance of single-phase SRF-PLL under (a) fre- quency shift of +2Hz (b) noisy grid . . . . .	48
4.7	Experimental performance of single-phase SRF-PLL under (a) phase- shift of $\pi/2$ (b) 20% DC-offset . . . . .	48
4.8	Structure of EPLL . . . . .	50
4.9	Simulation Performance of EPLL under voltage sag of 0.3pu and pol- luted grid . . . . .	53
4.10	Simulation performance of EPLL under frequency shift of +2Hz and noisy grid . . . . .	54
4.11	Simulation performance of EPLL under phase-shift of $\pi/2$ and DC- offset of 20% . . . . .	55
4.12	Experimental performance of single-phase EPLL under (a) voltage sag of 20% (b) polluted grid (THD 18.0%) . . . . .	56
4.13	Experimental performance of single-phase EPLL under (a) frequency shift of +2Hz (b) noisy grid . . . . .	56
4.14	Experimental performance of single-phase EPLL under (a) phase-shift of $\pi/2$ (b) 20% DC-offset . . . . .	56
4.15	Structure of SOGI-PLL . . . . .	58

4.16	Bode plot of SOGI for (a) In-phase component $D(s)$ (b) Quadrature component $Q(s)$ . . . . .	60
4.17	Step response of SOGI for (a) In-phase component $D(s)$ (b) Quadrature component $Q(s)$ . . . . .	60
4.18	Simulation performance of SOGI-PLL under voltage sag of 0.3pu and polluted grid . . . . .	61
4.19	Simulation performance of SOGI-PLL under frequency shift of 2Hz and noisy grid . . . . .	62
4.20	Simulation performance of SOGI-PLL under phase-shift of $\pi/2$ and DC-offset of 20% . . . . .	63
4.21	Experimental performance of single-phase SOGI-PLL under (a) voltage sag of 20% (b) polluted grid (THD 18.0%) . . . . .	64
4.22	Experimental performance of single-phase SOGI-PLL under (a) frequency shift of +2Hz (b) noisy grid . . . . .	64
4.23	Experimental performance of single-phase SOGI-PLL under (a) phase-shift of $\pi/2$ (b) 20% DC-offset . . . . .	64
4.24	Structure of SOGI-FLL . . . . .	66
4.25	Simulation performance of SOGI-FLL under voltage sag of 0.3pu and polluted grid . . . . .	68
4.26	Simulation performance of SOGI-FLL under frequency shift of 2Hz and noisy grid . . . . .	69
4.27	Simulation performance of SOGI-FLL under phase-shift of $\pi/2$ and DC-offset of 20% . . . . .	70
4.28	Experimental performance of single-phase SOGI-FLL under (a) voltage sag of 20% (b) polluted grid (THD 18.0%) . . . . .	70
4.29	Experimental performance of single-phase SOGI-FLL under (a) frequency shift of +2Hz (b) noisy grid . . . . .	71
4.30	Experimental performance of single-phase SOGI-FLL under (a) phase-shift of $\pi/2$ (b) 20% DC-offset . . . . .	71



4.31	Structure of SOGI-FLL cascaded with ROGI . . . . .	72
4.32	Bode plot of (a) SOGI-ROGI for $D(s)$ and $Q(s)$ (b) SOGI and SOGI-ROGI for in-phase component . . . . .	74
4.33	Simulation performance of SOGI-FLL-ROGI under voltage sag of 0.3pu and polluted grid . . . . .	75
4.34	Simulation performance of SOGI-FLL-ROGI under frequency shift of +2Hz and noisy grid . . . . .	76
4.35	Simulation performance of SOGI-FLL-ROGI under phase-shift of $\pi/2$ and DC-offset of 20% . . . . .	77
4.36	Experimental performance of single-phase SOGI-FLL-ROGI under (a) voltage sag of 20% (b) polluted grid (THD 18.0%) . . . . .	78
4.37	Experimental performance of single-phase SOGI-FLL-ROGI under (a) frequency shift of +2Hz (b) noisy grid . . . . .	78
4.38	Experimental performance of single-phase SOGI-FLL-ROGI under (a) phase-shift of $\pi/2$ (b) 20% DC-offset . . . . .	78
4.39	FFT analysis of (a) grid voltage signal (b) $u_g$ obtained from ROGI (c) $u_g$ obtained from SOGI-FLL (d) $u_g$ obtained from SOGI-FLL and ROGI . . . . .	79
4.40	Structure of conventional ZCD . . . . .	81
4.41	Structure of adaptive ZCD synchronization algorithm . . . . .	86
4.42	Simulation Performance of AZCD under voltage sag of 0.3pu and polluted grid . . . . .	87
4.43	Simulation Performance of AZCD under frequency shift of 2Hz and noisy grid . . . . .	88
4.44	Simulation performance of AZCD under phase-shift of $\pi/2$ and 20% DC-offset . . . . .	88
4.45	Experimental performance of single-phase AZCD based synchronization under (a) voltage sag of 30% (b) polluted grid (THD 18.0%) . . .	89

4.46	Experimental performance of single-phase AZCD based synchronization under (a) frequency shift of +2Hz (b) noisy grid . . . . .	89
4.47	Experimental performance of single-phase AZCD based synchronization under (a) phase-shift of $\pi/2$ (b) 20% DC-offset . . . . .	90
4.48	Simulation results of unit template based synchronization technique .	94
4.49	Experimental performance of three-phase unit-template based synchronization under (a) voltage sag of 30% (b) voltage swell of 30% . .	95
4.50	Experimental performance of three-phase unit-template based synchronization under (a) phase shift of $90^\circ$ (b) Polluted grid . . . . .	95
4.51	Structure three-phase SRF-PLL . . . . .	96
4.52	Simulation results of SRF-PLL . . . . .	97
4.53	Simulation results of SRF-PLL . . . . .	98
4.54	Experimental performance of three-phase SRF-PLL under (a) voltage sag of 30% (b) voltage swell of 30% . . . . .	98
4.55	Experimental performance of three-phase SRF-PLL under (a) phase shift of $90^\circ$ (b) Polluted grid . . . . .	99
4.56	Structure of conventional Adaline . . . . .	100
4.57	Structure of Improved Adaline based PLL . . . . .	102
4.58	Simulation results of IAdaline PLL under voltage sag and phase-shift	104
4.59	Simulation results of IAdaline PLL under polluted grid and frequency-shift . . . . .	105
4.60	Simulation results of IAdaline PLL under noisy signal and DC-offset of 20% . . . . .	106
4.61	Experimental performance of three-phase IAdaline-PLL under (a) voltage sag of 30% (b) voltage swell of 30% . . . . .	106
4.62	Experimental performance of three-phase IAdaline-PLL under (a) phase shift of $90^\circ$ (b) Polluted grid (c) Frequency shift of 2Hz . . . .	107
4.63	Experimental performance comparison of three-phase IAdaline-PLL and Adaline-PLL under (a) voltage sag of 30% (b) phase shift of $90^\circ$ .	107

4.64	Experimental performance comparison of three-phase IAdaline-PLL and Adaline-PLL under (a) frequency change of 2Hz (b) polluted grid	108
4.65	Structure of Spline-PLL . . . . .	111
4.66	Simulation results of Spline-PLL . . . . .	112
4.67	Simulation results of Adaptive Spline based PLL . . . . .	112
4.68	Experimental performance of three-phase Spline-PLL under (a) volt- age sag of 30% (b) voltage swell of 30% . . . . .	113
4.69	Experimental performance of three-phase Spline-PLL under (a) phase- shift of 90° (b) frequency change of 2Hz (c) polluted grid . . . . .	114
5.1	Single-phase SAPF configuration for simulation . . . . .	117
5.2	Single-phase SAPF configuration for experimental setup . . . . .	118
5.3	Structure of SOGI control applied to load current signal ( $i_L$ ) . . . . .	119
5.4	Step response of SOGI for in-phase component $D_2(s)$ . . . . .	121
5.5	Single-phase SAPF control structure . . . . .	123
5.6	Single-phase SAPF performance of SOGI with unit template synchro- nization . . . . .	124
5.7	Single-phase SAPF performance of SOGI with unit template synchro- nization . . . . .	124
5.8	THD analysis of (a) Grid voltage (b) Grid current (c) Load current .	125
5.9	Estimation of in-phase and quadrature load component by SOGI for (a) Load decrease (b) Load increase . . . . .	125
5.10	Experimental dynamic performance of SOGI control (a) transition of without SAPF to with SAPF (b) load decrease . . . . .	126
5.11	Steady-state experimental performance (a) $v_g$ and $i_L$ (b)THD of $i_L$ (c) $v_g$ and $i_g$ (d) THD of $i_g$ . . . . .	127
5.12	Structure of cascaded SOGI . . . . .	127
5.13	Bode plot for cascaded SOGI . . . . .	128
5.14	Single-phase SAPF control structure for cascaded SOGI and unit tem- plate synchronization . . . . .	129

5.15	Open-loop performance of cascaded SOGI . . . . .	129
5.16	Experimental closed-loop steady-state performance under cascaded SOGI with unit template synchronization (a) $v_g$ and $i_L$ (b) THD of $i_L$ , 27.3% (c) $v_g$ , $i_g$ for 4 <sup>th</sup> order GI (d) THD of $i_g$ for 4 <sup>th</sup> order GI, 4.0% (e) $v_g$ , $i_g$ for 6 <sup>th</sup> order GI (f) THD of $i_g$ for 6 <sup>th</sup> order GI, 3.9% (g) $v_g$ , $i_g$ for 8 <sup>th</sup> order GI (h) THD of $i_g$ for 8 <sup>th</sup> order GI , 3.8% . . .	131
5.17	Single-phase SAPF control structure under polluted grid condition . .	134
5.18	Simulation performance of single-phase SAPF with SOGI control and A-ZCD synchronization . . . . .	135
5.19	Simulation performance for power of single-phase SAPF with SOGI control and A-ZCD synchronization . . . . .	136
5.20	THD analysis for SAPF with SOGI and AZCD synchronization under normal and polluted grid (a) THD of polluted grid ( $v_g$ ) (b) THD of $i_L$ (c) THD of $i_g$ with unit template synchronization (d) THD of $i_g$ under AZCD synchronization . . . . .	137
5.21	Steady-state results for SAPF with SOGI control and AZCD syn- chronization under normal grid(a) $v_g$ and $i_L$ (b) load current THD (c) grid voltage THD (d) $v_g$ and $i_g$ (e) grid current THD . . . . .	137
5.22	Steady-state results for SAPF with SOGI control and AZCD synchro- nization under polluted grid(a) $v_g$ and $i_L$ (b) load current THD (c) grid voltage THD (d) $v_g$ and $i_g$ (e) grid current THD . . . . .	138
5.23	Structure of SOGI-ROGI for fundamental current component estima- tion . . . . .	139
5.24	Control structure for single-phase SAPF for SOGI-ROGI . . . . .	142
5.25	Simulation results (a) SOGI-ROGI performance (b) Comparison of ROGI, SOGI and SOGI-ROGI . . . . .	142
5.26	Simulation performance of single-phase SAPF with SOGI-ROGI con- trol and SOGI-FLL-ROGI synchronization . . . . .	143

5.27	Simulation performance for power of single-phase SAPF with SOGI-ROGI control and SOGI-FLL-ROGI synchronization . . . . .	144
5.28	THD analysis for SAPF with SOGI-ROGI and SOGI-FLL-ROGI synchronization, Case I: Standard/Normal grid (a) THD of $v_g$ (b) THD of $i_L$ (c) THD of $i_g$ Case II: Polluted grid (d) THD of polluted grid ( $v_g$ ) (e) THD of $i_L$ (f) THD of $i_g$ . . . . .	145
5.29	Experimental results for fundamental load component and intermediates (a) Load increase ( $i_L$ , $i'_\alpha$ , $i_\alpha$ , $I_f$ ) (b) Load increase ( $i_L$ , $I_f$ by ROGI, SOGI-FLL and SOGI-FLL-ROGI) (C) Load decrease ( $i_L$ , $I_f$ by ROGI, SOGI-FLL and SOGI-FLL-ROGI) . . . . .	146
5.30	Steady-state experimental performance of single-phase SAPF with non-linear load and normal grid condition by SOGI-FLL-ROGI algorithm (a) $v_g$ and $i_L$ (b) $v_g$ and $i_g$ (c) $v_g$ and $i_c$ (d) load power (e) grid power (f) load current THD (g) grid voltage THD (h) grid current THD . . . . .	147
5.31	Steady-state experimental performance of single-phase SAPF with non-linear load and polluted grid condition by SOGI-ROGI algorithm (a) $v_g$ and $i_L$ (b) $v_g$ and $i_g$ (c) $v_g$ and $i_c$ (d) load power (e) grid power (f) load current THD (g) grid voltage THD (h) grid current THD . .	148
5.32	Closed-loop dynamic performance of SOGI-ROGI with sudden load change (a) load decrease ( $v_g$ , $i_g$ , $i_L$ and $V_{dc}$ )(b) load increase ( $v_g$ , $i_g$ , $i_L$ and $V_{dc}$ ) . . . . .	149
5.33	Structure of three-phase system with three phase 3-leg SAPF . . . .	150
5.34	Control structure of three-phase SAPF control with unit template synchronization . . . . .	151
5.35	Fundamental current component by SRF technique . . . . .	154
5.36	Three-phase simulation performance under SRF control and unit-template synchronization . . . . .	155

5.37	Three-phase power performance under SRF control and unit-template synchronization . . . . .	156
5.38	THD analysis for three-phase SAPF with SRF and unit-template synchronization, Case I: Normal grid (a) THD of $v_{ga}$ (b) THD of $i_{La}$ (c) THD of $i_{ga}$ Case II: Polluted grid (d) THD of polluted grid $v_{ga}$ (e) THD of $i_{La}$ (f) THD of $i_{ga}$ . . . . .	157
5.39	Control structure of three-phase SAPF control with SRF-PLL based synchronization . . . . .	158
5.40	Three-phase simulation performance under SRF control and SRF-PLL based synchronization . . . . .	159
5.41	Three-phase power performance under SRF-PLL based synchronization	159
5.42	THD analysis for three-phase SAPF with SRF-PLL based synchronization, Case I: Normal grid (a) THD of $v_{ga}$ (b) THD of $i_{La}$ (c) THD of $i_{ga}$ Case II: Polluted grid (d) THD of polluted grid $v_{ga}$ (e) THD of $i_{La}$ (f) THD of $i_{ga}$ . . . . .	160
5.43	Control structure of three-phase SAPF control with adaptive spline based synchronization . . . . .	162
5.44	Three-phase simulation performance under SRF control and adaptive spline based synchronization . . . . .	163
5.45	Three-phase power performance under SRF-PLL based synchronization	164
5.46	THD analysis for three-phase SAPF with spline based synchronization, Case I: Normal grid (a) THD of $v_{ga}$ (b) THD of $i_{La}$ (c) THD of $i_{ga}$ Case II: Polluted grid (d) THD of polluted grid $v_{ga}$ (e) THD of $i_{La}$ (f) THD of $i_{ga}$ . . . . .	164
5.47	Experimental results for Spline based synchronization for polluted grid condition (a) Three-phase polluted grid ( $v_{gabc}$ ) and extracted synchronizing signal ( $u_{pa}$ ) (b) SAPF operation during load unbalancing ( $v_{ga}, i_{ga}, i_{La}$ and $V_{dc}$ ) . . . . .	166

5.48	Experimental steady-state performance with Spline based synchronization under distorted grid voltage (a) $v_{LL}$ and $i_{ga}$ (b) $v_{LL}$ and $i_{La}$ (d) THD of polluted grid voltage (e) THD of load current (f) THD of grid current . . . . .	167
6.1	Single-phase single-stage grid connected PV system . . . . .	169
6.2	Single-phase double-stage grid connected PV system . . . . .	169
6.3	Fundamental load current component by SRFT . . . . .	170
6.4	Structure of SOGI-ROGI for fundamental current component estimation . . . . .	171
6.5	P-V and I-V curve of PV module (a) $25^{\circ}C$ and at specified irradiance (b) $1000W/m^2$ and at specified temperatures . . . . .	173
6.6	Flow chart of P&O MPPT . . . . .	174
6.7	Single-phase single-stage SRFT control structure for grid-connected PV system . . . . .	177
6.8	Single-phase double-stage SRFT control structure for grid-connected PV system . . . . .	177
6.9	Simulation performance of PV string under single-stage grid-connected PV system . . . . .	178
6.10	Simulation performance for grid parameters of single-phase single-stage grid-connected PV system . . . . .	179
6.11	THD analysis for single-phase single-stage grid-connected PV system with SRFT technique with additional LPF, Case I: Standard/Normal grid (a) THD of $v_g$ (b) THD of $i_L$ (c) THD of $i_g$ Case II: Polluted grid (d) THD of polluted grid ( $v_g$ ) (e) THD of $i_L$ (f) THD of $i_g$ . . .	180
6.12	THD analysis for single-phase single-stage grid-connected PV system with SRFT technique without additional LPF, Case I: Standard/Normal grid (a) THD of $i_g$ , Case II: Polluted grid (b) THD of $i_g$ . . . . .	181

6.13	Simulation performance for power transfer under single-phase single-stage grid-connected PV system . . . . .	181
6.14	Simulation performance of PV string under double-stage grid-connected PV system . . . . .	182
6.15	Simulation performance for grid parameters of single-phase double-stage grid-connected PV system . . . . .	183
6.16	THD analysis for single-phase double-stage grid-connected PV system with SRFT technique with additional LPF, Case I: Standard/Normal grid (a) THD of $v_g$ (b) THD of $i_L$ (c) THD of $i_g$ Case II: Polluted grid (d) THD of polluted grid ( $v_g$ ) (e) THD of $i_L$ (f) THD of $i_g$ . . .	184
6.17	Simulation performance for power transfer under single-phase double-stage grid-connected PV system . . . . .	185
6.18	Single-phase single-stage SOGI-ROGI control structure for grid-connected PV system . . . . .	186
6.19	Single-phase double-stage SOGI-ROGI control structure for grid-connected PV system . . . . .	186
6.20	Simulation performance of PV string under single-stage grid-connected PV system . . . . .	187
6.21	Simulation performance for grid parameters of single-phase single-stage grid-connected PV system . . . . .	188
6.22	Simulation performance for power transfer under single-phase single-stage grid-connected PV system . . . . .	188
6.23	THD analysis for single-phase single-stage grid-connected PV system with SOGI-ROGI technique, Case I: Standard/Normal grid (a) THD of $v_g$ (b) THD of $i_L$ (c) THD of $i_g$ Case II: Polluted grid (d) THD of polluted grid ( $v_g$ ) (e) THD of $i_L$ (f) THD of $i_g$ . . . . .	190
6.24	Experimental closed-loop steady-state performance of PV array under single-stage grid-connected PV system . . . . .	191



6.25	Simulation performance of PV array for double-stage grid-connected PV system with varying irradiance level . . . . .	192
6.26	Simulation performance for grid parameters of single-phase double-stage grid-connected PV system . . . . .	192
6.27	Simulation performance for power transfer under single-phase double-stage grid-connected PV system . . . . .	193
6.28	THD analysis for single-phase double-stage grid-connected PV system with SOGI-ROGI technique, Case I: Standard/Normal grid (a) THD of $v_g$ (b) THD of $i_L$ (c) THD of $i_g$ Case II: Polluted grid (d) THD of polluted grid ( $v_g$ ) (e) THD of $i_L$ (f) THD of $i_g$ . . . . .	194
7.1	Three-phase single-stage grid-connected PV system . . . . .	197
7.2	Three-phase double-stage grid-connected PV system . . . . .	197
7.3	Structure of Improved Adaline control technique . . . . .	199
7.4	Performance comparison of Improved Adaline versus conventional Adaline . . . . .	201
7.5	Structure of SRFT control technique for three-phase single-stage grid-connected PV system . . . . .	204
7.6	Structure of SRFT control technique for three-phase double-stage grid-connected PV system . . . . .	205
7.7	Simulation performance of PV string under single-stage grid-connected PV system . . . . .	205
7.8	Simulation performance for grid parameters of single-stage grid-connected PV system . . . . .	206
7.9	THD analysis for single-stage grid-connected PV system with SRFT technique Case I Normal grid (a) THD of $v_{ga}$ (b) THD of $i_{Lb}$ (c) THD of $i_{ga}$ Case II Polluted grid (d) THD of $v_{ga}$ (e) THD of $i_{La}$ (f) THD of $i_{ga}$ . . . . .	207
7.10	Simulation performance for power transfer in single-stage grid-connected PV system . . . . .	208

7.11	Simulation performance of PV string under double-stage grid-connected PV system . . . . .	209
7.12	Simulation performance for grid parameters of double-stage grid-connected PV system . . . . .	210
7.13	THD analysis for double-stage grid-connected PV system with SRFT technique Case I Normal grid (a) THD of $v_g$ (b) THD of $i_L$ (c) THD of $i_g$ Case II Polluted grid (d) THD of $v_g$ (e) THD of $i_L$ (f) THD of $i_g$	211
7.14	Simulation performance for power transfer in double-stage grid-connected PV system . . . . .	211
7.15	Structure of IAdaline control technique for three-phase single-stage grid-connected PV system . . . . .	213
7.16	Structure of IAdaline control technique for three-phase double-stage grid-connected PV system . . . . .	214
7.17	Simulation performance of PV string under single-stage grid-connected PV system . . . . .	215
7.18	Simulation performance for grid parameters of single-stage grid-connected PV system . . . . .	216
7.19	THD analysis for single-stage grid-connected PV system with Im- proved Adaline technique Case I Normal grid (a) THD of $v_{ga}$ (b) THD of $i_{La}$ (c) THD of $i_{ga}$ Case II Polluted grid (d) THD of $v_{ga}$ (e) THD of $i_{La}$ (f) THD of $i_{ga}$ . . . . .	217
7.20	Simulation performance for power transfer in single-stage grid-connected PV system . . . . .	217
7.21	Experimental performance of single-stage SAPF grid-connected PV system (a) $v_{ga}$ and $i_{La}$ (b) $v_{ga}$ and $i_{ga}$ (c) $v_{ga}$ and $i_{ca}$ (d) THD of $i_{La}$ (e) THD of $i_{ga}$ (f) Load power (g) Grid power (h) Compensator power	218
7.22	Simulation performance of PV array under double-stage grid-connected PV system . . . . .	219

7.23	Simulation performance for grid parameters of double-stage grid-tied PV system . . . . .	220
7.24	THD analysis for double-stage grid-connected PV system with Im- proved Adaline technique Case I: Normal grid (a) THD of $v_{ga}$ (b) THD of $i_{La}$ (c) THD of $i_{ga}$ Case II: Polluted grid (d) THD of $v_{ga}$ (e) THD of $i_{La}$ (f) THD of $i_{ga}$ . . . . .	221
7.25	Simulation performance for power transfer in double-stage grid-connected PV system . . . . .	222

# List of Tables

3.1	Ideality factor (A) [1] . . . . .	25
3.2	Module Parameters at STC (Vikram Solar ELDORA270) . . . . .	26
3.3	PV string parameters at STC for single-stage grid-connected PV system	28
3.4	PV array parameters at STC for double-stage grid-tied PV system . .	30
3.5	PV string parameters at STC for single-stage grid-tied PV system . .	40
3.6	PV array parameters at STC for double-stage grid-tied PV system . .	41
4.1	Summary of simulation and experimental performance of delay based SRF-PLL . . . . .	49
4.2	Summary of simulation and experimental performance of EPLL . . .	57
4.3	Summary of simulation and experimental performance of SOGI-PLL .	65
4.4	Summary of simulation and experimental performance of SOGI-FLL .	72
4.5	THD of the synchronizing signal ( $u_g$ ) obtained by ROGI, SOGI-FLL and SOGI-FLL-ROGI . . . . .	80
4.6	Summary of simulation and experimental performance of AZCD . . .	90
4.7	Performance comparison for single-phase synchronization techniques .	92
4.8	Performance comparison for three-phase synchronization techniques .	114
5.1	Performance of SOGI control with unit template synchronization un- der normal grid condition . . . . .	126
5.2	Performance summary of SOGI and cascaded SOGI control . . . . .	131
5.3	Performance summary of SOGI with AZCD synchronization under normal and polluted grid . . . . .	138

5.4	Performance comparison of control and synchronization technique for single-phase SAPF . . . . .	149
5.5	Performance comparison of synchronization techniques for three-phase SAPF . . . . .	165
6.1	Performance summary of SRFT and SOGI-ROGI control algorithm for single-stage and double-stage grid-connected PV system . . . . .	194
7.1	Performance summary of SRFT and IAdaline control algorithm for three-phase single-stage and double-stage grid-connected PV system .	222
8.1	Parameters for single-phase and three-phase grid-connected PV system	250

# List of Symbols

$v_g$	Single-phase grid voltage
$v_{gabc}$	Three-phase grid voltages
$i_g$	Single-phase grid current
$i_{gabc}$	Three-phase grid currents
$i_l$	Single-phase load current
$i_{labc}$	Three-phase load currents
$i_c$	Single-phase inverter Current
$i_{cabc}$	Three-phase inverter currents
$V_{dc}$	DC-link voltage
$C_{dc}$	DC-link capacitor
$V_{dcref}$	DC-link reference voltage
$I_{ff}$	Feed-forward current
$L_f$	Interfacing inductor
$V_{pv}$	PV voltage
$I_{pv}$	PV current
$P_{pv}$	PV power
D	Duty-cucle of DC-DC boost converter
$V_{mpp}$	Maximum power point voltage

$\theta_i$	Phase angle of grid voltage
$\theta_o$	Estimated phase angle
$\phi_o$	Initial phase angle
$\omega$	Grid voltage frequency (rad/s)
$\omega_o$	Estimated grid voltage frequency (rad/s)
$\omega_n$	Standard frequency of grid voltage (rad/s)

# List of Abbreviations

SAPF	Shunt Active Power Filter
VCO	Voltage Controlled Oscillator
FFT	Fast Fourier Transform
PCC	Point of Common coupling
SRFT	Synchronous Reference Frame Theory
PV	Photovoltaic
MPPT	Maximum Power Point Technique
PLL	Phase-Locked Loop
EPLL	Enhanced Phase-Locked Loop
FLL	Frequency-Locked Loop
SOGI	Second-Order Generalized Integrator
VSC	Voltage Source Converter
CSI	Current Source Converter
IGBT	Insulated-Gate Bipolar Transistor
ROGI	Reduced-Order Generalized Integrator
IAdaline	Improved Adaline
HCC	Hysteresis Current Controller
PWM	Pulse Width Modulation



AZCD	Adaptive Zero-Crossing Detection
THD	Total Harmonic Distortion
STC	Standard Test Conditions
UPQC	Unified Power Quality Conditioner

# Chapter 1

## Introduction

### 1.1 General

Energy is the main factor for the development of any country. For the developing countries, the energy sector assumes a critical importance in view of the ever-increasing energy needs and it requires huge investments to meet them. Among the different form of energy, electrical energy is most useful and efficient as it have various advantages such as ease of distribute and transport, store, control, ease of use and cleaner than other forms of energy [2]. Electrical energy can be generated by the renewable sources and non-renewable sources. Due to the alarming situation of global warming the world is looking towards the renewable energy sources as these have less negative impact on the environment and inexhaustible in nature. In India, production of electrical energy from the renewable energy sources is fourth largest in the world and growing at fastest rate among the major countries. Indian government has scaled up the target of 100GW by solar power by the end of 2022 [3]. Solar energy specifically solar PV is the most prominent than other renewable energy sources such as hydro, wind, biomass and geothermal because of various advantages. The main advantages of solar energy are: found abundant in nature, non-polluting (except during the manufacturing), noiseless operation, low maintenance required, can be installed as modular basis and can be expanded over time and can be installed in remote location. Also they can be installed in places with no other use, such as roofs and deserts, where there is no electricity network

available.

Generation of the electrical energy from the solar PV is largely dependent on the environmental conditions mainly the solar irradiance and temperature. The characteristics of PV is non-linear in nature. Hence, to extract maximum power from the solar PV, Maximum Power Point Tracking (MPPT) techniques are required. Energy generation from solar PV is growing at a very fast rate and is quickly becoming an important part of the energy mix in some regions and power systems. This has been driven by a reduction in the cost of PV modules. This growth has also triggered the evolution of classic PV power converters from conventional single-phase and three-phase grid-connected inverters to more complex topologies to increase efficiency, power extraction from the modules, and reliability without impacting the cost.

Energy harvested from the PV can be configured as grid-connected mode and stand-alone mode. In grid-connected mode, PV has been connected to the distribution grid and the excess power can be feed to the distribution grid. In a conventional PV system, the PV cells (arranged in a single module, a string of series-connected modules, or an array of parallel-connected strings) generate a DC that greatly depends on the solar irradiance, temperature and voltage at the terminals of the PV system. This dc power is transformed and interfaced to the grid via Voltage Source Converter (VSC). Another option is an intermediate DC-DC power stage between the PV modules and the grid-connected VSC. This optional stage decouples the PV system operating point from the PV inverter grid control. Additionally, it can boost the PV system dc output voltage if required or provide galvanic isolation and perform MPPT implementation. The increase in the PV installed capacity has also sparked a continuous evolution of the PV power conversion stage. Gradually, PV power converters have become extremely efficient, compact, and reliable, allowing the maximum power to be obtained from the sun in domestic, commercial, and industrial applications. The PV converter industry has evolved rapidly from childhood to adulthood in the last two decades and has become a distinct power converter

category. One of the drivers behind this progress is that the PV converter market demanded very hard to meet specifications, including high efficiency, long warranty periods, high power quality, transformer less operation, and special control requirements. The integration of PV to the grid increases the reliability of the system. There are already a number of power quality issues in the grid and connecting the PV to the grid can create power quality issues if it cannot done by proper synchronization methods. So, it requires to first understand the power quality issues, its reasons and its mitigation techniques.

## 1.2 Modern Distribution System and Power Quality

The term electric Power Quality (PQ) is used to assess and to maintain the good quality of power at the level of generation, transmission, distribution, and utilization of AC electrical power [4, 5]. There are a number of reasons for the pollution of the AC supply systems, including natural ones such as lightning, flashover, equipment failure, and faults and forced ones such as voltage distortions and notches.

A number of customer's equipment also pollute the supply system as they draw non-sinusoidal current and behave as non-linear loads. Therefore, power quality is quantified in terms of voltage, current, or frequency deviation of the supply system, which may result in failure or mal-operation of customer's equipment [6]. Typically, some power quality problems related to the voltage at the Point of Common Coupling (PCC) where various loads are connected are the presence of voltage harmonics, surge, spikes, notches, sag/dip, swell, unbalance, fluctuations, glitches, flickers, outages and so on. These problems are present in the supply system due to various disturbances in the system or due to the presence of various nonlinear loads such as furnaces, uninterruptible power supplies, and adjustable speed drives. However, some power quality problems related to the current drawn from the AC mains are poor power factor, reactive power burden, harmonic currents, unbalanced

currents, and an excessive neutral current in poly-phase systems due to unbalancing and harmonic currents generated by some nonlinear loads. These power quality problems cause failure of capacitor banks, increased losses in the distribution system and electric machines, noise, vibrations, over-voltages and excessive current due to resonance, negative sequence currents in generators and motors, especially rotor heating, de-rating of cables, dielectric breakdown, interference with communication systems, signal interference in relay and breaker malfunctions, false metering, interferences to the motor controllers and digital controllers, and so on. A number of techniques have evolved for the mitigation of these problems either in existing systems or in equipment to be developed in the near future [7]. It has resulted in a new direction of Research and Development (R&D) activities for the design and development engineers working in the fields of power electronics, power systems, electric drives, digital signal processing, and sensors. It has changed the scenario of power electronics as most of the equipment using power converters at the front end need modifications in view of these newly visualized requirements. In existing non-linear loads, having the power quality problems of poor power factor, harmonic currents, unbalanced currents, and an excessive neutral current, a series of power filters of various types such as passive, active, and hybrid in shunt, series, or a combination of both configurations are used externally depending upon the nature of loads such as voltage-fed loads, current-fed loads, or a combination of both to mitigate these problems. However, in many situations, the power quality problems may be other than those of harmonics such as in distribution systems, and the custom power devices such as Distribution Static Compensators (DSTATCOMs), Dynamic Voltage Restorers (DVRs), and Unified Power Quality Conditioners (UPQCs) [8] are used for mitigating the current, voltage or both types of power quality problems.

### 1.3 State of Art

A substantial literature has been reported on the control of single-phase and three-phase grid-connected PV system with the capability of improving the power quality

under normal and distorted grid conditions feeding the non-linear load. Due to the inherent non-linear characteristics of PV, maximum power point tracking technique become necessity. Various techniques have been proposed by the researchers such as Perturb and Observe (P&O), incremental conductance, fuzzy-based and neural network-based techniques. In these techniques, the P&O is the most simple and efficient technique and hence is developed in the thesis work.

The research work in this thesis revolves around the development of appropriate controllers designed to mitigate several power quality problems. The control algorithms need to achieve several tasks viz. fundamental component estimation, synchronizing signal estimation, DC-link voltage controller and the feed-forward current estimation.

Synchronization techniques commonly employed focus on a Phase Locked-Loop (PLL) circuit. The most general PLL circuit comprises a phase detector, loop filter and a voltage-controlled oscillator. All phase-locked loops are designed to compute the input signal's amplitude, phase angle and frequency. Synchronous Reference Frame Theory-based PLL (SRF-PLL) is a very common and popular synchronization technique. It is found to work very well under normal operating conditions but its performance deteriorates immensely under the influence of harmonics in grid voltage. Hence, there is a need to design, study and analyse the behaviour of new synchronization circuits. Some improved PLLs are reported such as Enhanced Phase Locked-Loop (EPLL), Second Order Generalized Integrator (SOGI)-PLL, Double Decoupled Synchronous Reference Frame (DDSRF)- PLL and others have been studied and investigated for single-phase and three-phase circuits.

Due to the nature of single-phase circuits, only one voltage signal makes the use of available transformations such as Clarke's and Park's are difficult; and hence there is a need to generate quadrature signal also. Now, with the input signal ( $v_\alpha$ ) and its quadrature component ( $v_\beta$ ),  $\alpha\beta$  to dq transform can be realized and PLL can be designed. Many Quadrature Signal Generators (QSG) have been reported in the literature, and these include the  $T/4$  delay and the SOGI-PLL. A few papers on

comparison between the performance of single-phase PLLs have been reported in the literature.

Different control-techniques have been proposed for the estimation of the fundamental component of the load current. The focus while designing these control algorithms is based on fast response and minimum oscillations during steady-state and dynamic conditions under different loading conditions. Different algorithms have been employed to improve the power quality in single-phase and three-phase systems. Some conventional algorithms that have been reported in the literature which include Instantaneous Reactive Power Theory (IRPT), Power Balance Theory (PBT), SRFT. SOGI controller and its different variants have been implemented in single-phase and three-phase systems. Adaptive control algorithms have made good improvements in the mitigation of PQ problems with Adaline, Least Means Forth (LMF) and various versions of Least Mean Square (LMS) based techniques.

## 1.4 Scope of Work

Based on the exhaustive literature review on the design, control and analysis of grid-connected PV system, some major gaps have been identified. These issues deal with synchronization and adequate compensation. The estimation of synchronization techniques from the grid voltage under various conditions as well as estimating the fundamental component of non-linear load current are equally important. Appropriate synchronization techniques and control algorithms need to be designed and selected. Performance of the selected techniques should be fast under dynamic conditions, having zero steady state error and robust performance without increasing the complexity of the algorithm.

The main objectives of the proposed research work are to design and develop single-phase and three-phase grid-connected PV systems in the laboratory which are able to improve the various power quality issues. Such power quality issues include reactive power compensation, harmonic mitigation, power factor improvement, load balancing and voltage regulation. The detailed description of the proposed work for

single-phase and three-phase systems are given below:

- **Design and development of SAPF for grid-connected PV system**

System configuration of single-phase and three-phase systems have been designed. The power components for the single-phase system are IGBT based H-bridge VSC, DC-link capacitor, interfacing inductors, single-phase programmable supply, linear and non-linear loads. Voltage and current sensors are employed to sense the different required parameters from the single-phase grid-connected PV system for the hardware setup. In a three-phase system, three-phase IGBT based VSC has been employed. The design of the PV array has been done as per the specification of grid voltage and as per the configuration of PV.

- **Developments of synchronization techniques**

Both conventional and proposed synchronization techniques have been developed in this research work. These synchronization techniques have been tested under different grid voltage issues such as sag, harmonic, noisy, dc-offset, phase-change and frequency change. Synchronization techniques investigated and proposed in the thesis include SRF-PLL, EPLL, SOGI-PLL, SOGI-Frequency Locked-Loop (SOGI-FLL), SOGI-FLL-Reduced Order Generalized Integrator (SOGI-FLL-ROGI) and Adaptive Zero-Crossing Detector (AZCD) for a single phase. Unit-template, SRF-PLL, Improved Adaline and Spline based synchronization techniques has been designed, developed and tested for three-phase system. Simulation and experimental validation of the developed techniques is presented in the research work.

- **Development of algorithms for fundamental component estimation**

Shunt compensation using advanced control techniques is also an important objective of this thesis work. Techniques such as SOGI, cascaded-SOGI, SOGI-ROGI have been employed for single-phase SAPF and SRF based control algorithm has been employed for three-phase SAPF.

- **Application of synchronization techniques for SAPF**



Application of some single-phase and three-phase synchronization techniques have been proposed for obtaining the fundamental component of distorted load current. Such control algorithms have been used for the control of SAPF. The developed SAPF system has been employed for reactive power compensation, power factor correction and harmonic mitigation.

- **VSC application to grid-integration to solar PV**

Solar PV has been integrated into the grid in single-phase and three-phase systems. Now the system enables the active power feeding to the grid from PV along with reactive power compensation. MPPT technique has also been employed to receive maximum power from the PV array. Both simulation and experimental results are presented to show the performance of the developed algorithms.

## 1.5 Thesis Structure

The content of the thesis work has been divided into the following chapters:

**Chapter-1:** This chapter presents an introduction and background for PV integration to the grid, power quality causes, issues and solutions.

**Chapter-2:** This chapter includes a literature review on system configuration and control for single-phase and three-phase grid-tied PV systems, synchronization techniques and fundamental component estimation techniques.

**Chapter-3:** This chapter discusses the modelling of PV and design of PV array for grid integration. The design of power components and other equipment for both single-phase and three-phase systems are also discussed in this chapter.

**Chapter-4:** This chapter includes various synchronization techniques, their modeling and implementation for single-phase and three-phase systems under various grid voltage conditions. Single-phase synchronization techniques discussed include delay based SRF-PLL, EPLL, SOGI-PLL, SOGI-FLL, SOGI-FLL-ROGI and Adaptive ZCD techniques have been discussed. Three-phase synchronization techniques discussed are unit-template, SRF-PLL, Improved Adaline PLL and Adaptive Spline

based techniques.

**Chapter-5:** This chapter discusses the implementation of synchronization techniques and control techniques for power quality improvement in single-phase and three-phase systems without PV interface. It also discusses the Shunt Active Power Filter (SAPF) under both ideal and polluted grid-voltage conditions. SOGI, cascaded SOGI and SOGI-FLL-ROGI have been used for development of controller.

**Chapter-6:** This chapter discusses PV integration to the grid in single-stage and double-stage configuration for single-phase SAPF. SOGI-FLL based control and synchronization technique has been developed to improve the PQ under both ideal and polluted grid conditions feeding non-linear load.

**Chapter-7:** This chapter discusses the PV integration to the grid in single-stage and double-stage for three-phase system. Improved Adaline based technique has been designed and developed for synchronization and control to improve PQ under ideal and polluted grid condition feeding non-linear load.

**Chapter-8:** This chapter summarizes of different grid synchronization techniques, control algorithms and the PV integration to the grid in single-phase and three-phase systems. The future scope of work in this area is also presented at the end of this chapter.

# Chapter 2

## Literature Survey

### 2.1 General

In previous chapter, introduction to requirement of solar PV, PQ issues, effect and its solutions in a grid-connected PV system have been presented. The state of art, scope of work and the layout of the thesis work has been discussed. PV integration to the grid enables active power injection to the grid. To study the PV characteristics and extract the power from the PV require precise modelling which matches the characteristics of practical PV. Modern distribution system has been connected to the different types of loads which impacts the quality of power and has been reviewed. In this chapter, the extensive literature review for the synchronization and control algorithms has been done which further enable the robust working of the SAPF under different loading and grid voltage conditions. PV is connected to the DC-link of VSC to transfer the excess power to distribution grid. The detailed review for different system configuration has been done to transfer excess power to distribution grid.

### 2.2 Literature Survey on PV Modelling and MPPT Techniques

Efficiency of solar cell varies from 6% for amorphous silicon-based solar cells to 44% for multi-junction production cells and is achieved in laboratories [9–11]. In practical

solar cells, efficiency of solar cells varies from 15% to 22% [12, 13]. Efficiency of solar cells largely vary due to the environmental conditions such as solar irradiance, temperature, dust and other suspended particles. A solar cell can be modelled in single-diode model or diode model [14–17]. A single-diode model with series and shunt resistance considered identical with the practical solar cell with less complexity [1]. Solar cell is the current source type and its characteristics is non-linear in nature [18]. A single-cell can not produce enough energy to use it for power applications. Hence, number of cell has been connected in series makes it solar PV module and number of PV modules have been connected in series or parallel as per requirement to get large amount of power. To extract maximum power from the PV module or array it require MPPT technique. Various literature have been available on MPPT technique [19–22]. P&O and incremental conductance are conventional algorithms which are easy to implement, less complex and works good under varying irradiance and temperature condition [23–26].

## **2.3 Literature Survey on PQ Problems, Impacts and Their Solutions**

Modern distribution systems are very complex and have been connected to different types of loads. Different PQ issues may occurred due to different loading conditions and natural reasons. Broadly, main PQ issues are transients, short-duration voltage variation, long-time voltage variation, voltage imbalance, voltage flicker and waveform distortion. The main causes of these PQ issues are lightning strike, capacitor switching, single line to ground faults, switching on/off loads, single-phase loads connected to three-phase supply, adjustable speed drives, power electronic converters, half-wave rectification, arc furnaces and other non-linear loads [27, 28]. These PQ issues cause failure, mal-operation of electrical equipments and energy loss which further leads to the economic loss directly or indirectly [29]. The injection of harmonics at the PCC in modern distribution system are the serious concerns of

power engineers. The main reason is the advancement of power electronics devices which are connected to the distribution system which introduces harmonics in the system. Integration of large scale PV and the fast charging EV battery connected to distribution system also impacted adversely specially on voltage magnitude and harmonics [30,31].

Non-linear loads alter the sinusoidal nature of the AC power current, thereby resulting in the flow of harmonic currents in the ac power system that can cause interference with communication system and other types of sensitive equipment. These harmonic currents also lead to increased losses and heating in numerous electromagnetic devices. When reactive power compensation, in the form of power factor improvement capacitors, is used, resonant conditions can occur that may result in high levels of harmonic voltage and current distortion when the resonant condition occurs at a harmonic associated with non-linear loads. Institute of Electrical and Electronics engineers (IEEE) and International Electrochemical Commission (IEC) have been proposed PQ standards [32,33]. IEEE 1159:2009 (revision of IEEE Std 1159-1995 [34]) recommended practice encompasses the monitoring of electrical characteristics of single-phase and polyphase ac power systems. This recommended practice presents definitions of nominal conditions and deviations from these nominal conditions that may originate within the source of supply or load equipment or may originate from interactions between the source and the load. The purpose of this recommended practice is to assist users as well as equipment and software manufacturers and vendors by describing techniques for defining, measuring, quantifying, and interpreting electromagnetic disturbances on the power system [35]. IEEE recommended practice and requirements for harmonic control in electric power systems has been discussed in IEEE 519:1992 [36]. IEEE 1547:2018 (revision of IEEE 1547:2003 [37]) standard establishes criteria and requirements for interconnection of distributed energy resources with Electric Power Systems (EPSs) and associated interfaces [38]. Different techniques have been used to mitigate the PQ issues. Active power filters are one of more prominent and it can also be divided into three

type series, shunt and hybrid active power filters [39]. Series active compensator is connected in series at load end and used to mitigate PQ problems related to voltage such as voltage sag, voltage swell, flickers, voltage fluctuations, voltage imbalance and voltage harmonics. Solid State Static Series Compensators (SSSCs) and DVRs are the example of series active power filters [40–42]. Shunt active power filters employed in the distribution system is commonly known as the DSTATCOM [43–45]. It can be employed as a VSC or Current Source Inverter (CSI) to the PCC in a shunt connected mode. DSTATCOM has been used for current related PQ problems like harmonic mitigation, reactive power compensation, load balancing and also voltage regulation. DSTATCOM is now quite popular to mitigate the PQ issues due to the advancement in the switching devices [46,47]. Previously Metal Oxide Semiconductor Field Effect Transistors (MOSFET) and Gate Turn Off Thyristor (GTO) are used and presently it uses Insulated-Gate Bipolar Transistor (IGBT) as switching devices which enables easy operation and robust performance. Combined operation of series active power filter and shunt active power filter is known as hybrid active power filter. UPQC is the example of hybrid active power filter [48–51]. It enables the PQ improvement in both voltage and current related PQ problems but it is complex to control, required more number of switches and hence increases the cost.

## 2.4 Literature Survey on Synchronization Schemes

Control algorithms employed for shunt compensation require the estimation of synchronizing signals from grid voltage and the fundamental load component estimation from the load current signal. The simplest method to generate the synchronizing signal is the unit template method, but it works only under the ideal grid voltage condition [52,53]. However, if the grid voltage has several power quality issue such as distortion, noise and DC-offset, then new and improved methods are required to estimate synchronizing signals. Further, different PLL techniques have been proposed by researchers and some of these do not work well under non-ideal grid conditions. SRF-PLL has been used as a conventional PLL and used by re-

searchers for the phase and frequency estimation and realized for generation of synchronizing signals [54–56]. EPLL has the capability of removing double-frequency oscillations [57–59]. SOGI-PLL algorithm is widely used for its simplicity and effectiveness [60, 61] in grid synchronization. The performance of the SOGI-PLL is observed to be non-satisfactory in the case of high grid distortions and DC-offset conditions. SOGI-FLL has been proposed for the effective working of SOGI in case of varying frequency condition [60, 62]. The FLL block is realized to estimate the frequency of the input signal. However, SOGI-FLL has limited filtering capacity and does not give satisfactory results in case of DC-offset in the grid voltage. Modified SOGI-FLL has been presented for the rejection of the DC-offset in grid voltage [63, 64]. It is also observed that the frequency estimated by the FLL shows varying degree of oscillations under steady-state conditions under highly distorted grid.

Cascaded Delayed Signal Cancellation Operator (CDSC) based PLL has been investigated in three phase system. This requires transform equations and also additional Proportional Integral (PI) controller [65, 66]. Robust frequency estimation technique has been proposed under distorted grid conditions and has not been used for estimation of synchronizing signals [67, 68]. Further, a method based on Three Consecutive Sampling (3CS) has been proposed to estimate synchronizing signal in three phase grid [69]. These techniques have been employed under frequency change and distorted conditions and DC-offset condition has not been discussed. These techniques give zero steady state error in case of frequency estimation except under DC-offset conditions.

The role of Artificial Neural Networks (ANN) in power system parameter estimation is unparalleled. They have been used for the detection of phase and symmetrical components, harmonics, etc [70, 71]. Some of the earliest ANN techniques employed back-propagation techniques [72] and repeated training of neurons for correct weight estimation [73, 74]. Offline training techniques have found better alternatives in the form of online and supervised training algorithms. Moreover, real-time implemen-

tation algorithms designed on the basis of ANN techniques should be fast, accurate and converge approximately within a few cycles if it has to replace the conventional PLL. Adaline comprises a single neuron that receives stimulus from several inputs and outputs a single output by proper training of involved weights. The Adaline based PLL is simple and training can be achieved online making it feasible to train and track instantaneous variations in voltage amplitude, phase angle and frequency.

## 2.5 Literature Survey on Control Algorithms of SAPF

SAPF are widely used and investigated technique in literature for harmonic mitigation and other PQ improvement in the distribution system. PQ improvement technique requires the appropriate control algorithms. Literature review suggests a large number of control algorithms have been employed such as IRPT [75–77], SRFT [78–81], PBT [82, 83], LMS [84–86] etc for both in single-phase and three-phase distribution system [87, 88]. The control algorithm is developed for extracting or estimating fundamental load component. However, the nature of load current is non-linear and constantly changing, so the designed algorithms should give correct and precise results quickly and under all cases. A number of algorithms have been designed for shunt compensation, yet differences on the basis of steady state performance, faster dynamic response, convergence time, mathematical complexity need to be investigated in detail. Recent literature on SOGI suggests it is an effective filter and best suited to develop control algorithm for improvement of power quality in both single-phase and three-phase distribution system [89]. Different variants of SOGI have been reported in literature [90–94]. Reduced-order generalized integrator has been introduced in [95] and considered to be less complex than SOGI but it requires  $\alpha\beta$  component of the load current [96–98]. The application of ANN-based adaptive control algorithms is reported in research papers for harmonics estimation and mitigation in the distribution system network. LMS algorithm and its im-



proved variants are widely reported for power quality improvement in distribution network [88, 99–102]. Recurrent Neural Network (RNN) based algorithm has been also reported in the research literature for different applications [103–106] and it can also be used as control algorithm for SAPF.

## 2.6 Literature Survey on PV Integration to Distribution Grid

Single-phase and three-phase distribution system have been existed and different type of loads have been connected as per user need [107, 108]. Integration of PV to the distribution grid is possible in both the case with the help of single-phase H-bridge VSC and three-phase VSC [109, 110]. In [111, 112], authors have been proposed single-phase multilevel photovoltaic (PV) inverter topology for grid-connected PV systems with a novel Pulse Width-Modulated (PWM) control scheme. In literature, PV system has been integrated to distribution grid in single-stage [113–117] and double-stage configuration for power quality improvement along with the capability of active power injection [118]. Design of PV array is most important thing for the solar PV integration for effective power injection [119, 120]. Battery storage system has also been deployed for reducing the intermittency effect of solar PV and power backup under power failure [121, 122]. Tsai-Fu et. al [123] presented the power loss comparison of single-stage and two-stage grid-connected PV systems. According to the loss analysis, the total power loss in a single-stage grid-connected PV system is close to a two-stage grid-connected PV system, while the single-stage one can save a stage of a boost converter. Integration of PV enables the active power injection to the grid if the load requirement is less than power generation for power. In single-stage configuration, no DC-DC converter is used while in double-stage configuration DC-DC converter has been employed. MPPT techniques have been employed in both the configurations and reported in literature. In single-stage configuration MPPT technique gives the reference DC-link voltage to regulate the

DC-link voltage at maximum power point [124,125] and in double-stage configuration MPPT has been used to generate duty-cycle of the DC-DC converter [126,127].

## 2.7 Identified Research Gap

Based on the extensive literature review, following research gaps are identified:-

1. A number of Phase locked loop based circuits are available in literature; and new PLLs are being designed which are efficient, fast and work in the polluted grid conditions. More PLLs for control of grid-connected PV system used for synchronization are needed.
2. Non-PLL based fast and efficient synchronization techniques based on different types of adaptive filters etc are required for grid-connected PV system.
3. Use of synchronization techniques (with/without modification) as active power compensation techniques is not adequately addressed in recent papers.
4. Advanced control techniques for single-phase and three-phase grid connected PV system for improvement in power quality are required. Some advanced techniques have been studied for shunt compensators ; how these can be modified in the presence of PV source requires thorough studies and investigation.
5. Synchronization techniques considering polluted grid and different loading conditions is to be addressed. Also, a fair comparison of these synchronization algorithms are required in both simulation and experimental environment.

## 2.8 Objectives of Research Work

1. Design, development and performance analysis of single-phase and three-phase grid-connected PV system under different loading conditions.
2. Design of synchronization schemes for grid-connected PV system.

3. Testing, performance analysis and comparison of proposed synchronization schemes with conventional techniques.
4. Experimental verification of developed control algorithms under different loading, irradiance level on PV and under polluted grid conditions.

## **2.9 Conclusions**

In this chapter, extensive literature survey has been presented based on the PV modelling, MPPT techniques, synchronization techniques, control algorithms and configuration and power management for single-phase and three-phase grid-connected PV system. Based on the literature review and the motivation of the application of PV, research gap and research objectives have been identified.

## Chapter 3

# Design and Development of Single-Phase and Three-Phase Grid-Connected PV System

In this chapter, design and development of single-phase and three-phase SAPF with and without PV connected to the grid has been explained. Design calculation is critical for the proper operation of SAPF system. Design calculation of different components for simulation and real time experimental validation of SAPF system has been illustrated. It also discusses the modelling of the PV module and the design of PV array for the single-phase and three-phase system, which are connected in single-stage or double-stage. The design of the components required in simulation are based upon the standards required for single-phase system and three-phase system. The experimental rating of components selected depends on the availability of equipments in the laboratory.

### 3.1 Design and Development of Single-Phase Grid-Connected PV System

Figure 3.1 shows the system configuration for single-phase SAPF system. It has been used for harmonic mitigation and reactive power compensation in single-phase system under different loading conditions. This system has also been used for power quality improvement under normal and polluted grid conditions.

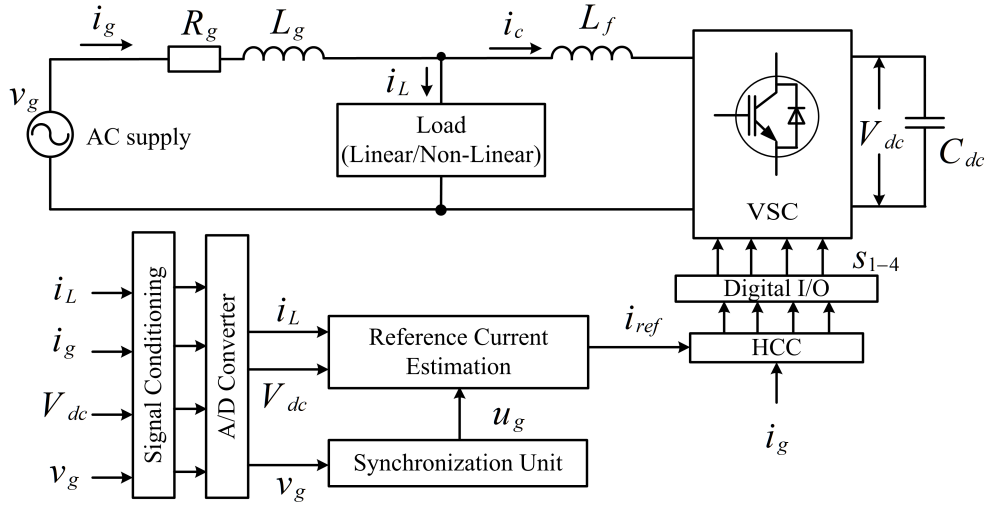


Figure 3.1: Single-phase SAPF system

Figure 3.2 shows the system configuration for single-phase single-stage grid connected PV system. In this configuration, PV array has been connected directly at DC-link of the VSC. No DC-DC conversion device has been used in this configuration. The MPPT technique has been used for the generation of reference voltage for the DC-link voltage and it is the maximum power point voltage. This configuration enables active power injection to the grid.

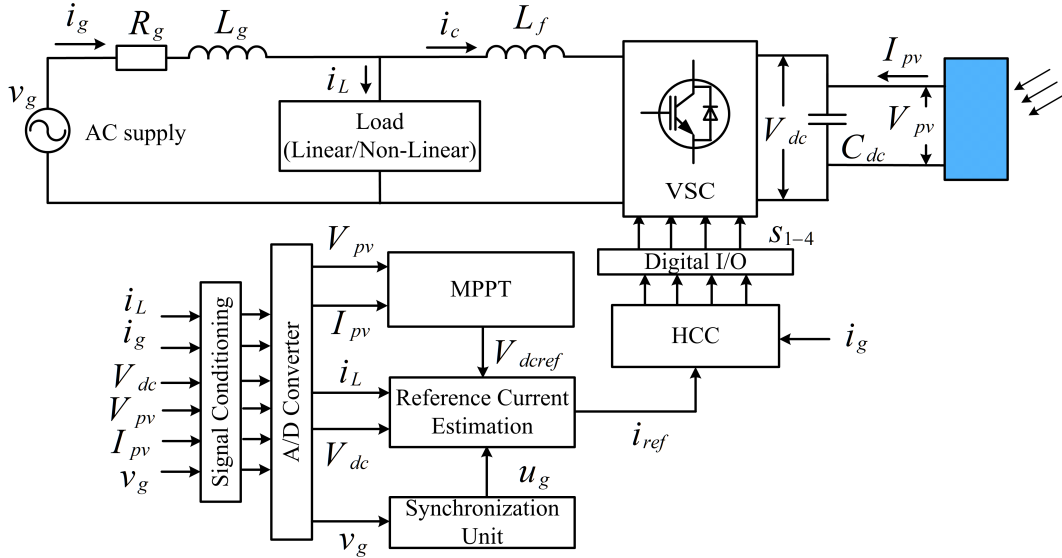


Figure 3.2: Single-phase single-stage grid connected PV system

Figure 3.3 shows the experimental setup for single-phase single-stage grid-tied PV system. The main components are listed as- (1) Personal computer (2) Single-phase

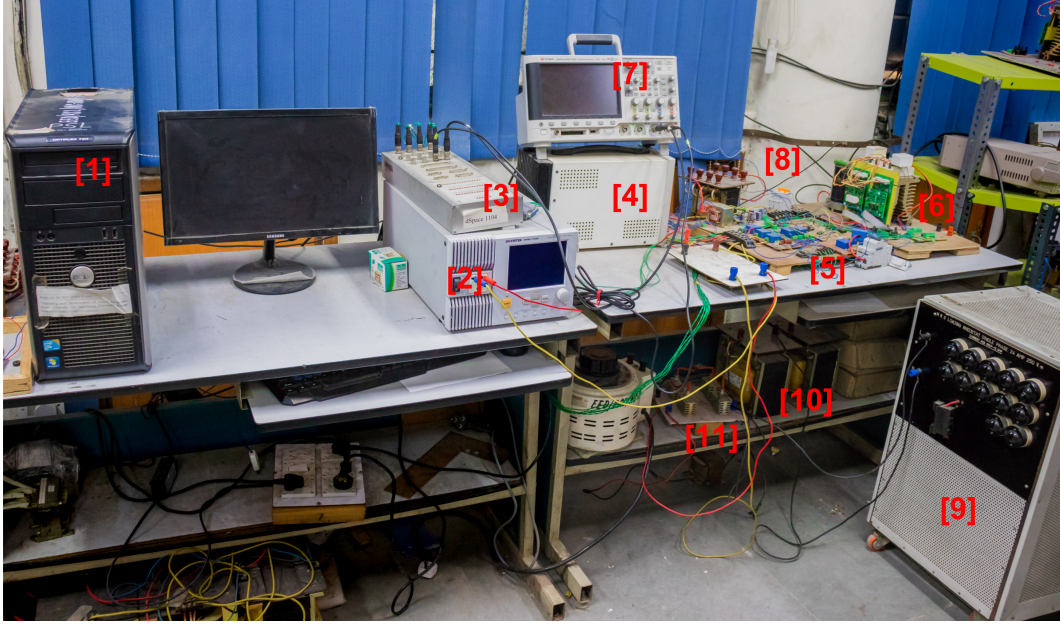


Figure 3.3: Experimental setup for single-phase single-stage grid connected PV system

programmable supply (3) dSpace 1104 board (4) Auxiliary DC supply (5) Voltage and current sensors (6) H-bridge VSC (7) DSO (8) Interfacing inductor (9) Resistive load (10) Load side inductor (11) Bridge rectifier.

Figure 3.4 shows the system configuration for the single-phase double-stage grid connected PV system. In this configuration, PV array has been connected to the input

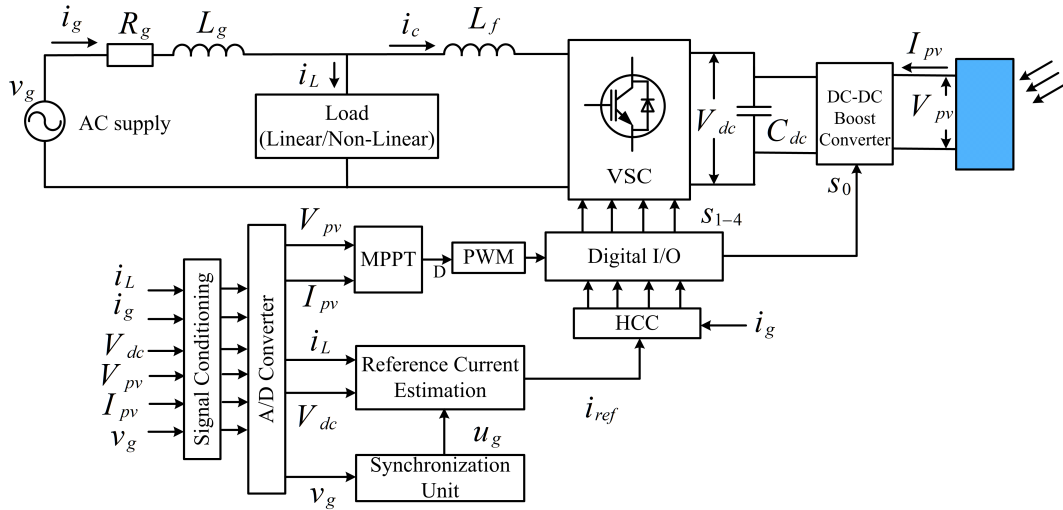


Figure 3.4: Single-phase double-stage grid connected PV system

of the DC-DC boost converter and the output of the DC-DC converter is connected

to the DC-link of the VSC. This configuration is advantageous over single stage because a lower output voltage rating of PV array can be used. The performance of double-stage is robust as compared to the single-stage grid connected PV system. The design of all the components of single-phase grid connected with PV or without PV has been discussed next. Design of the following quantities is considered:

1. DC-link reference voltage
2. DC-link capacitance
3. Interfacing inductor
4. PV array
5. DC-DC boost converter
6. Hysteresis current controller
7. Sensors and amplifier circuit

### 3.1.1 Calculation of DC-link Reference Voltage

DC-link voltage is estimated such that it can inject reactive power to the grid. So, that the DC-link voltage of single-phase VSC should be greater than the applied grid voltage. Magnitude of the grid voltage can be calculated by 3.1.

$$A_v = \sqrt{2}v_g \quad (3.1)$$

Here,  $A_v$  is the magnitude of the grid voltage and  $v_g$  is the grid voltage. Rating of supply voltage is 230V, 50Hz for simulation studies and 110V, 50Hz for experimental implementation. DC-link reference voltage calculation for the simulation is-

$$V_{dcref} > V_{dcm} = \sqrt{2}v_g = \sqrt{2} \times 230 = 325.27V \quad (3.2)$$

Here,  $V_{dcm}$  is minimum DC-link voltage. Hence, the reference DC-link voltage ( $V_{dcref}$ ) is considered as 400V. DC-link reference voltage calculation for the experimental system is-

$$V_{dcref} > V_{dcm} = 2\sqrt{2}v_g = \sqrt{2} \times 110 = 155.56V \quad (3.3)$$

Hence, the reference DC-link voltage ( $V_{dcref}$ ) is selected as 200V.

### 3.1.2 Design of DC-link Capacitor

DC-link voltage of the VSC is very sensitive to input grid voltage and the load current. The value of DC-link capacitance should be large enough to sustain DC-link voltage during dynamics. The DC-link capacitance can be calculated using 3.4.

$$C_{dc} = \frac{v_g h i_c \tau g}{\frac{1}{2}(V_{dcref}^2 - V_{dcm}^2)} \quad (3.4)$$

Here,  $h(1.2)$  is the overloading factor,  $i_c(25A)$  is the compensator or VSC current,  $\tau(0.02s)$  is time-constant,  $g(0.3)$  is gain constant,  $V_{dcref}(400V)$  is the reference DC-link voltage and  $V_{dcm}(375.27V)$  is minimum DC-link voltage. Applying these values in 3.4, gives

$$C_{dc} = \frac{v_g h i_c \tau g}{\frac{1}{2}(V_{dcref}^2 - V_{dcm}^2)} = 1527.6\mu F \quad (3.5)$$

A little higher value of DC-link capacitor has been chosen for the simulation and it is  $C_{dc} = 2000\mu F$ . Similarly, for the experimental system,  $i_c$  is 25A,  $V_{dcref}$  is 200V and  $V_{dcm}$  is 155.56V and the calculated value of DC-link capacitor by 3.4 is  $2506.33\mu F$ . Value of DC-link capacitance for the experimental setup is little higher than calculated and it is  $4700\mu F$

### 3.1.3 Design of Interfacing Inductor

Interfacing inductor is used to filter out the ripples in the current. Higher value of inductor provides better filtering but at the same time power loss is higher. Hence,



proper design of interfacing or filter inductor ( $I_f$ ) is very necessary and is calculated by 3.6.

$$L_f = \frac{\sqrt{3}mV_{dcref}}{12hf_s\Delta i} \quad (3.6)$$

Here,  $m$  is the modulation index,  $V_{dcref}$  is DC-link reference voltage,  $h$  is the overloading factor,  $f_s$  is the switching frequency and  $\Delta i$  is the ripples in the current and is considered 5% of maximum current. For simulation purpose its value is-

$$L_f = \frac{\sqrt{3}mV_{dcref}}{12hf_s\Delta i} = \frac{\sqrt{3} \times 1 \times 400}{12 \times 1.2 \times 10 \times 10^3 \times 1.5} = 3.20mH \quad (3.7)$$

For experimental purpose its value is-

$$L_f = \frac{\sqrt{3}mV_{dcref}}{12hf_s\Delta i} = \frac{\sqrt{3} \times 1 \times 200}{12 \times 1.2 \times 10 \times 10^3 \times 1.5} = 1.6mH \quad (3.8)$$

A little higher value of inductance of interfacing inductor than calculated is used for experimental system and it is 2.0 mH.

### 3.1.4 Modelling and Design of PV Array

#### 3.1.4.1 Modelling of PV Module

A solar cell can be modelled in different ways considering different parameters. Single-diode model with series resistance and parallel resistance is considered nearer to practical diode and easier to model [1,128]. The practical single diode model with series and shunt resistance has been shown in Fig. 3.5. The output current ( $I_c$ ) of

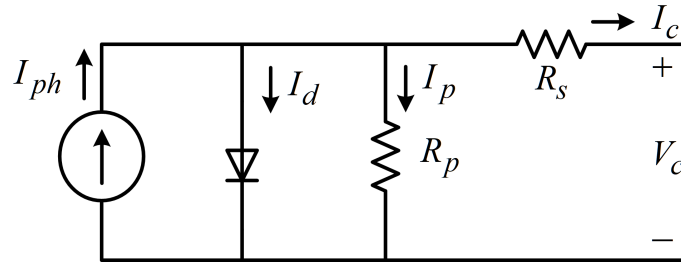


Figure 3.5: Practical single diode model of PV cell

PV cell is obtained by using Kirchhoff's current law;

$$I_c = I_{ph} - I_d - I_p \quad (3.9)$$

$$I_c = I_{ph} - I_o \left[ \exp\left(\frac{V_c + IR_s}{a}\right) - 1 \right] - \frac{V_c + IR_s}{R_p} \quad (3.10)$$

where,  $I_{ph}$  is the photon current,  $I_d$  is the diode current,  $I_p$  is the leakage current in the parallel resistor and  $a$  is known as modified ideality factor [129]. Equation for  $a$  is termed as-

$$a = \frac{N_s A k T_c}{q} \quad (3.11)$$

where,  $N_s$ =no. of series cells in PV panel,  $k$ =Boltzmann's constant= $1.381 \times 10^{-23}$ ,  $q$ =electron charge= $1.602 \times 10^{-19}$  coulombs and  $A$  is the diode ideality factor.

Ideality factor of different PV technology has different values as shown in Table 3.1. Here, the value of ideality factor is 1.3 as the considered module is silicon-polycrystalline.

The photocurrent ( $I_{ph}$ ) depends on both irradiance and temperature ( $T_c$ ) and it is

Table 3.1: Ideality factor (A) [1]

Technology	Si-mono	Si-poly	a-Si-H	a-Si-H tandem	a-Si-H triple	CdTe	AsGa
<b>Ideality factor</b>	1.2	1.3	1.8	3.3	1.5	1.5	1.3

given as 3.12.

$$I_{ph} = \frac{G}{G_{ref}} (I_{phref} + \mu_{sc} \Delta T) \quad (3.12)$$

Ideally,  $I_{phref} \approx I_{scref}$  and  $\Delta T = T_c - T_{cref}$ . Here,  $G_{ref}$  denotes the irradiance at standard test conditions (STC)= $1000W/m^2$ ,  $T_{cref}$  is the PV cell temperature at STC (298K).  $\mu_{sc}$  is the temperature co-efficient of short-circuit current (A/K) and is provided by the manufacturer.  $I_{scref}$  is the short-circuit current at STC and  $I_{phref}$  denotes photocurrent at STC. The diode current ( $I_d$ ) is directly proportional

to reverse saturation current ( $I_o$ ) and it is calculated by 3.13.

$$I_d = I_o[\exp(\frac{V_c + IR_s}{a}) - 1] \quad (3.13)$$

The reverse saturation current of the diode can be calculated using 3.14.

$$I_o = \frac{I_{scref}}{\exp \frac{V_{ocref}}{a} - 1} (\frac{T_c}{T_{cref}})^3 \exp[(\frac{q\epsilon_g}{Ak})(\frac{1}{T_{cref}} - \frac{1}{T_c})] \quad (3.14)$$

where,  $V_{ocref}$  is the open-circuit voltage of the PV module at STC and  $\epsilon_g$ =energy band gap= $1.12eV$  for silicon based solar cells. A single PV module gives very small amount of power. Hence, to extract significant power, we require PV string or PV array which consists of number of modules connected in series ( $N_{ss}$ ) and in parallel ( $N_{pp}$ ). So, PV cell equation is modified to make array of PV and is represented using 3.15. Now, the output voltage and current of PV array is is termed as  $V_{pv}$  and  $I_{pv}$ .

$$I_{pv} = N_{pp}I_{ph} - I_o[\exp(\frac{V_{pv} + IR_s(\frac{N_{ss}}{N_{pp}})}{a}) - 1] - \frac{V_{pv} + IR_s(\frac{N_{ss}}{N_{pp}})}{R_p(\frac{N_{ss}}{N_{pp}})} \quad (3.15)$$

The module parameters of the considered Vikram Solar ELDORA270 module is shown in Table 3.2.

Table 3.2: Module Parameters at STC (Vikram Solar ELDORA270)

Parameters	Module rating
Maximum Power ( $P_{mp}$ )	270.66 W
No. of cells per module	72
Open-circuit voltage ( $V_{oc}$ )	44 V
Short-circuit current ( $I_{sc}$ )	8.1 A
Voltage at maximum power point ( $V_{mp}$ )	34.7 V
Current at maximum power point ( $I_{mp}$ )	7.8 A
Temperature coefficient of ( $V_{oc}$ )	-0.3583 (%/ $^{\circ}C$ )
Temperature coefficient of ( $I_{sc}$ )	0.024975 (%/ $^{\circ}C$ )
Shunt resistance of a cell ( $R_p$ )	3126.5623 $\Omega$
Series resistance of a cell ( $R_s$ )	0.52303 $\Omega$

As the environmental condition varies, the output voltage and current varies according the P-V and I-V curve. P-V and I-V curve of the considered module is

shown in Fig. 3.6. Figure 3.6(a) shows the P-V and I-V curve of a module for difference irradiance ( $100W/m^2$ ,  $500W/m^2$ ,  $1000W/m^2$ ) and fixed temperature ( $25^\circ C$ ) and it shows the as the temperature increases the PV output current and power increases. Figure 3.6(b) shows the P-V and I-V curve of a module at different temperature ( $25^\circ C$ ,  $35^\circ C$ ,  $45^\circ C$ ) and fixed irradiance ( $1000W/m^2$ ). In this case, output power and current increases as the temperature of PV module decreases. These curve shows the non-linear behaviour of PV modules as the environmental condition changes. In these curves, there is a point which shows maximum power of

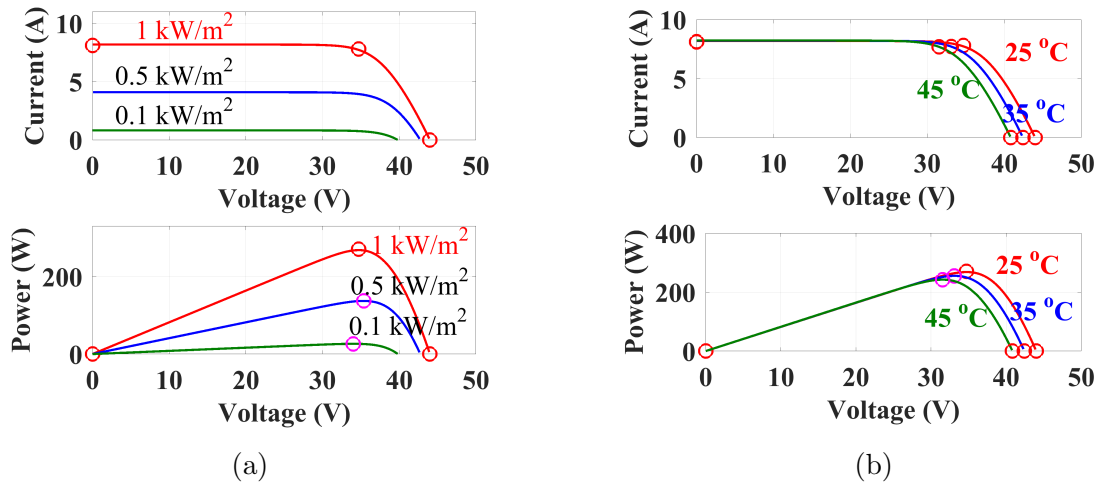


Figure 3.6: P-V and I-V curve of PV module (a)  $25^\circ C$  and at specified irradiance (b)  $1000W/m^2$  and at specified temperatures

the PV module and it is called maximum power point of the PV module. Voltage at maximum power point is called as the maximum power point voltage ( $V_{mp}$ ) and current at maximum power point is called as the maximum power point current ( $I_{mp}$ ). MPPT has been used to achieve the maximum power from the PV module or string or array. MPPT technique forces the PV module to work at maximum power point of the PV curve. In single-stage grid tied PV system MPPT technique gives the reference voltage for the DC-link and in double-stage grid-tied PV system it generates duty cycle to the DC-DC converter to impose the module to work at maximum power point.

### 3.1.4.2 Design of PV Array

A single PV module can generate small amount of power. So, for getting higher power requirement more number of PV modules can be connected in series or in parallel as per requirement of voltage and current rating. The number of modules connected in series constitutes PV string and number of such string connected in parallel forms PV array. PV modules connected in series increase the voltage level and modules connected in parallel increase the current level.

For single-stage PV system there is no DC-DC converter is required. Hence, the output of the PV array should be greater than the minimum DC-link voltage ( $V_{dcm}$ ). Hence, the reference DC-link voltage generated by MPPT technique should be selected higher than the minimum DC-link voltage ( $V_{dcm}$ ). The minimum number of PV modules required to be connected in series is calculated using 3.16.

$$N_{ss} = \frac{V_{dcm}}{V_{mp}} = \frac{325.22}{34.7} = 9.3 \quad (3.16)$$

Hence, 12 modules has been considered and connected in series for the single-phase single-stage grid connected PV system. P-V and I-V curve of the designed string has been shown in Fig. 3.7 and its parameters are shown in Table 3.3.

In double-stage grid-connected PV system, output of the PV is first connected to

Table 3.3: PV string parameters at STC for single-stage grid-connected PV system

Parameters	Rating
No. of series modules	12
No. of parallel strings	1
Maximum Power ( $P_{mp}$ )	3247.92 W
Open-circuit voltage ( $V_{oc}$ )	528.00 V
Short-circuit current ( $I_{sc}$ )	8.1 A
Voltage at maximum power point ( $V_{mp}$ )	416.4 V
Current at maximum power point ( $I_{mp}$ )	7.8 A

DC-DC converter and the output of DC-DC converter is connected to the DC-link of the VSC. Boost converter has been chosen because of simple in construction, less components required and the capability to up the voltage level. Double-stage PV system has been preferred for the lesser number of PV modules can be connected in

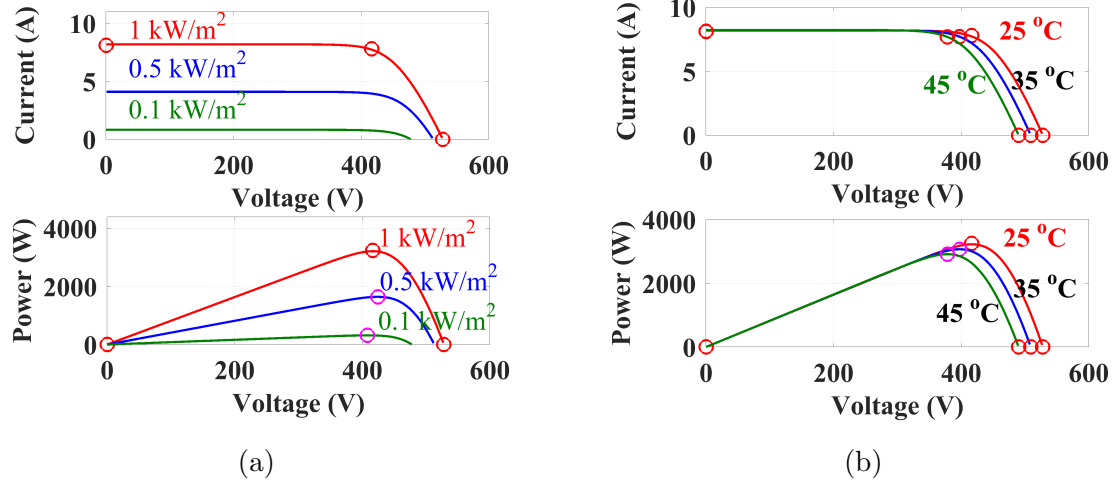


Figure 3.7: P-V and I-V curve of PV string for single-stage grid-tied PV system at STC (a) 25°C and at specified irradiance (b) 1000W/m<sup>2</sup> and at specified temperatures

series than double-stage system. Here, MPPT technique gives the output as duty cycle given to DC-DC boost converter. DC-DC-DC boost converter is designed such that it can work around 0.5 duty cycle. Hence, the minimum number of PV module connected in series is calculated by 3.17.

$$N_{ss} = \frac{V_{dcm}}{V_{mp}} \times 0.5 = \frac{325.22}{34.7} \times 0.5 = 4.65 \quad (3.17)$$

Here, five modules has been connected in series so that the duty cycle of the boost converter works around on 0.5 for the single-phase double-stage grid connected PV system. Also, for higher power capacity two strings of 5 modules each have been connected in parallel. P-V and I-V curve of the designed string has been shown in Fig. 3.8 and its parameters are shown in Table 3.4.

### 3.1.5 Design of DC-DC Boost Converter

A boost converter is a DC-DC conversion device which step up the input voltage. Configuration of boost converter [130–132] is shown in Fig. 3.9. Design of the boost converter parameters have been done through the following steps.

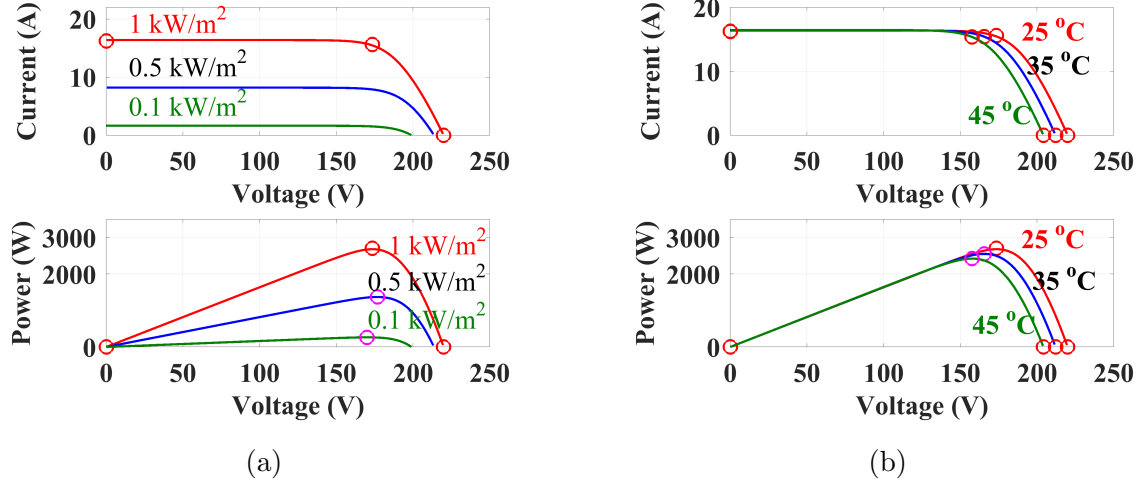


Figure 3.8: P-V and I-V curve of PV array for double-stage grid-tied PV system at STC (a) 25°C and at specified irradiance (b) 1000W/m² and at specified temperatures

Table 3.4: PV array parameters at STC for double-stage grid-tied PV system

Parameters	Rating
No. of series modules	5
No. of parallel strings	2
Total no. of PV modules	10
Maximum Power ( $P_{mp}$ )	2706.60 W
Open-circuit voltage ( $V_{oc}$ )	220.0 V
Short-circuit current ( $I_{sc}$ )	16.2 A
Voltage at maximum power point ( $V_{mp}$ )	173.50 V
Current at maximum power point ( $I_{mp}$ )	15.6 A

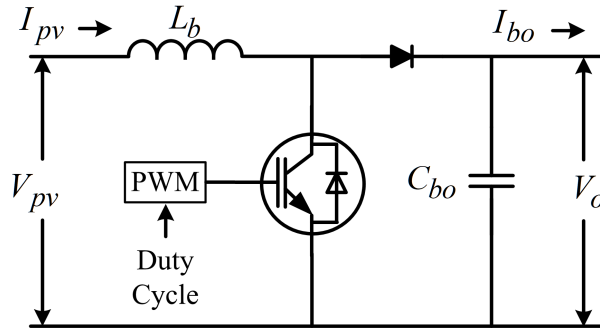


Figure 3.9: DC-DC boost converter circuit

1. Duty cycle calculation (D)

$$D = 1 - \frac{V_{pv}}{V_o} \mu_b \quad (3.18)$$

Here,  $D$  is the duty cycle,  $V_{pv}$  input PV voltage,  $V_o$  is the output voltage of

the converter,  $\mu_b$  is the boost converter efficiency and considered as 95%.

$$D = 1 - \frac{V_{pv}}{V_o} \mu_b = 1 - \frac{173.5}{400} 0.95 \approx 0.6 \quad (3.19)$$

## 2. Design of inductor ( $L_b$ )

$$L_b \geq \frac{V_{pv(min)} D}{f_s \Delta I_{pv}} \quad (3.20)$$

Here,  $V_{pv(min)}$  is 173.5V,  $D = 0.6$ ,  $f_s$  = switching frequency = 5kHz and  $\Delta I_{pv}$  is the ripple current and it ranges from 20% to 40%. Here,  $\Delta I_{pv}$  is considered 30% of PV current.

$$L_b \geq \frac{V_{pv(min)} D}{f_s \Delta I_{pv}} = \frac{173.5 \times 0.6}{5 \times 10^3 \times 0.3 \times 15.6} \approx 4.45mH \quad (3.21)$$

A little higher value of inductor (5.0mH) is selected.

## 3. Design of output capacitance ( $C_{bo}$ )

$$C_{bo} = \frac{I_{o(max)} D}{f_s \Delta V_{bo}} \quad (3.22)$$

Here,  $I_{o(max)}$  is 15.6 A and  $\Delta V_{bo}$  is 1% to 5% of  $V_{bo}$  and 2% ripple is considered here.

$$C_{bo} = \frac{I_{o(max)} D}{f_s \Delta V_{bo}} = \frac{15.6 \times 0.6}{5 \times 10^3 \times 0.02 \times 400} = 234\mu F \quad (3.23)$$

The output capacitor value selected is 400 $\mu F$ .

## 4. IGBT, Diode and Driver circuit

In simulation, an ideal IGBT and diode has been considered while in experimental setup Semikron make SKM50GAL12T4 (50A, 1200V) has been used. This IGBT switch has been integrated with diode also. PWM technique has been used for generating the pulses for IGBT. The output of the DSP unit gives 5V signal so a suitable amplifying circuit has been used to amplify the signal to 15V. Semikron make Skyper32 Pro driver has been used to generate the required pulses for IGBT.



### 3.1.6 Design of Hysteresis Current Controller (HCC)

Hysteresis current control is a method of controlling a voltage source inverter so that an output current is generated to follow a reference current waveform. This method controls the switches in the APF asynchronously to ramp the current through an inductor up and down so that it follows the reference [133–137]. The voltage equation for the DC-link voltage can be written as 3.24.

$$V_{dc} = L_f \frac{di_g}{dt} + v_g \quad (3.24)$$

The output current can be considered as the reference current plus the error component. The structure of the hysteresis current controller is shown in Fig. 3.10.

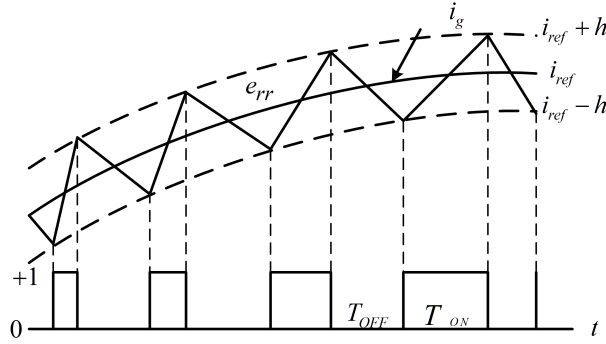


Figure 3.10: Hysteresis current controller

$$i_g = i_{ref} + e_{rr} \quad (3.25)$$

Now, putting the value of  $i_g$  from 3.25 into 3.24,

$$V_{dc} = L_f \frac{d(i_g + e_{rr})}{dt} + v_g \quad (3.26)$$

For the dynamic condition,

$$V_{dc} - v_g = L_f \frac{de_{rr}}{dt} \quad (3.27)$$

When the output for the switch is ON condition, the error changes from  $-h$  to  $+h$ , so the ON time ( $T_{ON}$ ) can be calculated as,

$$T_{ON} = \frac{2L_f h}{(V_{dc} - v_g)} \quad (3.28)$$

Similarly, OFF time ( $T_{OFF}$ ) can be calculated as

$$T_{OFF} = \frac{2L_f h}{(V_{dc} + v_g)} \quad (3.29)$$

The switching frequency ( $f_{sw}$ ) can be written as

$$f_{sw} = \frac{1}{T_{sw}} = \frac{1}{(T_{ON} + T_{OFF})} = \frac{(V_{dc}^2 - V_g^2)}{(4V_{dc}L_f h)} = \frac{V_{dc}}{(4L_f h)(1 - (\frac{v_g}{V_{dc}})^2)} \quad (3.30)$$

Here,  $v_g = A_v \sin \omega t$  and  $k_b = \frac{A_v}{V_{dc}}$  Hence,

$$f_{sw} = \frac{V_{dc}}{(4L_f h)(1 - k_b^2 \sin^2 \omega t)} \quad (3.31)$$

From the equation 3.31, the maximum switching frequency can be obtained by 3.32.

$$f_{sw,max} = \frac{V_{dc}}{4L_f h} \quad (3.32)$$

In, the experimental setup Semikron made SKM50GB12T4 has been used which having the maximum switching frequency of 20 kHz. SKM50GB12T4 is combination of two IGBT switches connected in series and each switch has been integrated with diode also. Selected values of  $L_f$  is 4mH and DC-link voltage  $V_{dc}$  are 400V. Putting these values in 3.32, value of  $h$  obtained is 1.25. Same value of  $h$  has been used for experimental as the DC-link voltage (200V) is half and also the value of interfacing inductor ( $2mH$ ) is half .

### 3.1.7 Design and Development of Sensor Circuits

Sensors are an integral part of the SAPF system. They are utilized to sense the different parameters (V & I) and give to ADC channels of dSpace1104. Circuit diagram for the voltage and current sensors has been shown in Fig. 3.11(a) and 3.11(b). Figure 3.11(c) shows the practical voltage and current circuits. For sensing

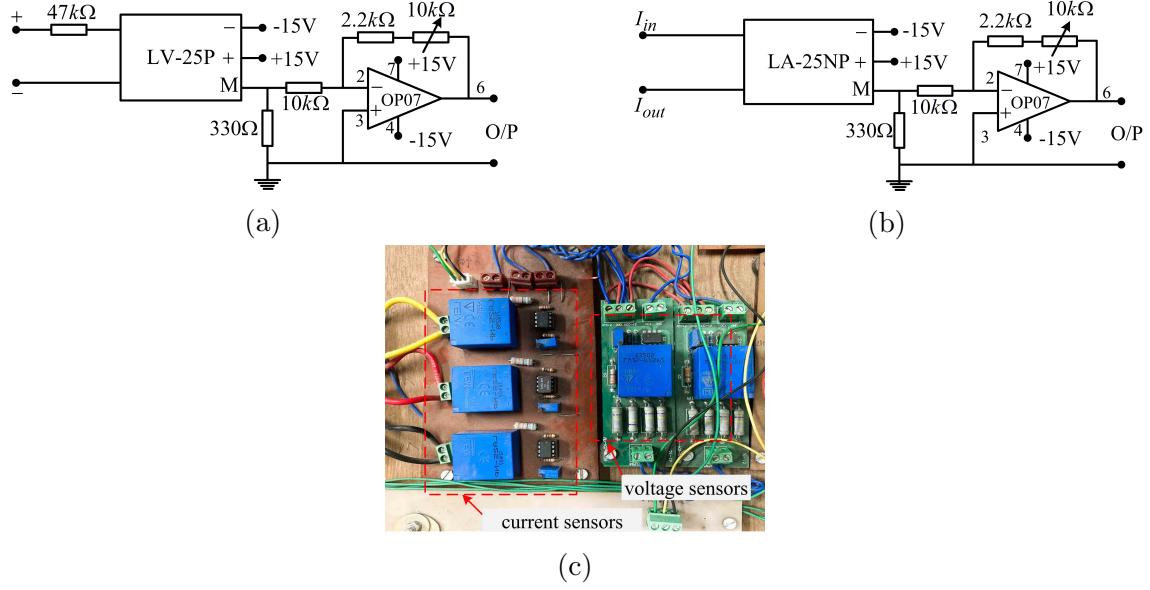


Figure 3.11: Sensor circuits (a) voltage sensor circuit (b) current sensor circuit (c) practical voltage and current sensors

the voltage parameters LEM make Hall-effect based LV25-P/sp2 model is used. Its maximum input voltage range is 1500V. Maximum current of 14mA is limited in input terminal. To reduce the input current a high resistance of 47kΩ has been used with power capacity of 2W. In the output of the sensor OP07 IC has been used to change the gain ratio of current sensor such that the output of voltage sensor should not exceed 5V.

For sensing the current parameters LEM make Hall-effect based LA25-NP model is used and its conversion ratio is 1:1000. In the output of the sensor OP07 IC has been used to change the gain ratio of voltage sensor such that the output voltage of sensor should not exceed 5V. The operational amplifier circuit is same for both the voltage and current circuits.

### 3.1.8 Design of Amplifier Circuit for IGBT Driver

Signal generated from dSpace1104 has the magnitude of 5V and to drive the Skyper32 Pro. It requires magnitude of 15V. Hence, there is a requirement of an amplifier circuit which is shown in Fig. 3.12(a). The practical implementation of amplifying circuit is shown in Fig. 3.12(b). It consists of 7406 IC and 2N2222 transistor. 7406 IC requires 5V DC supply and the NPN transistor 2N2222 requires 15V DC supply.

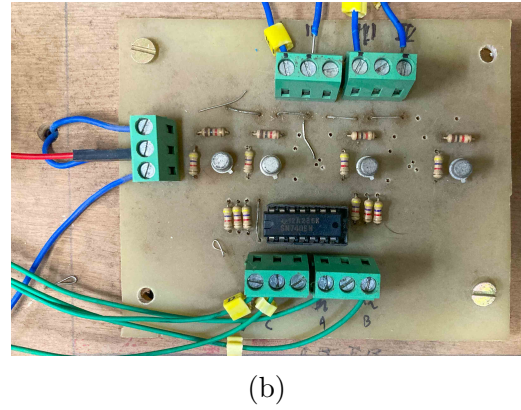
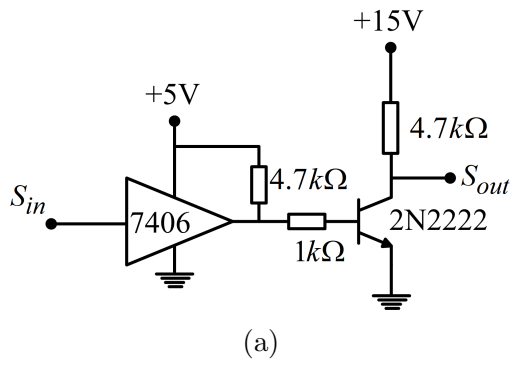


Figure 3.12: Sensor circuits (a) Amplifier circuit for IGBT driver circuit (b) Practical amplifier for Skyper 32 Pro

## 3.2 Design and Development of Three-Phase Grid-Connected PV System

Three-phase three-wire system has been realized for SAPF and the configuration has been shown in Fig. 3.13. This configuration is used for reactive power compensation and harmonic mitigation under non-linear or linear load condition. Same system has also been tested under normal and distorted grid voltage condition.

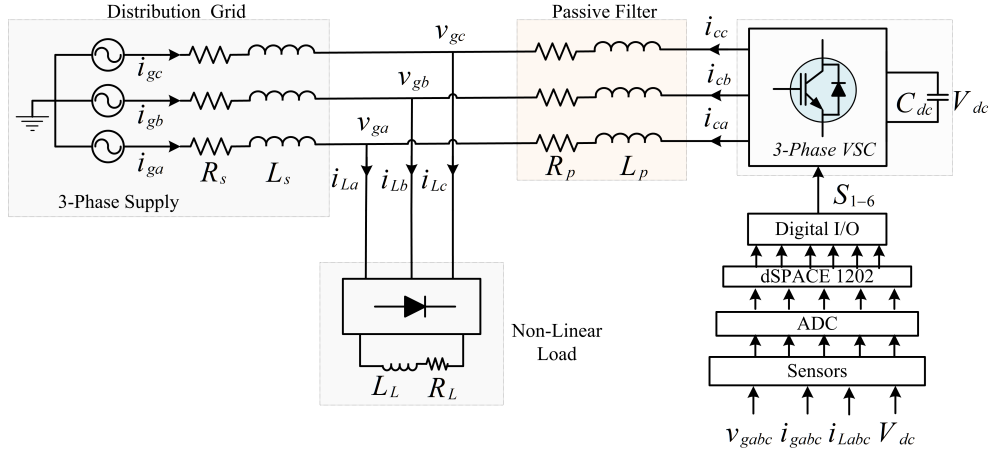


Figure 3.13: Three-phase SAPF system

Figure 3.14 shows the system configuration for three-phase three-wire single stage grid-tied PV system. PV string or array is connected to DC-link voltage of the three-phase VSC. In this type of system no DC-DC converter required. The MPPT technique is used to generate the reference DC-link voltage ( $V_{dcref}$ ). This system can be used for both active and reactive power compensation along with harmonic mitigation of grid current under linear/non-linear load condition.

Figure 3.15 shows the experimental setup for three-phase grid-tied PV system. The main components are listed as- (1) Personal computer (2) dSpace1202 (3) DSO (4) PV simulator (5) DC supplies (6) Sensors and gating circuit (7) 3-phase VSC (8) Interfacing inductors (9) 3-phase variable ac supply (10) Resistive load (11) Inductive load (12) Bridge rectifier.

Figure 3.16 shows the system configuration of three-phase three-wire double-stage grid-tied PV system. In this configuration, a DC-DC boost converter has been used

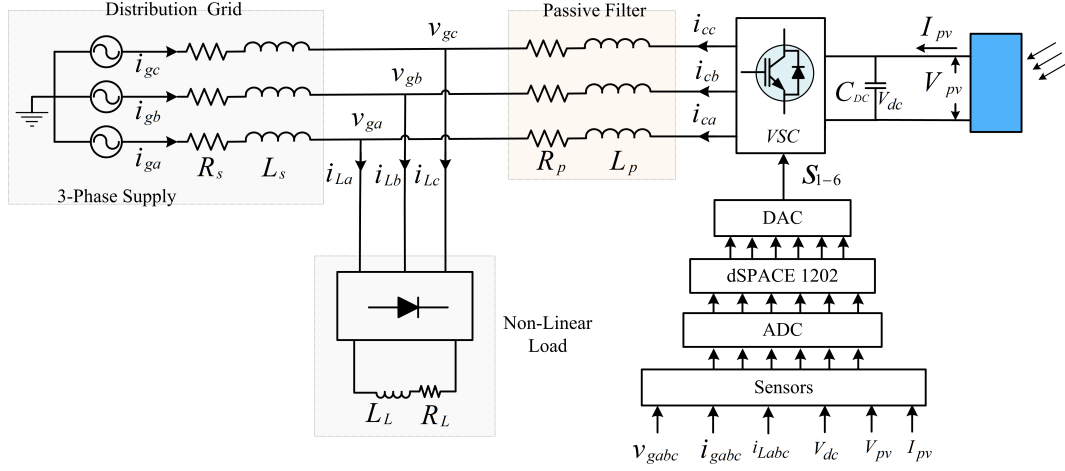


Figure 3.14: Three-phase single-stage grid-tied PV system

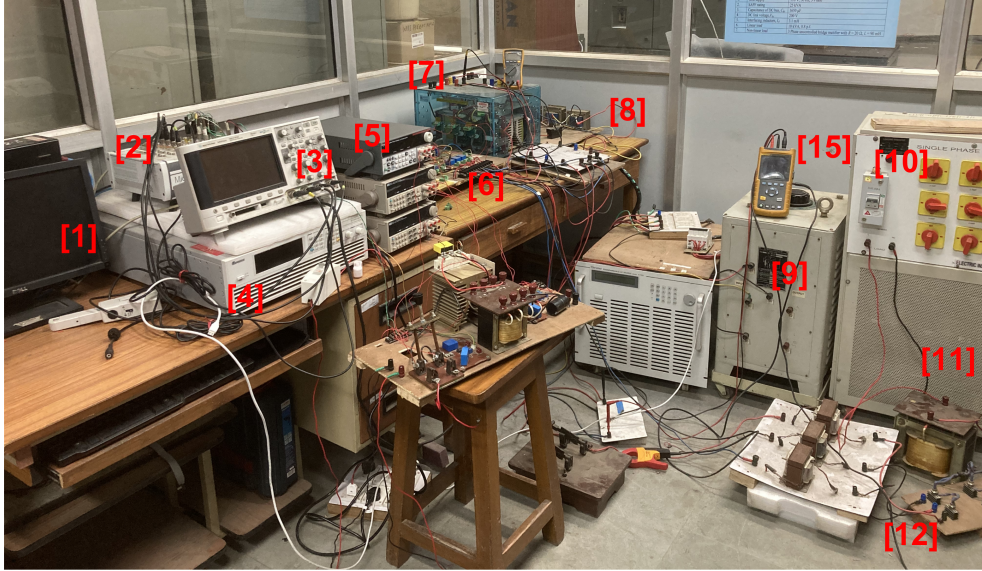


Figure 3.15: Experimental setup for three-phase grid tied PV system

to level up the PV output voltage. Output of the MPPT technique which is duty cycle and is given to the DC-DC boost converter. In this configuration lower number of PV module can be used than single-stage grid-tied PV system.

Further, design of different system have been discussed. HCC and sensor part have been discussed earlier. In a single-phase system HCC generates 4-pulses while HCC for three-phase generates six pulses [138]. Grid voltages for simulation is  $230V(V_{ph})/400V(V_{LL})$ , 50Hz has been used and for experimental validation  $63.5V(V_{ph})/110V(V_{LL})$ , 50Hz has been used. Both the normal balanced grid and the

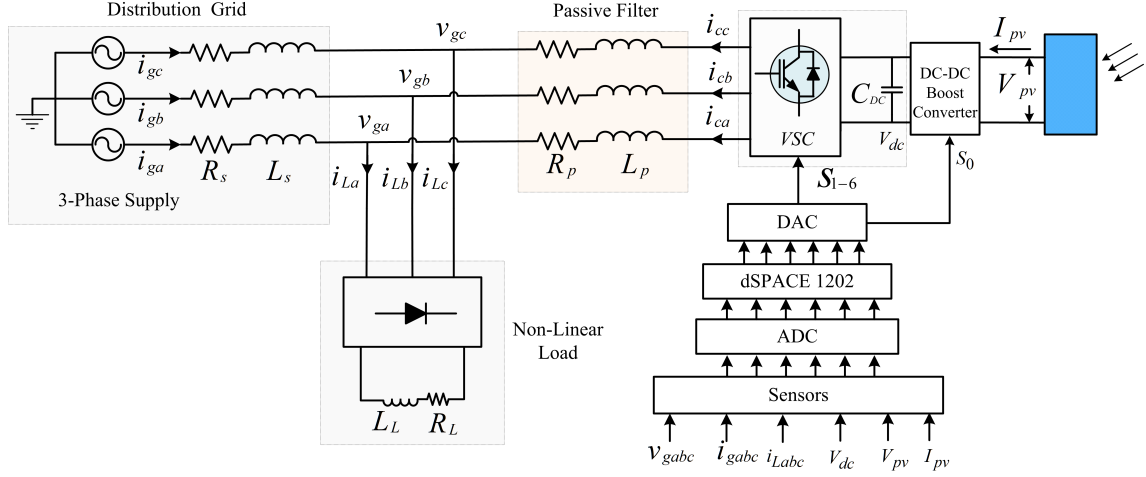


Figure 3.16: Three-phase double-stage grid-tied PV system

distorted grid has been applied and tested in simulation and experimental results.

### 3.2.1 Calculation of DC-link Reference Voltage

DC-link voltage is estimated such that it can inject reactive power to the grid. So, that the DC-link voltage of single-phase VSC should be little greater than the applied grid voltage [139]. Magnitude of the grid voltage can be calculated by 3.33.

$$A_v = \frac{2\sqrt{2}V_{LL}}{\sqrt{3}} \quad (3.33)$$

Here,  $A_v$  is the magnitude of the grid voltage,  $V_{LL}$  is the line to line RMS grid voltage and 'm' is the modulation index and its value is considered '1'. Rating of supply voltage is  $415V(V_{ph})$ , 50Hz for simulation studies and  $110V(V_{LL})$ , 50Hz for experimental implementation. DC-link reference voltage calculation for the simulation is achieved by 3.35.

$$V_{dcref} > V_{dcm} = \frac{2\sqrt{2}v_{LL}}{\sqrt{3}m} = \frac{2\sqrt{2} \times 415}{\sqrt{3}} = 677.67V \quad (3.34)$$

Here,  $V_{dcm}$  is minimum DC-link voltage. Hence, the reference DC-link voltage ( $V_{dcref}$ ) is considered as 800V. DC-link reference voltage calculation for the ex-

perimental system is-

$$V_{dcref} > V_{dcm} = \frac{2\sqrt{2} \times 110}{\sqrt{3}} = 179.30V \quad (3.35)$$

Hence, the reference DC-link voltage ( $V_{dcref}$ ) is considered as 200V.

### 3.2.2 Design of DC-link Capacitor

DC-link voltage of the VSC is very sensitive to input grid voltage and the load current. The value of DC-link capacitance should be large enough to sustain DC-link voltage during dynamics [139]. The DC-link capacitance can be calculated using 3.36.

$$C_{dc} = \frac{6v_{ph}hi_c\tau g}{(V_{dcref}^2 - V_{dcm}^2)} \quad (3.36)$$

Here,  $h(1.2)$  is the overloading factor,  $i_c(25A)$  is the compensator or VSC current,  $\tau(0.02s)$  is time-constant,  $g(0.04)$  is gain constant,  $V_{dcref}(800V)$  is the reference DC-link voltage and  $V_{dcm}(653.18V)$  is minimum DC-link voltage. Applying these values in 3.36, gives

$$C_{dc} = \frac{6v_{ph}hi_c\tau g}{(V_{dcref}^2 - V_{dcm}^2)} = 3881.85\mu F \quad (3.37)$$

A little higher value of DC-link capacitor has been chosen for the simulation and it is  $C_{dc} = 4000\mu F$ . Similarly, for experimental system the capacitance calculated is  $1476.01\mu F$  and chosen value is  $1640\mu F$ .

### 3.2.3 Design of Interfacing Inductor

Interfacing inductor is used to filter out the ripples in the current. Higher value of inductor provides better filtering but at the same time loss is higher [139]. Hence, proper design of interfacing or filter inductor ( $I_f$ ) is very necessary and is calculated by 3.38.

$$L_f = \frac{\sqrt{3}mV_{dcref}}{12hf_s\Delta i} \quad (3.38)$$



Here,  $m$  is the modulation index,  $V_{dcref}$  is DC-link reference voltage,  $h$  is the over-loading factor,  $f_s$  is the switching frequency and  $\Delta i$  is the ripples in the current and is considered 5% of maximum current. For simulation purpose its value is-

$$L_f = \frac{\sqrt{3}mV_{dcref}}{12hf_s\Delta i} = \frac{\sqrt{3} \times 1 \times 800}{12 \times 1.2 \times 10 \times 10^3 \times 1.5} = 6.40mH \quad (3.39)$$

Similarly, the value of interfacing inductor has been calculated and it is  $3.20mH$ .

### 3.2.4 Design of PV Array

For single-stage PV system, no DC-DC converter has been used. Hence, the output of the PV array should be greater than the minimum DC-link voltage ( $V_{dcm}$ ). So that the reference DC-link voltage generated by MPPT technique should be higher than the minimum DC-link voltage ( $V_{dcm}$ ). Number of PV module connected in series is calculated by 3.40.

$$N_{ss} = \frac{V_{dcm}}{V_{mp}} = \frac{653.18}{34.7} = 18.82 \quad (3.40)$$

From 3.40, 22 modules have been considered and connected in series for the three-phase single-stage grid connected PV system. Parameters of PV array has been shown in Table 3.5.

Table 3.5: PV string parameters at STC for single-stage grid-tied PV system

Parameters	Rating
No. of series modules	22
No. of parallel strings	1
Maximum Power ( $P_{mp}$ )	5954.52 W
Open-circuit voltage ( $V_{oc}$ )	968.00 V
Short-circuit current ( $I_{sc}$ )	8.1 A
Voltage at maximum power point ( $V_{mp}$ )	763.40 V
Current at maximum power point ( $I_{mp}$ )	7.8 A

In double-stage grid-connected PV system, output of the PV is first connected to DC-DC converter and the output of DC-DC converter is connected to the DC-link of the VSC. Boost converter has been chosen because of simple in construction, less

components required and the capability to up the voltage level. Double-stage PV system has been preferred for the less no of PV modules connected in series and having lesser maximum power point voltage than minimum DC-link voltage  $V_{dcm}$  of the PV array. Here, MPPT technique gives the output as duty cycle given to DC-DC boost converter. Number of PV module connected in series is calculated by 3.40. Here, the array of 10 modules has been connected in series, so that the duty cycle of the boost converter works around on 0.5 for the three-phase double-stage grid connected PV system. To increase the power capacity two strings have been connected in parallel. Parameters of PV array has been shown in Table 3.6.

Table 3.6: PV array parameters at STC for double-stage grid-tied PV system

Parameters	Rating
No. of series modules	10
No. of parallel strings	2
Maximum Power ( $P_{mp}$ )	5413.2 W
Open-circuit voltage ( $V_{oc}$ )	440.0 V
Short-circuit current ( $I_{sc}$ )	16.2 A
Voltage at maximum power point ( $V_{mp}$ )	347.0 V
Current at maximum power point ( $I_{mp}$ )	15.6 A

### 3.3 Conclusions

In this chapter, design and development of single-phase and three-phase grid-connected PV system have been discussed in detail. Design equations, system configuration and the figures of experimental prototype setup have also been presented. PV array can be connected in single-stage and double-stage manner in single-phase and three-phase grid-connected PV system. These system configurations will be used in simulations as well as in experimental prototype to improve the quality of power, provide reactive power compensation and active power injection to the grid.

# Chapter 4

## Grid Synchronization Techniques

Synchronization of the VSC with grid voltage and achievement of high power quality requires a accurate and precise detection of phase and frequency in the grid side. Hence, the use of grid synchronization techniques is mandatory. Out of several grid synchronization techniques discussed in literature phase locked loops is popular. However, the design of PLL circuits in single phase circuits is more challenging than in three phase circuits as the three-phase grid voltages have a natural phase shift of  $120^\circ$ . Moreover, three phase signals allow the use of Clarke and Park transformations easily. However, in single phase circuits, it becomes necessary to create or estimate quadrature signal by using different methods. Some conventional and proposed synchronization techniques for single-phase and three-phase PLLs are discussed in this chapter for estimation of phase, frequency, amplitude and the synchronizing signals under various grid voltage conditions. The designed PLLs are further applied for the power quality improvement and reactive power compensation in single-phase and three-phase system.

### 4.1 Single-Phase Grid Synchronization Techniques

The following single-phase grid synchronization techniques have been discussed in this section: delay based SRF-PLL, EPLL, SOGI-PLL, SOGI-FLL and SOGI-FLL-ROGI.

### 4.1.1 Delay based SRF-PLL

SRF requires transformation to  $\alpha$  and  $\beta$  components of the grid-voltage signal. The  $\alpha$  component can be considered as the original voltage signal and the  $\beta$  component is obtained by applying the phase shift of  $90^\circ$  to the supply voltage signal. The phase shift of  $90^\circ$  is obtained by applying time delay of  $T/4$  to the grid voltage signal as explained in 4.1 and 4.2. Here,  $T$  is the time-period of input grid-voltage. Further, Park-Transformation is applied, and the dq component of voltage signal is obtained. The PI controller is applied to  $v_q$  and its output is termed as error in frequency. Adding with the standard grid frequency ( $\omega_n$ ) gives the estimated frequency  $\omega_0$  and after integration the phase angle  $\theta_0$  is calculated as shown in Fig. 4.1.

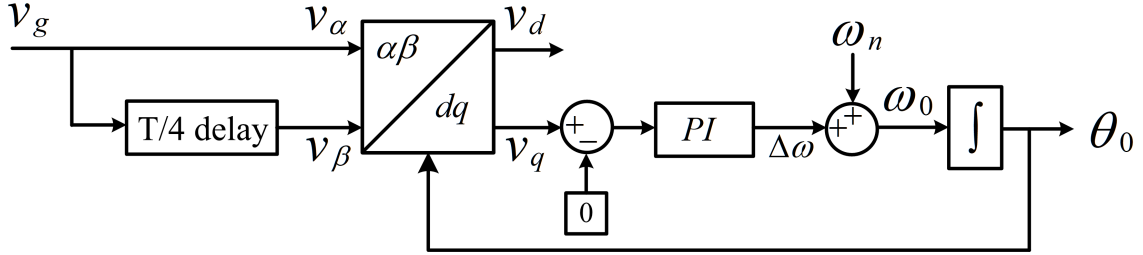


Figure 4.1: Structure of single-phase SRF-LL

The supply voltage  $v_g(t)$  is given in 4.1 and it is also assumed as  $v_\alpha(t)$ :

$$v_g(t) = v_\alpha(t) = A_v \sin(\underbrace{\omega t + \phi_i}_{\theta_i}) \quad (4.1)$$

and the quadrature component of the supply voltage  $v_g(t)$  is expressed as :

$$\begin{aligned} v_\beta(t) &= v_\alpha(t - T/4) = A_v \sin(\omega t + \phi_i - \omega T/4) \\ &= A_v \sin(\theta_i - \omega T/4) = -A_v \cos(\theta_i - \Delta\omega T/4) \end{aligned} \quad (4.2)$$

$\Delta\omega$  is defined as  $\Delta\omega = \omega_o - \omega_n$ , where  $\omega_o$  is the estimated supply voltage frequency and the  $\omega_n$  is the standard frequency of the voltage signal. When the frequency of the supply voltage signal changes from natural frequency, then  $\Delta\omega \neq 0$ , which causes to the lack of perfect orthogonality between  $v_\alpha(t)$  and  $v_\beta(t)$  and it gives the

double frequency oscillations in estimation of different parameters of delay based PLL. The Park-Transformation is given by 4.3:

$$\begin{bmatrix} v_d(t) \\ v_q(t) \end{bmatrix} = \begin{bmatrix} \sin \theta_o & -\cos \theta_o \\ \cos \theta_o & \sin \theta_o \end{bmatrix} \begin{bmatrix} v_\alpha(t) \\ v_\beta(t) \end{bmatrix} \quad (4.3)$$

For estimating the phase and the frequency of the signal,  $v_q(t)$  is used as input signal to PI controller which is used as loop-filter (LF) and gives the error signal.

$$\begin{aligned} v_q(t) &= v_\alpha(t) \cos \theta_o + v_\beta(t) \sin \theta_o \\ &= A_v \sin \theta_i \cos \theta_o + [-A_v \cos(\theta_i - \Delta\omega T/4)] \sin \theta_o \\ &= A_v/2[\sin(\theta_i + \theta_o) + \sin(\theta_i - \theta_o)] - A_v/2[\sin(\theta_i - \Delta\omega T/4 + \theta_o) - \sin(\theta_i - \Delta\omega T/4 - \theta_o)] \\ &= A_v/2[\sin(\theta_i - \theta_o) + \sin(\theta_i - \Delta\omega T/4 - \theta_o)] + \underbrace{A_v/2[\sin(\theta_i + \theta_o) - \sin(\theta_i - \Delta\omega T/4 + \theta_o)]}_{\text{double frequency term}} \end{aligned} \quad (4.4)$$

Now,  $v_q(t)$  is given to the loop filter which provides the error signal ( $\Delta\omega$ ) and it is further added to the natural frequency ( $\omega_n$ ), then the resultant signal ( $\omega_o$ ) is obtained. The frequency signal ( $\omega_o$ ) passed through the voltage-controlled oscillator (VCO) gives the phase ( $\theta_o$ ) of the voltage signal. Explanation of the delay based SRF-PLL is shown in Fig. 4.1. The Primary objective of PI in SRF-PLL is to converge  $V_q \rightarrow 0$ .

#### 4.1.1.1 Simulation Results

The performance of the SRF-PLL has been shown and explained under different grid voltage conditions. The following variations in grid voltage supply are simulated;

- Voltage sag and polluted grid (Fig. 4.2)
- Frequency change and noisy grid voltage (Fig. 4.3)
- Phase-shift and DC-offset (Fig. 4.4)

Figure 4.2 shows the simulation performance of SRF-PLL under voltage sag and polluted grid environment.

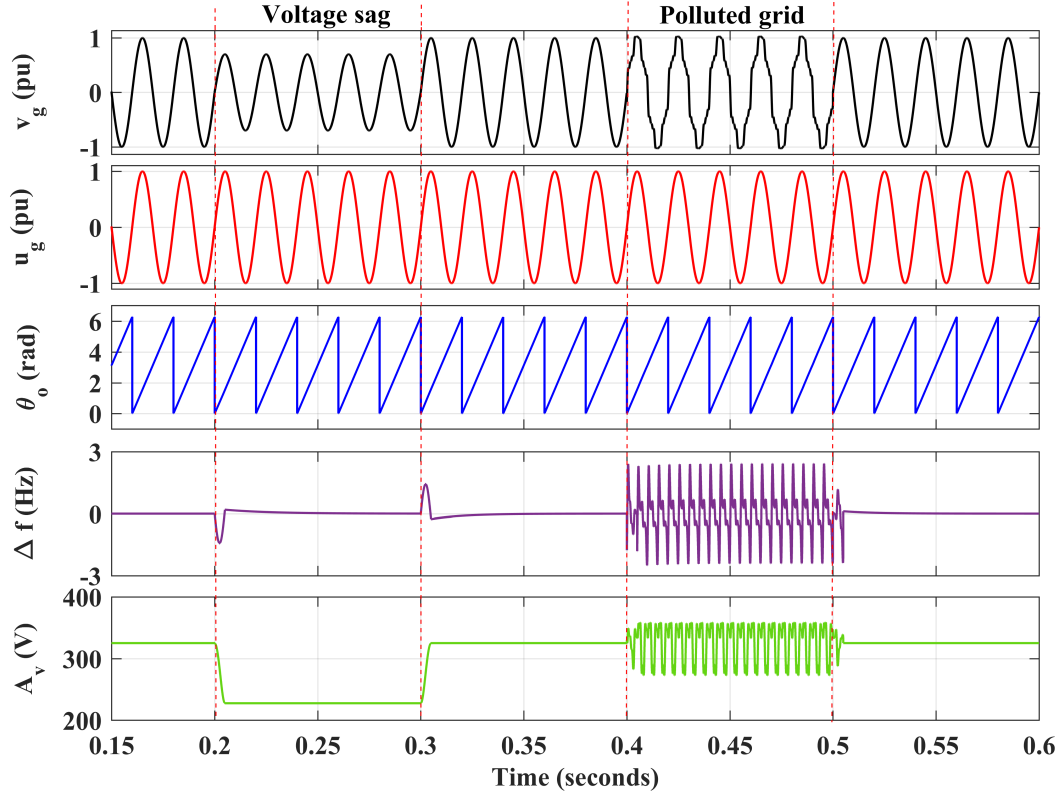


Figure 4.2: Simulation performance of single-phase SRF-PLL under voltage sag of 0.3pu and polluted grid

In Fig. 4.2, voltage sag is introduced at  $t=0.2s$  and removed at  $t=0.3s$ , also the harmonics are introduced at  $t=0.4s$  and removed at  $t=0.5s$ . During the polluted grid condition, ripples of 4.89Hz have been observed in frequency estimation and ripples of 86.67V has been seen in amplitude estimation. Settling time of amplitude estimation during the voltage sag is 4.8ms. During the voltage sag condition, grid parameters estimation gives good results but during the polluted grid conditions it shows ripples in amplitude and frequency estimation.

Fig. 4.3 shows the simulation performance of SRF-PLL under frequency change of +2Hz and noisy grid voltage signal. The SRF-PLL is able to estimate frequency but it shows oscillations of 0.8Hz when the frequency deviates from the standard grid frequency of 50Hz to 52Hz and the dynamic response is slow and takes almost 3 cycles. During the noisy signal condition the output of the SRF-PLL is also noisy

for both voltage amplitude and frequency estimation. The unit synchronizing signal generated is also noisy when noise is present in grid voltage.

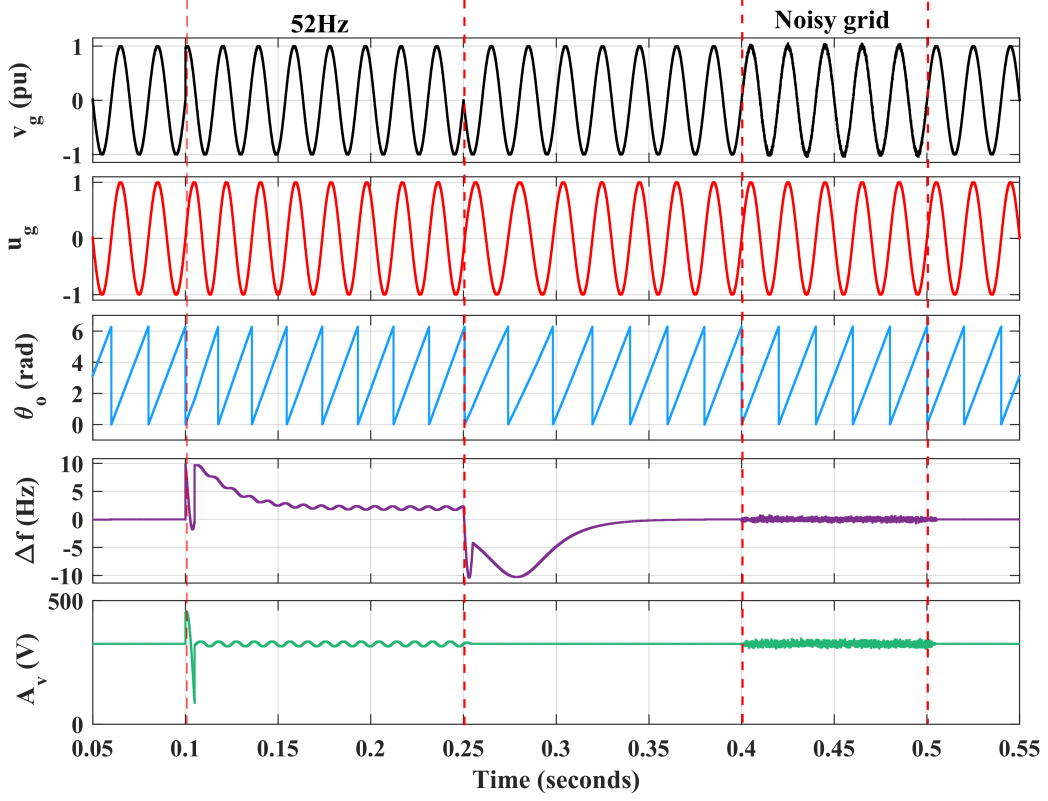


Figure 4.3: Simulation performance of single-phase SRF-PLL under frequency shift of +2Hz and noisy grid

Figure 4.4 shows the simulation performance of SRF-PLL under phase shift and the DC-offset in the input voltage signal. Phase shift of  $\pi/2$  is introduced at  $t=0.1s$  and removed at  $t=0.25s$ . The frequency estimation show transient of 5Hz and slow response. During the DC-offset in grid voltage signal, the phase, frequency and amplitude show high oscillations from  $t=0.4s$  to  $t=0.5s$ . The peak to peak value is 183.8V and 5.76Hz for amplitude and frequency estimation respectively during DC-offset condition.

#### 4.1.1.2 Experimental Results

Performance of the single-phase delay based SRF-PLL has been also tested on experimental prototype setup. SRF-PLL has been tested under different grid voltage

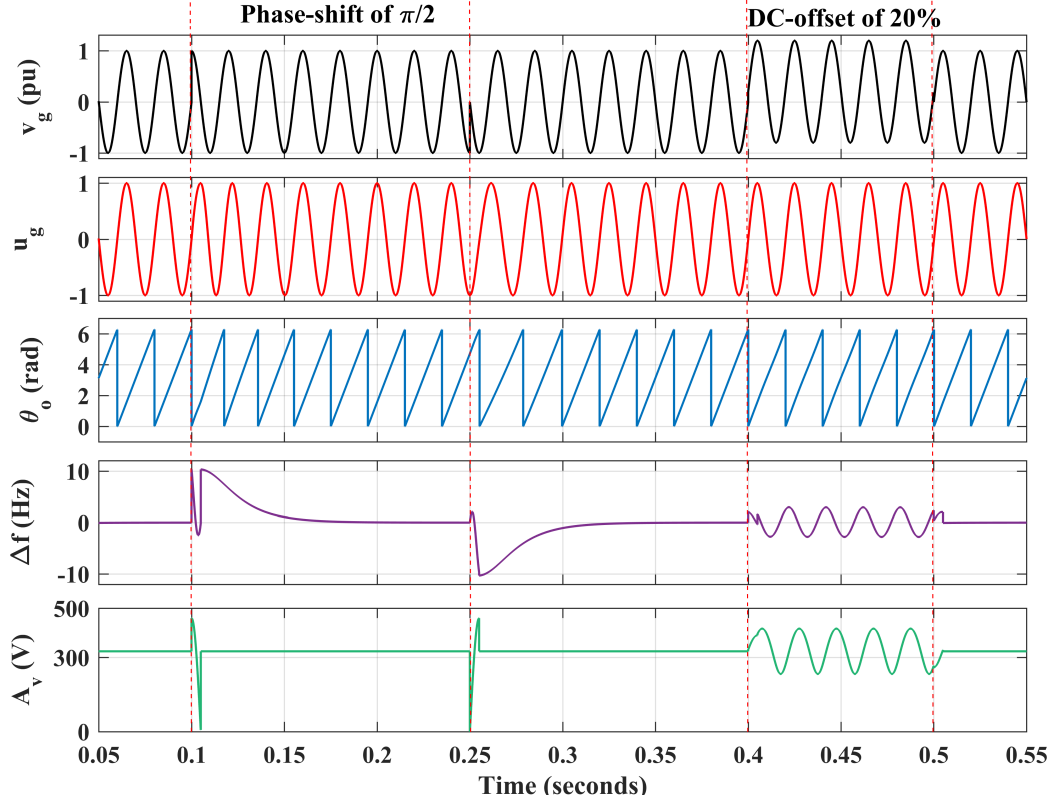


Figure 4.4: Simulation performance of single-phase SRF-PLL under phase-shift of  $\pi/2$  and 20% DC-offset

conditions. Figure 4.5(a) and 4.5(b) show the performance for the voltage sag and the polluted grid condition. During the polluted grid condition, the voltage mag-

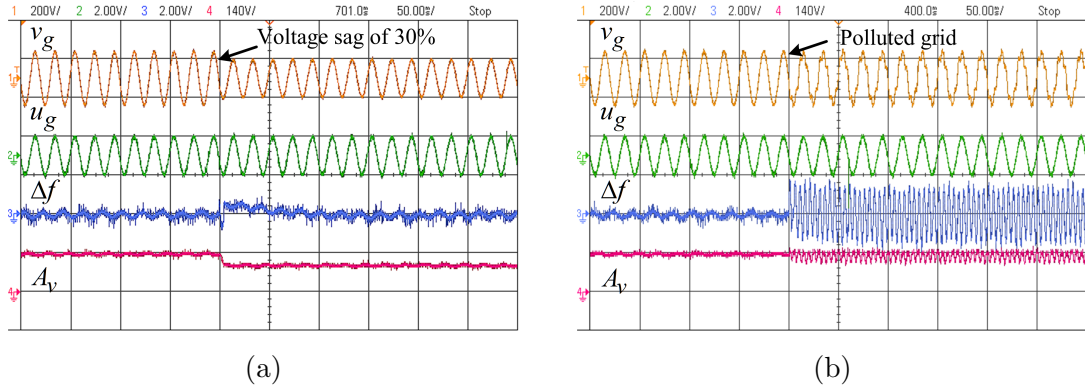


Figure 4.5: Experimental performance of single-phase SRF-PLL under (a) voltage sag of 20% (b) polluted grid (THD 18.0%)

nitude and the frequency estimation is tracked instantaneously. In steady state, during normal grid voltage the estimated frequency shows oscillations. During the polluted grid condition, the voltage estimated and frequency show high oscillations.



High frequency oscillations leads to non-sinusoidal synchronizing signal.

Figure 4.6(a) and 4.6(b) show the experimental performance of the SRF-PLL under frequency variation and the noisy grid voltage signal. Dynamic response for the frequency estimation is almost 2.5 cycles and shows oscillations of 3Hz during noisy grid voltage.

Figure 4.7(a) and 4.7(b) show the experimental performance of the SRF-PLL under

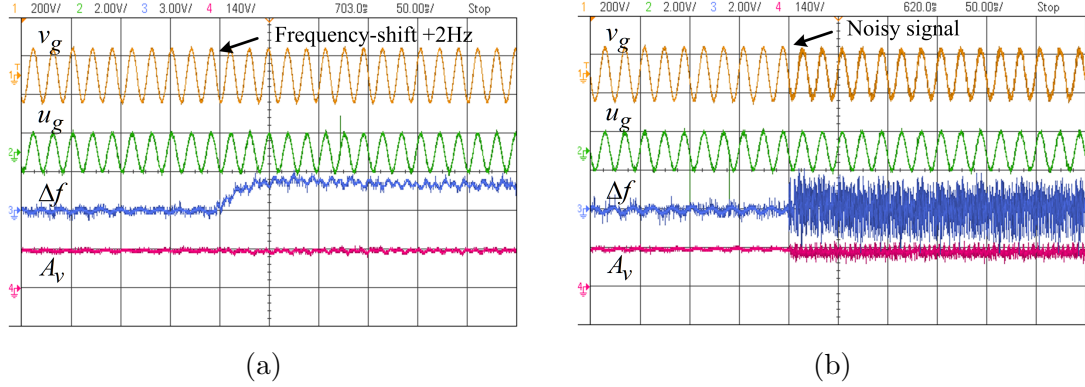


Figure 4.6: Experimental performance of single-phase SRF-PLL under (a) frequency shift of +2Hz (b) noisy grid

phase-shift of  $90^\circ$  and the DC-offset of 20% in the grid voltage signal. During the

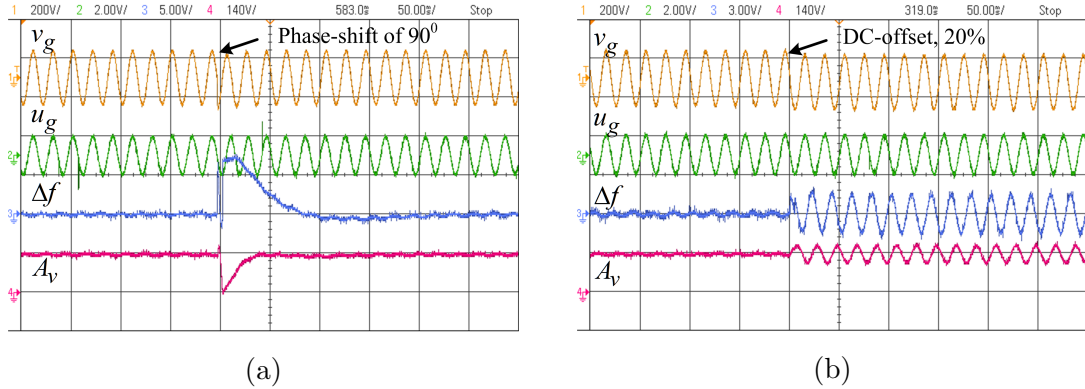


Figure 4.7: Experimental performance of single-phase SRF-PLL under (a) phase-shift of  $\pi/2$  (b) 20% DC-offset

sudden phase-shift an overshoot of 7Hz in frequency estimation and an overshoot of 140V has been occurred. During the DC-offset condition estimated frequency shows oscillations of 6Hz and the estimated grid voltage shows the oscillations of 60V.

The SRF-PLL has been tested here under both in simulation and in experimental environment. Simulation and experimental performance of delay based single-phase

SRF-PLL has been summarized in Table 4.1. The results for SRF-PLL shows good performance under normal grid condition but performance is not satisfactory under the polluted grid and noisy grid voltage condition.

Table 4.1: Summary of simulation and experimental performance of delay based SRF-PLL

Cases	Parameters	Simulation performance	Experimental performance
<b>Voltage sag of 30%</b>	$\Delta f$	$t_s = 4.8ms$	$t_s = 5ms$
	$A_v$	$t_s = 4.8ms$	$t_s = 5ms$
<b>Polluted grid (THD 14.18%)</b>	$\Delta f$	$\Delta f_{pp} = 4.89Hz$	$\Delta f_{pp} = 3.9Hz$
	$A_v$	$A_{vpp} = 86.67V$	$A_{vpp} = 50.0V$
<b>Frequency change of +2Hz</b>	$\Delta f$	$t_s = 16.25ms$	$t_s = 40ms$
		$\Delta f_{pp} = 0.81Hz$	
	$A_v$	$t_s = 10.0ms$	$t_s = 10ms$
		$A_{vpp} = 20.42V$	
<b>Noisy voltage</b>	$\Delta f$	$\Delta f_{pp} = 1.27Hz$	$\Delta f = 3.8Hz$
	$A_v$	$A_{vpp} = 40.5V$	$A_{vpp} = 40V$
<b>Phase-shift of <math>\pi/2</math></b>	$\Delta f$	$t_s = 16.0ms$	$t_s = 80ms$
	$A_v$	$t_s = 50ms$	$t_s = 40ms$
<b>DC-offset of 20%</b>	$\Delta f$	$\Delta f_{pp} = 5.76Hz$	$\Delta f_{pp} = 3.6Hz$
	$A_v$	$A_{vpp} = 183.8V$	$A_{vpp} = 40.0V$

### 4.1.2 Enhanced Phase Locked Loop (EPLL)

EPLL is the enhanced version of standard PLL which removes the main drawback of the presence of double frequency oscillation errors [140, 141]. The structure of the EPLL is shown in Fig. 4.8 and it is very simple and robust such that the small variation in its internal parameters do not affect much the performance of the EPLL. One of the most significant feature of EPLL is that it has locking capability of phase angle and amplitude both. It can accurately estimate different important parameters of the grid voltage signal such as phase angle, frequency, amplitude, synchronizing signal, quadrature signal, fundamental component, distortions etc. The removal of double frequency error using mathematical modelling has been explained here.

Considering the input voltage signals as 4.5:

$$v_g(t) = A_v \sin(\underbrace{\omega_i t + \phi_i}_{\theta_i}) \quad (4.5)$$

From the Fig. 4.8 the output is  $y = A_o \sin \theta_o$ . When  $A_o = A_v$  and  $\theta_o = \theta_i$ , EPLL is under steady-state condition and the error ( $e_v$ ) will be zero. This condition also shows the correct solution for the zero steady-state error for the estimation of phase and frequency.

As observed from Fig. 4.8, the error signal is,

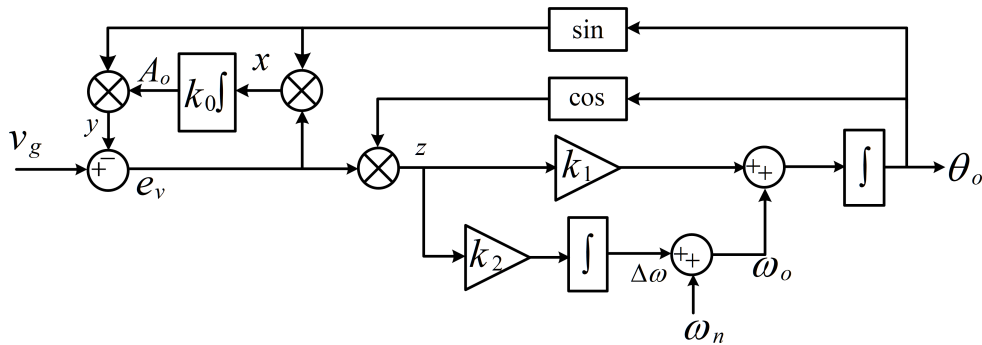


Figure 4.8: Structure of EPLL

$$e_v = v_g - y = A_v \sin \theta_i - A_o \sin \theta_o \quad (4.6)$$

The output,

$$\begin{aligned}
z &= e_v \cos \theta = (A_v \sin \theta_i - A_o \sin \theta_o) \cos \theta_o \\
&= A_v/2 \sin(\theta_i - \theta_o) + \underbrace{\frac{A_v}{2} \sin(\theta_i + \theta_o) - A_o \sin(2\theta_o)}_{\text{double frequency term}}
\end{aligned} \tag{4.7}$$

If,  $A_o = A_v$  and  $\theta_o = \theta_i$  is asymptotically stable, the system approaches to steady state condition and the double frequency term approaches zero in 4.7. Then, the estimated phase and frequency are free from double frequency ripple. The output,

$$\begin{aligned}
x &= e_v \sin \theta_o = (A_v \sin \theta_i - A_o \sin \theta_o) \sin \theta_o \\
&= A_v/2 \cos(\theta_i - \theta_o) - \frac{A_o}{2} + \underbrace{\frac{A_o}{2} \cos(2\theta_o) - \frac{A_v}{2} \cos(\theta_i + \theta_o)}_{\text{double frequency term}}
\end{aligned} \tag{4.8}$$

Similarly as in 4.7, the double frequency error approaches zero in 4.8. Hence there is no double frequency in the estimated amplitude of the input signal also. The phase angle of the input signal is estimated by given as 4.9:

$$\theta_o = \int [k_1 e_v(t) \cos \theta_o + k_2 \int e_v(t) \cos \theta_o dt + \omega_n] dt \tag{4.9}$$

From the control structure of Fig. 4.8, the differential equations of the EPLL can be written as

$$\begin{aligned}
\dot{A}_o &= k_0 e_v \sin \theta_o \\
\Delta \dot{\omega} &= k_1 e_v \cos \theta_o \\
\dot{\theta}_o &= \omega_o + k_2 e_v \cos \theta_o
\end{aligned} \tag{4.10}$$

From 4.7 and 4.8, neglecting the double frequency term, i.e. at the steady state

condition, the following differential equations can be obtained.

$$\begin{aligned}\dot{A}_o &= k_0 \frac{A_v}{2} \cos(\theta_i - \theta_o) - k_0 \frac{A_o}{2} \\ \dot{\omega} &= k_1 \frac{A_v}{2} \sin(\theta_i - \theta_o) \\ \dot{\theta}_o &= \omega_o + \Delta\omega + k_2 e_v \frac{A_v}{2} \sin(\theta_i - \theta_o)\end{aligned}\tag{4.11}$$

Now, defining the new small signal variables  $\tilde{A}_o = A_o - A_v$ ,  $\tilde{\omega}_o = \omega_o - \omega_i$  and  $\tilde{\theta}_o = \theta_o - \theta_i$  and after linearising the above equation, it gives the following equation:

$$\begin{aligned}\dot{\tilde{A}}_o &= -\frac{k_o}{2} \tilde{A}_o \\ \dot{\tilde{\omega}}_o &= -k_1 \frac{A_v}{2} \tilde{\theta}_o \\ \dot{\tilde{\theta}}_o &= \tilde{\omega}_o - k_2 \frac{A_v}{2} \tilde{\theta}_o\end{aligned}\tag{4.12}$$

From 4.12, it can be analysed that the amplitude estimation is isolated with the phase or frequency estimation loop. The equation for the amplitude estimation is the first-order equation and the time constant is calculated as  $\tau = \frac{2}{k_o}$ .

The design parameters of the  $k_1$  and  $k_2$  of the EPLL are same as conventional PLL. Characteristic equation for the phase angle estimation is given as:

$$\ddot{\theta}_o + \frac{k_2 A_v}{2} \dot{\theta}_o + \frac{k_1 A_v}{2} \theta_o = 0\tag{4.13}$$

The transfer function for the phase angle estimation is given by 4.14

$$\frac{\theta_o(s)}{\theta_i(s)} = \frac{\frac{k_2 A_v}{2} s + \frac{k_1 A_v}{2}}{s^2 + \frac{k_2 A_v}{2} s + \frac{k_1 A_v}{2}} = \frac{2\zeta\omega_r s + \omega_r^2}{s^2 + 2\zeta\omega_r s + \omega_r^2}\tag{4.14}$$

From 4.14, the values  $k_1$  and  $k_2$  can be calculated for the specified value of  $\omega_r$ ,  $A_v$  and damping ( $\zeta$ ) of the system.

Figure 4.8 shows the basic structure of EPLL and the gain  $k_0$  here controls the speed of convergence for calculating magnitude. The parameters  $k_1$  and  $k_2$  of EPLL are responsible for controlling the rate of phase and frequency change.

#### 4.1.2.1 Simulation Results

Performance of the EPLL has been implemented and tested in MATLAB/Simulink. Its simulation performance under different grid voltage conditions has been shown in Fig. (4.9)-(4.11). These figures shows the grid voltage, synchronizing signal, phase angle, frequency deviation and amplitude of the grid voltage.

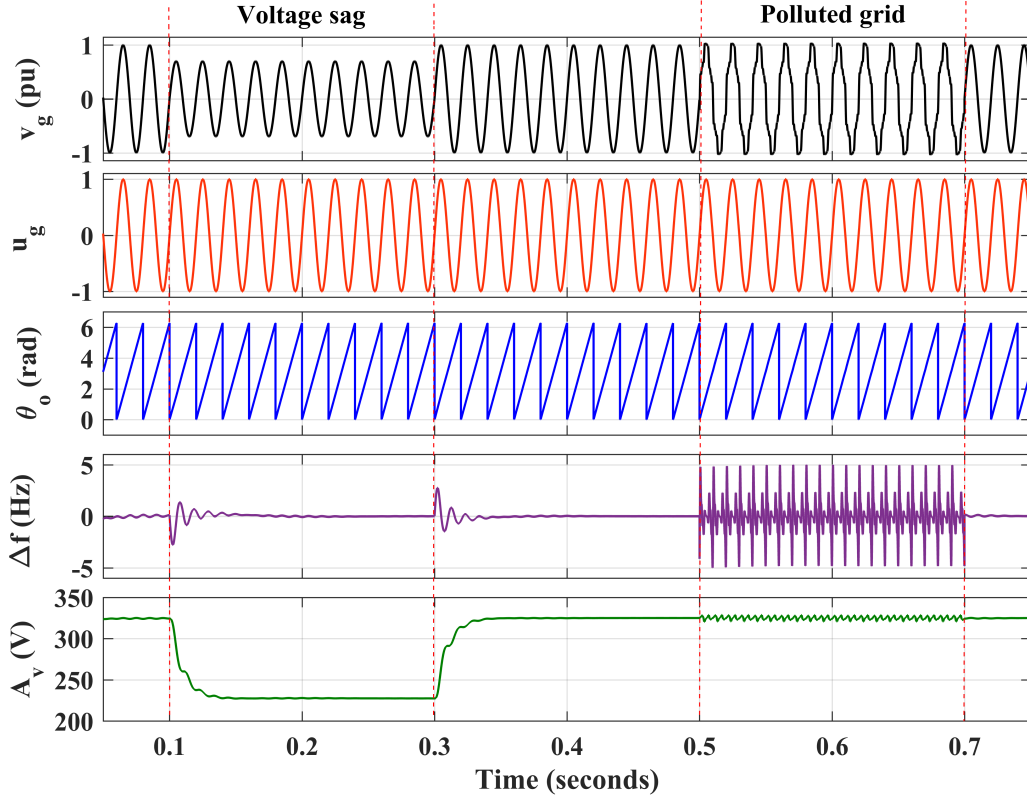


Figure 4.9: Simulation Performance of EPLL under voltage sag of 0.3pu and polluted grid

Figure 4.9 shows the simulation performance under 0.3pu voltage sag ( $t=0.1s$  to  $t=0.3s$ ) and polluted grid ( $t=0.5s$  to  $t=0.7s$ ) environment. During the voltage sag, the settling time for the amplitude estimation is 2 cycles. During the polluted or harmonic grid condition, peak to peak value of frequency is 9.83Hz and peak to peak value of voltage amplitude is 8.15V.

Simulation performance of EPLL under frequency deviation of +2Hz and the noisy grid voltage has been shown in Fig. 4.10. Initially, frequency of the voltage is 50Hz and at  $t=0.1s$ , frequency has been changed to 52Hz. After 0.2s it is set back to

normal condition. The settling time for frequency estimation is almost 2.5cycles . During this condition, the peak to peak frequency in steady-state is almost zero, which is main advantage of EPLL. Ripple in frequency estimation is 1.92Hz and in amplitude estimation is 1.25V the during noisy grid voltage signal. High undershoot has been observed in amplitude estimation during frequency change.

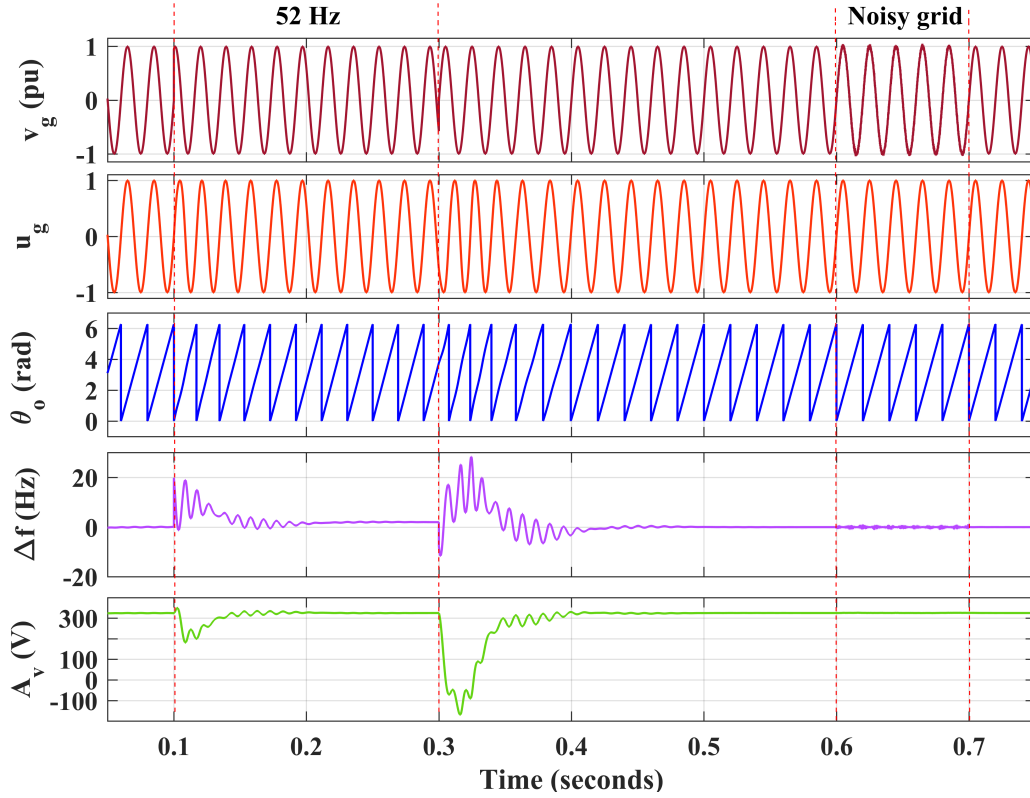


Figure 4.10: Simulation performance of EPLL under frequency shift of +2Hz and noisy grid

Simulation performance of EPLL under phase-shift of  $\pi/2$  and DC-offset of 20% has been shown in Fig. 4.11. Phase-shift of  $\pi/2$  is simulated at  $t=0.1s$  and again at  $t=0.3s$ . The frequency estimation shows almost zero-steady state error and amplitude estimation shows high undershoot to 127.3V. 20% DC-offset has been occurred during  $t=0.5s$  to  $t=0.7s$ . Both frequency and amplitude estimation show high oscillation during this condition. The results indicate that the EPLL gives better steady-state performance during the frequency shift but it is not immune to DC-offset.

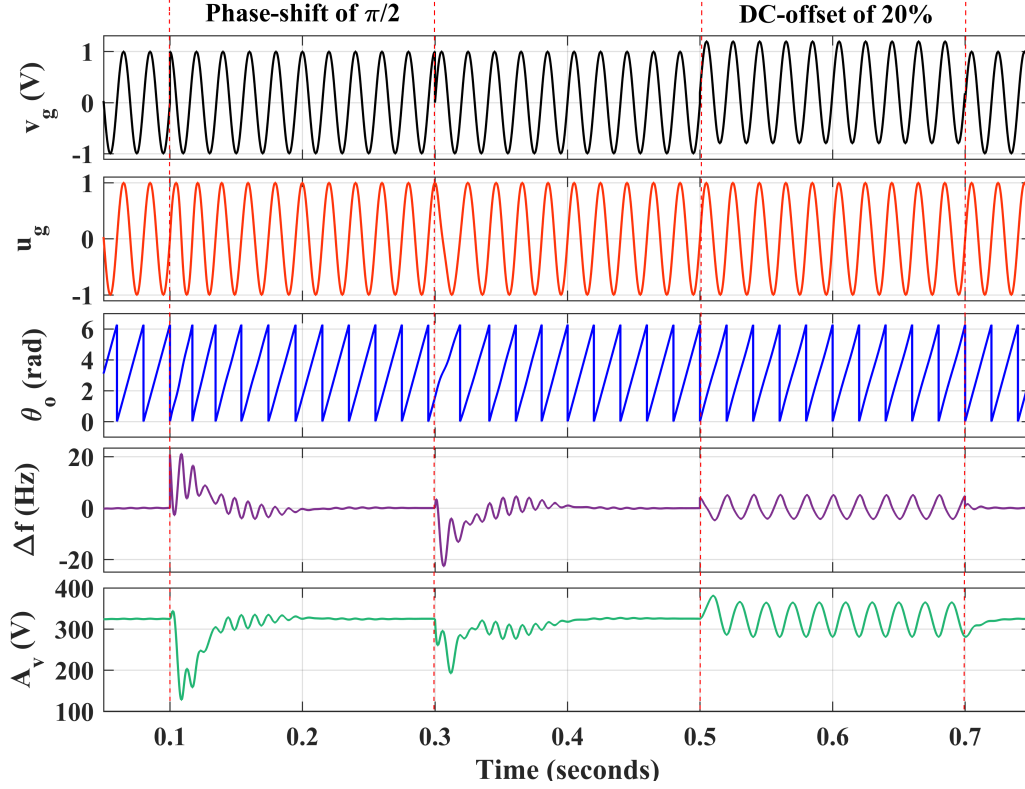


Figure 4.11: Simulation performance of EPLL under phase-shift of  $\pi/2$  and DC-offset of 20%

#### 4.1.2.2 Experimental Results

Experimental performance of EPLL has been shown here for the different PQ problems in grid voltage issues. Figure 4.12(a) and 4.12(b) show the performance of EPLL under voltage sag and the polluted grid conditions. During normal grid voltage condition the estimated frequency shows almost zero oscillations and it takes only 1 cycle to estimate frequency during voltage sag dynamics. The voltage estimation also shows almost zero oscillations during steady-state condition and during dynamic voltage sag condition it takes less than 1cycle to estimate magnitude.

Figure 4.13(a) and 4.13(b) show the performance of EPLL under frequency shift of +2Hz and the noisy grid voltage signal. During the frequency shift of +2Hz, frequency has been tracked accurately within 2.5cycles but initially, it shows some oscillations and these oscillations persist. During the noisy grid voltage, the frequency estimation shows persisted oscillations of 3.5Hz.



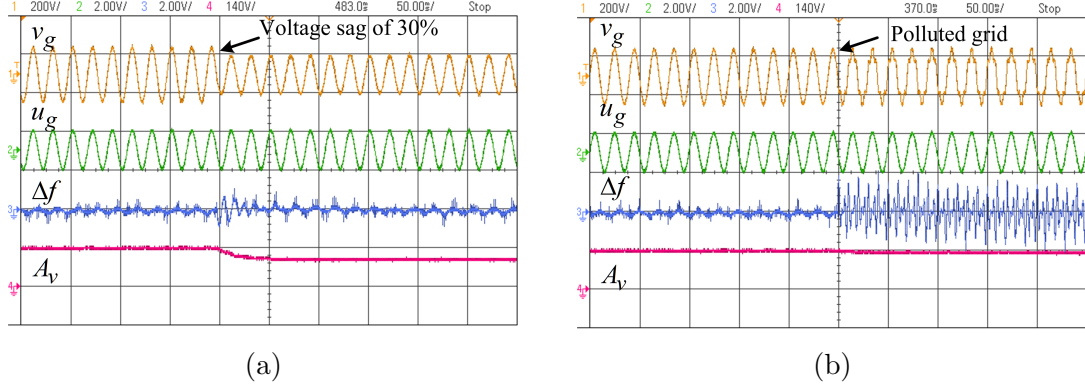


Figure 4.12: Experimental performance of single-phase EPLL under (a) voltage sag of 20% (b) polluted grid (THD 18.0%)

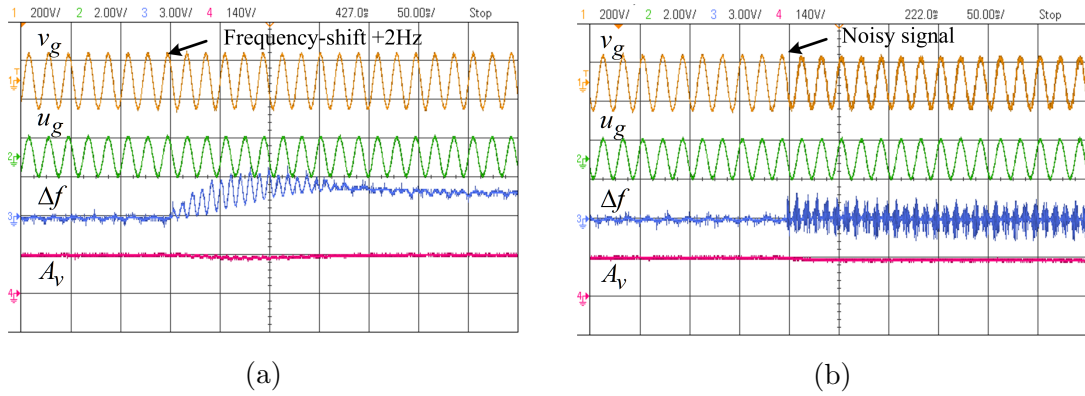


Figure 4.13: Experimental performance of single-phase EPLL under (a) frequency shift of +2Hz (b) noisy grid

Figure 4.14(a) and 4.14(b) show the performance of single-phase EPLL under

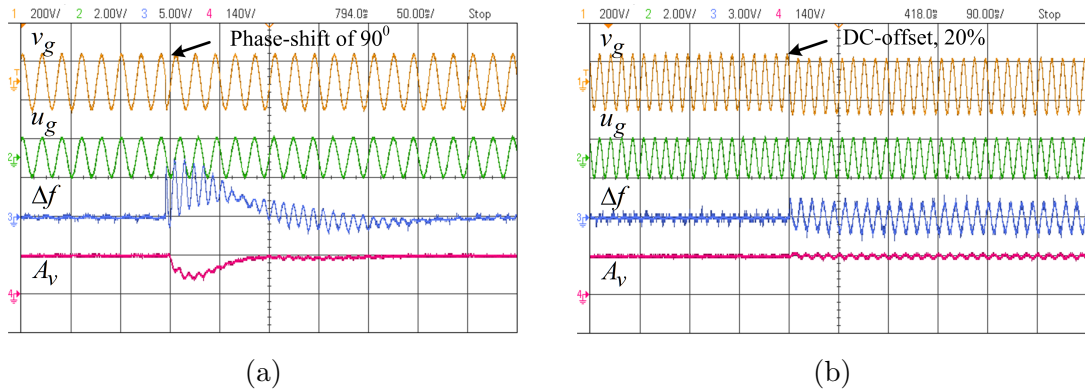


Figure 4.14: Experimental performance of single-phase EPLL under (a) phase-shift of  $\pi/2$  (b) 20% DC-offset

phase-shift of  $\pi/2$  and 20% DC-offset in grid voltage. In both the cases, the performance EPLL is not good as the oscillations during dynamic phase-shift takes 12.5 cycles to damped out. During the DC-offset condition the oscillations in estimated

frequency is 4Hz.

Table 4.2: Summary of simulation and experimental performance of EPLL

Cases	Parameters	Simulation performance	Experimental performance
<b>Voltage sag of 30%</b>	$\Delta f$	$t_s = 40ms$	$t_s = 50ms$
	$A_v$	$t_s = 40ms$	$t_s = 50ms$
<b>Polluted grid (THD 14.18%)</b>	$\Delta f$	$\Delta f_{pp} = 9.83Hz$	$\Delta f_{pp} = 4.0Hz$
	$A_v$	$A_{vpp} = 8.15V$	Very low oscillations
<b>Frequency change of +2Hz</b>	$\Delta f$	$t_s = 51.82ms$	$t_s = 150ms$
		$\Delta f_{pp} = 0.07Hz$	
	$A_v$	$t_s = 51.82ms$	$t_s = 150ms$
		$A_{vpp} = 0.335V$	
<b>Noisy voltage</b>	$\Delta f$	$\Delta f_{pp} = 1.92Hz$	$\Delta f = 3.6Hz$
	$A_v$	$A_{vpp} = 1.25V$	Very low Oscillations
<b>Phase-shift of <math>\pi/2</math></b>	$\Delta f$	$t_s = 60ms$	$t_s = 250ms$
	$A_v$	$t_s = 60ms$	$t_s = 75ms$
<b>DC-offset of 20%</b>	$\Delta f$	$\Delta f_{pp} = 9.34Hz$	$\Delta f_{pp} = 3Hz$
	$A_v$	$A_{vpp} = 83.9V$	$A_{vpp} = 100.0V$

EPLL shows almost zero oscillations in frequency estimation in steady-state under normal grid voltage conditions. During large phase-shift of the order of  $90^\circ$  its performance is not acceptable. EPLL has the good capability to filter out lower order harmonics but not higher order harmonics. Simulation and experimental performance of EPLL has been summarized in Table 4.2.

### 4.1.3 Second-Order Generalized Integrator Phase-Locked Loop (SOGI-PLL)

The structure of SOGI-PLL has been shown in Fig. 4.15. SOGI is widely reported in literature and used to generate filtered in-phase ( $v_\alpha$ ) and quadrature-phase ( $v_\beta$ ) components of the input grid voltage. SOGI is used with loop filter and the VCO can

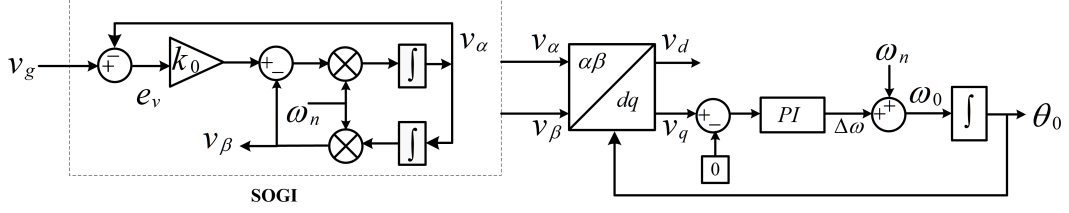


Figure 4.15: Structure of SOGI-PLL

be used as PLL. Firstly, output of the SOGI is converted into dq components of the grid voltage. The q-component  $v_q$  of the grid voltage contains phase and frequency information. Hence, it is used to estimate phase and frequency information of the grid voltage signal. The resonating frequency of the SOGI is fixed and is selected as standard grid frequency of 50 Hz.

Consider the grid voltage signal in simpler form;

$$v_g(t) = A_v \sin(\underbrace{\omega_i t + \phi_i}_{\theta_i}) \quad (4.15)$$

The error in voltage signal is estimated by subtracting the in-phase filtered component to the grid voltage.

$$e_v(t) = v_g(t) - v_\alpha(t) \quad (4.16)$$

The quadrature component of the input grid voltage signal is given by 4.17,

$$v_\beta(t) = \omega_n \int v_\alpha(t) dt \quad (4.17)$$

Here,  $\omega_n$  is the standard grid frequency or the resonating frequency of the SOGI-PLL. Applying Laplace transformation on 4.17, it gives

$$v_\beta(s) = \omega_n \frac{v_\alpha(s)}{s} \quad (4.18)$$

From Fig. 4.15,  $v_\alpha(t)$  is given by 4.19,

$$\begin{aligned} v_\alpha(t) &= \int \omega_n [k_0 e_v(t) - v_\beta(t)] dt \\ &= \int \omega_n k_0 [v_g(t) - v_\alpha(t)] dt - \omega_n \int v_\beta(t) dt \end{aligned} \quad (4.19)$$

Laplace transform of the above equation is given as,

$$v_\alpha(s) = \omega_n k_0 \left[ \frac{v_g(s)}{s} - \frac{v_\alpha(s)}{s} \right] - \omega_n \frac{v_\beta(s)}{s} \quad (4.20)$$

Putting the value of  $v_\beta(s)$  from (4.18) and arranging them it gives the closed-loop transfer function of in-phase signal and is written as 4.21,

$$D(s) = \frac{v_\alpha(s)}{v_g(s)} = \frac{k_o \omega_n s}{s^2 + k_o \omega_n s + \omega_n^2} \quad (4.21)$$

Transfer function of the quadrature component is given as 4.22,

$$Q(s) = \frac{v_\beta(s)}{v_g(s)} = \frac{k_o \omega_n^2}{s^2 + k_o \omega_n s + \omega_n^2} \quad (4.22)$$

Transfer function of the SOGI is given as 4.23,

$$SOGI(s) = \frac{v_\alpha(s)}{k_o e_v(s)} = \frac{\omega_n s}{s^2 + \omega_n^2} \quad (4.23)$$

Transfer function of the error signal ( $e_v$ ) is given as 4.24:

$$E(s) = \frac{e_v(s)}{v_g(s)} = \frac{s^2 + \omega_n^2}{s^2 + k_o \omega_n s + \omega_n^2} \quad (4.24)$$

Bode plots of SOGI are shown in Fig. 4.16 for in-phase and quadrature phase component transfer functions from the different SOGI gains. Bode-plot for  $D(s)$  shows the characteristics of the band pass filter while the bode plot of  $Q(s)$  shows the characteristics of low pass filter and the  $90^\circ$  behind the in-phase component. Step response of the in-phase and quadrature phase transfer functions have been shown in Fig. 4.17 for the different value of  $k_0$ . The selected value of  $k_0$  is 1.414 as it shows the optimal response in terms of convergence rate and the transient value.

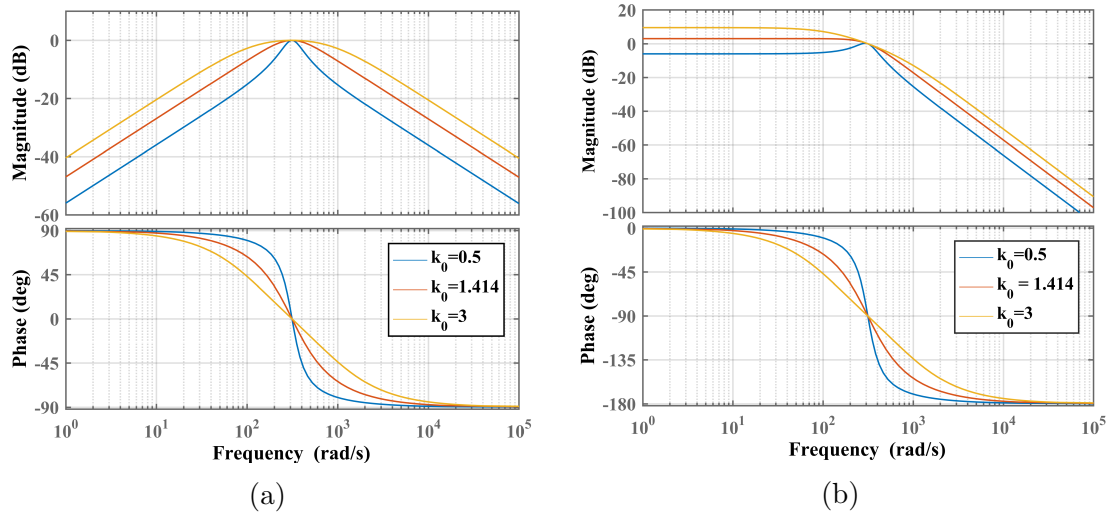


Figure 4.16: Bode plot of SOGI for (a) In-phase component  $D(s)$  (b) Quadrature component  $Q(s)$

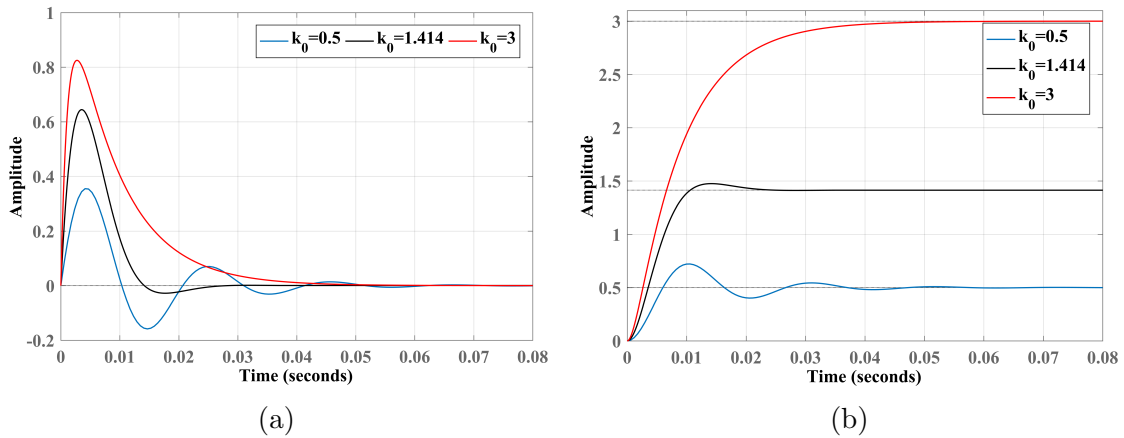


Figure 4.17: Step response of SOGI for (a) In-phase component  $D(s)$  (b) Quadrature component  $Q(s)$

#### 4.1.3.1 Simulation Results

Simulation results for SOGI-PLL under different cases of grid voltage conditions has been shown in Fig. (4.18)-(4.19). Performance of SOGI-PLL under grid voltage sag and harmonic grid have been shown in Figure 4.18. Voltage sag of 0.3pu has been simulated at  $t=0.1s$  and recovered back to normal at  $0.3s$ . The frequency has been estimated accurately with very low oscillations ( $f_{pp}=0.85Hz$ ) during polluted grid condition. The amplitude has been estimated within 0.5cycle during sag and peak to peak voltage ( $A_{vpp}$ ) is 16.99V during harmonic grid voltage condition.

SOGI-PLL has been tested under frequency shift of +2Hz and noisy grid voltage

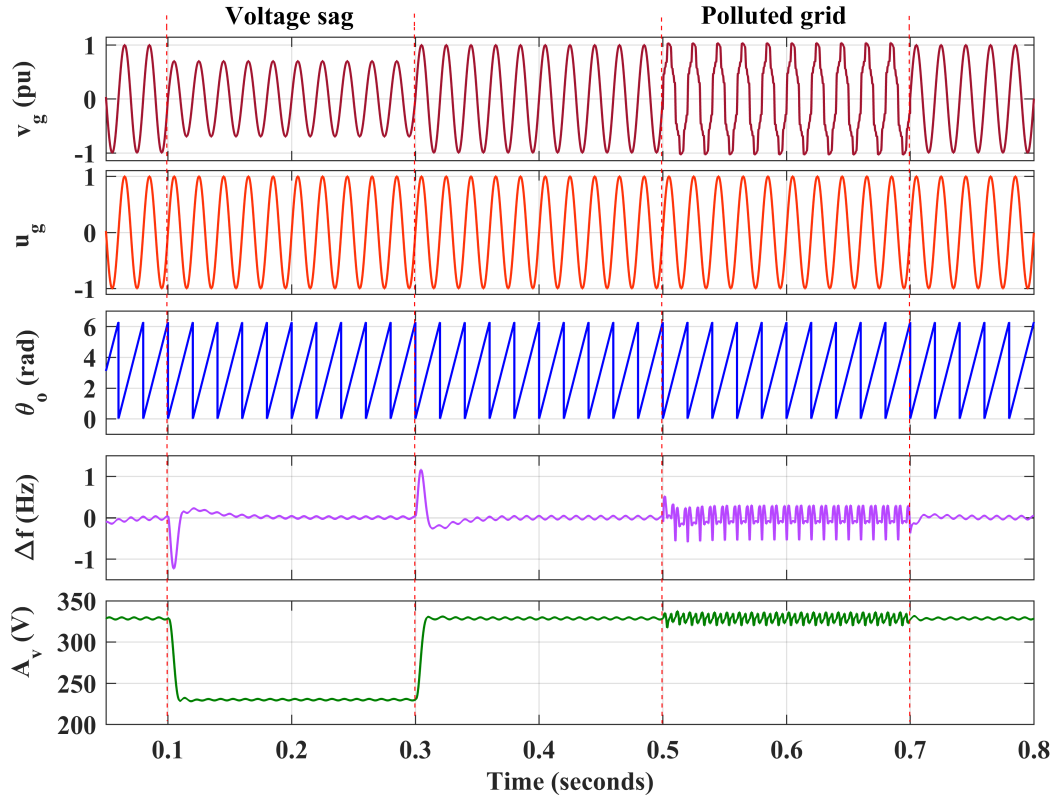


Figure 4.18: Simulation performance of SOGI-PLL under voltage sag of 0.3pu and polluted grid

signal and shown in Fig. 4.19. The frequency has been changed to 52Hz at  $t=0.1s$  and brought back to standard condition at  $t=0.3s$ . The frequency has been estimated within 3 cycles by SOGI-PLL and in steady-state  $f_{pp}$  is 0.42Hz during grid voltage of 52Hz . The response time for phase angle will be same as frequency estimation as

it calculated from frequency. Noise in grid voltage signal has been simulated during  $t=0.6s$  to  $t=0.7s$ . During this condition all the parameters have been estimated perfectly.

Simulation performance of SOGI-PLL under phase-shift of  $\pi/2$  and DC-offset

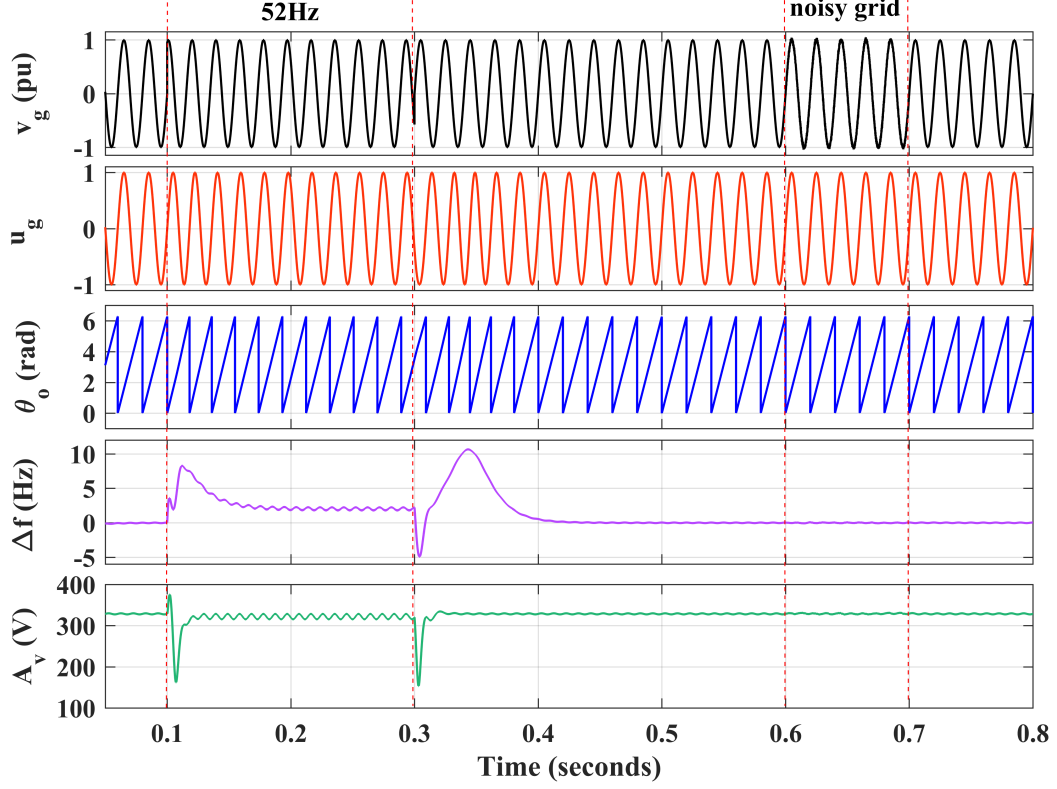


Figure 4.19: Simulation performance of SOGI-PLL under frequency shift of 2Hz and noisy grid

condition has been shown in Fig. 4.20. Phase-shift of  $\pi/2$  is happened at  $t=0.1s$  and it occurred again at  $t=0.3s$ . Overshoot of 10Hz has been observed at  $t=0.1s$  for frequency estimation and estimated within 3 cycles. The amplitude estimation shows the undershoot of 101.10V and its settling time is 20ms. DC-offset of 20% has been simulated during  $t=0.5s$  to  $t=0.7s$ . During this condition, frequency estimation shows oscillations and  $f_{pp}$  is 5.75Hz and amplitude estimation shows oscillations of 183.90V. Hence, the SOGI-PLL works good in all conditions except the DC-offset in grid voltage signal.

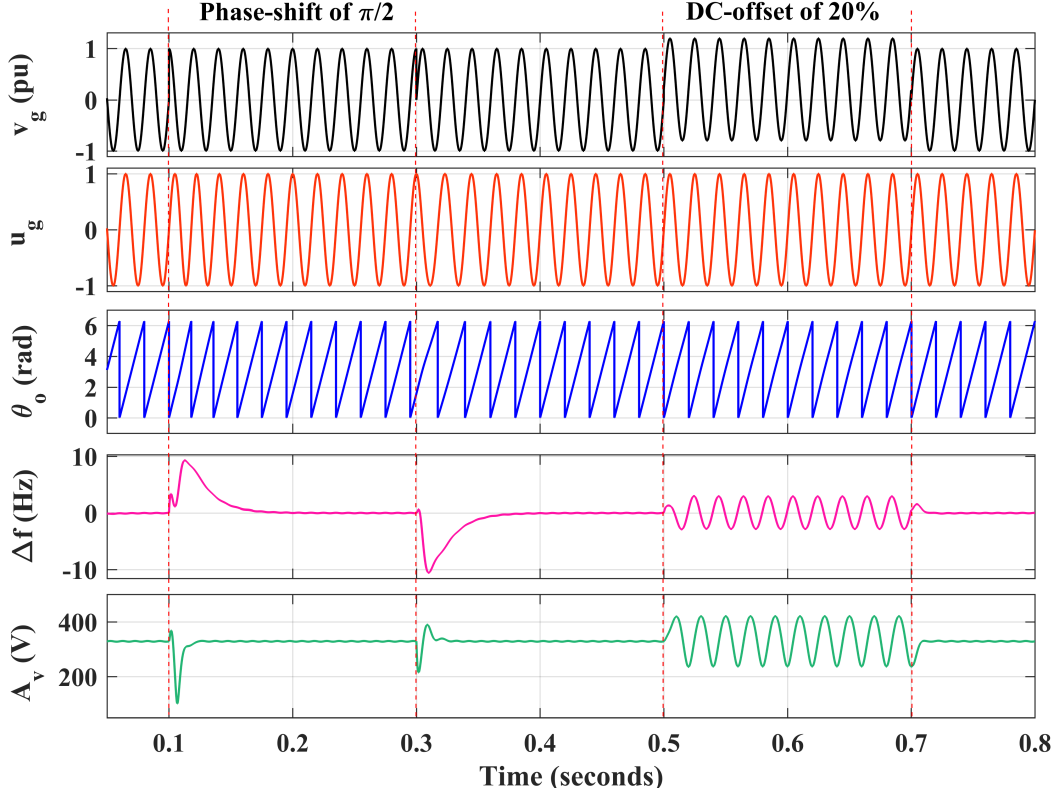


Figure 4.20: Simulation performance of SOGI-PLL under phase-shift of  $\pi/2$  and DC-offset of 20%

#### 4.1.3.2 Experimental Results

Experimental performance of SOGI-PLL has been shown in Fig. 4.21(a) and 4.21(b) under voltage sag and the polluted grid condition. Voltage magnitude has been estimated accurately within half-cycle and very low oscillations have been observed in estimated frequency under normal grid condition. During the polluted grid condition, the peak to peak value of estimated frequency is only 0.8Hz as the SOGI-PLL has good filtering capability.

Experimental performance of SOGI-PLL has been shown in Fig. 4.22(a) and 4.22(b) under frequency-shift of +2Hz and the noisy grid signal. During frequency variation of +2Hz, the frequency has been estimated within 2.5 cycles. During the noisy grid voltage condition, due to the excellent filtering capability almost no oscillation has been observed in estimated frequency.

Experimental performance of SOGI-PLL has been shown in Fig. 4.23(a) and 4.23(b)



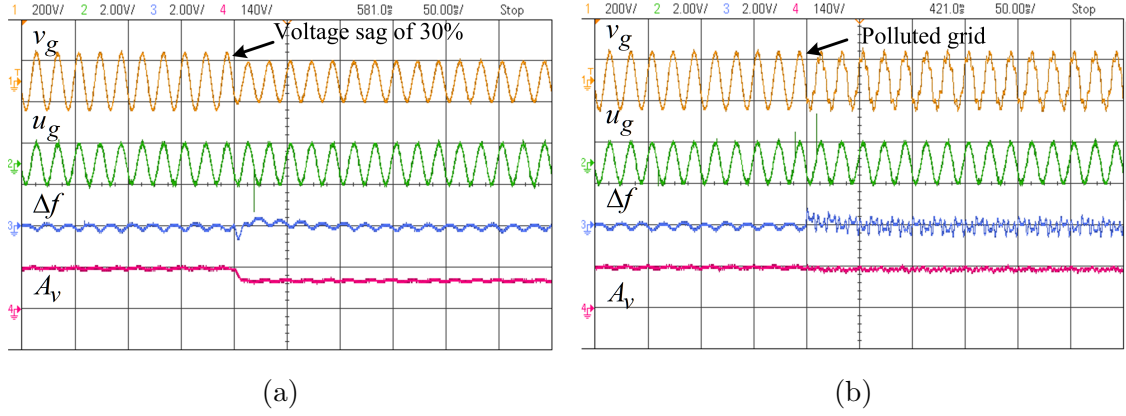


Figure 4.21: Experimental performance of single-phase SOGI-PLL under (a) voltage sag of 20% (b) polluted grid (THD 18.0%)

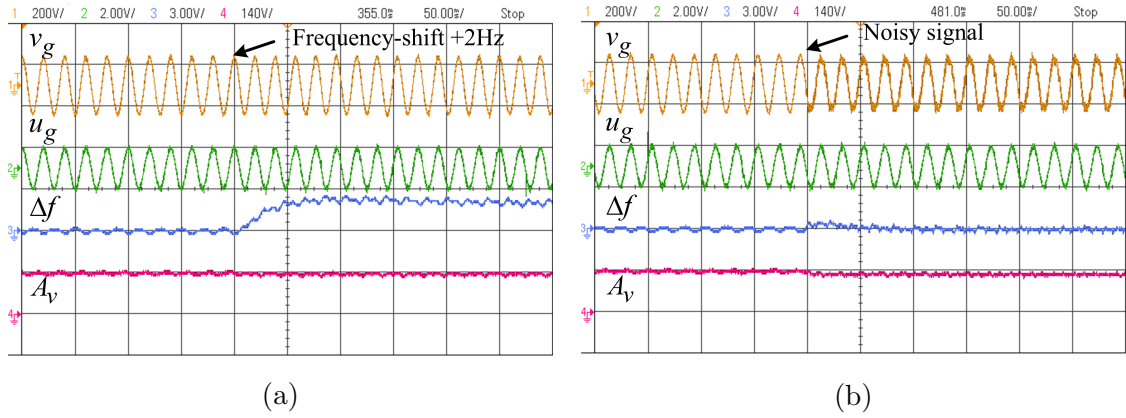


Figure 4.22: Experimental performance of single-phase SOGI-PLL under (a) frequency shift of +2Hz (b) noisy grid

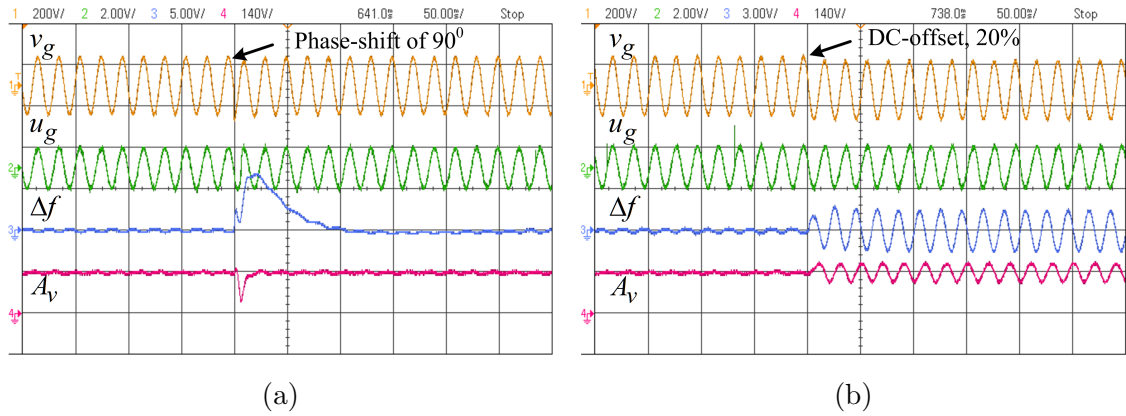


Figure 4.23: Experimental performance of single-phase SOGI-PLL under (a) phase-shift of  $\pi/2$  (b) 20% DC-offset

under phase-shift of  $\pi/2$  and DC-offset of 20%. During the phase-shift condition, an overshoot of 7Hz has been seen in frequency estimation and undershoot of 50V has been seen in voltage magnitude estimation. The settling time is almost 50ms.

The SOGI-PLL has the limited DC-offset rejection capability, it shows oscillations of 1.8Hz in estimated frequency.

Table 4.3: Summary of simulation and experimental performance of SOGI-PLL

Cases	Parameters	Simulation performance	Experimental performance
<b>Voltage sag of 30%</b>	$\Delta f$	$t_s = 10.95$ , $\Delta f_{pp} = 0.06Hz$	$t_s = 10ms$ $\Delta f_{pp} = 0.3Hz$
	$A_v$	$t_s = 10.95ms$ $A_{vpp} = 2.58V$	$t_s = 10ms$
<b>Polluted grid</b>	$\Delta f$	$\Delta f_{pp} = 0.85Hz$	$\Delta f_{pp} = 0.8Hz$
	$A_v$	$A_{vpp} = 16.99V$	$A_{vpp} = 14.0V$
<b>Frequency change of +2Hz</b>	$\Delta f$	$t_s = 60.33ms$ $\Delta f_{pp} = 0.42Hz$	$t_s = 50ms$
	$A_v$	$t_s = 13.56ms$ $A_{vpp} = 13.85V$	$t_s =$ Very less time
<b>Noisy voltage</b>	$\Delta f$	$\Delta f_{pp} = 0.15Hz$	$\Delta f_{pp} = 0.6Hz$
	$A_v$	$A_{vpp} = 3.95V$	$A_{vpp} = 7V$
<b>Phase-shift of <math>\pi/2</math></b>	$\Delta f$	$t_s = 59.22ms$	$t_s = 80ms$
	$A_v$	$t_s = 20.79ms$	$t_s = 25ms$
<b>DC-offset of 20%</b>	$\Delta f$	$\Delta f_{pp} = 5.75Hz$	$\Delta f_{pp} = 1.5Hz$
	$A_v$	$A_{vpp} = 183.9V$	$A_{vpp} = 70.0V$

SOGI-PLL has the excellent filtering and dynamic performance capability. It shows good performance under polluted grid and the noisy grid voltage signal. Since the SOGI-PLL has been designed without frequency locked loop, it shows some oscillations during the frequency change condition. Simulation and experimental performance of single-phase SOGI-PLL has been summarized in Table 4.3. The design of SOGI-FLL is discussed in next section.

#### 4.1.4 Second-Order Generalized Integrator Frequency Locked Loop (SOGI-FLL)

Figure 4.24 shows the structure of SOGI-FLL and here it is used as single-phase grid synchronization technique. SOGI-FLL contains two parts, first part is SOGI which filters the grid voltage signal and the second part is FLL which estimates frequency. SOGI-FLL is designed for better frequency estimation under the frequency change. It doesn't require PI controller and Park transformation block to estimate phase and frequency. Hence, its structure is simple and shown in Fig. 4.24. The SOGI-FLL

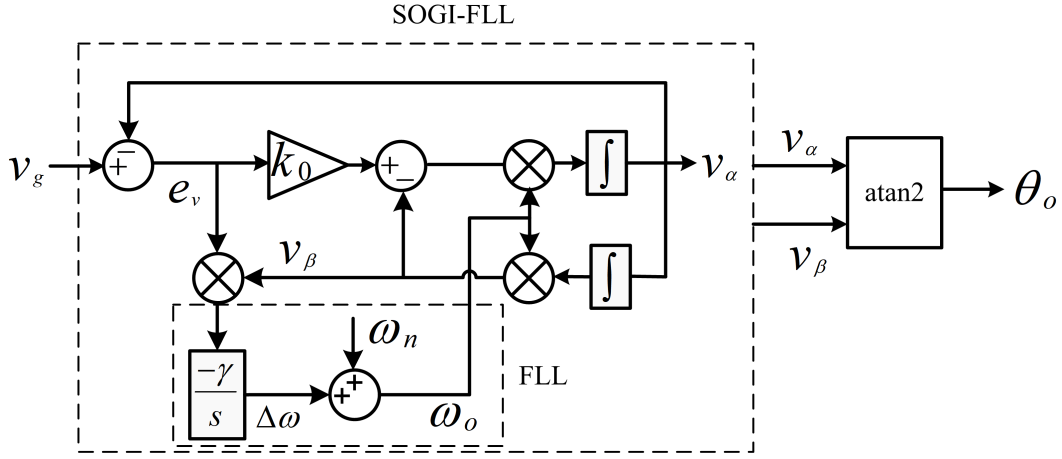


Figure 4.24: Structure of SOGI-FLL

is implemented to estimate filtered  $\alpha - \beta$  component of the grid voltage even under large variation in grid frequency. The resonating frequency changes according to the grid frequency. The  $\alpha$ -component ( $v_\alpha$ ) is the in-phase filtered component and  $\beta$ -component ( $v_\beta$ ) is the quadrature component of the grid voltage signal.

Error in the voltage signal is estimated by 4.25,

$$e_v(t) = v_g(t) - v_\alpha(t) \quad (4.25)$$

The quadrature component of the input grid voltage signal is given by 4.26,

$$v_\beta(t) = \omega_o \int v_\alpha(t) dt \quad (4.26)$$

Here,  $\omega_o$  is the estimated frequency or the resonating frequency of the SOGI-FLL. The closed-loop transfer function of in-phase signal and quadrature can be written as 4.27 and 4.28,

$$D(s) = \frac{v_\alpha(s)}{v_g(s)} = \frac{k_o \omega_o s}{s^2 + k_o \omega_o s + \omega_o^2} \quad (4.27)$$

$$Q(s) = \frac{v_\beta(s)}{v_g(s)} = \frac{k_o \omega_o^2}{s^2 + k_o \omega_o s + \omega_o^2} \quad (4.28)$$

Transfer function of the error signal ( $e_v$ ) is given as 4.29:

$$E(s) = \frac{e_v(s)}{v_g(s)} = \frac{s^2 + \omega_o^2}{s^2 + k_o \omega_o s + \omega_o^2} \quad (4.29)$$

Here,  $\omega_o = \omega_n + \Delta\omega$  and  $\Delta\omega$  is estimated by 4.30,

$$\Delta\omega = \int -\gamma e_v(t) v_\beta(t) dt \quad (4.30)$$

where,  $\gamma$  is FLL gain and its optimum selected value is 0.2.  $e_v$  is the error in voltage signal. The filtering level of SOGI greatly depends upon the gain  $k_o$ . Lower value of  $k_o$  results in heavy filtering action but at the same time dynamic response becomes slower and vice-versa. The value of  $k_o$  is taken as  $\sqrt{2}$  for the optimal response. SOGI-PLL estimates the phase and frequency of the grid voltage signal when the resonating frequency equals to the standard grid frequency ( $\omega_n$ ). But, when the frequency of the grid voltage differs from the standard frequency, then the frequency estimated by SOGI-PLL can not be tracked precisely. Hence, an additional circuit is required which automatically adjusts the resonating frequency of the SOGI. This second part is FLL, which is used to adjust the resonating frequency of SOGI to that of the grid voltage frequency. FLL estimates the frequency ( $\omega_o$ ) by computing the product of the quadrature grid voltage signal and the error signal, then it is passed through the gain ( $\gamma$ ) and the integrator function. The dynamic response for the frequency estimation depends on FLL gain  $\gamma$ . The magnitude of the grid voltage and the phase angle can be estimated with the help of in-phase and quadrature

phase signals as shown in 4.31 and 4.32 respectively .

$$A_v(t) = \sqrt{v_\alpha^2(t) + v_\beta^2(t)} \quad (4.31)$$

$$\angle v_g(t) = \theta_o = \arctan \frac{v_\beta(t)}{v_\alpha(t)} \quad (4.32)$$

#### 4.1.4.1 Simulation Results

Simulation performance of six different grid voltage cases has been shown in Fig. (4.25)-(4.27). SOGI-FLL is designed to perform better for phase angle, frequency and

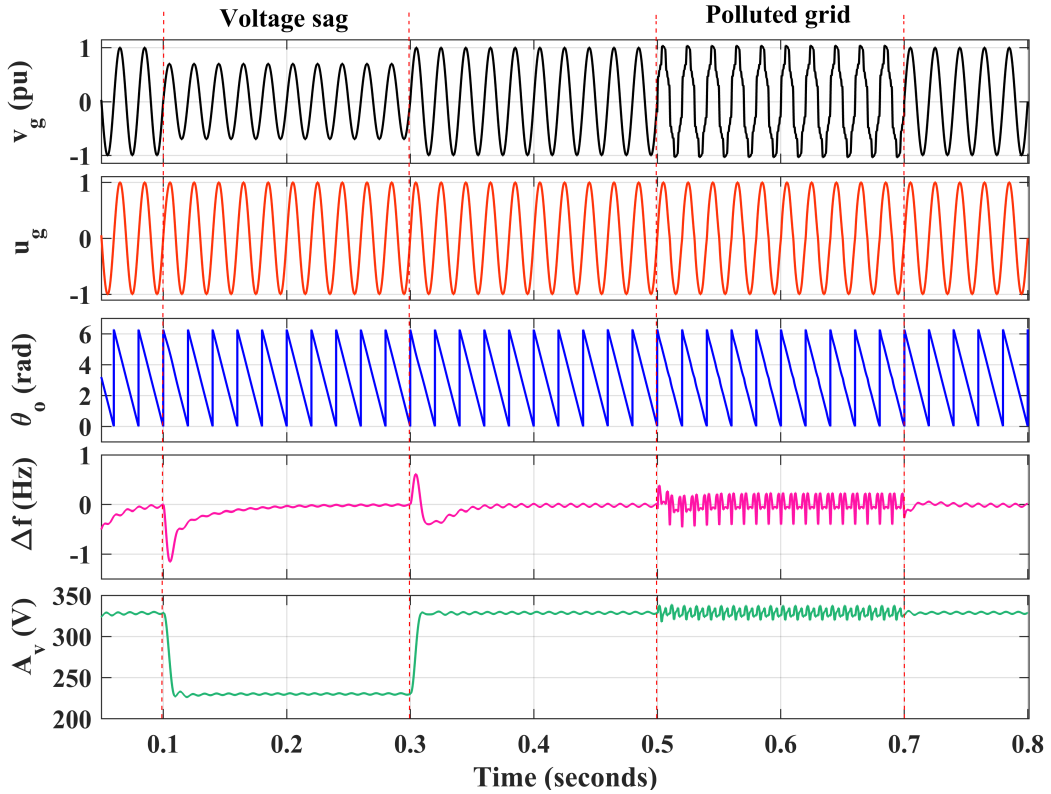


Figure 4.25: Simulation performance of SOGI-FLL under voltage sag of 0.3pu and polluted grid

amplitude estimation than SOGI-PLL during the frequency change condition. Figure 4.25 shows the simulation performance under voltage sag ( $t=0.1s$  to  $t=0.3s$ ) and polluted grid condition ( $t=0.5$  to  $t=0.7$ ). In steady state, oscillations in estimated frequency  $f_{pp}$  is almost negligible and it is 0.006Hz. The amplitude has been estimated within 0.5cycles and the steady-state oscillations is 2.5V. During the polluted

grid condition, ripples in output frequency is 0.65Hz and in estimated amplitude is 18.08V.

Simulation performance under frequency shift of +2Hz and noisy grid condition has been shown in Fig. 4.26. The frequency shift has been detected in 1.5 cycles and the

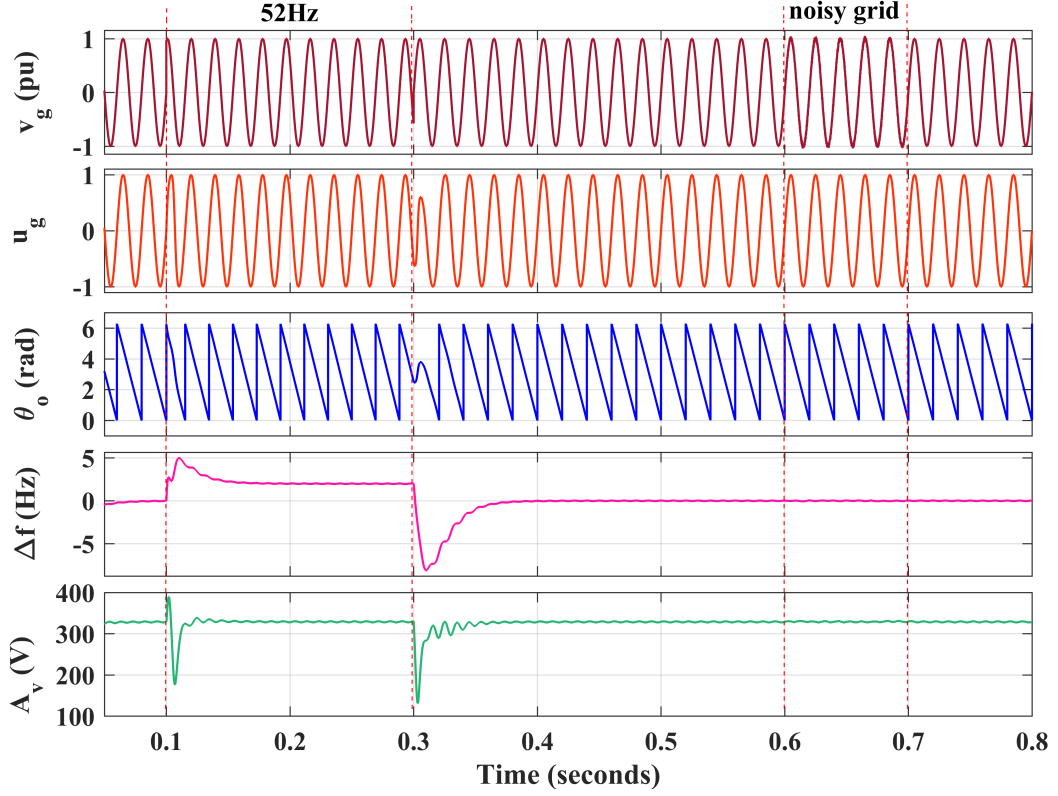


Figure 4.26: Simulation performance of SOGI-FLL under frequency shift of 2Hz and noisy grid

amplitude has been tracked within 1 cycle. The ripples in estimated frequency is very low and negligible and its peak to peak value is 0.06Hz. During the noisy grid condition, the peak to peak value of estimated frequency is 0.11Hz and in amplitude estimation it is only 4.07V. As expected, SOGI-FLL works better than SOGI-PLL, EPLL or SRF-PLL during the frequency deviation.

Response of the SOGI-FLL under phase shift of  $\pi/2$  and DC-offset of 20% has been displayed in Fig. 4.27. The phase-shift has been detected in 27.47ms, The peak to peak value of estimated grid frequency is 3.66Hz and the peak to peak value of estimated voltage amplitude is 185.5V during DC-offset case. It perform better than SOGI-PLL but still it has no DC-rejection capability.

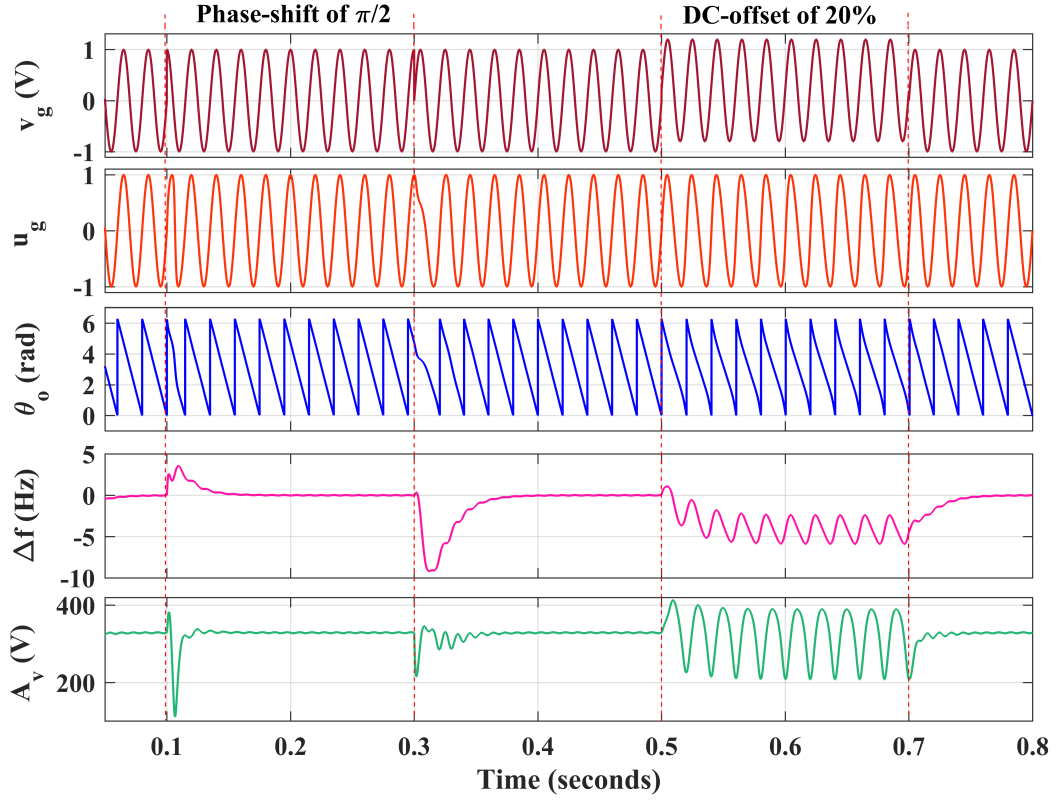


Figure 4.27: Simulation performance of SOGI-FLL under phase-shift of  $\pi/2$  and DC-offset of 20%

#### 4.1.4.2 Experimental results

Experimental performance of the SOGI-FLL has been shown in Fig. 4.28, 4.29 and 4.30 for the six different grid voltage conditions. The performance of SOGI-FLL

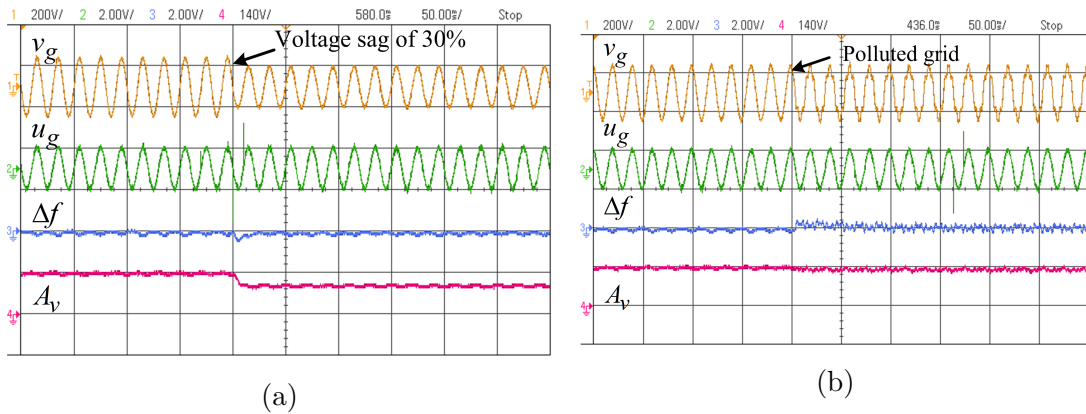


Figure 4.28: Experimental performance of single-phase SOGI-FLL under (a) voltage sag of 20% (b) polluted grid (THD 18.0%)

is almost similar to SOGI-PLL under different grid voltage cases except under frequency variation as it contains frequency-locked loop. In Fig. 4.29(a), the frequency

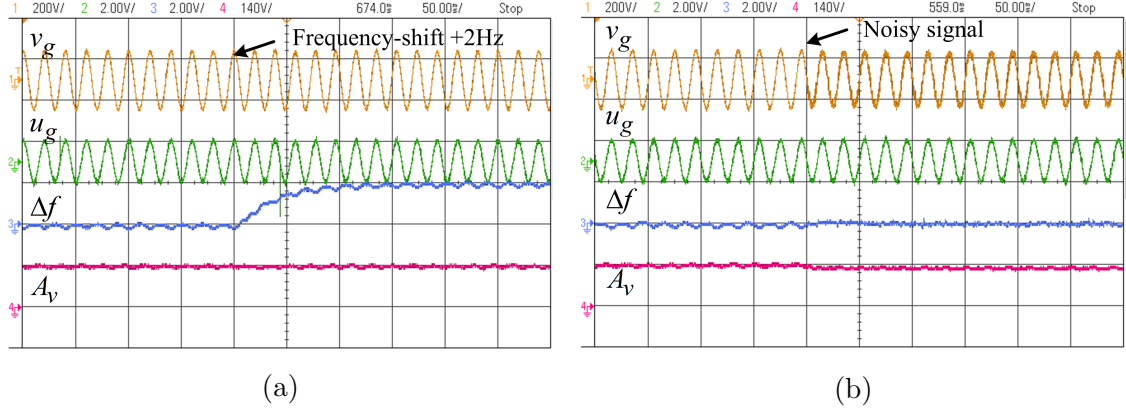


Figure 4.29: Experimental performance of single-phase SOGI-FLL under (a) frequency shift of +2Hz (b) noisy grid

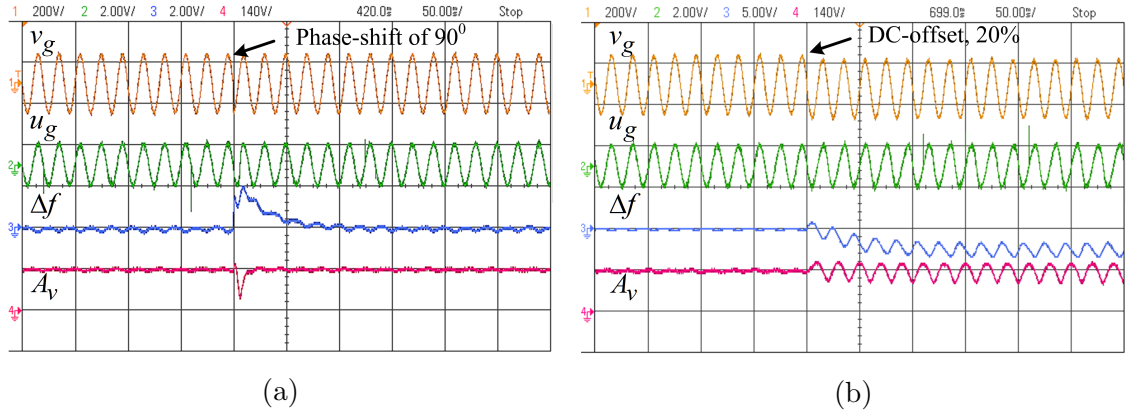


Figure 4.30: Experimental performance of single-phase SOGI-FLL under (a) phase-shift of  $\pi/2$  (b) 20% DC-offset

estimated by the SOGI-FLL shows less oscillations than frequency estimated by the SOGI-PLL during the variations in grid frequency from the standard grid frequency.

Summary of the simulation and experimental performance of SOGI-FLL has been summarized in Table 4.4.



Table 4.4: Summary of simulation and experimental performance of SOGI-FLL

Cases	Parameters	Simulation performance	Experimental performance
Voltage sag of 30%	$\Delta f$	$t_s = 8.5ms$	$t_s = 15ms$
	$A_v$	$\Delta f_{pp} = 0.06Hz$	
		$t_s = 8.5ms$ $A_{vpp} = 2.5V$	$t_s = 8ms$
Polluted grid	$\Delta f$	$\Delta f_{pp} = 0.65Hz$	$\Delta f_{pp} = 0.2Hz$
	$A_v$	$A_{vpp} = 18.08V$	$A_{vpp} = 10.0V$
Frequency change of +2Hz	$\Delta f$	$t_s = 29.65ms$	$t_s = 100ms$
		$\Delta f_{pp} = 0.06Hz$	
	$A_v$	$t_s = 13.56ms$ $A_{vpp} = 2.66V$	$t_s = \text{Very less time}$
Noisy voltage	$\Delta f$	$\Delta f_{pp} = 0.11Hz$	$\Delta f_{pp} = 0.1Hz$
	$A_v$	$A_{vpp} = 4.07V$	$A_{vpp} = 7V$
Phase-shift of $\pi/2$	$\Delta f$	$t_s = 27.47ms$	$t_s = 70ms$
	$A_v$	$t_s = 13.79ms$	$t_s = 20ms$
DC-offset of 20%	$\Delta f$	$\Delta f_{pp} = 3.66Hz$	$\Delta f_{pp} = 3.0Hz$
	$A_v$	$A_{vpp} = 185.5V$	$A_{vpp} = 70.0V$

#### 4.1.5 SOGI-FLL and Reduced Order Generalized Integrator (ROGI) based Synchronization Technique

The proposed synchronization technique consists of three parts viz. the SOGI block, FLL block and the ROGI block. The structure of SOGI-FLL-ROGI based synchronization technique is shown in Fig. 4.31. The SOGI block generates the in-phase

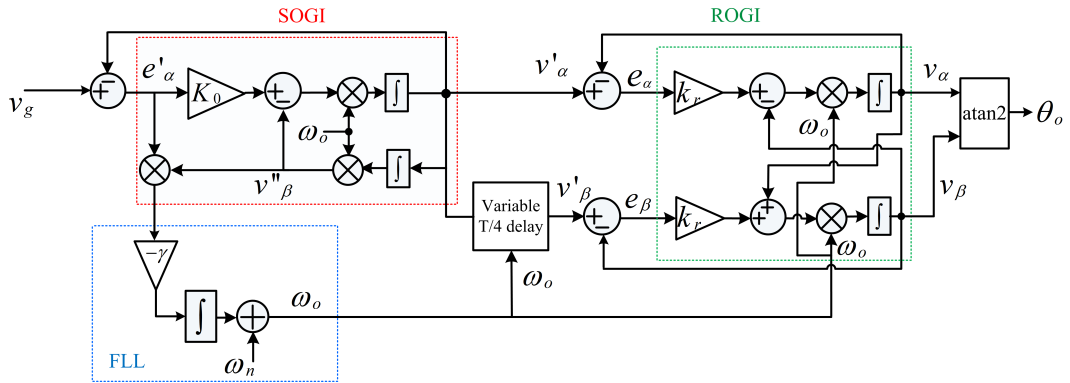


Figure 4.31: Structure of SOGI-FLL cascaded with ROGI

and the quadrature signals of the input signal. Here, the SOGI has been used as a pre-filtering stage of the grid voltage signal. The FLL block has been designed

for detecting the frequency deviations of the input signal. The ROGI block requires two input signals viz. the in-phase and quadrature signals, which are taken from the SOGI. Now, the SOGI-ROGI combination is designed to give perfect sinusoidal in-phase and quadrature phase signals. Individual SOGI/ROGI blocks do provide filtering but are not as effective as the combination. If the ROGI block alone has been used without pre-filtering, the quadrature-phase input for the ROGI blocks needs to be generated using a quadrature signal generator, say a T/4-delay. T/4-delay gives satisfactory quadrature signal only when the frequency of the signal is 50Hz without any frequency deviation. Here, the variable transport delay has been used to generate quadrature signal even under frequency shifts from standard grid frequency. The frequency for the ROGI and variable transport delay has been taken from the FLL block. The in-phase output of the SOGI is immune to DC-offset. Hence, the output of the proposed SOGI-FLL-ROGI is free from DC-offset.

In Fig. 4.31,  $v_g$  is the input signal and  $(v'_\alpha, v''_\beta)$  are the outputs of the SOG-FLL and represent the in-phase and quadrature signals of the input.  $v_\alpha$  and  $v_\beta$  are the final outputs obtained from the cascaded operation of the SOGI-FLL and ROGI technique. The open-loop transfer function of SOGI is given as in 4.33.

$$SOGI(s) = \frac{k_o \omega_o s}{s^2 + \omega_o^2} \quad (4.33)$$

The closed-loop transfer functions of  $(v'_\alpha, v''_\beta)$  of the SOGI block considering error signal  $(e'_\alpha)$  are given as in 4.34 and 4.35.

$$\frac{v'_\alpha(s)}{v_g(s)} = \frac{k_o \omega_o s}{s^2 + k_o \omega_o s + \omega_o^2} \quad (4.34)$$

$$\frac{v''_\beta(s)}{v_g(s)} = \frac{k_o \omega_o^2}{s^2 + k_o \omega_o s + \omega_o^2} \quad (4.35)$$

From the FLL, the estimated frequency  $\omega_o$  is given as 4.36,

$$\omega_o = \omega_n + \int (v_g - v'_\alpha) v'_\beta \gamma dt \quad (4.36)$$

As discussed in [95], ROGI is an algorithm with a single complex pole. The transfer function of the ROGI is represented as

$$\frac{v_{\alpha\beta}(s)}{e_{\alpha\beta}(s)} = \frac{k_r}{s - j\omega_o} \quad (4.37)$$

where,  $e_{\alpha\beta} = v'_{\alpha\beta} - v_{\alpha\beta}$  is the error signal for the ROGI. Now, the closed-loop transfer function with the ROGI for in-phase and quadrature signal are given as in 4.38-4.40.

$$\frac{v_{\alpha}(s)}{v'_{\alpha}(s)} = \frac{v_{\beta}(s)}{v'_{\beta}(s)} = \frac{k_r\omega_o s}{s^2 + 2k_r\omega_o s + (1 + k_r^2)\omega_o^2} \quad (4.38)$$

$$Q(s) = \frac{v_{\beta}(s)}{v_g(s)} = \frac{k_0 k_r \omega_o^2 (2\omega_o s + k_0 \omega_o^2)}{s^4 + (k_o + 2k_r)\omega_o s^3 + (2 + 2k_o k_r + k_r^2)\omega_o^3 s^2 + (1 + k_r^2)\omega_o^4} \quad (4.39)$$

$$D(s) = \frac{v_{\alpha}(s)}{v_g(s)} = \frac{k_0 k_r \omega_o^2 (s^2 + k_r \omega_o s - \omega_o^2)}{s^4 + (k_o + 2k_r)\omega_o s^3 + (2 + 2k_o k_r + k_r^2)\omega_o^3 s^2 + (1 + k_r^2)\omega_o^4} \quad (4.40)$$

The response of proposed technique depends on selection of three gains viz  $k_0$ ,  $k_r$  and  $\gamma$ . These gains significantly affect the individual performance of SOGI, ROGI and FLL and hence the combined response. Here,  $k_o = k_r = 1.414$  has been taken as optimal response of the algorithm and for  $\gamma$  its value is 0.2.

The bode plot for the  $D(s)$  and  $Q(s)$  has been shown in Fig. 4.32(a). The magnitude

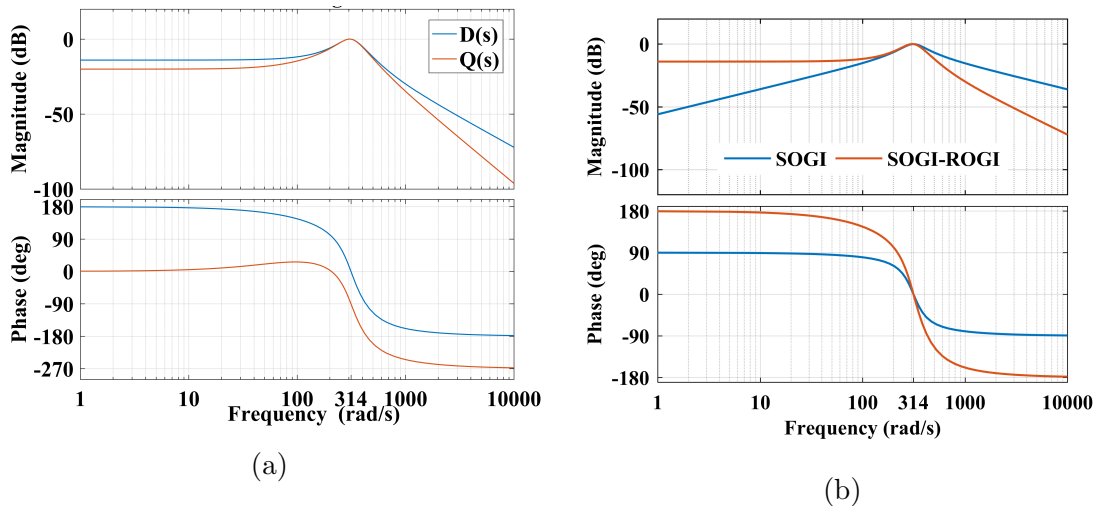


Figure 4.32: Bode plot of (a) SOGI-ROGI for  $D(s)$  and  $Q(s)$  (b) SOGI and SOGI-ROGI for in-phase component

response of the bode plot shows that the it works as a low pass filter and rejects

higher order harmonics effectively. The phase plot of both the transfer functions clearly shows a phase-shift of  $90^\circ$  at  $\omega_n = 314 \text{ rad/s}$ . The bode response of the SOGI and SOGI-ROGI has been compared in Fig. 4.32(b). The response shows magnitude plot slope reduces by a factor of 40dB/decade for cascade SOGI-ROGI combination, where as 20dB/decade slope observed with the SOGI algorithm. Hence, better and more effective filtering for higher-harmonics is observed with the SOGI-FLL-ROGI algorithm. Using tan-inverse function on output of the ROGI provides the phase angle information and further applying the sine function gives the synchronizing signal.

#### 4.1.5.1 Simulation Results

Simulation results of the SOGI-FLL-ROGI have been shown in Fig. (4.33)- (4.35). Figure 4.33 shows the performance analysis of SOGI-FLL-ROGI as compared to SOGI-FLL under voltage sag and polluted grid condition. Frequency has not been

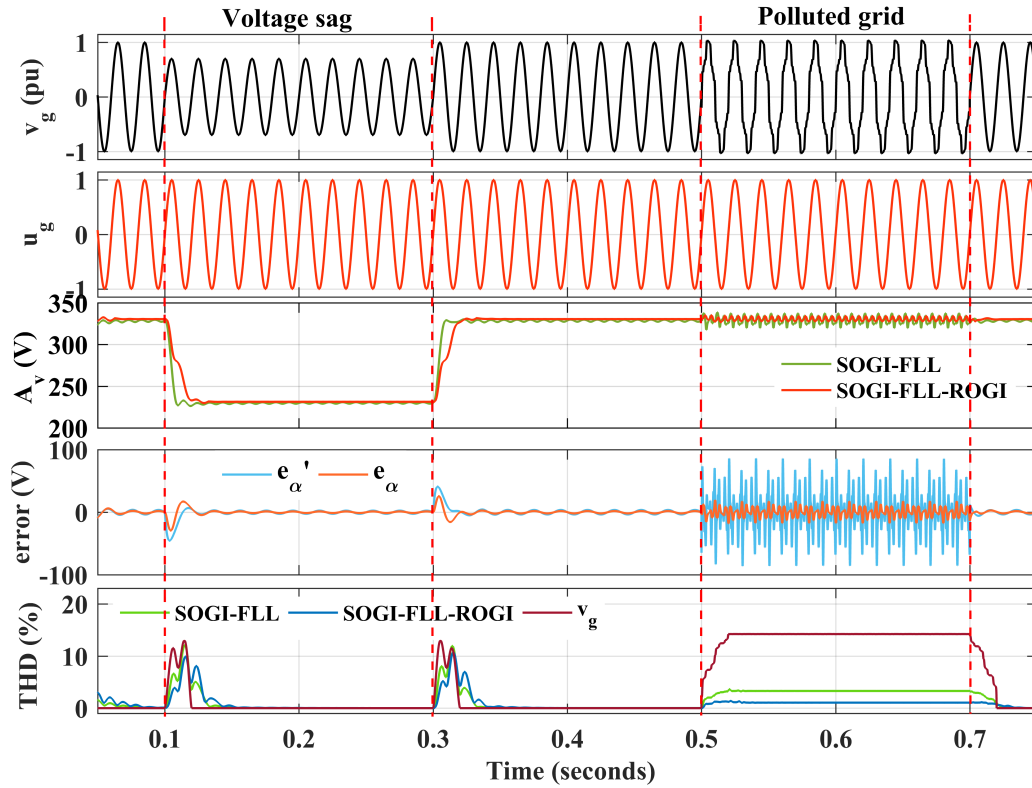


Figure 4.33: Simulation performance of SOGI-FLL-ROGI under voltage sag of 0.3pu and polluted grid

shown as the FLL estimates the frequency and is already shown in previous section. Voltage sag has been introduced from  $t=0.1\text{s}$  to  $t=0.3\text{s}$  and harmonic has been introduced from  $t=0.5\text{s}$  to  $t=0.7\text{s}$ . In case of voltage sag of  $0.3\text{pu}$ , the amplitude estimated by SOGI-FLL within 0.5 cycles. While, it is estimated by SOGI-FLL-ROGI is in 1 cycle. But the ripples in amplitude by SOGI-FLL and SOGI-FLL-ROGI is  $1.97\text{V}$  and  $0.05\text{V}$  respectively in steady state. Also error (peak to peak) in voltage signal is  $5.18\text{V}$  in SOGI-FLL and  $2.70\text{V}$  in SOGI-FLL-ROGI. Hence the proposed algorithm is little slower but the steady-state response is better than SOGI-FLL. During the polluted grid condition, it easily observed that the SOGI-FLL-ROGI shows better filtering capability than SOGI-FLL. The FFT analysis also shows the better filtering capability of proposed algorithm. Grid voltage THD of  $14.22\%$  is filtered the synchronizing signal obtained by SOGI-FLL THD is  $3.31\%$ , while THD of the synchronizing signal obtained by SOGI-FLL-ROGI is only  $1.06\%$ .

Simulation performance of SOGI-FLL-ROGI has been shown in Fig. 4.34 under frequency shift and noisy grid voltage condition. Synchronizing signal, voltage am-

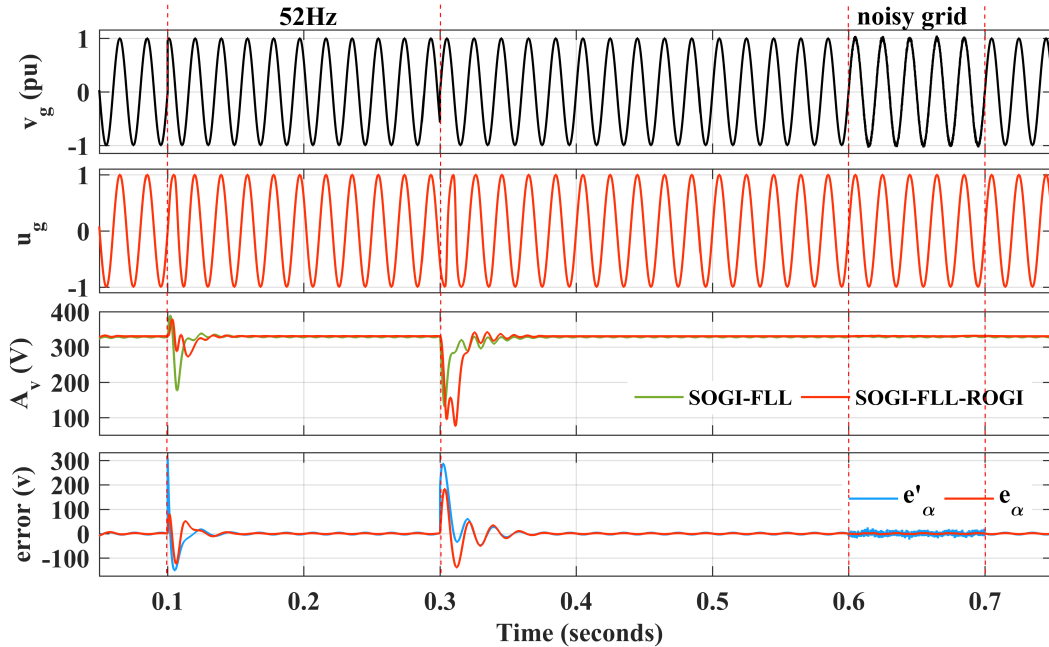


Figure 4.34: Simulation performance of SOGI-FLL-ROGI under frequency shift of  $+2\text{Hz}$  and noisy grid

plitude and estimated error has been shown. The voltage amplitude estimated by

SOGI-FLL-ROGI shows less ripples ( $A_{vpp} = 0.51V$ ) than amplitude estimated by SOGI-FLL ( $A_{vpp} = 2.71V$ ) during grid voltage of 52Hz. During the noisy grid condition, ripples in voltage error is 43.06V and 5.83V estimated by SOGI-FLL and SOGI-FLL-ROGI respectively.

Simulation performance of SOGI-FLL-ROGI under phase shift of  $\pi/2$  and DC-offset condition has been shown in Fig. 4.35. The performance of SOGI-FLL-ROGI has

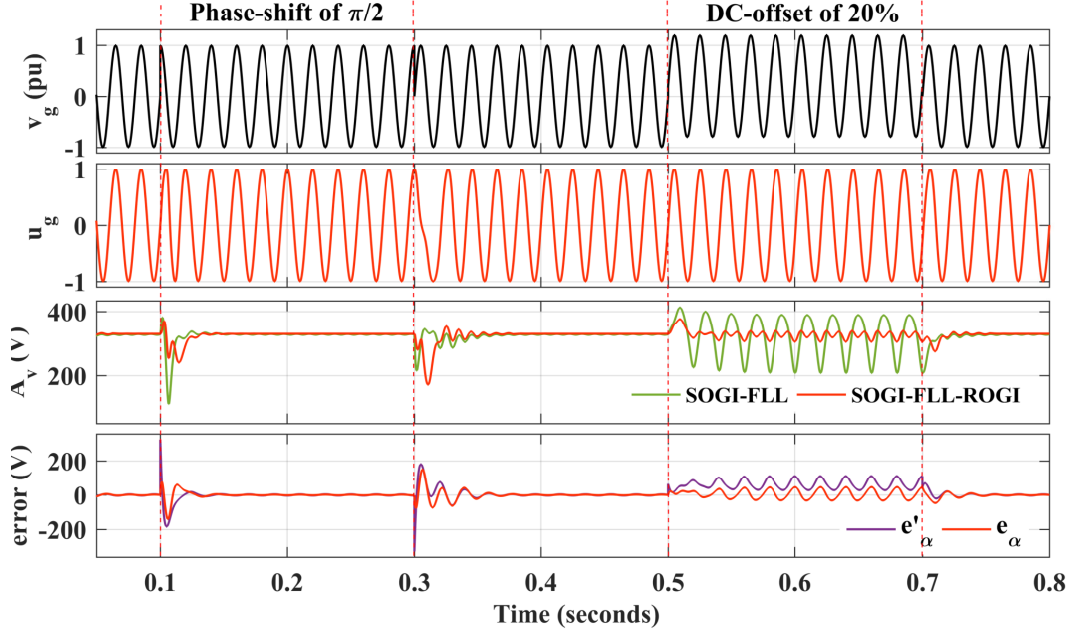


Figure 4.35: Simulation performance of SOGI-FLL-ROGI under phase-shift of  $\pi/2$  and DC-offset of 20%

also been compared with SOGI-FLL. The amplitude estimation shows high overshoot by SOGI-FLL than SOGI-FLL-ROGI during dynamic condition. During the DC-offset in grid voltage, the amplitude estimated by SOGI-FLL shows high oscillations while SOGI-FLL-ROGI shows less oscillations. The voltage error signal has also lower oscillation obtained by SOGI-FLL-ROGI than voltage error obtained by SOGI-FLL.

#### 4.1.5.2 Experimental Results

Experimental performance of the SOGI-FLL has been shown in Fig. 4.36, 4.37 and 4.38 for the six different grid voltage conditions. Here, the SOGI-FLL is used as pre-

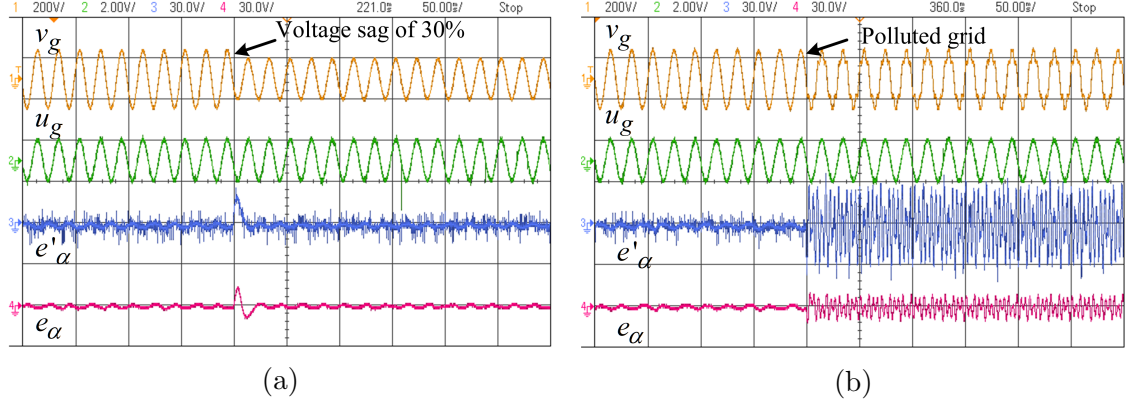


Figure 4.36: Experimental performance of single-phase SOGI-FLL-ROGI under (a) voltage sag of 20% (b) polluted grid (THD 18.0%)

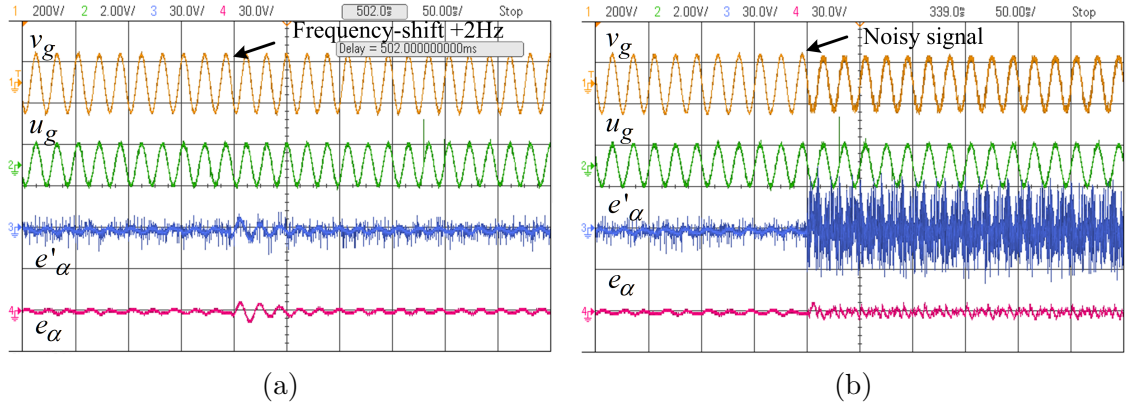


Figure 4.37: Experimental performance of single-phase SOGI-FLL-ROGI under (a) frequency shift of +2Hz (b) noisy grid

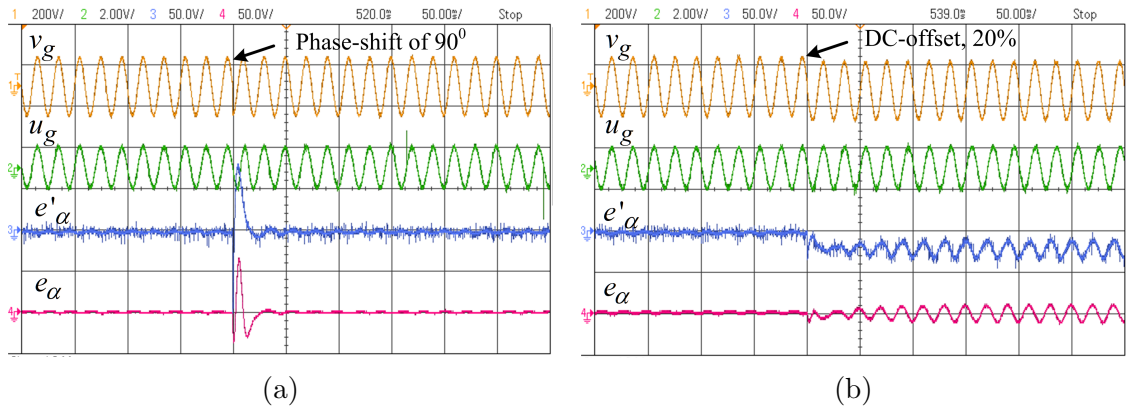


Figure 4.38: Experimental performance of single-phase SOGI-FLL-ROGI under (a) phase-shift of  $\pi/2$  (b) 20% DC-offset

filter of the ROGI and hence the frequency estimated is similar to SOGI-FLL. Here, we require the distortion free synchronizing signal for the power quality improvement applications. Here, the error in grid voltage has been measured at pre-filter stage and the second stage. Lesser the error leads to the better synchronizing signal. In

all the six different grid voltage cases, the error ( $e_\alpha$ ) at first stage is lesser than error ( $e'_\alpha$ ) at second stage. The experimental performance of the SOGI-FLL-ROGI shows better performance than the SOGI-FLL. It also shows better performance under DC-offset in grid-voltage condition.

#### 4.1.5.3 Performance Comparison of SOGI-FLL, ROGI and SOGI-FLL-ROGI

As the main aim of these algorithms is to generate a perfect synchronization signal replicated from input grid voltage signal. Hence, the THD of the unit synchronizing signal obtained from the SOGI-FLL, ROGI and SOGI-FLL-ROGI are shown in Fig. 4.39 and compared. The result obtained using the proposed SOGI-FLL-ROGI

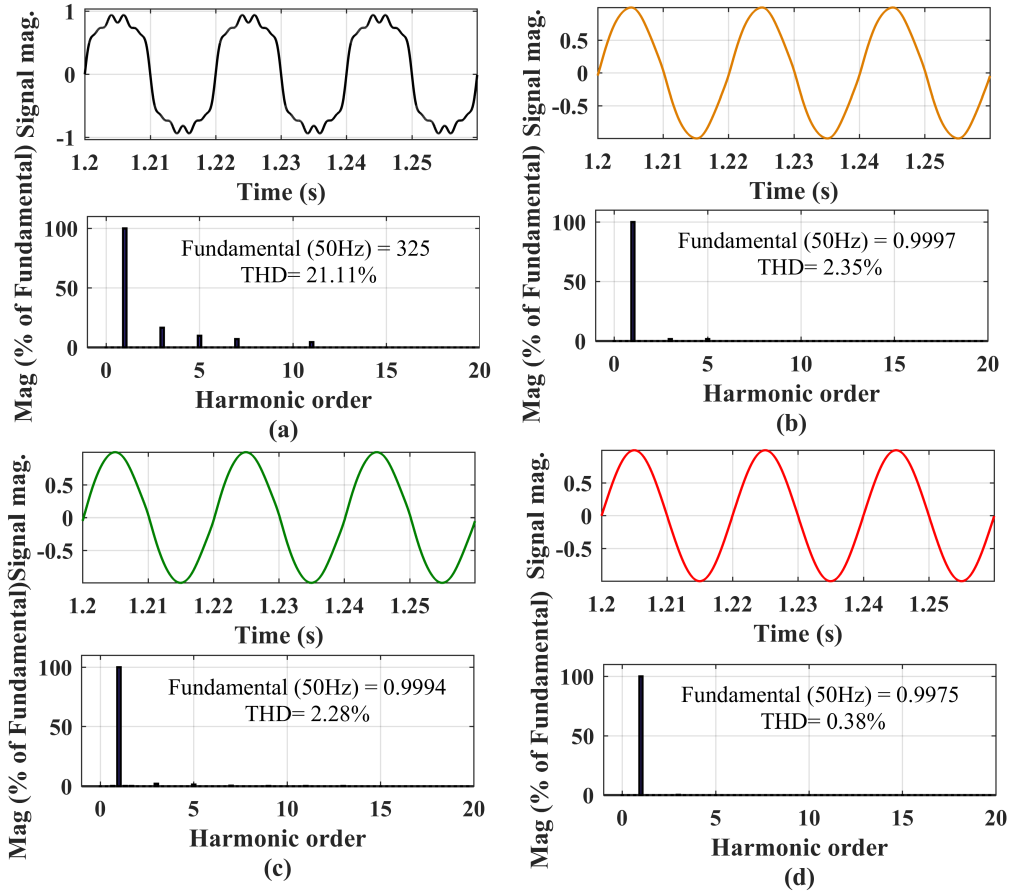


Figure 4.39: FFT analysis of (a) grid voltage signal (b)  $u_g$  obtained from ROGI (c)  $u_g$  obtained from SOGI-FLL (d)  $u_g$  obtained from SOGI-FLL and ROGI

algorithm is more accurate than the individual algorithms. The FFT analysis of



the grid voltage and the synchronizing signals obtained are depicted in Fig. 4.39. Figure 4.39(a) shows the FFT analysis of the grid voltage, which shows the THD of 21.11% and contains 3rd, 5th, 7th and 11th harmonic as dominant terms. The THD of the synchronizing signal obtained by ROGI, SOGI-FLL and SOGI-FLL-ROGI is 2.35%, 2.28% and 0.38% respectively. THD comparison of obtained synchronizing signal ( $u_g$ ) by ROGI, SOGI-FLL and SOGI-FLL-ROGI has been summarized in Table 4.5.

Table 4.5: THD of the synchronizing signal ( $u_g$ ) obtained by ROGI, SOGI-FLL and SOGI-FLL-ROGI

<b>Parameters</b>	<b>ROGI</b>	<b>SOGI-FLL</b>	<b>SOGI-FLL-ROGI</b>
<b>THD of grid voltage</b>	21.11%	21.11%	21.11%
<b>THD of output signal (<math>u_g</math>)</b>	2.35%	2.28%	0.38%

The result in Table 4.5 shows that out of ROGI, SOGI-FLL and SOGI-FLL-ROGI, almost perfect unit template have been generated by SOGI-FLL-ROGI based technique from the same distorted grid voltage signal.

### 4.1.6 Adaptive Zero-Crossing Detection (AZCD) based Synchronization

A zero-crossing detection technique can also be used to generate synchronizing signals. The conventional ZCD generates perfect synchronizing signals with a simple algorithm. However, the conventional ZCD has the disadvantage that it can generate synchronizing signals of only fixed frequency. When the grid frequency varies, perfect synchronizing can not be obtained by ZCD. Hence, the ZCD requires a robust grid frequency estimator to estimate the precise frequency of the grid voltage. the block diagram and working principle of ZCD technique is discussed.

#### 4.1.6.1 Zero-Crossing Detector

The ZCD is based on the detection of zero crossings of the input signal. It is based on the simple “if” and “then” logic. If the sinusoidal voltage signal crosses the zero value and is moving towards positive -half cycle then the ZCD generates the unit sine wave of positive-cycle. If the voltage signal crosses the zero value and moving towards negative-half cycle then the ZCD generates the unit sine wave of negative-half cycle. After combining both the positive-half cycle and negative-half cycle, the generation of the complete unit sinusoidal wave of 50Hz frequency takes place. The generated wave has frequency of 50Hz and is in-phase with the input grid voltage and free from distortion. Structure of the ZCD has been shown in Fig. 4.40.

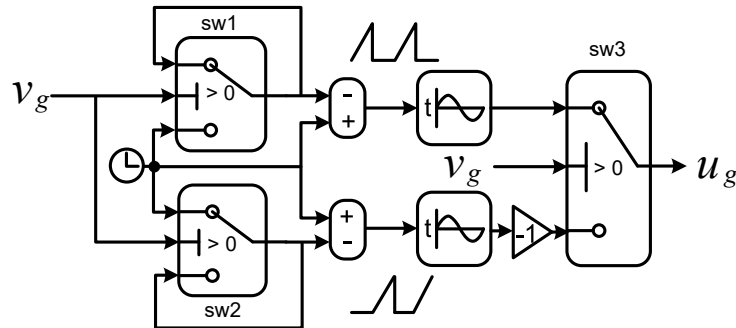


Figure 4.40: Structure of conventional ZCD

The output of ZCD doesn't depend on the magnitude of the input waveform. Its

drawback is that the conventional ZCD generates the sinusoidal waveform of the frequency of 50Hz even when the frequency of the grid voltage deviates from the standard frequency. In this case, there will be some error at zero crossings. Hence, the conventional ZCD requires a frequency estimator, which can detect the frequency of the input grid voltage signal and correspondingly generate the pure sine wave in-phase with the input signal. This is the basis of design of frequency adaptive ZCD technique.

#### 4.1.6.2 Frequency Adaptive ZCD

Under practical conditions, the grid voltage in the distribution grid contains harmonics. The grid voltage in single-phase distribution grid can be expressed as

$$v_g(t) = A_v \sin(\omega_i t + \phi_1) + h_n(t) \quad (4.41)$$

In 4.41,  $A_v, \omega_i$  and  $\phi_1$  are the magnitudes of the fundamental load component, grid frequency and phase angle of the fundamental component of the grid voltage respectively.  $h_n(t)$  denotes the harmonic content in the grid voltage. Equation 4.41 is discretized and written as 4.42.

$$v_g(k) = A_v \sin(\omega_i k T_s + \phi_1) + h_n(k T_s) \quad (4.42)$$

In 4.42,  $k=1, 2, 3 \dots$  and  $T_s$  denotes the sampling time. The estimation of frequency is based on three-consecutive sampling (3CS) method discussed in literature. Three consecutive samples can be obtained by applying the transfer delay of  $\tau$  and  $2\tau$  and can be written as 4.43 and 4.44.

$$v_1(k) = v_g(k - \tau) = A_v \sin(\omega_i k T_s - \omega_i \tau + \phi_1) + h_n(k T_s - \tau) \quad (4.43)$$

$$v_2(k) = v_g(k - 2\tau) = A_v \sin(\omega_i k T_s - 2\omega_i \tau + \phi_1) + h_n(k T_s - 2\tau) \quad (4.44)$$

Expanding 4.43 and 4.44, we get the following equations,

$$v_1(k) = \gamma_1 A_v \sin(\omega_i k T_s + \phi_1) - \gamma_2 A_v \cos(\omega_i k T_s + \phi_1) + h_n(k T_s - \tau) \quad (4.45)$$

$$v_2(k) = \gamma_3 A_v \sin(\omega_i k T_s + \phi_1) - \gamma_4 A_v \cos(\omega_i k T_s + \phi_1) + h_n(k T_s - 2\tau) \quad (4.46)$$

where,

$$\gamma_1 = \cos \omega_i \tau, \quad \gamma_2 = \sin \omega_i \tau, \quad \gamma_3 = \cos 2\omega_i \tau \text{ and } \gamma_4 = \sin 2\omega_i \tau \quad (4.47)$$

Applying the algebraic operations of trigonometric functions on 4.48 and after simplifying, the relationship obtained as

$$\gamma_3 = 2\gamma_1^2 - 1 \quad (4.48)$$

$$\gamma_4 = 2\gamma_1 \gamma_2 \quad (4.49)$$

Also, the value of  $\omega_i \tau$  is specified as  $0 < \omega_i \tau < \pi$  for  $\gamma_2 \neq 0$ . Equation 4.45 and 4.46 can also be written as:

$$\gamma_2 A_v \cos(\omega_i k T_s + \phi_1) = \gamma_1 A_v \sin(\omega_i k T_s + \phi_1) + h_n(k T_s - \tau) - v_1(k) \quad (4.50)$$

$$\gamma_4 A_v \cos(\omega_i k T_s + \phi_1) = \gamma_3 A_v \sin(\omega_i k T_s + \phi_1) + h_n(k T_s - 2\tau) - v_2(k) \quad (4.51)$$

Multiplying  $2\gamma_1$  on both sides of 4.50 and substituting the values from 4.48, 4.49 and 4.51 into it, it gives

$$v_g(k) + v_2(k) = 2\gamma_1 v_1(k) + h_n(k T_s) - 2\gamma_1 h_n(k T_s - \tau) + h_n(k T_s - \tau) \quad (4.52)$$

$$v_g(k) + v_2(k) = 2\gamma_1 v_1(k) - \Delta k \quad (4.53)$$

In 4.54,  $\Delta k$  denotes the sum of time-delayed harmonic components of the grid voltage. In 4.54,  $\gamma_1$  is the only parameter which is unknown and other parameters are either known or can be obtained easily. Under ideal grid voltage condition, the har-

monic component in grid voltage is zero, hence  $\Delta k = 0$ . Under this condition, 4.54 can be written as

$$v_g(k) + v_2(k) = 2\gamma_1 v_1(k) \quad (4.54)$$

Here, the frequency ( $\omega$ ) can be estimated by 4.55,

$$\omega = \frac{\arccos[(v_g(k) + v_2(k))/2v_1(k)]}{\tau} \quad (4.55)$$

Equation 4.55 estimates the frequency under standard test conditions and is valid for the ideal case when the voltage signal is not polluted. The effect of the harmonics is eliminated using a robust technique which estimates the fundamental frequency with zero-steady error. The error is defined as

$$e(k) = 2\hat{\gamma}_1(k)v_1(k) - v_g(k) - v_2(k) \quad (4.56)$$

In 4.56,  $\hat{\gamma}_1$  is the new estimated value of  $\gamma_1$ . Once the value of  $\gamma_1$  is estimated, the precise frequency of the fundamental component of the voltage signal can be estimated. A robust update law is developed for the estimation of  $\gamma_1$  and is expressed as in 4.57.

$$\hat{\gamma}_1(k+1) = \hat{\gamma}_1(k) - \frac{2\alpha e(k)v_1(k)}{1 + 4\alpha v_1^2(k)} \quad (4.57)$$

$$\hat{\gamma}_1(k+1) = \hat{\gamma}_1(k) - \frac{2\alpha v_1(k)}{1 + 4\alpha v_1^2(k)}(2\hat{\gamma}_1(k)v_1(k) - v_g(k) - v_2(k)) \quad (4.58)$$

In 4.58,  $\alpha$  denotes the convergence factor. Once  $\hat{\gamma}_1(k)$  is estimated, the estimated frequency of the grid voltage is expressed as

$$\omega_o(k) = \frac{\arccos[\hat{\gamma}_1(k)]}{\tau} \quad (4.59)$$

The estimation error is expressed as

$$\tilde{\gamma}_1(k) = \hat{\gamma}_1(k) - \gamma_1 \quad (4.60)$$

Also, this expression can be written as

$$\begin{aligned}
\tilde{\gamma}_1(k+1) &= \hat{\gamma}_1(k+1) - \gamma_1 \\
&= \hat{\gamma}_1(k) - \frac{2\alpha v_1(k)}{1+4\alpha v_1^2(k)}(2\hat{\gamma}_1(k)v_1(k) - v_g(k) - v_2(k)) - \gamma_1 \\
&= \hat{\gamma}_1(k) - \frac{2\alpha v_1(k)}{1+4\alpha v_1^2(k)}(2\hat{\gamma}_1(k)v_1(k) - 2\gamma_1(k)v_1(k)) \\
&= \hat{\gamma}_1(k) - \frac{4\alpha v_1^2(k)}{1+4\alpha v_1^2(k)}\tilde{\gamma}_1(k) \\
&= \frac{1}{1+4\alpha v_1^2(k)}\tilde{\gamma}_1(k)
\end{aligned} \tag{4.61}$$

Iterating 4.61, it yields

$$\begin{aligned}
\tilde{\gamma}_1(k) &= \frac{1}{1+4\alpha v_1^2(k-1)}\tilde{\gamma}_1(k-1) \\
&= \frac{1}{1+4\alpha v_1^2(k-1)} \frac{1}{1+4\alpha v_1^2(k-2)}\tilde{\gamma}_1(k-2) \\
&= \frac{1}{1+4\alpha v_1^2(k-1)} \frac{1}{1+4\alpha v_1^2(k-2)} \cdots \frac{1}{1+4\alpha v_1^2(0)}\tilde{\gamma}_1(0)
\end{aligned} \tag{4.62}$$

In 4.62,  $v_1(0)$  is the initial grid voltage with  $\tau$  delay and  $\tilde{\gamma}_1(0)$  is the initial estimation error. In 4.62, there are  $m$  non-zero values of  $\{v_1(0), v_1(1), v_2(2), \dots, v_1(k-1)\}$  and these are assumed as  $\{v_1(p_1), v_1(p_2), v_2(p_3), \dots, v_1(p_m)\}$ . Among all the non-zero values the minimum is considered as  $v_{1min}(p_m)$ .

Now, 4.62 can be re-written with the above assumption is:

$$\tilde{\gamma}_1(k) = \frac{1}{1+4\alpha v_1^2(p_1)} \frac{1}{1+4\alpha v_1^2(p_2)} \cdots \frac{1}{1+4\alpha v_1^2(p_m)}\tilde{\gamma}_1(0) \tag{4.63}$$

Applying the absolute value operation on 4.63, it gives

$$\begin{aligned}
|\tilde{\gamma}_1(k)| &= \left| \frac{1}{1+4\alpha v_1^2(p_1)} \frac{1}{1+4\alpha v_1^2(p_2)} \cdots \frac{1}{1+4\alpha v_1^2(p_m)}\tilde{\gamma}_1(0) \right| \\
&\leq \left| \left\{ \frac{1}{1+4\alpha v_{1min}^2(p)} \right\}^m \tilde{\gamma}_1(0) \right|
\end{aligned} \tag{4.64}$$

The number of terms expressing  $v_1(k)$  is infinite; hence the number of m non-zero value is also infinite. Applying the limit function on 4.64, it gives

$$\begin{aligned} \lim_{k \rightarrow \infty} |\tilde{\gamma}_1(k)| &= \lim_{k \rightarrow \infty} \left| \frac{1}{1 + 4\alpha v_1^2(p_1)} \frac{1}{1 + 4\alpha v_1^2(p_2)} \cdots \frac{1}{1 + 4\alpha v_1^2(p_m)} \tilde{\gamma}_1(0) \right| \\ &\leq \lim_{k \rightarrow \infty} \left\{ \frac{1}{1 + 4\alpha v_{1min}^2(p)} \right\}^m |\tilde{\gamma}_1(0)| \end{aligned} \quad (4.65)$$

Here,  $0 < \frac{1}{1 + 4\alpha v_{1min}^2(p)} < 1$ , 4.66 gives

$$\lim_{k \rightarrow \infty} |\tilde{\gamma}_1(k)| \leq \lim_{k \rightarrow \infty} \left\{ \frac{1}{1 + 4\alpha v_{1min}^2(p)} \right\}^m |\tilde{\gamma}_1(k)| = 0 \quad (4.66)$$

Hence, it can be observed that the estimation of frequency by this technique gives zero-steady state error. Once, the frequency is estimated it is given to the sine wave generator. The sine wave generator now generates pure synchronizing signal of the same frequency of the input grid voltage. The proposed Adaptive-ZCD (AZCD) based synchronizing signal generator is shown in Fig. 4.41

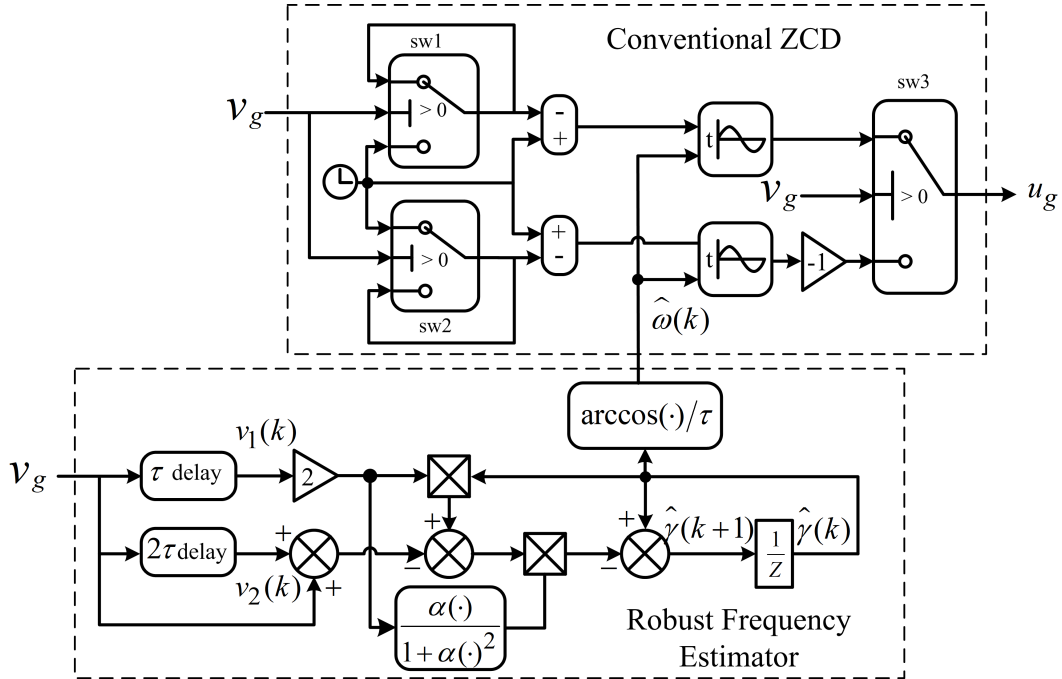


Figure 4.41: Structure of adaptive ZCD synchronization algorithm

#### 4.1.6.3 Simulation Results

Simulation results of proposed AZCD has been shown in Fig. (4.42)-(4.44) for different grid voltage cases. The proposed algorithm is expected to estimates frequency with minimum error and pure grid synchronizing signal. The AZCD algorithm is first tested under voltage sag and under harmonic grid condition and it is shown in Fig. 4.42. The proposed algorithm can not estimate magnitude of the grid voltage signal. The voltage sag of 30% has been occurred during  $t=0.1s$  to  $t=0.3s$  and harmonic is introduced during  $t=0.5s$  to  $t=0.7s$ . Deviation in in frequency during standard grid frequency is zero in both the situation. Hence, it gives pure synchronizing signal and the frequency is estimated within 1 cycle during dynamics of voltage sag.

Simulation performance of AZCD during the frequency shift of +2Hz and the noisy

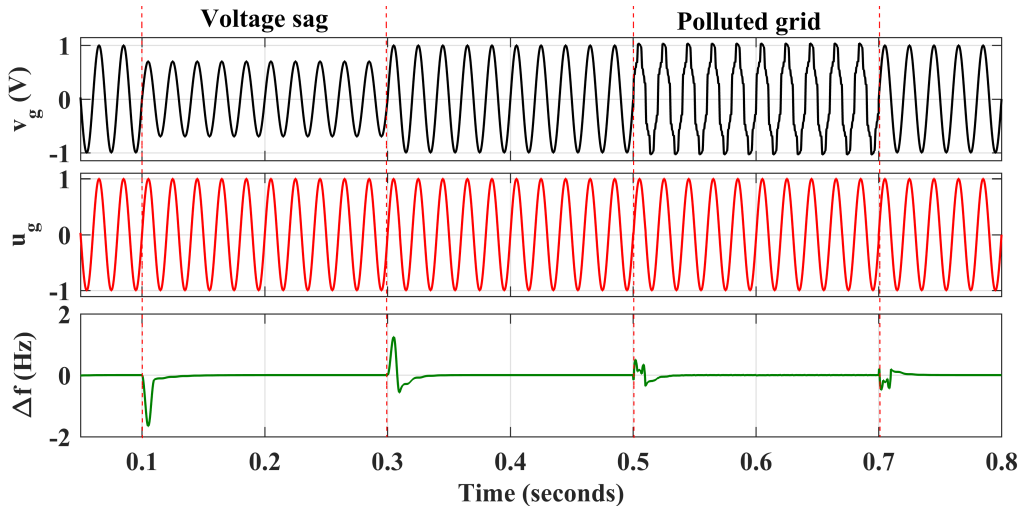


Figure 4.42: Simulation Performance of AZCD under voltage sag of 0.3pu and polluted grid

grid signal is shown in Fig. 4.43. The frequency change of +2Hz has been occurred at  $t=0.1s$  and it is estimated within 10.19ms. During the frequency variation from standard frequency there is no oscillations in estimated frequency. During the noisy grid voltage condition ripple in estimated grid frequency is only of 0.01Hz. Hence the grid synchronizing signal is tracked within half cycle.

Phase-shift of  $\pi/2$  has been given at  $t=0.1s$  and the frequency has been tracked



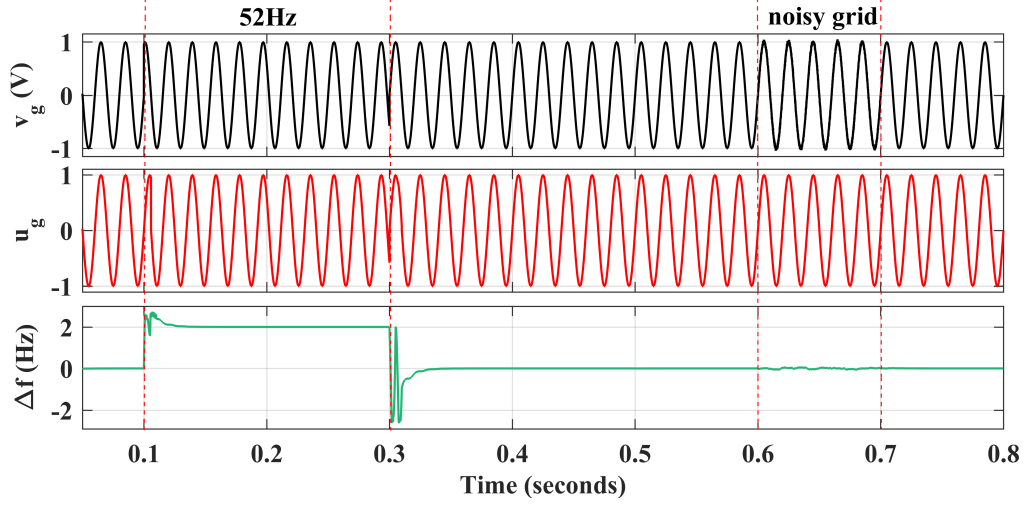


Figure 4.43: Simulation Performance of AZCD under frequency shift of 2Hz and noisy grid

within 1.5 cycles and the synchronizing signal is tracked within half cycle. During the DC-offset in grid voltage ( $t=0.5s$  to  $t=0.7s$ ), oscillations of 5.18Hz has been seen in frequency estimation and error at zero crossing in synchronizing signal has been observed.

The proposed algorithm has been tested under different grid voltage conditions. The

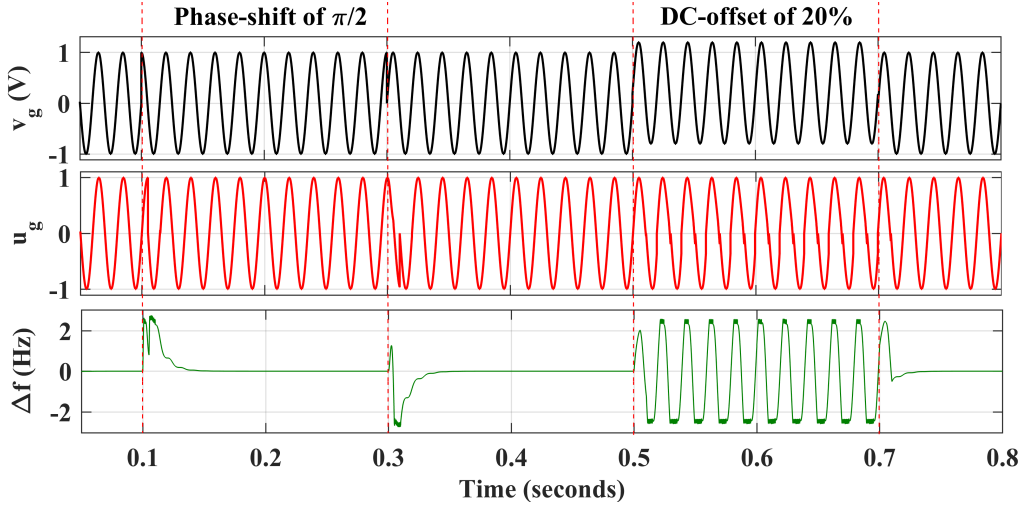


Figure 4.44: Simulation performance of AZCD under phase-shift of  $\pi/2$  and 20% DC-offset

proposed AZCD gives faster response with zero oscillations in steady state during frequency estimation. Also, in most cases the synchronizing signal has been tracked within half cycle during dynamic like voltage sag, phase and frequency shift.

#### 4.1.6.4 Experimental Results

Experimental performance of the SOGI-FLL has been shown in Fig. 4.45, 4.46 and 4.47 for the different grid voltage conditions. The proposed algorithm shows the excellent performance for the frequency estimation under different grid-voltage conditions except when the grid voltage has DC-offset (4.46(b)). Further the precise tracked frequency is used to estimate unit synchronizing signal. Simulation and

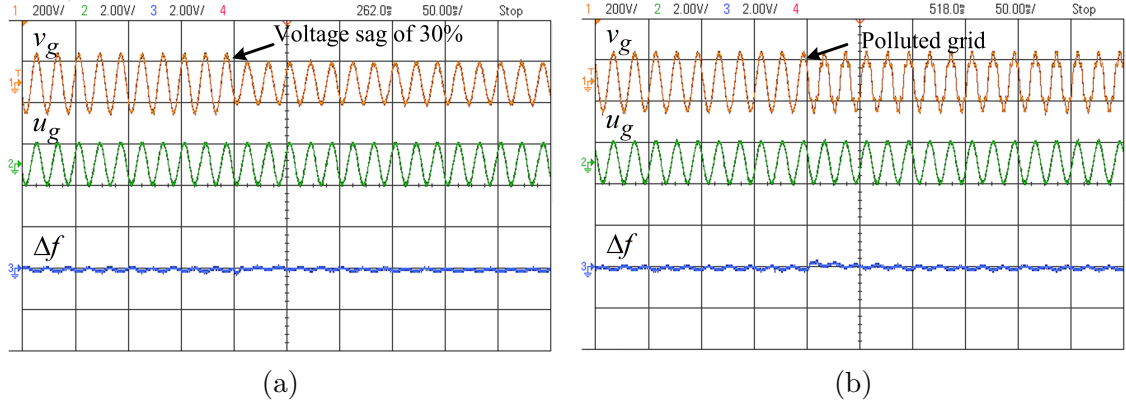


Figure 4.45: Experimental performance of single-phase AZCD based synchronization under (a) voltage sag of 30% (b) polluted grid (THD 18.0%)

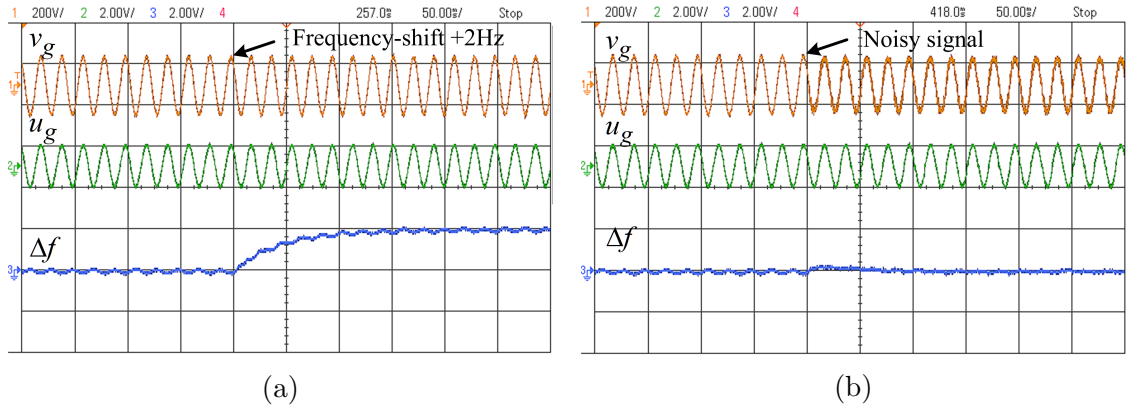


Figure 4.46: Experimental performance of single-phase AZCD based synchronization under (a) frequency shift of +2Hz (b) noisy grid

experimental performance of the AZCD synchronizing algorithm has been summarized in Table 4.6. The AZCD shows the excellent frequency estimation capability. It shows almost faster dynamic response and zero oscillation during steady-state except during DC-offset condition.

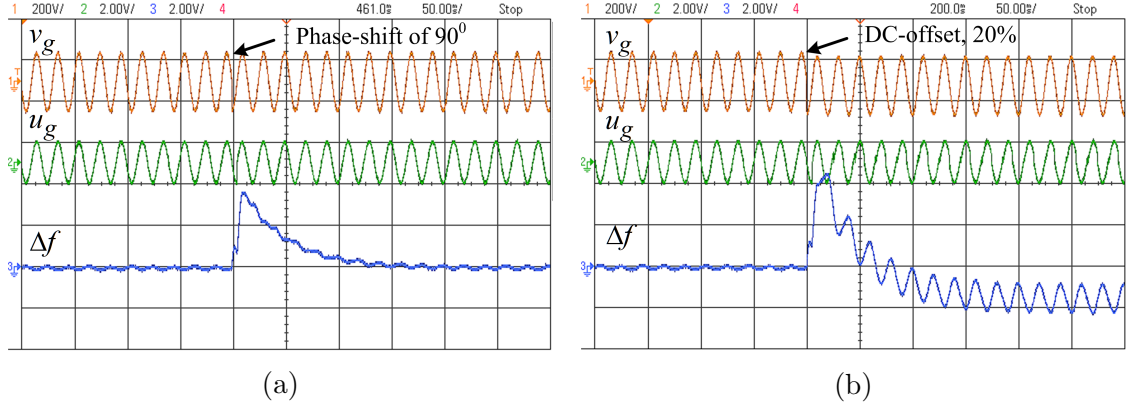


Figure 4.47: Experimental performance of single-phase AZCD based synchronization under (a) phase-shift of  $\pi/2$  (b) 20% DC-offset

Table 4.6: Summary of simulation and experimental performance of AZCD

Cases	Simulation performance	Experimental performance
Voltage sag of 30%	$\Delta f_{pp} \approx 0$ $t_s = 9.82ms$	$\Delta f_{pp} \approx 0$ $t_s = 10.0ms$
Polluted grid	$\Delta f_{pp} = 0.015Hz$	$\Delta f_{pp} \approx 0Hz$
Frequency change of +2Hz	$\Delta f_{pp} \approx 0$ $t_s = 10.19ms$	$\Delta f_{pp} \approx 0$ $t_s = 100ms$
Noisy voltage signal	$\Delta f_{pp} = 0.012Hz$	$\Delta f_{pp} \approx 0$
Phase-shift of $\pi/2$	$t_s = 29.87ms$	$t_s = 100ms$
DC-offset of 20%	$\Delta f_{pp} = 5.18Hz$	$\Delta f_{pp} = 1.6Hz$

#### 4.1.6.5 Comparison of Single-Phase Synchronization Techniques

After the detailed simulation and experimental performances of the designed synchronization techniques the evaluation of the different synchronization techniques under different grid voltage cases have been summarized in Table 4.7. Performance comparison of single-phase synchronization technique has been discussed for the different grid voltage conditions.

- Case I Voltage sag of 30% : During this condition, AZCD shows the best performance in terms of frequency estimation and SRF-PLL, SOGI-PLL and SOGI-FLL give best results for the amplitude estimation.
- Case II Polluted grid: During this condition AZCD and SOGI-FLL-ROGI give the best performance as the error in the estimated frequency signal is almost

zero. Performance of EPLL is best in steady-state but the dynamic response is not good.

- Case III Frequency change: During the frequency change the AZCD show best performance in both the steady-state and dynamic response for frequency estimation. The steady-state performance of SOGI-FLL and SOGI-FLL-ROGI is comparable to AZCD in term of frequency estimation.
- Case IV Noisy voltage signal: In this case, the AZCD and SOGI-FLL-ROGI gives almost zero frequency error while others show some noise in estimated frequency. Sam has been followed for the amplitude estimation.
- Case V Phase-shift of  $\pi/2$ : Performance of EPLL and SRF-PLL are unsatisfactory as these have large response time while the SOGI-FLL, SOGI-FLL-ROGI and AZCD give best performances for frequency estimation. SOGI-PLL, SOGI-FLL, SOGI-FLL-ROGI is best in case of amplitude estimation.
- Case VI DC-offset of 20% : In this case the AZCD performance is unsatisfactory and performance of SOGI-FLL-ROGI is best fro frequency estimation. The performance of SOGI-PLL and SOGI-FLL are satisfactory while the performance of SRF-PLL and EPLL are unsatisfactory.

Overall SOGI-FLL-ROGI and AZCD show best performance compared to EPLL, SOGI-PLL and SOGI-FLL. AZCD gives better performance than SOGI-FLL-ROGI except during DC-offset condition for estimation of frequency.

Table 4.7: Performance comparison for single-phase synchronization techniques

Case	SRF-PLL	EPLL	SOGI-PLL	SOGI-FLL	SOGI-FLL- ROGI	AZCD
Voltage sag of 30%	Best	moderate	best	best	moderate	best
Polluted grid	unsatisfactory	satisfactory	satisfactory	moderate	best	best
Frequency change of +2Hz	satisfactory	moderate	satisfactory	best	best	best
Noisy voltage sig- nal	unsatisfactory	unsatisfactory	satisfactory	moderate	best	best
Phase-shift of $\pi/2$	satisfactory	unsatisfactory	moderate	best	best	best
DC-offset of 20%	unsatisfactory	unsatisfactory	satisfactory	moderate	best	unsatisfactory

## 4.2 Three-Phase Grid Synchronization Techniques

Various three-phase synchronization techniques are discussed in this Section. These include Unit template estimation, SRF-PLL, Improved Adaline PLL and Adaptive Spline based PLL. Their individual simulation and experimental performances are tabulated and compared in the end in a comprehensive manner.

### 4.2.1 Unit Template Estimation

This is the simplest method to estimate unit templates of the voltage signal of each phase. This method is largely used by researchers under standard grid voltage condition for grid synchronization [101, 142, 143]. Three-phase voltages have been measured at PCC and depicted as  $v_{ga}$ ,  $v_{gb}$  and  $v_{gc}$ . Unit templates are obtained by simply dividing by the individual phase voltages by magnitude of three-phase grid voltage at PCC ( $A_v$ ). The in-phase unit templates of each phases are given by 4.67.

$$u_{pa} = \frac{v_{ga}}{A_v}, u_{pb} = \frac{v_{gb}}{A_v} \text{ and } u_{pc} = \frac{v_{gc}}{A_v} \quad (4.67)$$

where,  $A_v$  is the magnitude of three-phase grid voltage and is calculated by 4.68:

$$A_v = \sqrt{\frac{2}{3}(v_{ga}^2 + v_{gb}^2 + v_{gc}^2)} \quad (4.68)$$

Quadrature-phase templates of three-phase can also be evaluated by 4.69.

$$\begin{aligned} u_{qa} &= \frac{-u_{pb}}{\sqrt{3}} + \frac{u_{pc}}{\sqrt{3}} \\ u_{qb} &= \frac{\sqrt{3}}{2}u_{pa} + \frac{1}{2\sqrt{3}}(u_{pb} - u_{pc}) \\ u_{qc} &= \frac{-\sqrt{3}}{2}u_{pa} + \frac{1}{2\sqrt{3}}(u_{pb} - u_{pc}) \end{aligned} \quad (4.69)$$

#### 4.2.1.1 Simulation Results

The simulation performance of the unit template based synchronization technique has been shown in Fig. 4.48 under various grid voltage conditions. The unit template

method can estimate synchronizing signal perfectly under amplitude change, phase shift and frequency shift as shown in Fig. 4.48(a), 4.48(b) and 4.48(c) respectively.

During the polluted grid condition, the unit template is also polluted as shown

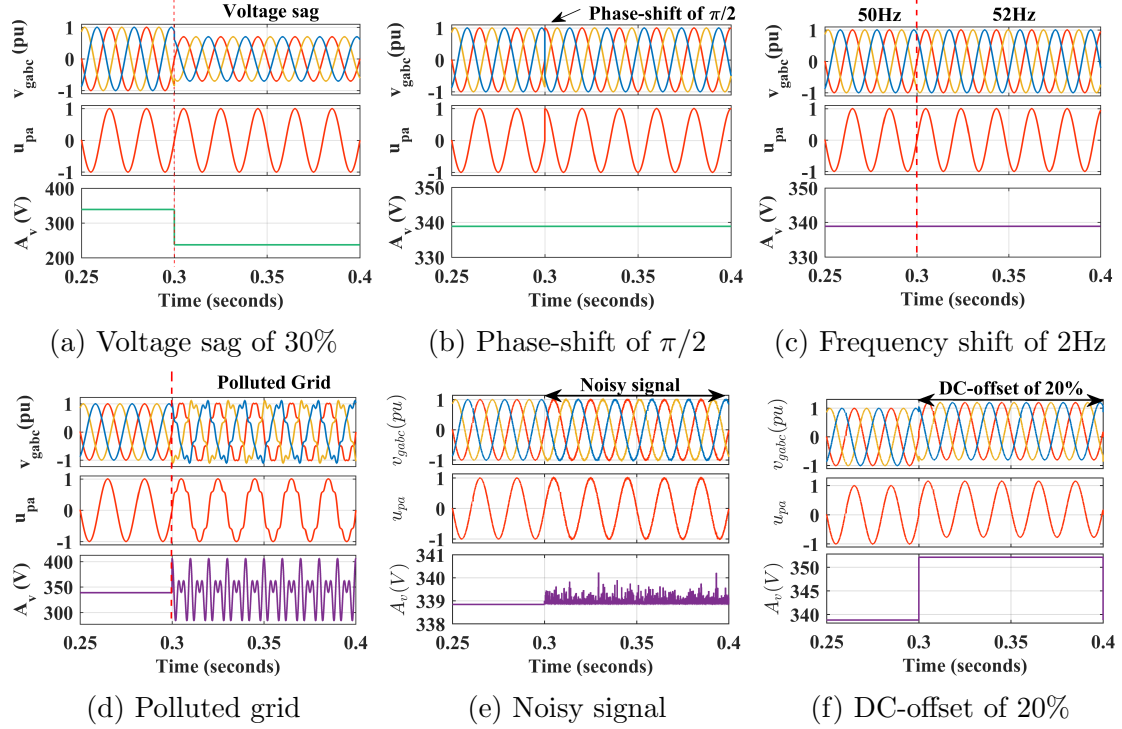


Figure 4.48: Simulation results of unit template based synchronization technique

in Fig. 4.48(d). Also, the amplitude estimated by this method shows high ripple content. During the noisy grid voltage signal (Fig. 4.48(e)) the unit template and PCC amplitude also show noise in the waveform. In case of DC-offset condition (Fig. 4.48(e)), unit-template shows DC-offset and the amplitude can not estimate accurate magnitude of fundamental component. Hence, it is observed that unit-template method work good only in standard grid condition and in adverse case it doesn't work appropriately.

#### 4.2.1.2 Experimental Results

The experimental results of the unit-template method for estimating the synchronizing signals have been shown in Fig. 4.49 and 4.50. Under ideal grid conditions, Fig. 4.49 shows the performance under voltage sag and swell condition. The unit synchronizing signal has been estimated instantly and distortion free.

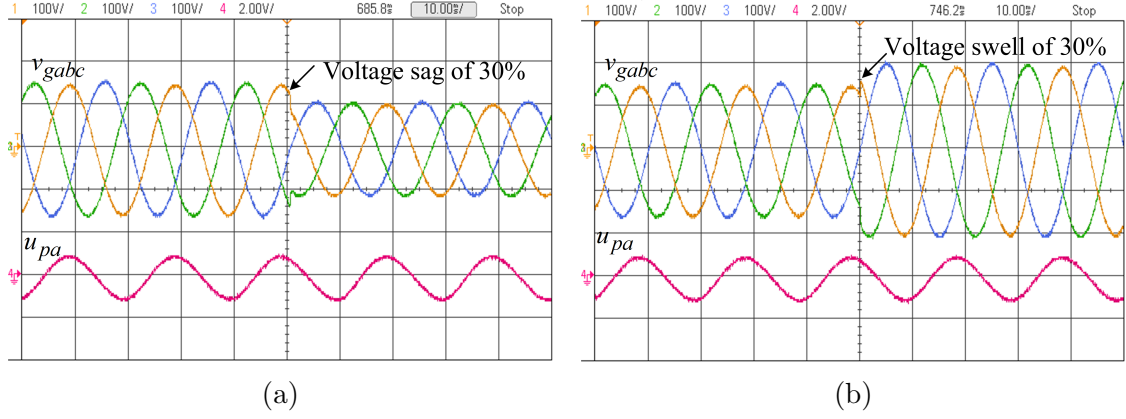


Figure 4.49: Experimental performance of three-phase unit-template based synchronization under (a) voltage sag of 30% (b) voltage swell of 30%

Figure 4.50 shows the experimental results under phase-shift of  $\pi/2$  and the polluted grid condition. The THD of the polluted grid voltage is 17.0%. During the phase-

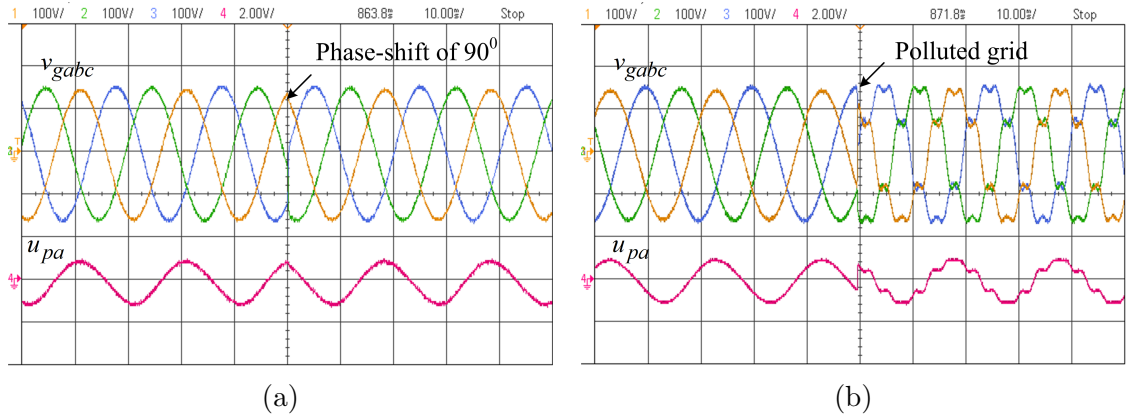


Figure 4.50: Experimental performance of three-phase unit-template based synchronization under (a) phase shift of  $90^\circ$  (b) Polluted grid

shift condition this method can estimate synchronizing signals instantly. While during polluted grid condition, the unit-synchronizing signals are also polluted and show the same amount of distortion as in the grid voltage. Hence, advanced algorithms are required which can give distortion free synchronizing signal even under polluted grid condition.

In the next sections conventional and modern three-phase synchronization techniques are discussed, which try to overcome the problems in unit-template method.



### 4.2.2 Three-Phase SRF-PLL

Synchronous reference frame phase-locked loop (SRF-PLL) is one of the most popular synchronization technique and it is extensively used [144–146]. It has simple structure and shows robust performance for the estimation of grid voltage parameters such as amplitude, phase and frequency [147–149]. Structure of the three-phase SRF-PLL has been shown in Fig. 4.52. SRF-PLL requires Clarke’s and Park trans-

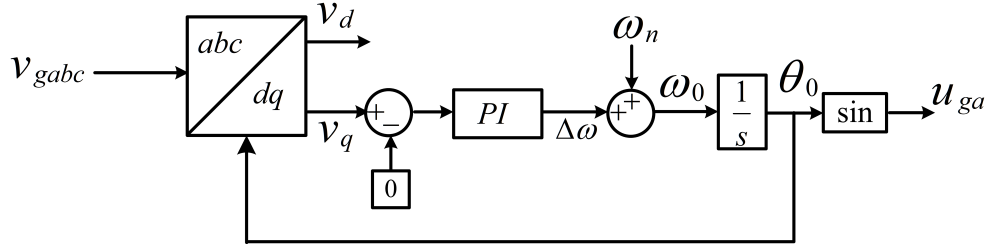


Figure 4.51: Structure three-phase SRF-PLL

formation to convert abc to dq frame of reference. The three-phase grid voltages are considering as in 4.70.

$$\begin{aligned} v_{ga} &= A_v \sin(\omega_i t) \\ v_{gb} &= A_v \sin(\omega_i t - \frac{2\pi}{3}) \\ v_{gc} &= A_v \sin(\omega_i t + \frac{2\pi}{3}) \end{aligned} \quad (4.70)$$

In case of rotating frame is  $90^\circ$  behind A-axis, the abc to dq transformation is written as:

$$\begin{bmatrix} v_d \\ v_q \\ v_0 \end{bmatrix} = \begin{bmatrix} \sin \omega_o t & -\cos \omega_o t & 0 \\ \cos \omega_o t & \sin \omega_o t & 0 \\ 0 & 0 & 1 \end{bmatrix} \begin{bmatrix} v_{ga} \\ v_{gb} \\ v_{gc} \end{bmatrix} \quad (4.71)$$

The q-component of dq reference frame is regulated using PI controller which forces the error term to zero or the q-component to zero. The output of PI gives the error in frequency estimation. Further, error ( $\Delta\omega$ ) is added with the standard grid frequency ( $\omega_n = 314 \text{ rad/s}$ ) gives the frequency estimation of the grid voltage. To achieve the phase information of the grid voltage, estimated frequency has been

integrated.

$$\omega_o = \omega_n + \Delta\omega \quad (4.72)$$

$$\theta_o = \int (\omega_n + \Delta\omega) dt \quad (4.73)$$

The phase information is given back to the system and it continuously tracks the phase of the grid voltage by minimizing the error.

#### 4.2.2.1 Simulation Results

Simulation results of SRF-PLL have been shown in Fig. 4.52 and 4.53. Figure 4.52(a)

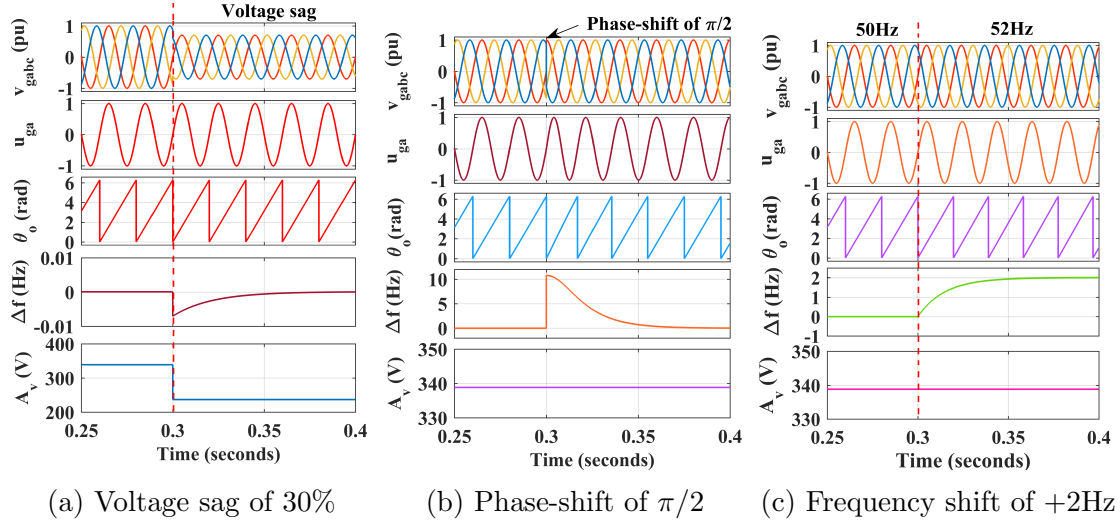


Figure 4.52: Simulation results of SRF-PLL

and 4.52(b) shows the dynamics results during voltage sag of 30% and the phase shift of  $\pi/2$  respectively. During voltage sag, the amplitude of grid voltage has been detected with small transient of 0.007Hz and the frequency has been estimated. During the phase-shift the frequency has been estimated within 3.5 cycles with a transient of 0.29Hz. Figure 4.52(c) show the dynamic result of frequency change of +2Hz. During this condition, frequency has been estimated correctly within 3 cycles and hence the synchronizing signal is also estimated perfectly within 3 ms.

The polluted grid contains 5th and 7th harmonics as shown in Fig. 4.53(a). The amplitude and frequency tracking using SRF-PLL show high value of ripples and are shown in Fig. 4.53(a). During the noisy signal (Fig. 4.53(b)) and the DC-offset

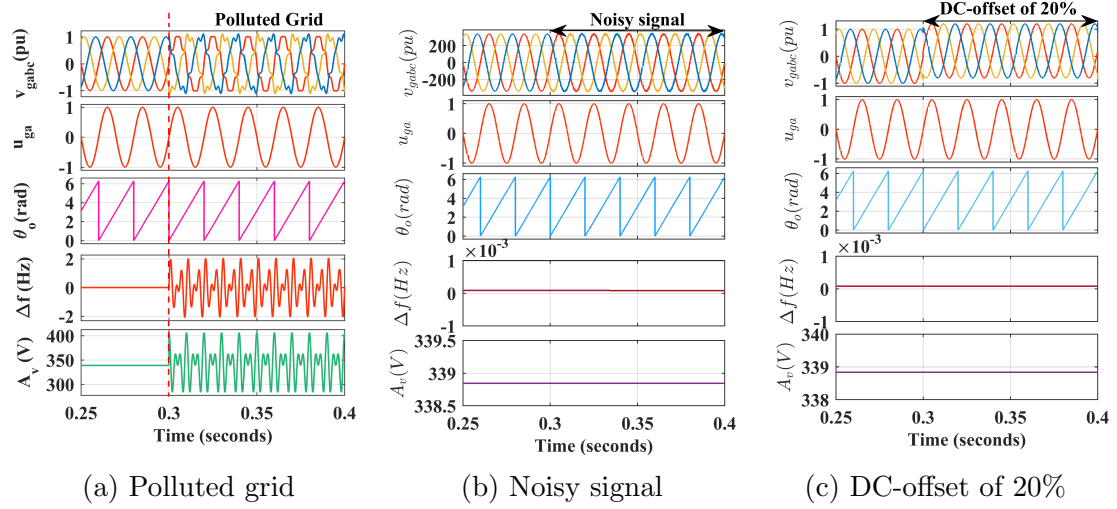


Figure 4.53: Simulation results of SRF-PLL

(Fig. 4.53(c)) condition SRF-PLL works good and estimates phase, amplitude and frequency accurately however, it is observed that the performance of SRF-PLL is not good under polluted grid condition but better than unit template method. Hence, new PLLs are required which show good performance under dynamic conditions and better steady-state performance during polluted grid condition.

#### 4.2.2.2 Experimental Results

Experimental performance of three-phase SRF-PLL have been shown in Fig. 4.54 and 4.55. In Fig. 4.54, synchronizing signal, amplitude of three-phase voltage and

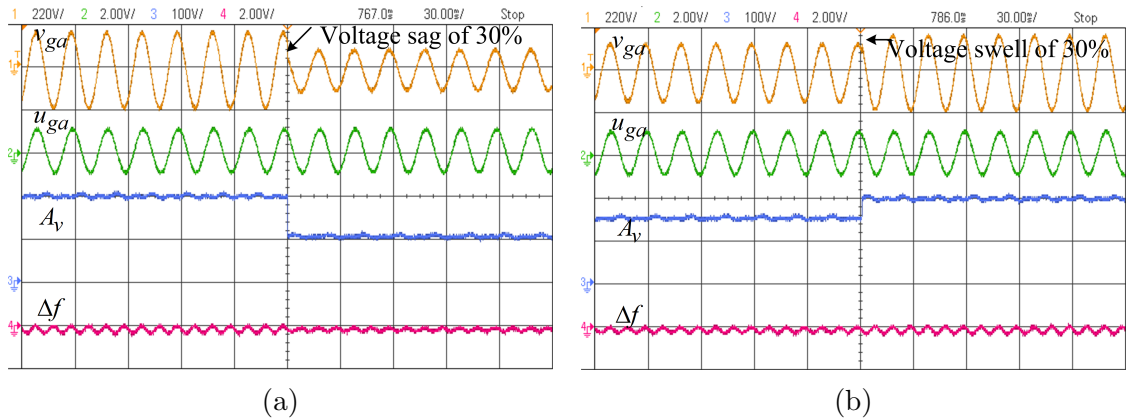


Figure 4.54: Experimental performance of three-phase SRF-PLL under (a) voltage sag of 30% (b) voltage swell of 30%

the error in frequency have been shown for voltage sag and voltage swell condition.

Under both the conditions, the voltage parameters has been tracked instantly; however show some oscillations in voltage amplitude estimation are observed.

Figure 4.55(a) and Fig. 4.55(b) show the voltage estimation under phase-shift of  $\pi/2$  and the polluted grid voltage condition respectively. During polluted grid con-

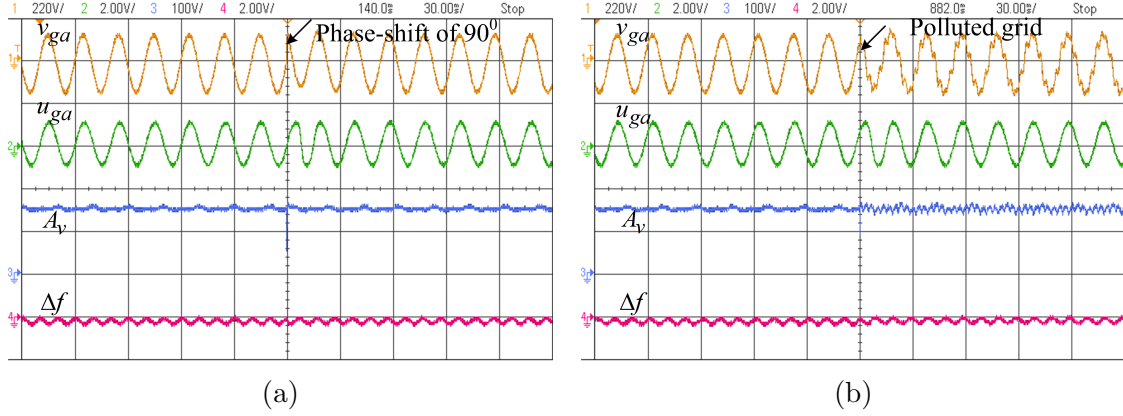


Figure 4.55: Experimental performance of three-phase SRF-PLL under (a) phase shift of  $90^\circ$  (b) Polluted grid

dition, the estimated frequency and amplitude show slightly higher oscillations than observed under normal grid condition. The three-phase SRF-PLL shows better performance than unit template method during polluted grid condition.

### 4.2.3 Improved Adaline PLL

The role of Artificial Neural Networks in estimation of power system parameters is unsurpassed. ANNs have been used for the detection of phase, frequency, amplitude and harmonic contents in the voltage or current signals. Adaline technique comprises a single neuron that receives stimulus from one or several inputs and a single output by proper training of involved weights. The technique is simple and training using LMS can be achieved online making it feasible to train and track instantaneous variations in voltage amplitude, phase angle and frequency. Conventional Adaline has fixed learning rate to update the weights. Here, the unique feature of the designed Improved Adaline is to incorporate a variable learning rate that achieves the convergence faster in minimum time while ensuring the lesser oscillations during steady-state condition.

#### 4.2.3.1 Mathematical Modelling of Adaline

Adaline can be depicted as an adaptive filter which can be used to extract time-varying amplitude, phase of the fundamental component and the harmonic component from different waveforms [150, 151]. Adaline algorithm was first proposed by Widrow and Hoff [71]. The basic structure of the Adaline algorithm has been shown in Fig. 4.56.

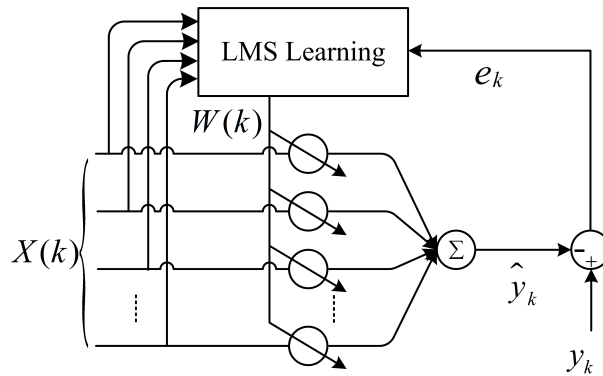


Figure 4.56: Structure of conventional Adaline

Consider a signal  $y_k$  having harmonics

$$\begin{aligned}
y_k &= \sum_{n=1}^N A_n \sin(n\omega t + \phi_n) \\
&= \sum_{n=1}^N (A_n \cos \phi_n \sin n\omega t + A_n \sin \phi_n \cos n\omega t) \\
&= \sum_{n=1}^N (a_n \sin n\omega t + b_n \cos n\omega t)
\end{aligned} \tag{4.74}$$

where,  $A_n$  = Amplitude of the nth harmonic,  $\phi_n$ =Phase angle of the nth harmonic signal, N= Total number of harmonics,  $a_n = A_n \cos \phi_n$ ,  $b_n = A_n \sin \phi_n$ . Also  $x_k$  and  $y_k$  denote the inputs and outputs respectively. Equation 4.74 can also be expressed in matrix form as

$$Y(k) = W^T(k)X(k) \tag{4.75}$$

$$\text{where, } W^T(k) = \begin{bmatrix} a_1 & b_1 & a_2 & b_2 & \dots & a_n & b_n \end{bmatrix} \tag{4.76}$$

$$\text{and } X(k) = \begin{bmatrix} \sin \theta_1 & \cos \theta_1 & \sin \theta_2 & \cos \theta_2 & \dots & \sin \theta_n & \cos \theta_n \end{bmatrix}^T \tag{4.77}$$

$\hat{y}_k$  is the estimated output of the algorithm and the error signal is defined as

$$e_k = y_k - \hat{y}_k \tag{4.78}$$

The adaptive rule employed for computing the weights uses the LMS method, which is based on Widrow-Hoff delta rule. The following expression governs this algorithm.

$$W(k+1) = W(k) + \alpha e_k X(k), \quad 0 < \alpha < 1 \tag{4.79}$$

where,  $\alpha$  is the learning rate of the algorithm. If the chosen value of  $\alpha$  is large then the learning is fast but at the same time, it may result in high oscillations. However, if the value of  $\alpha$  is small, then learning is slow but the oscillations in steady state response is lesser than the response with the higher learning rate.

#### 4.2.3.2 Estimation of Synchronizing Signals by Improved Adaline based PLL

The proposed algorithm is designed for extract the unit template for synchronization of the VSC to the grid and estimate other parameters of the signal such as phase, frequency and amplitude. Figure 4.57 shows the structure of the designed algorithm for the parameter estimation of phase "a" grid voltage. Here, the error between the

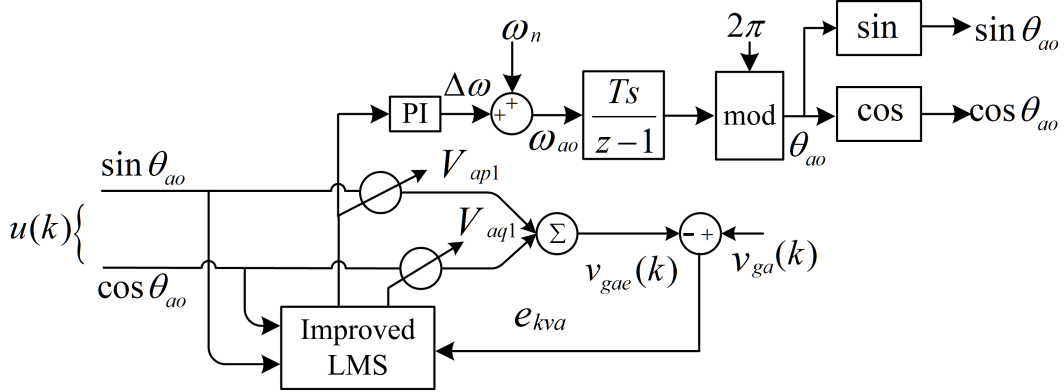


Figure 4.57: Structure of Improved Adaline based PLL

estimated and actual voltage signal in a-phase is expressed as:-

$$e_{kva} = v_{ga} - v_{gae} \quad (4.80)$$

$e_{kva}$  is the error in the grid voltage signal of phase "a",  $v_{ga}$  and  $v_{gae}$  denote the actual and estimated grid voltage signal. The estimated grid voltage is given as in 4.81.

$$v_{gae} = v_{ap1}u_{ga} + v_{aq1}w_{ga} \quad (4.81)$$

Here,  $v_{ap1}$  and  $v_{aq1}$  are the active and reactive fundamental weights of the a-phase grid voltage.  $u_{ga}(\sin \theta_{ao})$  and  $w_{ga}(\cos \theta_{ao})$  denote the in-phase and quadrature phase unit templates of the grid voltage.

The weights are updated using 4.82 and 4.83.

$$v_{ap}(k+1) = v_{ap}(k) + \alpha_{va}e_{kva}u_{ga} \quad (4.82)$$

$$v_{aq}(k+1) = v_{aq}(k) + \alpha_{va} e_{kva} w_{ga} \quad (4.83)$$

where,  $\alpha_{va}$  is the learning rate to update the weights. The conventional Adaline uses a fixed learning rate. The performance of conventional Adaline algorithm for training and faster convergence can be improved. One simple yet effective way for improving the performance of Adaline algorithm is by making the learning rate ( $\alpha_{va}$ ) variable instead of a constant value. This is achieved by incorporating an additional term as shown in equation 4.84 below;

$$\alpha_{va} = \alpha_{v0} + \alpha_{v1} |\bar{e}_{kva}| \quad (4.84)$$

Above,  $\alpha_{v0}$  and  $\alpha_{v1}$  are both fixed values and  $\alpha_{va}$  denotes the improved learning rate. The first term of the learning rate is fixed but the second term is incorporated to depend on the absolute value of the mean of the error signal. This makes the learning rate inherently adaptive and variable. Under steady state-state conditions, the absolute value of mean error is negligible and at that time learning rate will be constant ( $\alpha_{va} = \alpha_{v0}$ ). However, during dynamics the value of  $|\bar{e}_{kva}|$  is non-zero and the learning rate will be higher for higher error. A fast learning rate ensures faster convergence under both steady-state as well as dynamic conditions. The proposed simple modification helps to automatically achieve the benefits of low learning rate under steady-state conditions and higher learning rate during dynamic conditions.

#### 4.2.3.3 Simulation Results

Figure 4.58 and Fig. 4.59 show the simulation performance of the Improved Adaline based PLL and the comparison with Adaline-PLL. Figure 4.58 shows the estimation of voltage parameters including synchronizing signal under voltage sag of 20% and phase-shift of  $\pi/2$ . The voltage sag of 20% is introduced at  $t=0.3s$  and in normal condition it is restored at  $t=0.4s$ . The amplitude is estimated by Improve Adaline PLL within 19.43ms and by Adaline PLL within 79.05ms. The learning rate is high during the dynamics and hence shows faster convergence. During the



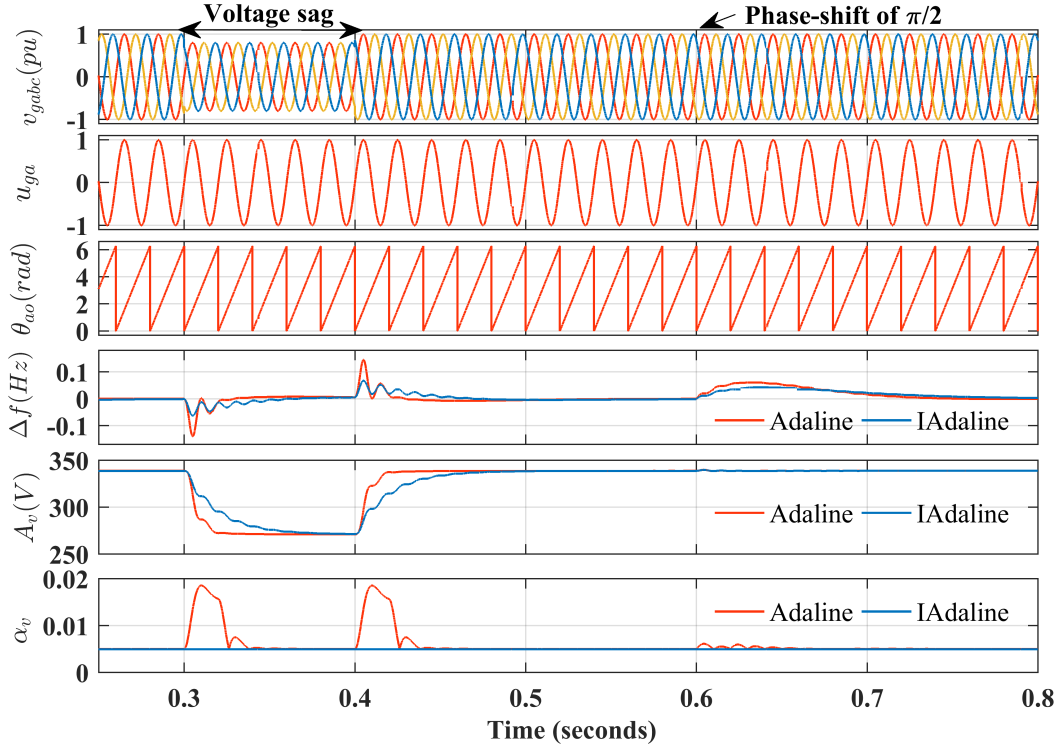


Figure 4.58: Simulation results of IAdaline PLL under voltage sag and phase-shift phase-shift, which is introduced at  $t=0.6s$ , the frequency is estimated by Improved Adaline within 74.04ms and by Adaline within 80.15ms.

Figure 4.59 shows the performance of proposed Improved Adaline under polluted grid condition and the frequency change of +2Hz. The period of polluted grid is from  $t=0.3s$  to  $t=0.4s$ . During this condition, the performance is same because of equal learning rate. During the frequency shift, the Improved Adaline shows faster dynamic response (4 cycles) than conventional Adaline based PLL (5 cycles). The learning rate is high in case of Improved Adaline during dynamics only and changes to small fixed learning rate.

Figure 4.60 shows the performance of proposed IAdaline under noisy signal and for DC-offset in grid voltage. During the noisy signal the performance of the conventional and IAdaline is same as the learning rate is same. During the DC-offset condition, Adaline PLL does not show good DC-rejection capability. Hence the output signal in the form of voltage amplitude or frequency estimation shows oscillations. Here, the IAdaline also shows inferior performance as it increases the

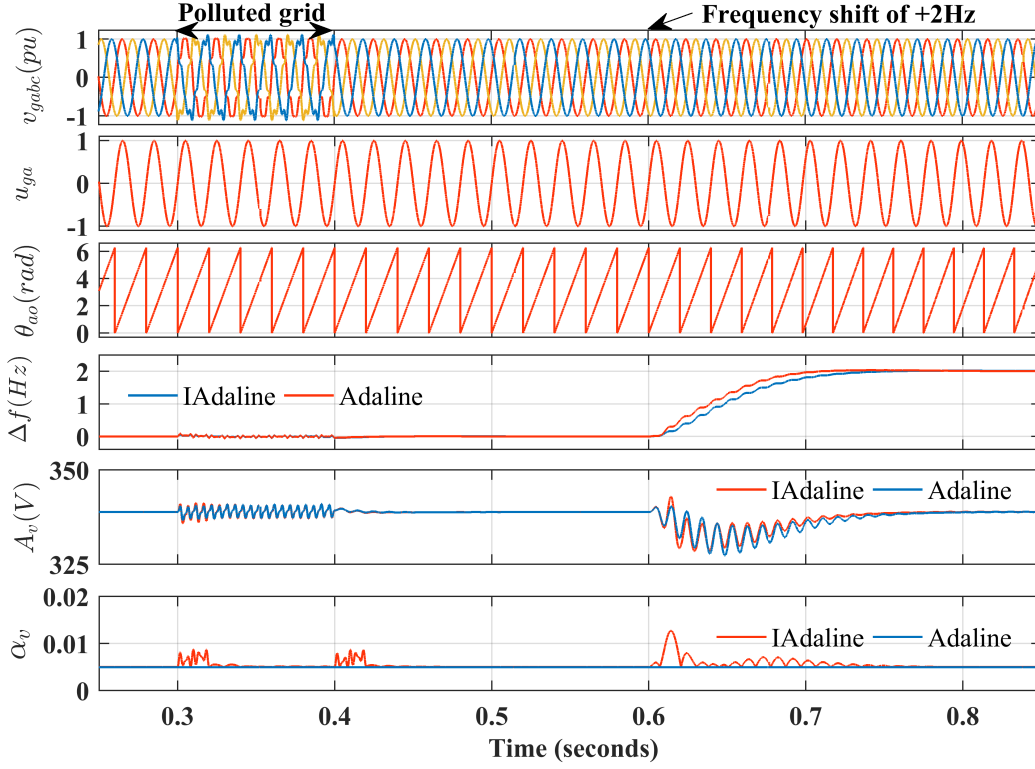


Figure 4.59: Simulation results of IAdaline PLL under polluted grid and frequency-shift

learning rate due to continuous DC-offset in grid voltage.

#### 4.2.3.4 Experimental Results

The experimental performance of Improved Adaline have been shown in Fig. 4.61 and 4.62 under different grid-voltage conditions such as voltage sag, voltage swell, phase-shift, polluted grid and the frequency change. Figure 4.61 show the parameter estimation under voltage sag (30%) and voltage swell (30%). During this condition the magnitude has been estimated within 40ms (2 cycles) and the error in frequency ( $\Delta f$ ) is almost zero in steady-state condition. The error in frequency during voltage change is also minimal ( $< 0.1Hz$ ).

Figure 4.62(a) shows the experimental performance of IAdaline-PLL during phase-shift condition. The frequency has been tracked within 100ms (5cycles) and the estimated amplitude shows minimal transient value. The experimental performance during polluted grid condition has been shown in Fig. 4.62(b). During the polluted

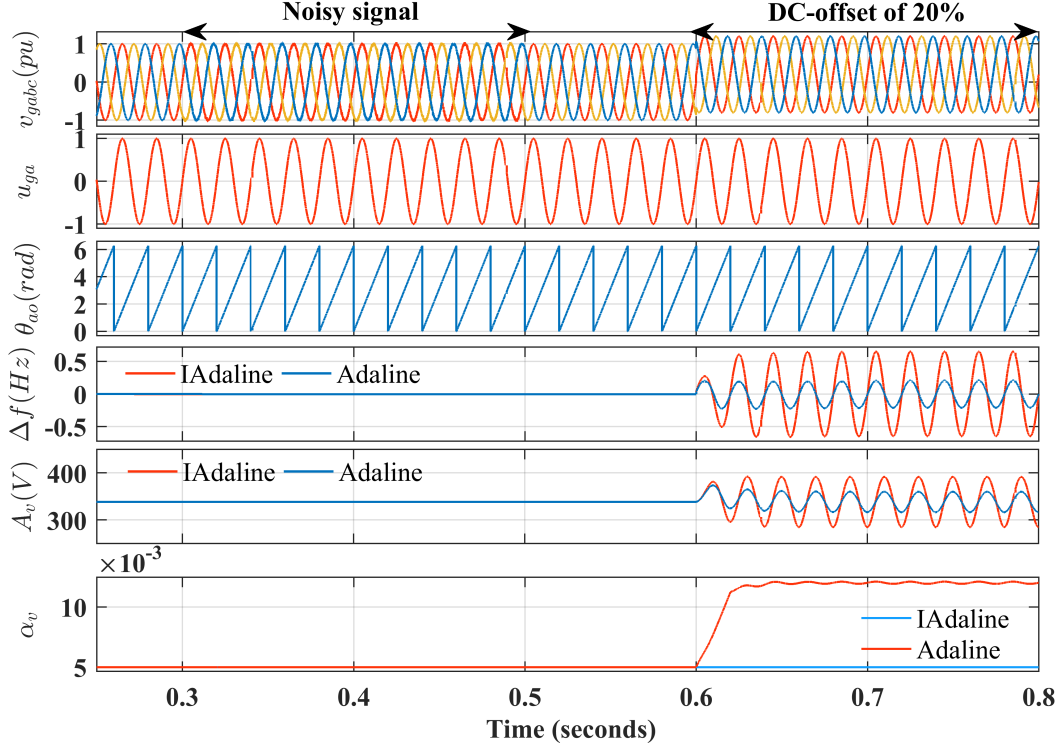


Figure 4.60: Simulation results of IAdaline PLL under noisy signal and DC-offset of 20%

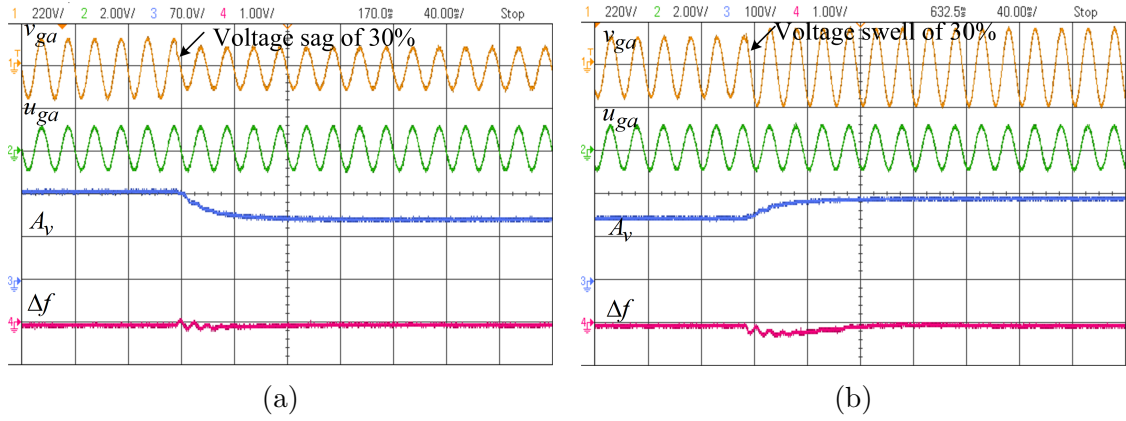


Figure 4.61: Experimental performance of three-phase IAdaline-PLL under (a) voltage sag of 30% (b) voltage swell of 30%

grid condition, the proposed IAdaline-PLL shows excellent performance as the ripple content in amplitude signal and in frequency error signal is almost zero. In Figure 4.62(c), during the frequency change of +2Hz, the frequency has been estimated correctly and precisely in 80ms (4 cycles).

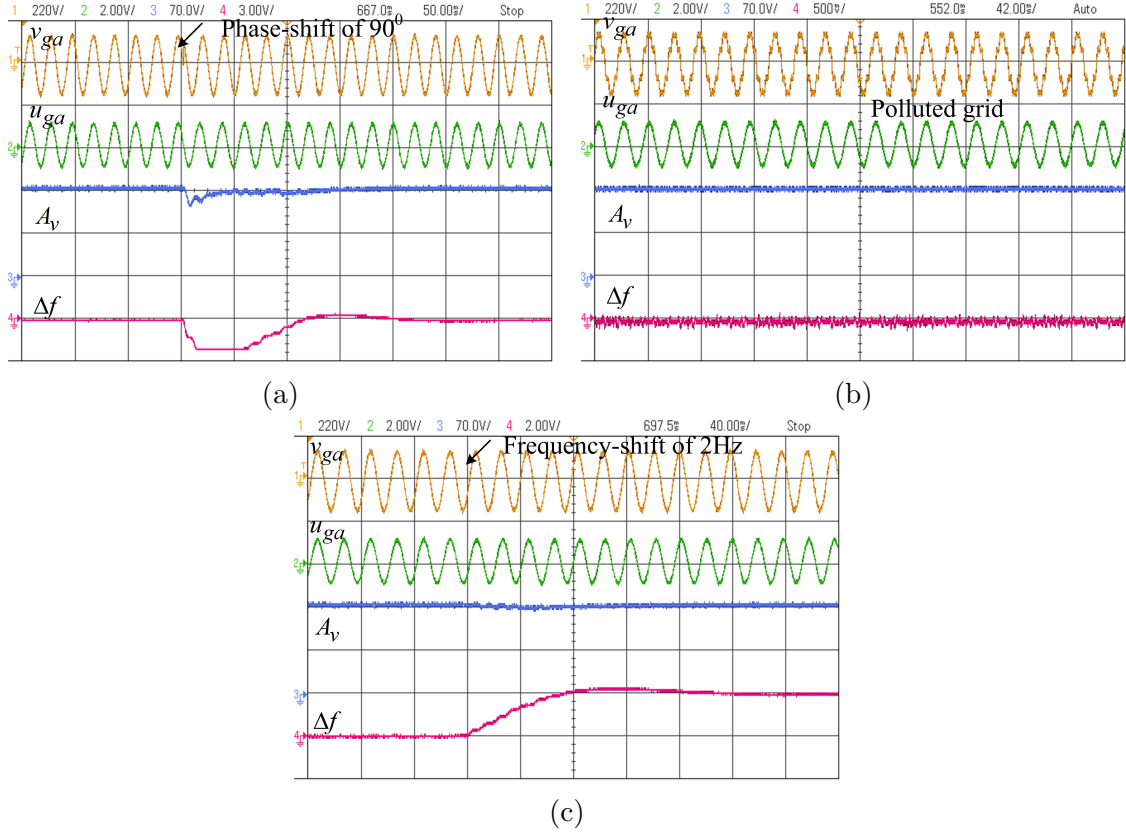


Figure 4.62: Experimental performance of three-phase IAdaline-PLL under (a) phase shift of 90° (b) Polluted grid (c) Frequency shift of 2Hz

#### 4.2.3.5 Performance Comparison of Adaline-PLL and IAdaline-PLL

IAdaline-PLL is designed as an improved version of Adaline-PLL and it is expected to perform better than Adaline-PLL under both steady-state and dynamic condition. Performance comparison of the IAdaline-PLL and Adaline-PLL have been shown in Fig. 4.63 and 4.64 for the different grid voltage condition. Figure 4.63(a)

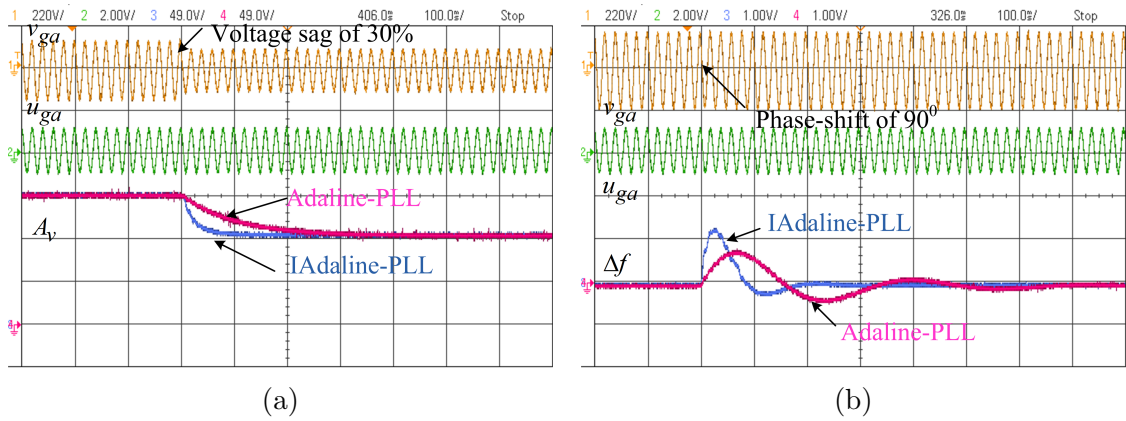


Figure 4.63: Experimental performance comparison of three-phase IAdaline-PLL and Adaline-PLL under (a) voltage sag of 30% (b) phase shift of 90°

and 4.63(b) show the experimental performance comparison under voltage sag of 30% and phase-shift of  $\pi/2$  respectively. Adaline-PLL takes almost 100ms and the IAdaline-PLL take 40ms to estimate the voltage correctly as the learning rate is higher during the dynamic condition. During the phase-shift the IAdaline-PLL response is faster than Adaline-PLL for estimating the frequency.

Figure 4.64(a) and 4.64(b) show the performance comparison under frequency shift of +2Hz and the polluted grid conditions respectively. Under both the cases, the

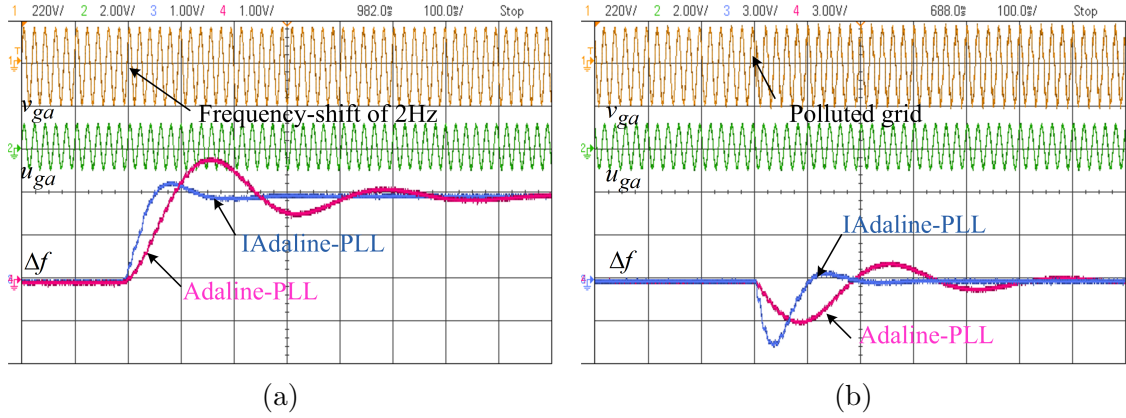


Figure 4.64: Experimental performance comparison of three-phase IAdaline-PLL and Adaline-PLL under (a) frequency change of 2Hz (b) polluted grid

IAdaline-PLL shows faster response while ensuring almost zero oscillations during steady-state condition. Experimental results of IAdaline-PLL and Adaline-PLL matches the simulation performance except the condition of frequency change. In experiment results it perform better than in simulation.

#### 4.2.4 Spline based PLL

Splines are piecewise polynomial functions with pieces that are smoothly connected together. Spline functions of degree  $p$  are  $(p-1)$  continuously differentiable [152, 153]. As a result, Splines have excellent approximation properties and very good convergence rate. A spline curve is an effective combination of some knots of a suitable  $p$  degree spline basis function.

The spline interpolation function can be represented as in 4.85.

$$\psi(n) = u^T C w \quad (4.85)$$

where the matrix  $C$  is a pre-computed matrix also called the spline basis matrix,  $u$  denotes the normalised abscissa value between two knots and  $w$  denotes the control points  $\begin{bmatrix} w_i & w_{i+1} & w_{i+p} \end{bmatrix}^T$ . For a polynomial of degree 2, the function can be depicted as

$$\psi(n) = \begin{bmatrix} u^2 & u & 1 \end{bmatrix} C \begin{bmatrix} 1 & -2 & 1 \\ -2 & 2 & 0 \\ 1 & 1 & 0 \end{bmatrix} \quad (4.86)$$

For a polynomial of degree 3, the function may be represented as

$$\psi(n) = u^T C w = \begin{bmatrix} u^3 & u^2 & u & 1 \end{bmatrix} C \begin{bmatrix} w_i \\ w_{i+1} \\ w_{i+2} \\ w_{i+3} \end{bmatrix} \quad (4.87)$$

where,  $C$  is the basis matrix for Catmull-Rom (CR) spline and it is defined as

$$C = 0.5 \begin{bmatrix} -1 & 2 & 0 & 0 \\ 2 & 0 & 1 & 0 \\ -1 & -5 & 4 & 1 \\ 0 & 3 & -3 & 1 \end{bmatrix} \quad (4.88)$$

$$f_i = [u^T C]^T = \frac{1}{2} \begin{bmatrix} -u_i + 2u_i^2 - u_i^3 & 2 - 5u_i^2 + 3u_i^3 & u_i + 4u_i^2 - 3u_i^3 & -u_i^2 + u_i^3 \end{bmatrix} \quad (4.89)$$

Equation 4.89 is observed as the non-linear expansion of the given input signal. The output of the  $p^{th}$  activation function can be calculated as

$$\psi_i(n) = f_i w_{pi} \quad (4.90)$$

For updating the weight of the input signal, an adaptive least mean square (LMS) algorithm has been used and the following equation has been applied.

$$w(n+1) = w(n) + \mu e_v x(n) \quad (4.91)$$

where,  $w(n) = \begin{bmatrix} w_{d1} & w_{q1} & w_{d2} & w_{q2} & \dots & w_{dn} & w_{qn} \end{bmatrix}$ ,  
 $x(n) = \begin{bmatrix} \sin \theta_1 & \cos \theta_1 & \sin \theta_2 & \cos \theta_2 & \dots & \sin \theta_n & \cos \theta_n \end{bmatrix}$  and  $\mu$  is known as the learning rate of the non-linear adaptive algorithm.  $e_v$  is the error function and is calculated by subtracting the estimated grid voltage ( $v_{ge}$ ) to the desired value ( $v_g$ );

$$e_v(n) = v_{ge}(n) - v_g(n) \quad (4.92)$$

The Spline-PLL can be used to extract different harmonics from the distorted waveform by using different weights and templates  $\sin \theta_o$ ,  $\cos \theta_o$ ,  $\sin 2\theta_o$ ,  $\cos 2\theta_o$ ,  $\sin 3\theta_o$ ,  $\cos 3\theta_o$ ,  $\sin 5\theta_o$ ,  $\cos 5\theta_o$  etc. However, for synchronization purpose, undistorted sine templates are required hence, only fundamental active and reactive weights and their updation is necessary and considered further in the design process. The block diagram of Spline-PLL has been shown in Fig. 4.65.

The proposed PLL is an adaptive weight-based technique. Active component ( $w_d$ ) and reactive component ( $w_q$ ) of the grid voltage signal are estimated by the LMS weight updating technique. These weights are fed to the Spline interpolation function  $\psi(n)$ , which gives the smooth and precise active ( $y_d$ ) and reactive component ( $y_q$ ) of the voltage signal. The reactive component is used to extract parameters of

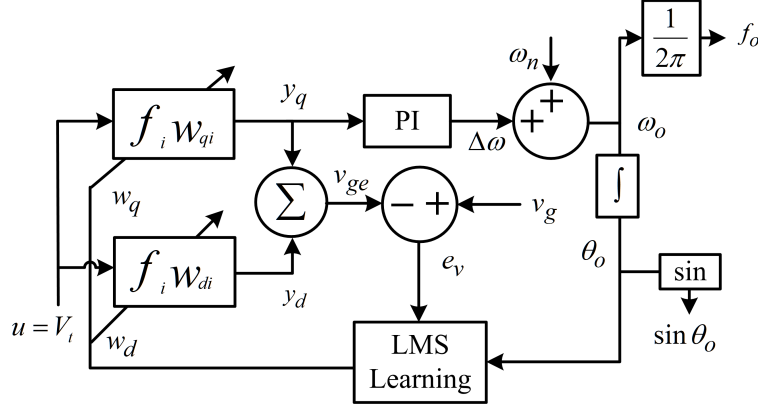


Figure 4.65: Structure of Spline-PLL

grid voltage signal which is given to the PI controller. The phase-angle  $\theta_o$  of the input grid voltage is estimated by 4.93:

$$\theta_o = \int (\omega_n + \Delta\omega) dt \quad (4.93)$$

The phase angles ( $\theta_{ao}$ ,  $\theta_{bo}$  and  $\theta_{co}$ ) have been calculated from three individual phase voltages  $v_{ga}$ ,  $v_{gb}$  and  $v_{gc}$  respectively with the help of 4.93. Further the sine templates ( $\sin \theta_a$ ,  $\sin \theta_b$ ,  $\sin \theta_c$ ) for each phase of the grid voltage have been obtained in a similar manner. Moreover, the frequency of the input voltage signal is estimated by dividing with  $2\pi$  to obtain the estimated grid frequency ( $f_o$ ) as shown in Fig. 4.65.

#### 4.2.4.1 Simulation Results

Spline-PLL has been tested in MATLAB/Simulink under six different grid voltage conditions and shown in Figure 4.66 and 4.67. Figure 4.66(a) and 4.66(b) shows the performance under 30% voltage sag and phase-shift condition respectively. Under voltage-sag condition, the frequency and amplitude of the grid voltage has been estimated correctly within 12.79ms. During the phase-shift of  $\pi/2$ , the frequency has been estimated in 1.5 cycles and the amplitude is also estimated within 1.5 cycles after some fluctuations. Figure 4.66(c) shows the simulation results of frequency change of 2Hz in grid voltage signal. The frequency has been estimated in 1.5 cycles and same time is taken for amplitude estimation. The steady-state error is zero



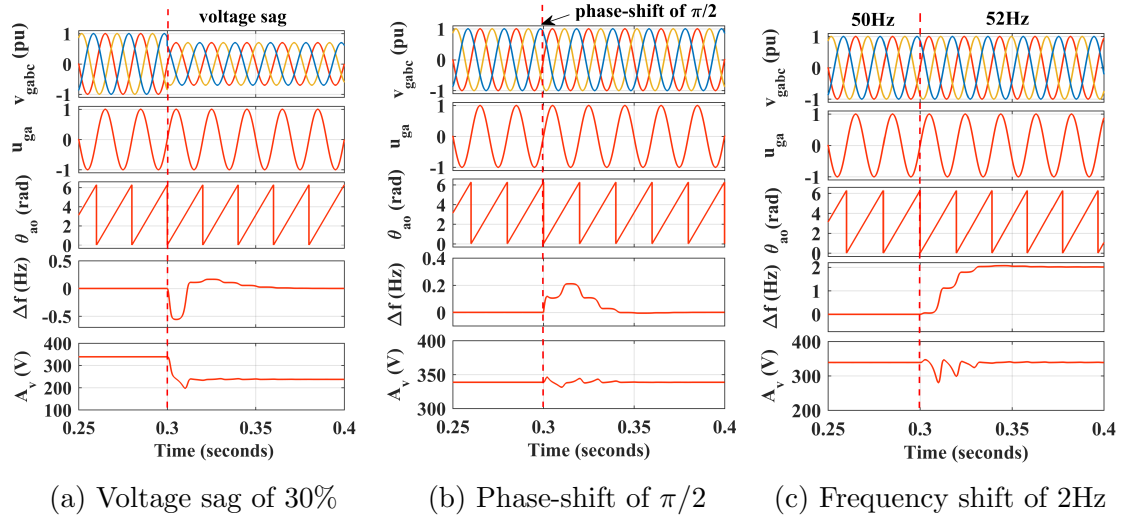


Figure 4.66: Simulation results of Spline-PLL

when frequency varies from the standard grid frequency. Hence, the estimated synchronizing signal is perfect and having no harmonics.

Figure 4.67(a) shows the simulation results of Spline-PLL under polluted grid condition. The peak-to-peak frequency estimated by spline PLL is 1.2Hz. Amplitude

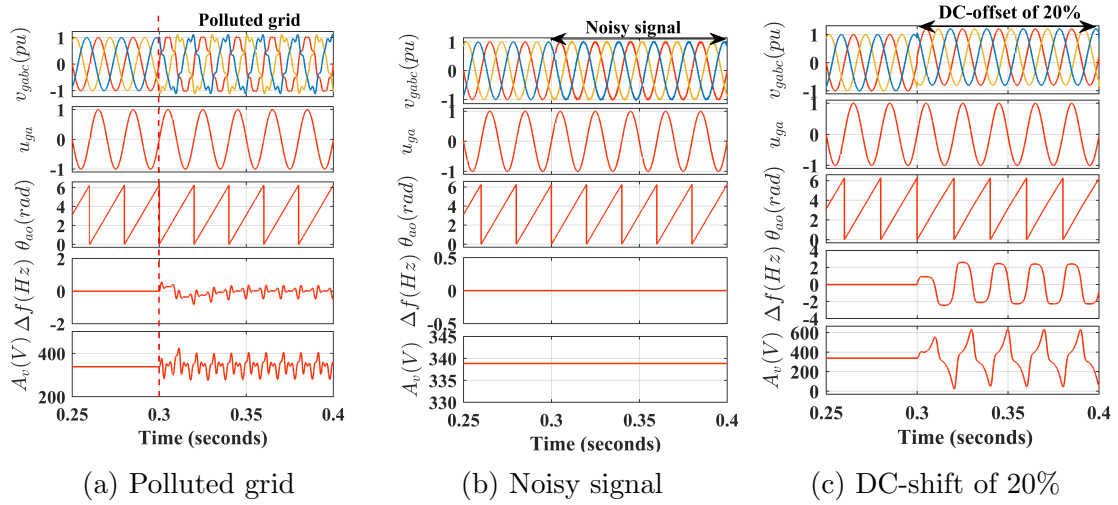


Figure 4.67: Simulation results of Adaptive Spline based PLL

estimation performance is moderate during this case. During the noisy signal input (Figure 4.67(b)) the Spline-PLL able to filter out the noise and gives perfect sinusoidal unit synchronizing signal and error free frequency. In Fig. 4.67(c), Spline-PLL has no DC-rejection capability hence in this condition it shows oscillations for the estimation of amplitude and frequency.

#### 4.2.4.2 Experimental Results

Experimental performance of Spline based adaptive PLL has been shown in Fig. 4.68 and 4.69. Figure 4.68(a) and 4.68(b) show the performance under voltage sag and swell

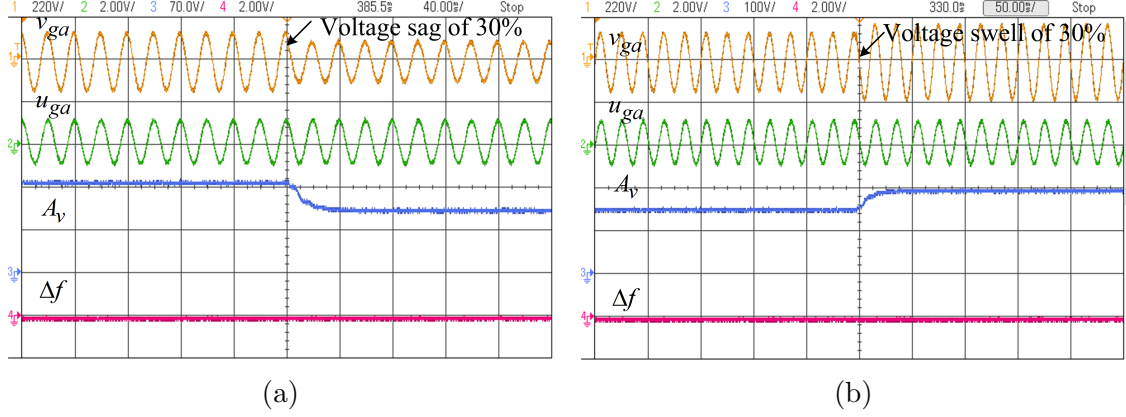


Figure 4.68: Experimental performance of three-phase Spline-PLL under (a) voltage sag of 30% (b) voltage swell of 30%

respectively. In both the cases, the estimated error in frequency ( $\Delta f$ ) is zero all the time and the amplitude is estimated within 30ms (1.5cycles).

Figure 4.69(a)-(c) show the experimental results under the condition of phase shift of  $\pi/2$ , frequency change of +2Hz and the polluted grid conditions respectively. The frequency error is less than 4Hz during the dynamic conditions and almost zero oscillations during the steady-state condition in these three cases. During the phase-shift condition a high transient has been observed in amplitude estimation. Based on the simulation and experimental performance of the three-phase PLLs the effectiveness of PLLs have been summarized in Table 4.8. Experimental results for the DC-offset and noisy condition could not taken due to device limitations. Hence, the performance of the PLLs have been compared on the basis of simulation performances. The comparison of performance of three-phase PLLs have been analyzed and discussed for different grid-voltage conditions

- Case I Voltage sag of 30%: During this condition , the SRF-PLL show best performance for the frequency and magnitude estimation. Performance of IAdaline-PLL and Spline-PLL have almost similar.

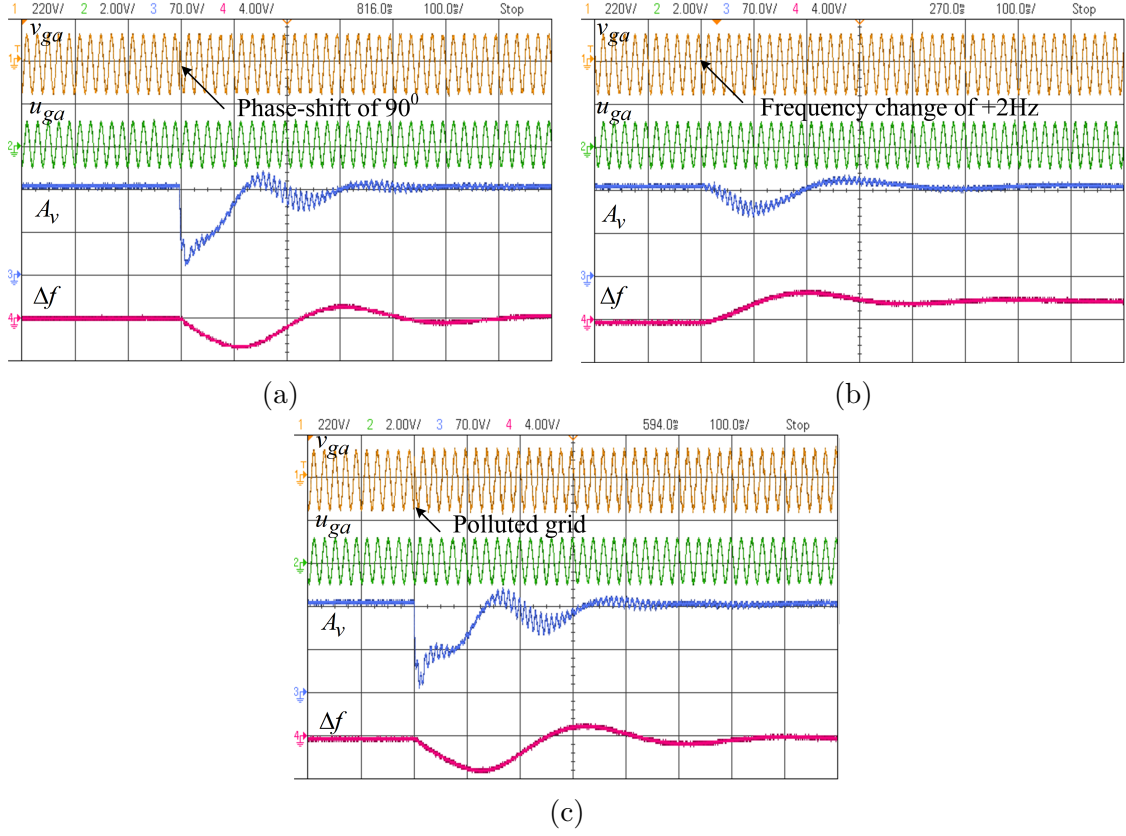


Figure 4.69: Experimental performance of three-phase Spline-PLL under (a) phase-shift of  $90^\circ$  (b) frequency change of  $2\text{Hz}$  (c) polluted grid

Table 4.8: Performance comparison for three-phase synchronization techniques

Case	SRF-PLL	Adaline-PLL	IAdaline-PLL	Spline-PLL
Voltage sag of 30%	best	moderate	best	best
Voltage swell of 30%	best	moderate	best	best
Polluted grid	unsatisfactory	moderate	best	moderate
Frequency change of $+2\text{Hz}$	moderate	moderate	best	moderate
Noisy voltage signal	moderate	moderate	moderate	best
Phase-shift of $\pi/2$	moderate	moderate	best	moderate
DC-offset of 20%	best	satisfactory	unsatisfactory	unsatisfactory

- Case II Voltage swell of 30%: In this condition the performance of PLLs are similar as in case for voltage sag in simulation and experimental results.
- Case III Polluted grid: In this case, IAdaline-PLL shows best performance as it has less learning rate during steady state. Adaline-PLL and Spline-PLL show moderate performance. The SRF-PLL performance is unsatisfactory as

it doesn't has filtering capability.

- Noisy voltage signal: Spline-PLL has the capability of smoothening the output signal. Hence, in this case it shows best results than other PLLs.
- Phase-shift of  $\pi/2$ : In this case, settling time of IAdaline is less than SRF-PLL, Adaline-PLL and Spline-PLL.
- DC-offset of 20%: Three-phase SRF-PLL has the inherent capability of DC-rejection and it shows best performance in this case. The performance of Adaline-PLL is satisfactory while the performance of IAdaline-PLL and Spline-PLL is unsatisfactory as these show high oscillations in frequency and amplitude estimation.

The performance of SRF-PLL is best except during the polluted grid condition. IAdaline-PLL and Spline based PLLs show best performance under different grid voltage conditions.

### 4.3 Conclusions

In this chapter, grid-synchronization techniques have been presented for both single-phase and three-phase grid voltage. Detailed mathematical modelling, simulation results and the experimental results have been shown. The synchronization techniques have been tested in both simulation and experimental under different grid voltage conditions, which shows the effectiveness of the synchronization techniques. In single-phase synchronization techniques PLL and non-PLL type techniques have been presented. For the variation in grid voltage, the AZCD shows best performance for both the amplitude estimation and frequency estimation. Frequency estimated by AZCD shows zero error and faster convergence. During the polluted grid condition SOGI-FLL-ROGI shows best performance as it filter out harmonic effectively and estimates amplitude and frequency without minimal or zero oscillations. SOGI-FLL and SOGI-FLL-ROGI has inherent frequency-locked loop hence it estimates

frequency precisely. The SOGI-PLL has no frequency-locked loop hence it shows oscillations during the frequency deviation. During the phase shift condition, the AZCD shows faster response than other PLLs. Noisy signals have wide range of frequency hence SOGI-PLL shows low oscillations for frequency estimation. In this case, SOGI-FLL-ROGI and AZCD show best results. During the DC-offset in grid voltage, the performance of EPLL and AZCD is not satisfactory, while the performance of SOGI-FLL-ROGI is observed to be the best.

For estimation of three-phase synchronizing signals and other voltage parameters unit-template method, SRF-PLL, IAdaline-PLL and Spline based PLL have been designed and presented in this chapter. Unit-template method can estimate only synchronizing signals and the magnitude of the grid voltage. Its performance is best under normal grid condition but during the polluted grid condition its performance is very poor and not acceptable. During the voltage variation, SRF-PLL shows better performance than other techniques. Moreover, during polluted grid condition, SRF-PLL show oscillations in both the tracked amplitude and frequency. IAdaline-PLL shows best performance under polluted grid condition. During the phase change or the frequency change the IAdaline-PLL shows best performance as it has faster response during dynamic condition and minimal error during steady-state condition. The SRF-PLL show best performance under DC-offset condition in the grid-voltage. Spline-PLL has the capability of smoothening the output waveform hence its performance is best during the noisy grid voltage condition. For other grid voltage conditions the performance of Spline-PLL is of moderate level.

Single-phase and three-phase synchronization techniques designed in this chapter has been further applied for the PQ improvement in the PV integrated SAPF.

## Chapter 5

# SAPF Operation under Normal and Polluted Grid

In the previous chapter, different synchronization techniques have been explained for single-phase and three-phase system under different grid-voltage conditions. In this chapter, Single-phase SAPF has been explained under ideal and polluted grid voltage conditions with non-linear loads for power quality improvement. The synchronization algorithms discussed in previous chapter have also been applied here for the development of controller.

The principle of SAPF is to effectively generate an equal and opposite harmonic current waveforms available in load current from shunt-connected VSC to cancel out the harmonics such that grid currents are sinusoidal. System configuration for single-phase SAPF system has been shown in Fig. 5.1.

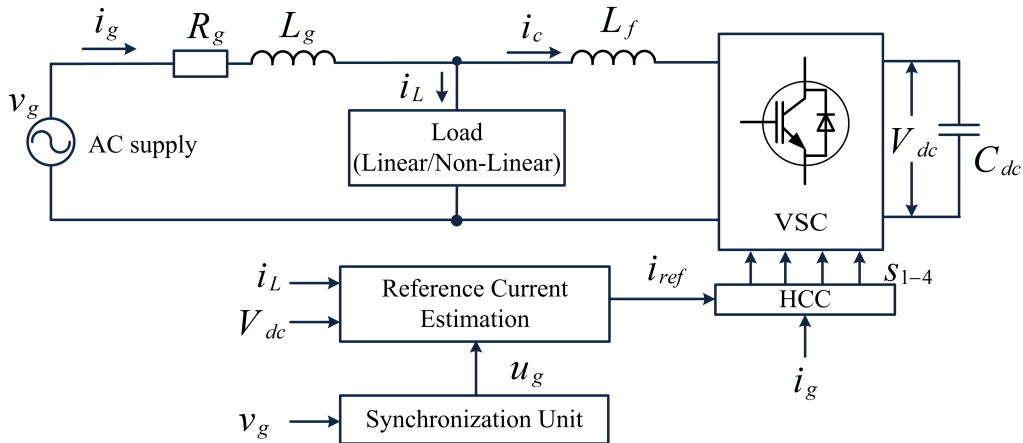


Figure 5.1: Single-phase SAPF configuration for simulation

Here linear/non-linear load have been connected at PCC and single-phase H-bridge

VSC has also connected at PCC via interfacing inductor. This system configuration with its control has been simulated in MATLAB/Simulink environment. Sampling time ( $T_s$ ) for the simulation is  $10\mu s$ .

Control algorithm and synchronization techniques have been employed to the developed prototype in the laboratory to improve the power quality in a single-phase system. Non-linear load has been connected at PCC and the VSC is also connected to PCC via interfacing inductor.

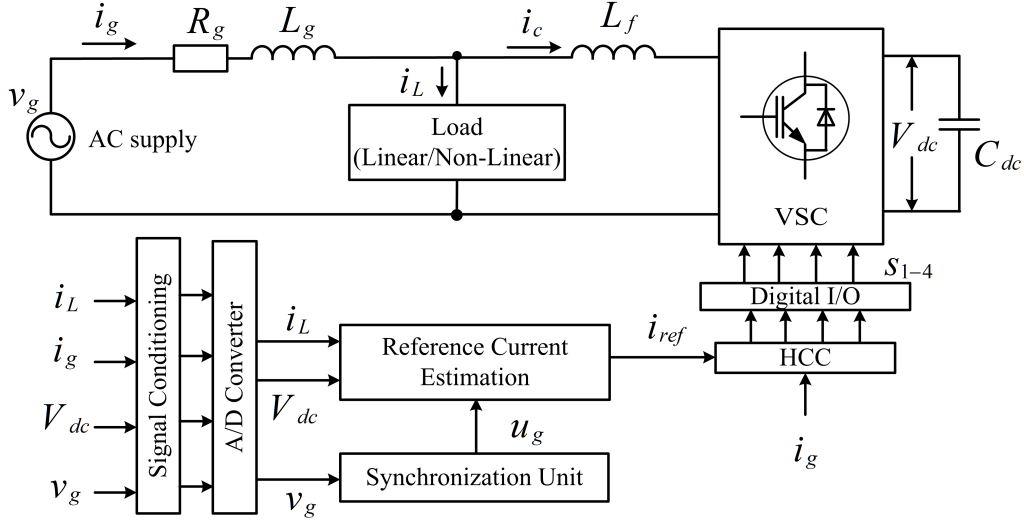


Figure 5.2: Single-phase SAPF configuration for experimental setup

Experimental configuration for single-phase system with non-linear load has been shown in Fig. 5.2. All the sensors have been connected to dSpace1104 at ADC channels and after processing the algorithm the required pulses for IGBT are generated at digital I/O pins of dSpace1104. Sampling time ( $T_s$ ) for the experimental analysis is  $50\mu s$ .

## 5.1 Single-Phase SAPF under Ideal Grid Condition

Residential distribution system are generally single-phase two wire system. Residential loads comprise different type of linear/non-linear loads and high non-linear

load content may impact the distribution grid adversely. The SAPF can be implemented at the user side for reactive power compensation and the improvement of power quality. Control algorithms and the synchronization methods are designed and discussed here for the proper functioning of single-phase SAPF under ideal grid condition. These includes SOGI control, Cascaded SOGI with unit template synchronization, SOGI control with Adaptive-ZCD synchronization and SOGI-FLL-ROGI for control and synchronization.

### 5.1.1 SOGI Control with Unit Template Synchronization

Fig. 5.3 represents the structure of the SOGI algorithm for load compensation. In

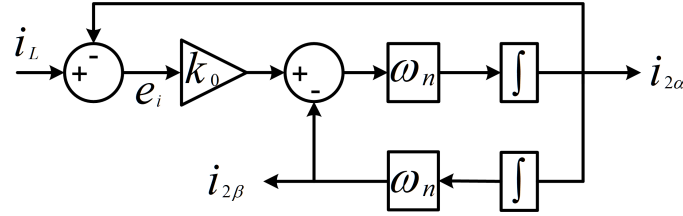


Figure 5.3: Structure of SOGI control applied to load current signal ( $i_L$ )

this figure,  $i_L(t)$  is the load current,  $k_0$  is gain of SOGI and  $\omega_n$  is the fundamental angular frequency.  $i_{2\alpha}$  and  $i_{2\beta}$  denote the two output signals of the SOGI, where  $i_{2\alpha}$  is the in-phase part and  $i_{2\beta}$  is the quadrature phase part of the load current respectively. Equation for the non-linear load current is given as-

$$\begin{aligned}
 i_L(t) &= \sum_{n=1}^N I_{fn} \sin(n\omega_i t + \psi) \\
 &= \sum_{n=1}^N [I_{fn} \sin \psi \cos(n\omega_i t) + I_{fn} \cos \psi \sin(n\omega_i t)] \\
 &= \sum_{n=1}^N [I_{2\alpha} \cos(n\omega_i t) + I_{2\beta} \sin n\omega_i t]
 \end{aligned} \tag{5.1}$$

where,  $I_{2\alpha} = I_{fn} \sin \psi$ ,  $I_{2\beta} = I_{fn} \cos \psi$ ,  $n$  denotes the harmonic order and  $I_{fn}$  is the amplitude of  $n^{th}$  harmonic component. The amplitude of the fundamental load current is estimated by considering the output signals having only fundamental



frequency ( $n = 1$ ). Estimation of fundamental load component is expressed as-

$$I_f = \sqrt{I_{2\alpha}^2 + I_{2\beta}^2} \quad (5.2)$$

The error in load current is estimated by subtracting the in-phase filtered component to the load current.

$$e_i(t) = i_L(t) - i_{2\alpha}(t) \quad (5.3)$$

The quadrature component of the load current signal is given by 5.4,

$$i_{2\beta}(t) = \omega_n \int i_{2\alpha}(t) dt \quad (5.4)$$

Here,  $\omega_n$  is the standard grid frequency or the resonating frequency of the SOGI. Applying Laplace transformation on above equation 5.4, it gives

$$i_{2\beta}(s) = \omega_n \frac{i_{2\alpha}(s)}{s} \quad (5.5)$$

From Fig. 5.3,  $i_{2\alpha}(t)$  is given by 5.6,

$$\begin{aligned} i_{2\alpha}(t) &= \int \omega_n [k_0 e_i(t) - i_{2\beta}(t)] dt \\ &= \int \omega_n k_0 [i_L(t) - i_{2\alpha}(t)] dt - \omega_n \int i_{2\beta}(t) dt \end{aligned} \quad (5.6)$$

Laplace transform of the above equation is given as,

$$i_{2\alpha}(s) = \omega_n k_0 \left[ \frac{i_L(s)}{s} - \frac{i_{2\alpha}(s)}{s} \right] - \omega_n \frac{i_{2\beta}(s)}{s} \quad (5.7)$$

Putting the value of  $i_{2\beta}(s)$  from 5.5 and arranging them it gives the closed-loop transfer function of in-phase signal and is written as 5.8,

$$D_2(s) = \frac{i_{2\alpha}(s)}{i_L(s)} = \frac{k_0 \omega_n s}{s^2 + k_0 \omega_n s + \omega_n^2} \quad (5.8)$$

Transfer function of the quadrature component is given as 5.9,

$$Q_2(s) = \frac{i_{2\beta}(s)}{i_L(s)} = \frac{k_0\omega_n^2}{s^2 + k_0\omega_n s + \omega_n^2} \quad (5.9)$$

Transfer function of the SOGI is given as 5.10,

$$SOGI(s) = \frac{i_{2\alpha}(s)}{k_0 e_i(s)} = \frac{\omega_n s}{s^2 + \omega_n^2} \quad (5.10)$$

Transfer function of the error signal ( $e_i$ ) is given as 5.11,

$$E(s) = \frac{e_i(s)}{i_L(s)} = \frac{s^2 + \omega_n^2}{s^2 + k_0\omega_n s + \omega_n^2} \quad (5.11)$$

Figure 5.4 displays the step response for different gain values. Three different gain

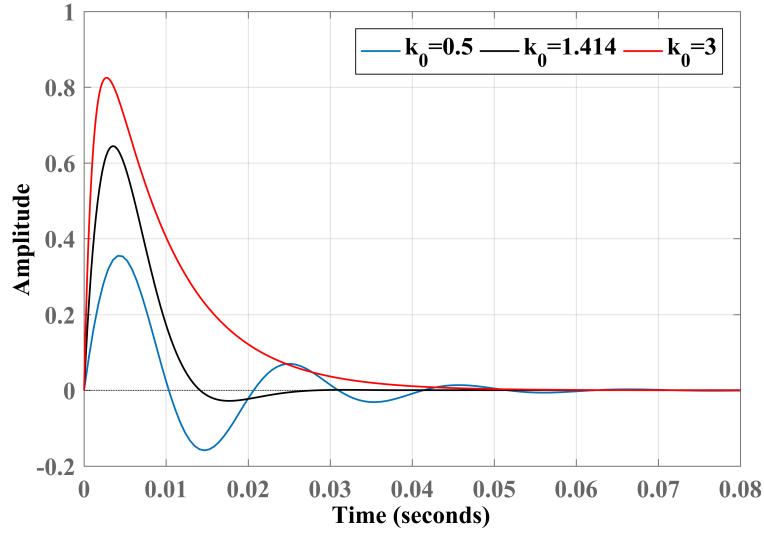


Figure 5.4: Step response of SOGI for in-phase component  $D_2(s)$

values (0.5, 1.414, 3) have been considered. It is observed that for larger value  $k_0 = 3$ , settling time is low but transient is high. Also, for lower gain  $k_0 = 0.5$ , the settling time is higher but the transient observed is lower in magnitude. Hence, an optimum value of gain ( $k_0 = 1.414$ ) has been chosen for the optimum response of the SOGI controller.

### 5.1.1.1 Estimation of Reference Current

The principle of SAPF is to effectively generate an equal and opposite harmonic current waveforms available in load current from shunt-connected VSC to cancel out the harmonics such that grid currents are sinusoidal. The developed controller is designed to generate the necessary gating signals for the IGBT switches of single-phase H-bridge inverter.

The reference current estimation requires the synchronizing signal ( $u_g$ ) from the grid voltage, fundamental load current component ( $I_f$ ) and the current loss ( $I_{loss}$ ) in the inverter. The synchronizing signal is estimated by dividing the grid-voltage to the grid voltage amplitude or unit-template method. Estimation of grid voltage amplitude and the synchronizing signal can be achieved by 5.12 and 5.13 respectively.

$$A_v = \sqrt{v_\alpha^2 + v_\beta^2} \quad (5.12)$$

$$u_g = \frac{v_g}{A_v} = \frac{v_g}{\sqrt{v_\alpha^2 + v_\beta^2}} \quad (5.13)$$

For shunt active compensation, DC-link voltage of the H-bridge inverter is controlled by the PI controller. The active compensation is performed by appropriate switching of IGBT switches. Some losses always occur during switching operation of VSC. The estimation of such losses is obtained with the help of following equation.

$$I_{loss}(n) = I_{loss}(n-1) + k_p[V_{dce}(n) - V_{dce}(n-1)] + k_i V_{dce}(n) \quad (5.14)$$

Here,  $V_{dce}(n) = V_{dc}^*(n) - V_{dc}(n)$  is the evaluated voltage error at DC-link inverter,  $k_p$  and  $k_i$  are the proportional and integral gains of the PI controller. The output of the PI controller is considered to depict the switching loss component  $I_{loss}(n)$ .

The grid reference current ( $i_{ref}$ ) is generated by the multiplying the synchronizing signal ( $u_g$ ) and the net current ( $I_{net}$ ) for compensation and expressed by 5.15.

$$i_{ref} = I_{net}u_g = (I_f + I_{loss})u_g \quad (5.15)$$

Hysteresis current controller (HCC) is used for its simplicity and robust working for generation of switching signals. The complete control structure is presented in Fig. 5.5.

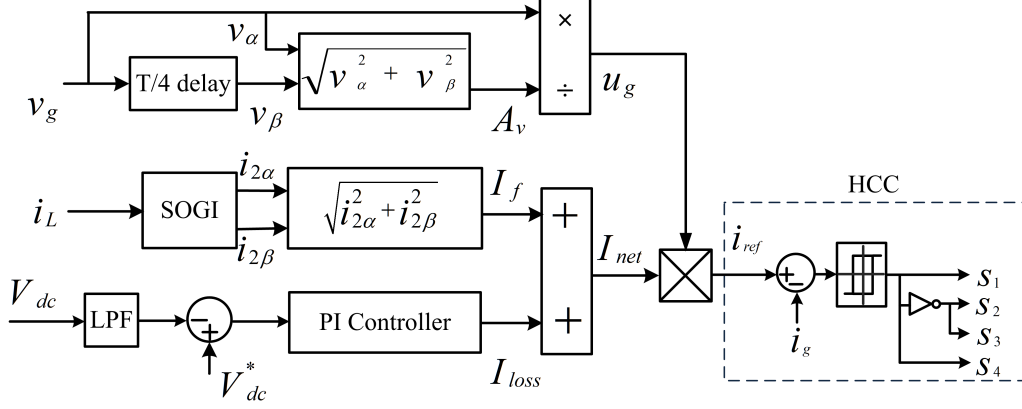


Figure 5.5: Single-phase SAPF control structure

#### 5.1.1.2 Simulation Results

Simulation performance of SOGI controller with unit template synchronization is shown in Fig. 5.6 and Fig. 5.7. Initially, the system is in normal condition i.e. the SAPF is not connected at PCC. In this condition, the grid current waveform is same as the load current waveform and the compensator current is zero. At  $t=0.01s$  the VSC has been connected at PCC and SAPF operation has started. Now, the grid current becomes sinusoidal and the DC-link voltage settles to fixed DC-link reference voltage. During the dynamic condition i.e during the load change the DC-link voltage is regulated to 400V by action of PI controller.

In Fig. 5.7, reactive power compensation is shown for the single-phase SAPF. Initially, under normal condition, the active (3.93kW) and reactive power (1.51kVar) demanded by load is supplied by the grid. Now, when the SAPF connected to PCC at  $t=0.1s$ , reactive power (1.51kVar) demanded by the load is now supplied by the SAPF and the active power (3.93kW) is supplied by the grid. At  $t=0.3s$ , load has been increased and the active power of 5.47kW demanded by the load is supplied by the grid (5.52kW) and the reactive power (4.34kVar) is compensated by compensator. There are also some losses of 54W approx which occur during compensation.

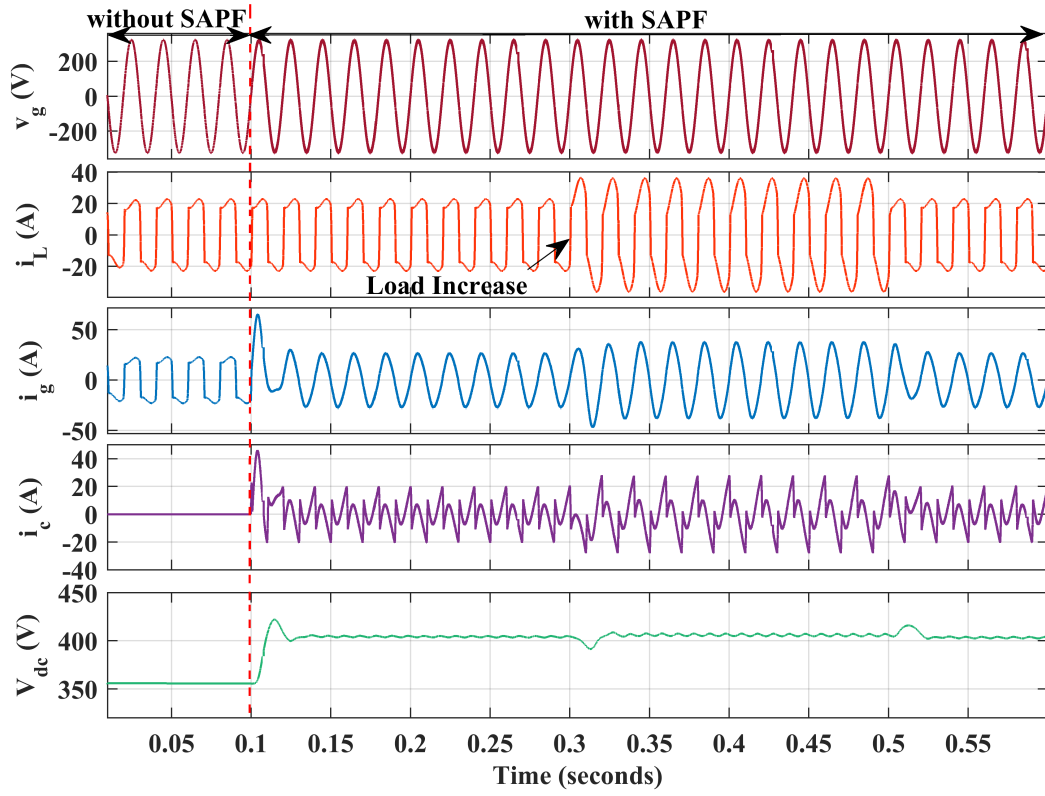


Figure 5.6: Single-phase SAPF performance of SOGI with unit template synchronization

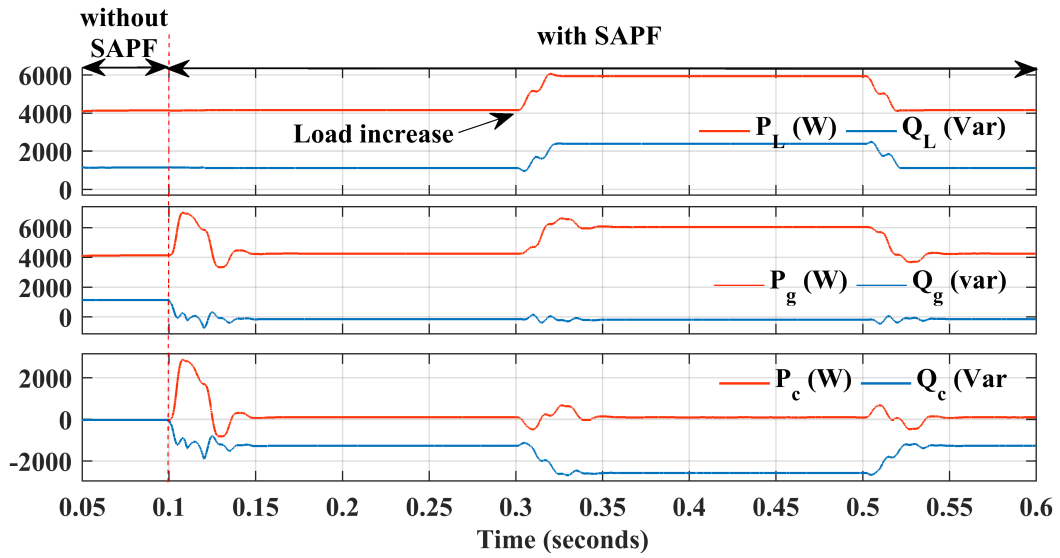


Figure 5.7: Single-phase SAPF performance of SOGI with unit template synchronization

Hence, the proposed algorithm is working satisfactory for reactive power compensation.

In Fig. 5.8, shows the THD analysis of the grid parameters with the SOGI control employing unit template grid synchronization technique.

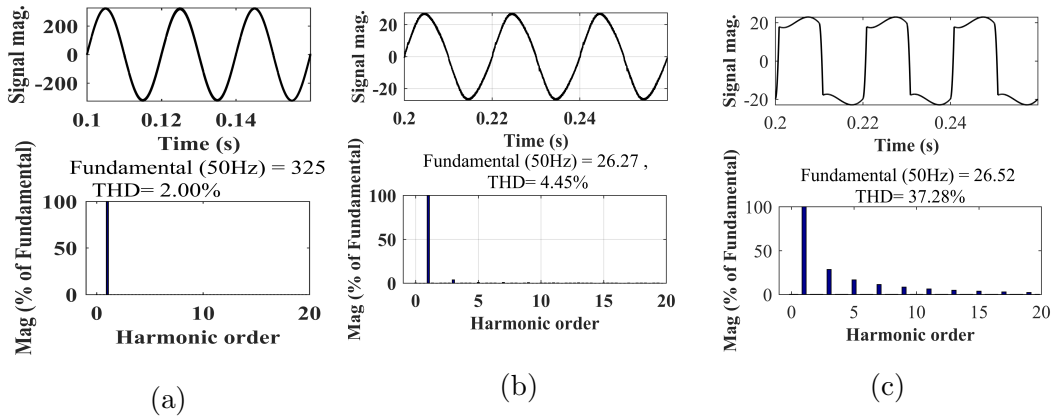


Figure 5.8: THD analysis of (a) Grid voltage (b) Grid current (c) Load current

### 5.1.1.3 Experimental Results

Figure 5.9, shows the open-loop experimental result for the filtered in-phase component and quadrature component for the non-linear load variation. The in-phase component of the load current is distortion free and the quadrature component is also distortion free and  $90^\circ$  shifted from the in-phase load component.

THD of the load current is 37.28% and under normal condition the THD of the grid

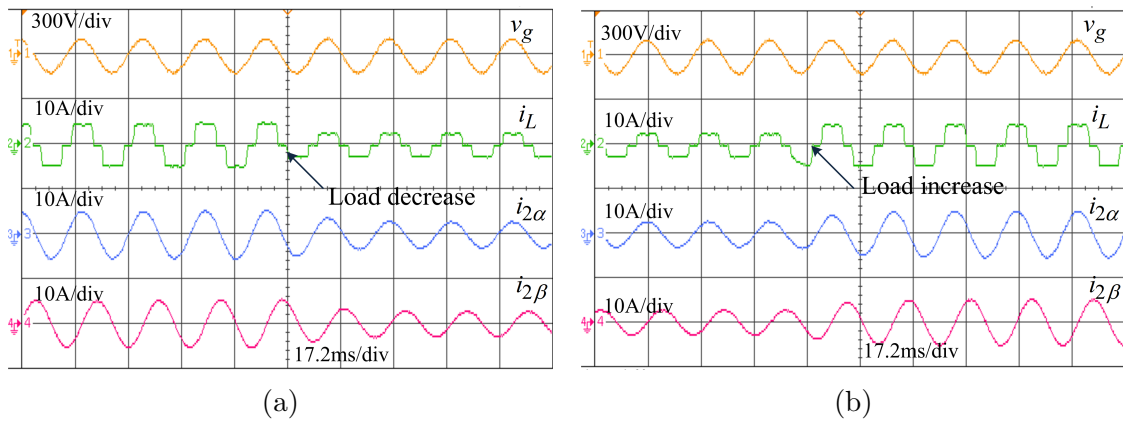


Figure 5.9: Estimation of in-phase and quadrature load component by SOGI for (a) Load decrease (b) Load increase

current is same as load current, when SAPF is switched off. After the application of SAPF, THD of the grid current is reduced to 4.45%. Hence, the power quality

improvement has been achieved as per IEEE Std-519. Figure 5.10(a) shows the dynamic performance of transition from without SAPF to with SAPF single-phase system feeding non-linear load. Initially, the SAPF is not connected to PCC then

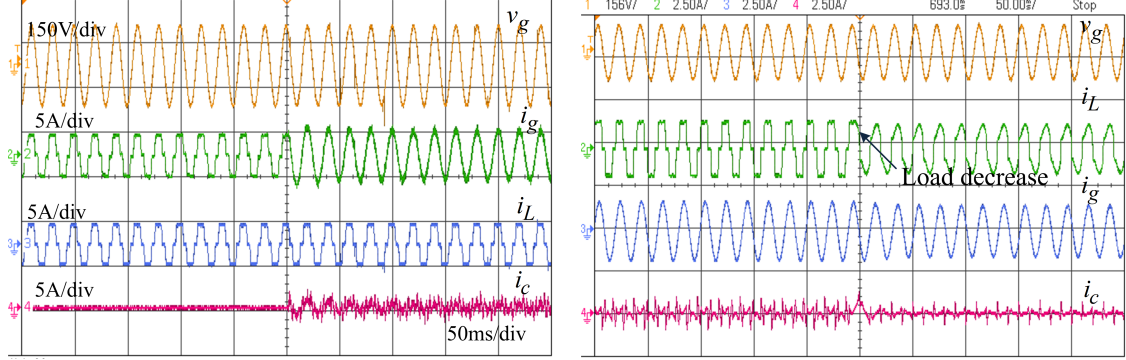


Figure 5.10: Experimental dynamic performance of SOGI control (a) transition of without SAPF to with SAPF (b) load decrease

the grid current has similar waveform as of load current. When the SAPF connected to PCC and starts working then the grid-current becomes sinusoidal. Figure 5.10(b) shows the experimental dynamic performance for the load decrease. As the load demand decreases the grid current also decreases and the grid current remains sinusoidal due to SAPF action.

The closed-loop experimental results have been shown in Fig. 5.11. Figure 5.11(a) shows the grid voltage and load current and THD of the load current is shown in Fig. 5.11(b). Before apply the SAPF the waveform of grid current will be same as load current and its THD value is 27.3%. After applying the SAPF the THD improves to 4.8% as shown in Fig. 5.11(d) and the respective waveform is shown in Fig. 5.11(c). Simulation and experimental performance of SOGI control algorithm with unit template synchronization has been summarized in Table 5.1.

Table 5.1: Performance of SOGI control with unit template synchronization under normal grid condition

Parameters	Simulation results	Experimental results
THD of $i_L$	37.28%	27.3%
THD of $i_g$	4.45%	4.8%
THD of $v_g$	2.0%	0.6%

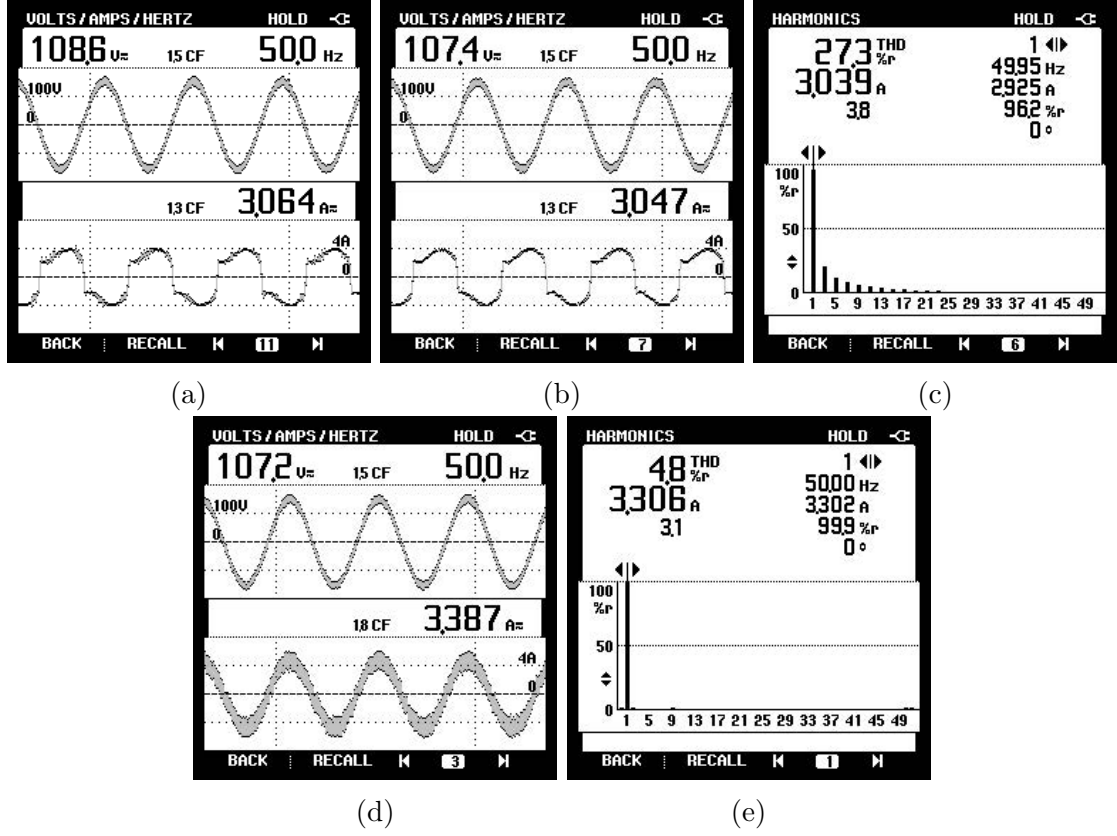


Figure 5.11: Steady-state experimental performance (a)  $v_g$  and  $i_L$  (b) THD of  $i_L$  (c)  $v_g$  and  $i_g$  (d) THD of  $i_g$

### 5.1.2 Cascaded SOGI with Unit-template Synchronization

Input of the single-stage SOGI is non-linear load current and its outputs are filtered in-phase and quadrature-phase current components. However, a single stage SOGI may not provide perfect filtering; specially if the distortion content of the load current is quite high. The cascading of multiple GI blocks has been designed in this and complete analysis has been done. Figure 5.12 demonstrates the block structure of the cascaded SOGI. The fundamental load component of the input current signal

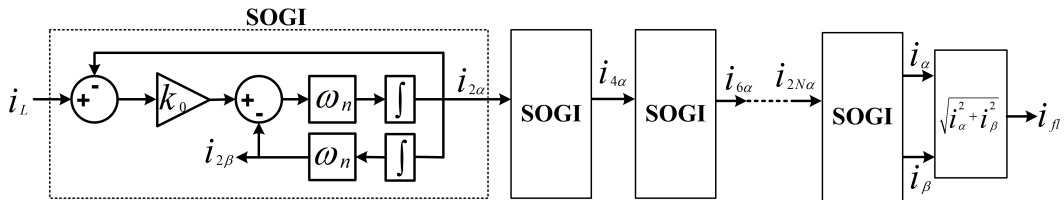


Figure 5.12: Structure of cascaded SOGI



is finally estimated by utilizing outputs of last stage.

The last stage in-phase component ( $i_\alpha$ ) and quadrature component  $i_\beta$  of the load current are utilized to compute the fundamental load current ( $I_f$ ), which is expressed as-

$$I_f = \sqrt{I_\alpha^2 + I_\beta^2} \quad (5.16)$$

The transfer function of the cascaded SOGI is estimated by computing the individual SOGI and multiplying the same for getting higher order filters. Bode-plot of in-phase closed-loop transfer function of the SOGI and higher order GI is shown in Fig. 5.13. It shows the characteristics of band pass filter. It is observed that higher

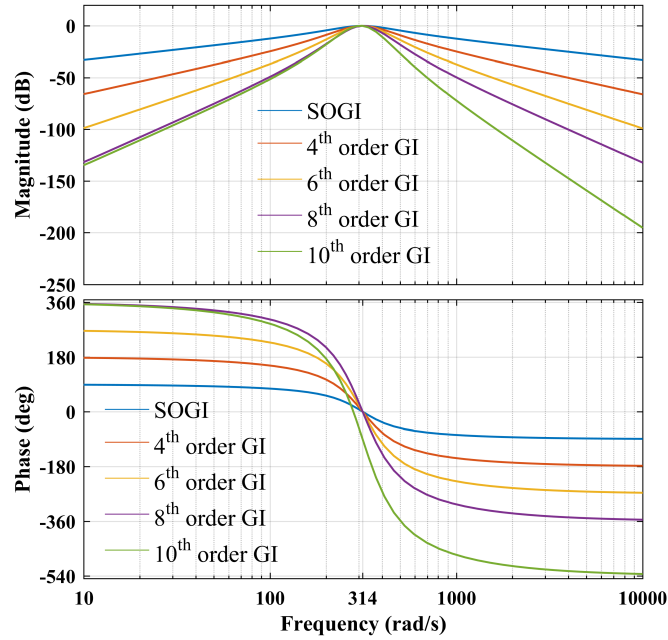


Figure 5.13: Bode plot for cascaded SOGI

the number of SOGI stages, filtering capability improves as shown in magnitude plot. The narrower bode curve indicates effective filtering as compared to flatten curve. No phase-shift has been observed at resonating frequency till 8<sup>th</sup> order. However, a slight phase-shift appears in 10<sup>th</sup> order GI at 50Hz, which is undesirable. Hence, more than eighth order has not been investigated as it will only add to mathematical complexity without providing significant improvement in performance level.

### 5.1.2.1 Simulation Results

Control structure for cascaded SOGI with unit template synchronization is shown in Fig. 5.14 for simulation. The reference current estimation and generation of

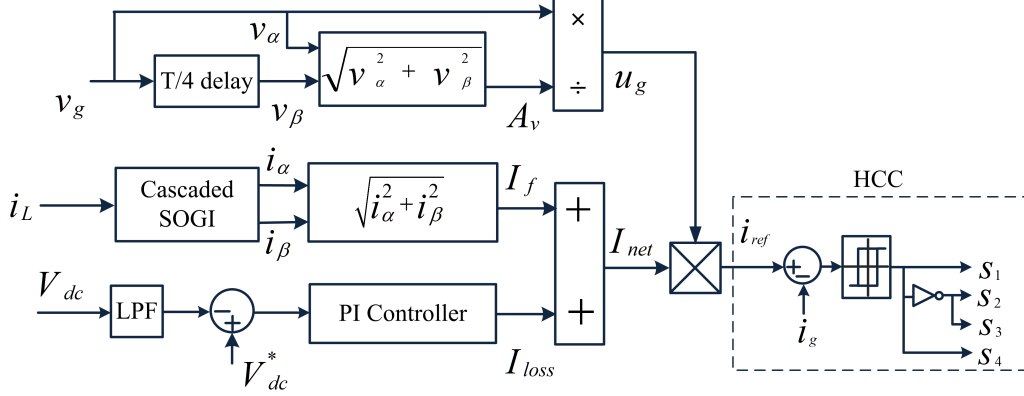


Figure 5.14: Single-phase SAPF control structure for cascaded SOGI and unit template synchronization

switching pulses has been explained in section 5.1.1.1. Here, the fundamental current is estimated by cascaded SOGI. It may be of fourth order GI, sixth order GI or even higher order GI.

The simulation results for cascading effect of SOGI has been shown in Fig. 5.15. It shows the estimation of fundamental current component ( $I_f$ ) and the % THD of

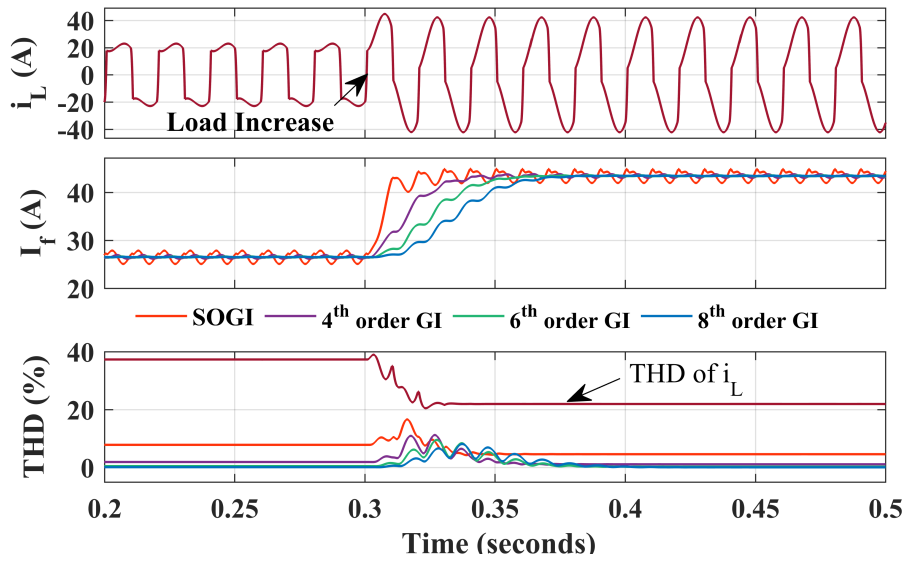


Figure 5.15: Open-loop performance of cascaded SOGI

the in-phase current component ( $i_\alpha$ ) with SOGI and higher order GI. As displayed in Fig. 5.15, the load increase is simulated at  $t=0.3s$  and the response of SOGI is faster but shows high oscillations in steady-state. Higher order GI shows high complexity, larger settling time and very low oscillations in steady-state. THD of the input non-linear load current is 37.28%. The THD of in-phase filtered output signal of SOGI, fourth order GI, sixth order GI and eighth order GI are observed to be 7.831%, 1.909%, 0.482% and 0.125% respectively.

Further, more detailed analysis has been shown in Table 5.2. It highlights the comparison between SOGI and the higher order GI for the steady-state and dynamic response analysis. It is clear that the higher order cascading effect translates into improved filtering capability. The THD of the filtered signal decreases with selecting higher order GI filters. However, there is a corresponding slowing down of dynamic response time as the GI order increases. The rise time increases for higher order cascaded SOGI blocks. Additionally, mathematical complexity is higher if large number of blocks used in cascade. This is also an important criteria when closed loop real time implementation is achieved. If more than three blocks of SOGI are cascaded, there is no appreciable change observed in THD of the filtered in-phase output signal. However, it is observed that the dynamic performance is adversely affected as SOGI order increases, so no further drastic improvement in performance is obtained.

### 5.1.2.2 Experimental Results

The cascaded SOGI with unit template synchronization technique has been implemented on experimental prototype system. The design control algorithm has been tested for power quality improvement under non-linear loading condition. FLUKE made single-phase power analyzer is employed for analyzing the closed-loop steady-state response. Closed-loop experimental results have been taken and shown in Fig. 5.16. Figure 5.16(a) and 5.16(b) show the grid-voltage, load current and THD of the load current. For the SOGI the THD analysis has been in previous section.

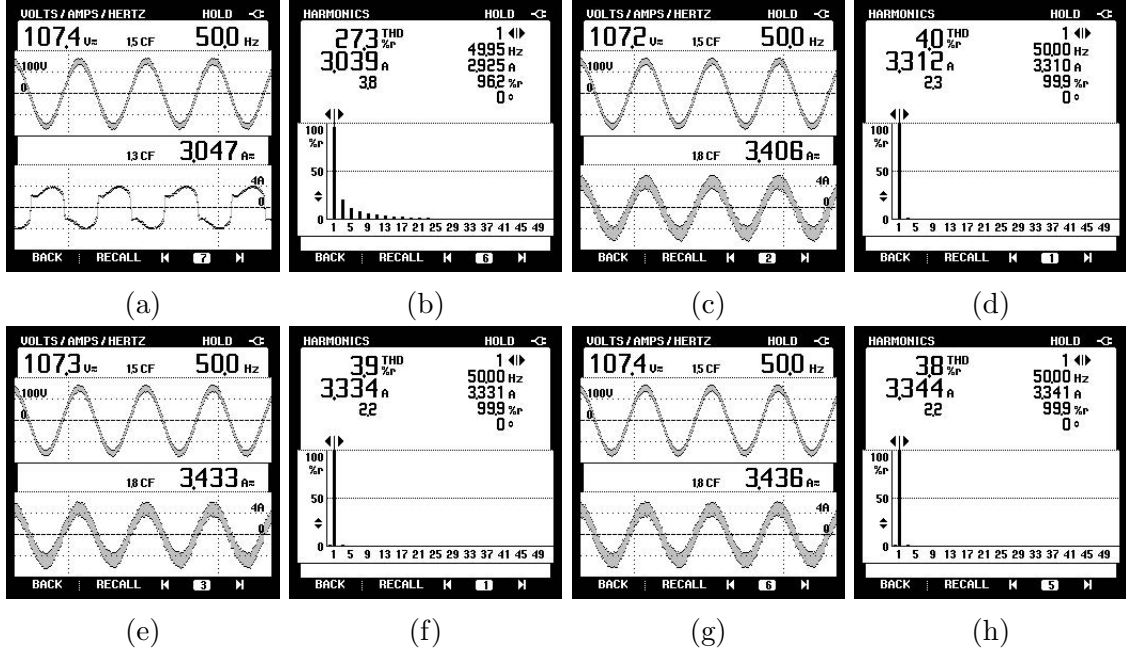


Figure 5.16: Experimental closed-loop steady-state performance under cascaded SOGI with unit template synchronization (a)  $v_g$  and  $i_L$  (b) THD of  $i_L$ , 27.3% (c)  $v_g$ ,  $i_g$  for 4<sup>th</sup> order GI (d) THD of  $i_g$  for 4<sup>th</sup> order GI, 4.0% (e)  $v_g$ ,  $i_g$  for 6<sup>th</sup> order GI (f) THD of  $i_g$  for 6<sup>th</sup> order GI, 3.9% (g)  $v_g$ ,  $i_g$  for 8<sup>th</sup> order GI (h) THD of  $i_g$  for 8<sup>th</sup> order GI , 3.8%

For 4<sup>th</sup> order GI, THD of the grid current obtained is 4.0%, which are shown in Fig. 5.16(c) and 5.16(d). For 6<sup>th</sup> order GI, THD of the grid current obtained is 3.9%, which are shown in Fig. 5.16(e) and 5.16(f). For 8<sup>th</sup> order GI, THD of the grid current obtained is 3.8%, which are shown in Fig. 5.16(g) and 5.16(h).

Table 5.2: Performance summary of SOGI and cascaded SOGI control

		SOGI	4 <sup>th</sup> order GI	6 <sup>th</sup> order GI	8 <sup>th</sup> order GI
<b>Simulation</b>	Rise time (ms)	6.79	24.79	33.28	40.49
	$I_f$ (peak to peak)	2.788	0.757	0.202	0.054
	THD of $i_\alpha$ (%)	7.831	1.909	0.482	0.125
<b>Experimental</b>	THD of $i_g$	4.8%	4%	3.9%	3.8%

These experimental results show SOGI as well as GIs of 4<sup>th</sup>, 6<sup>th</sup>, and 8<sup>th</sup> order meet the grid current harmonic distortion standards. GIs of 4<sup>th</sup> and 6<sup>th</sup> order are quite effective in improving the PQ but GI of order 8<sup>th</sup> and above do not really improve the performance significantly. In fact, higher order GI involve greater complexity and

slow the dynamic response. The simulation and experimental results follow similar pattern. Cascading of three SOGI gives the optimum result as analyzed from the simulation and experimental performance and is summarized in Table 5.2.

## 5.2 Single-Phase SAPF under Polluted Grid Condition

In Section 5.1, Single-phase SAPF under linear/non-linear load and normal grid voltage condition has been explained. In this section, single-phase SAPF under linear/non-linear load and polluted grid voltage condition has been explained. Power quality improvement under polluted grid condition requires advanced synchronization techniques which estimate distortion free synchronizing templates.

### 5.2.1 SOGI Control with Adaptive-ZCD Synchronization Technique

SOGI is a simple and effective algorithm to estimate the fundamental component of the load current ( $I_f$ ) and is explained in Section 5.1.1. Adaptive-ZCD method has been designed to achieve the unit synchronizing signal ( $u_g$ ) under polluted grid condition which is explained in Section 4.1.6. A-ZCD estimates synchronizing signal having almost 0% THD under polluted grid condition. Performance of A-ZCD does not depend on the level of distortion and the voltage level.

#### 5.2.1.1 Estimation of Reference Current and Switching Signals

Once the fundamental load component and the grid synchronizing signals are generated the switching loss needs to be estimated to compute the net current. The output of the PI regulator to regulate the DC-link voltage can be considered as the loss component and it can be estimated by 5.17.

$$I_{loss}(n) = I_{loss}(n-1) + k_p[V_{dce}(n) - V_{dce}(n-1)] + k_i V_{dce}(n) \quad (5.17)$$

Here,  $V_{dce}(n) = V_{dc}^*(n) - V_{dc}(n)$  is the evaluated voltage error at DC-link inverter,  $k_p$  and  $k_i$  are the proportional and integral gains of the PI controller.

The grid reference current ( $i_{ref}$ ) is generated by the multiplying the synchronizing

signal ( $u_g$ ) and the net current ( $I_{net}$ ) for compensation and expressed by 5.18.

$$i_{ref} = I_{net}u_g = (I_f + I_{loss})u_g \quad (5.18)$$

Hysteresis current controller (HCC) is used for its simplicity and robust working for generation of switching signals. accordingly. The complete control structure is presented in Fig. 5.17.

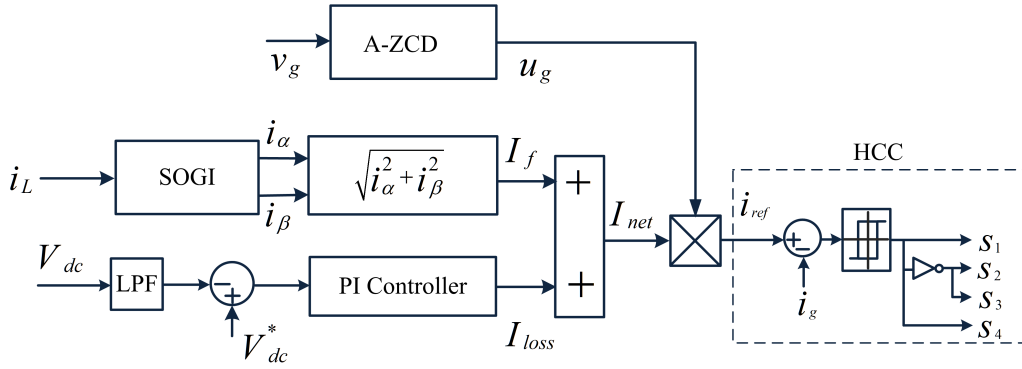


Figure 5.17: Single-phase SAPF control structure under polluted grid condition

### 5.2.1.2 Simulation Results

System configuration to test the proposed algorithm has been shown in Fig. 5.1. The proposed algorithm has been tested under both normal and polluted grid condition and the non-linear load has been connected to PCC. Simulation performance of the SOGI control algorithm with the A-ZCD based grid synchronization technique has been shown in Fig. 5.18, 5.19 and 5.20.

In Fig. 5.18, polluted grid voltage (THD 14.2%) has been considered for feeding the non-linear load and the grid becomes normal at  $t=0.4s$ . Initially, unit template synchronization has been applied till  $t=0.15s$  for the SAPF but it doesn't improved much the quality of the grid current (THD 11.50%). The AZCD based synchronization has been applied at  $t=0.15s$  and it improves the quality of the grid power (THD 4.26%). The load has been increased at  $t=0.3s$  and DC-link remains stable during the load change. The proposed AZCD based has also been tested under standard grid condition ( $t=0.4s$  to  $t=0.5s$ ) and it improve the quality of grid power.

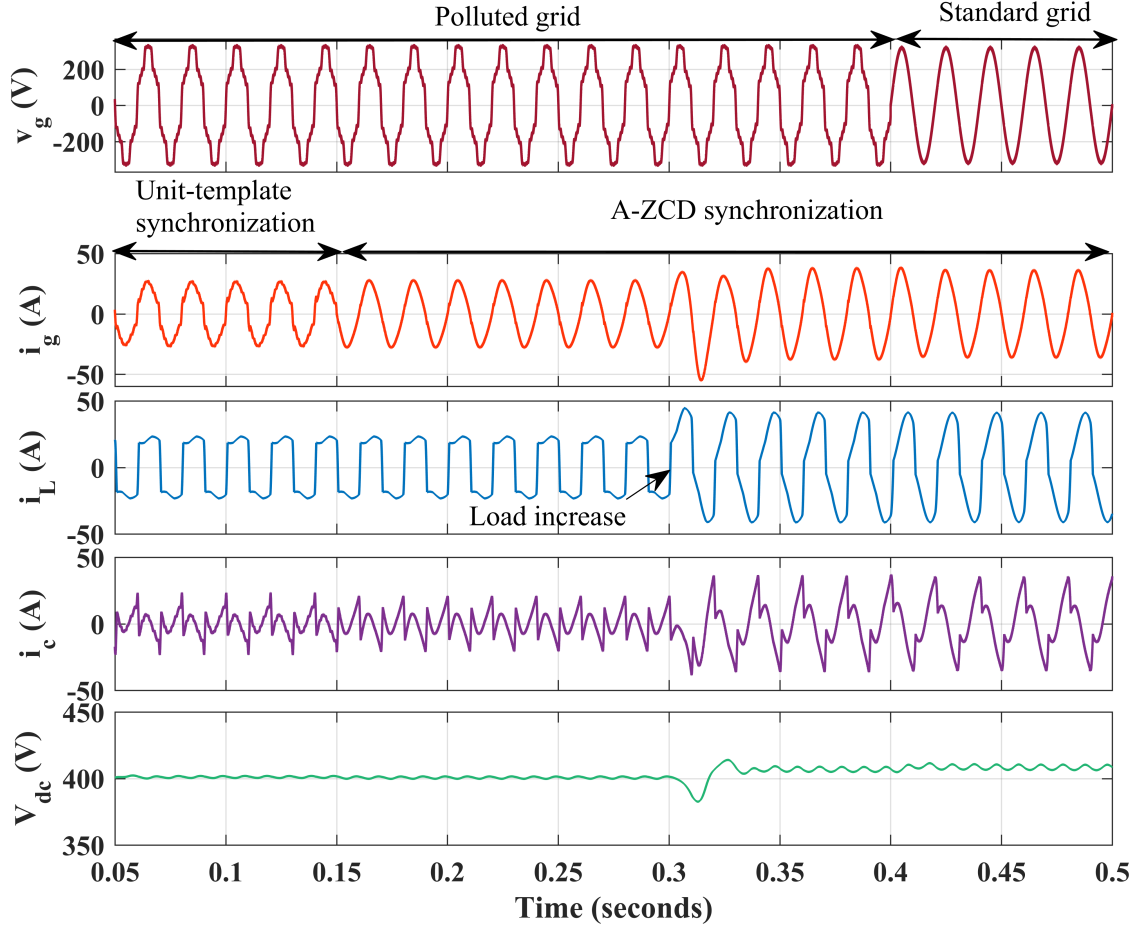


Figure 5.18: Simulation performance of single-phase SAPF with SOGI control and A-ZCD synchronization

Measurement of powers for SAPF has been shown in Fig. 5.18. During the SAPF operation with SOGI and AZCD synchronization the reactive power demanded by the load is supplied by the single-phase VSC. At  $t=0.2s$ , active power and reactive power demanded by the load is 4182W and 1145Var. The active power of 4340W is supplied by the grid and reactive power of 1176Var is supplied by the single-phase VSC.

THD analysis of different system parameters has been shown in Fig. 5.20. Figure 5.20(a) and 5.20(b) shows the THD of the polluted grid and the THD of the non-linear load current and its values are 14.20% and 38.50 respectively. Figure 5.20(c) shows the THD of the grid current (11.50%) and it is achieved by unit-template grid synchronization and it doesn't follow IEEE Std.519. Hence, unit-template method



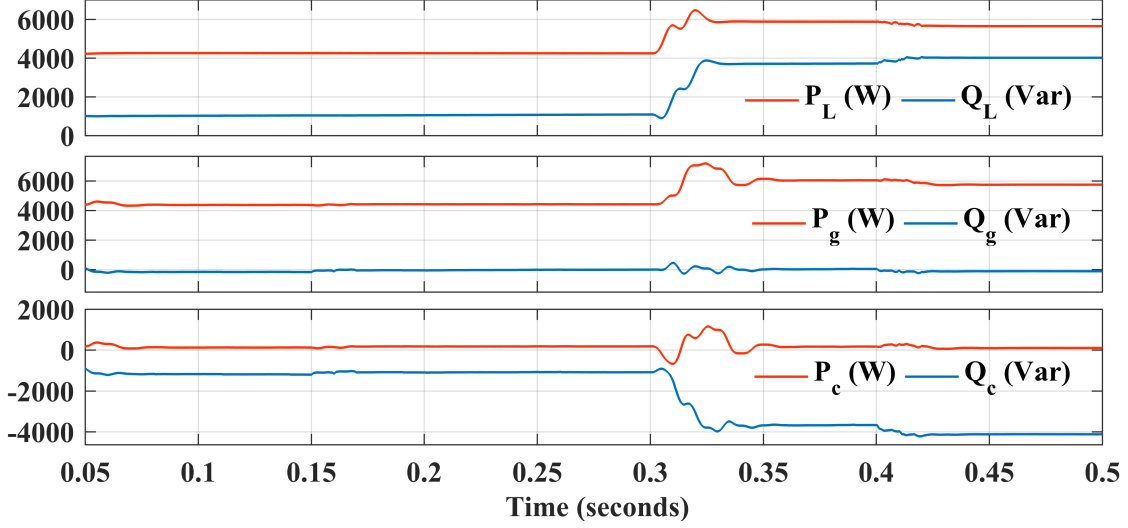


Figure 5.19: Simulation performance for power of single-phase SAPF with SOGI control and A-ZCD synchronization

can not be used for power quality improvement under distorted grid condition. Figure 5.20(d) shows the THD of the grid current under AZCD grid synchronization and it is observed to be 4.26% which follows IEEE Std. 519. Hence, the simulation performance shows that the proposed algorithm achieves both the reactive power compensation and power quality improvement.

### 5.2.1.3 Experimental Results

The proposed AZCD synchronization technique with the SOGI control has been tested on the experimental prototype developed in the laboratory. It is tested under both normal and polluted grid condition feeding non-linear load. Single-phase programmable supply has been used to generate polluted voltage supply. Figure 5.21, shows the steady-state results under normal grid voltage condition. Figure 5.21(a) and 5.21(b) shows the grid voltage, load current and THD of the load current (27.5%). THD of the grid voltage is 0.6% which is shown in Fig. 5.21(c). After applying the SAPF, the THD of the grid current is reduced to 4.3% as shown in Fig. 5.21(e) and the waveform is shown in Figure 5.21(d).

Figure 5.22 shows the performance of SAPF under polluted grid voltage condition and the AZCD based synchronization technique. Figure 5.22(a) and 5.22(b) shows

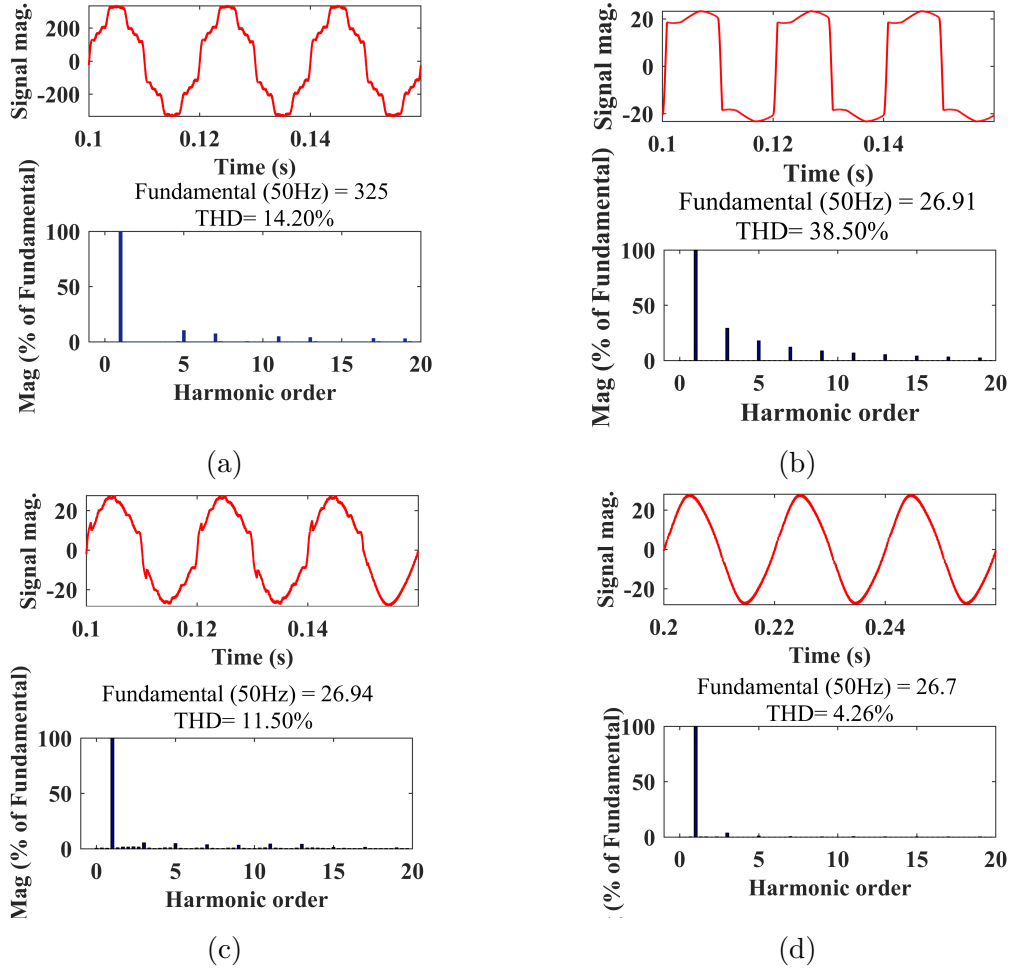


Figure 5.20: THD analysis for SAPF with SOGI and AZCD synchronization under normal and polluted grid (a) THD of polluted grid ( $v_g$ ) (b) THD of  $i_L$  (c) THD of  $i_g$  with unit template synchronization (d) THD of  $i_g$  under AZCD synchronization

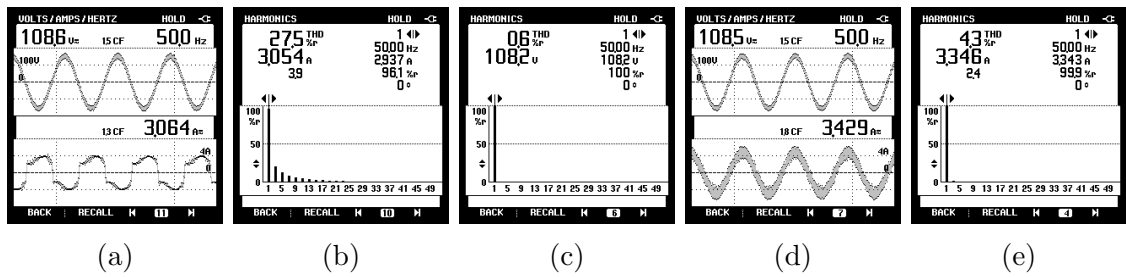


Figure 5.21: Steady-state results for SAPF with SOGI control and AZCD synchronization under normal grid (a)  $v_g$  and  $i_L$  (b) load current THD (c) grid voltage THD (d)  $v_g$  and  $i_g$  (e) grid current THD

the grid voltage, load current and THD of the load current (29.8%). THD of the grid voltage is 9.1% which is shown in Fig. 5.22(c). After applying the SAPF, the THD of the grid current is reduced to 4.4% as shown in Fig. 5.22(e) and the waveform is

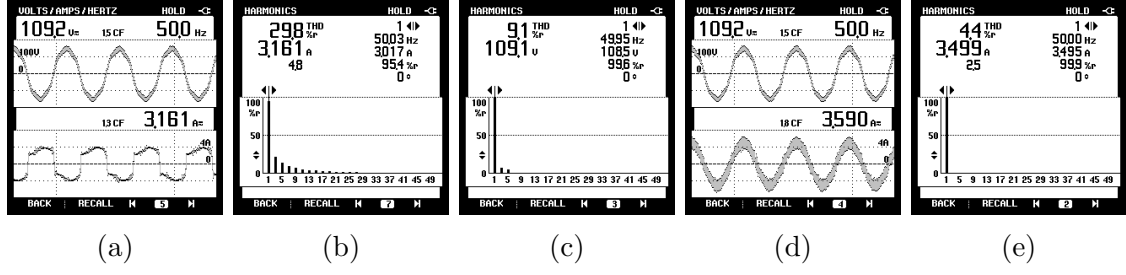


Figure 5.22: Steady-state results for SAPF with SOGI control and AZCD synchronization under polluted grid (a)  $v_g$  and  $i_L$  (b) load current THD (c) grid voltage THD (d)  $v_g$  and  $i_g$  (e) grid current THD

shown in Fig. 5.22(d).

Table 5.3: Performance summary of SOGI with AZCD synchronization under normal and polluted grid

	Normal grid			Polluted grid		
	$v_g$	$i_L$	$i_g$	$v_g$	$i_L$	$i_g$
<b>Simulation THD %</b>	2.01%	38.5%	4.27%	14.20%	38.5%	4.26%
<b>Experimental THD %</b>	0.6%	27.5%	4.3%	9.1%	29.8%	4.4%

Performance of SOGI control algorithm with the AZCD synchronization has been summarized in Table 5.3.

### 5.2.2 SOGI-ROGI for Control and Synchronization

Reactive power compensation and the power quality improvement require the algorithms to estimate the synchronization techniques and to estimate the fundamental component of the load current. Estimation of voltage parameters along with the synchronization signal ( $u_g$ ) by SOGI-FLL-ROGI has been explained in Section 4.1.5. Estimation of fundamental component by combination of SOGI and ROGI has been explained here. The block diagram representation for calculating the fundamental component of the load current is shown in Fig. 5.23. In Fig. 5.23,  $i_L$  denotes the in-

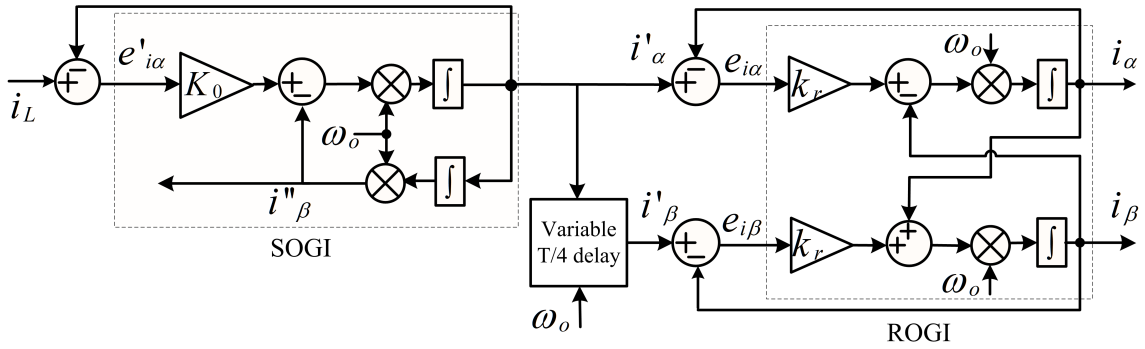


Figure 5.23: Structure of SOGI-ROGI for fundamental current component estimation

put signal and  $(i'_{\alpha}, i''_{\beta})$  are the filtered outputs of SOGI.  $(i_{\alpha}, i_{\beta})$  are the final outputs obtained after the cascaded operation for SOGI and ROGI technique.  $\omega_o$  is the estimated frequency obtained from grid-voltage by SOGI-FLL. The proposed algorithm has also the capability of removing DC-offset along with removing harmonics and find out ripple free fundamental load component.  $k_0$  and  $k_r$  are the gains of SOGI and ROGI respectively. Open-loop transfer function of SOGI is given as-

$$SOGI(s) = \frac{k_o \omega_o s}{s^2 + \omega_o^2} \quad (5.19)$$

The closed-loop transfer functions of  $(i'_{\alpha}, i''_{\beta})$  of the SOGI block considering error signal ( $e'_{i\alpha}$ ) are given as in 5.20 and 5.21.

$$\frac{i'_{\alpha}(s)}{i_L(s)} = \frac{k_o \omega_o s}{s^2 + k_o \omega_o s + \omega_o^2} \quad (5.20)$$

$$\frac{i''_{\beta}(s)}{i_L(s)} = \frac{k_o \omega_o^2}{s^2 + k_o \omega_o s + \omega_o^2} \quad (5.21)$$

As discussed in [95], ROGI is an algorithm with single complex pole. The transfer function of ROGI is represented as-

$$\frac{i_{\alpha,\beta}(s)}{e_{i\alpha,i\beta}(s)} = \frac{k_r}{s - j\omega_o} \quad (5.22)$$

where,  $e_{i\alpha,i\beta} = i'_{\alpha\beta} - i_{\alpha\beta}$  is the error signal for the ROGI. Now, the closed-loop transfer function with the ROGI for in-phase and quadrature signal is given as in equations (5.23)-(5.25).

$$\frac{i_{\alpha}(s)}{i'_{\alpha}(s)} = \frac{i_{\beta}(s)}{i'_{\beta}(s)} = \frac{k_r \omega_o s}{s^2 + 2k_r \omega_o s + (1 + k_r^2) \omega_o^2} \quad (5.23)$$

$$Q(s) = \frac{i_{\beta}(s)}{i_L(s)} = \frac{k_0 k_r \omega_o^2 (2\omega_o s + k_0 \omega_o^2)}{s^4 + (k_o + 2k_r) \omega_o s^3 + (2 + 2k_o k_r + k_r^2) \omega_o^3 s^2 + (1 + k_r^2) \omega_o^4} \quad (5.24)$$

$$D(s) = \frac{i_{\alpha}(s)}{i_L(s)} = \frac{k_0 k_r \omega_o^2 (s^2 + k_r \omega_o s - \omega_o^2)}{s^4 + (k_o + 2k_r) \omega_o s^3 + (2 + 2k_o k_r + k_r^2) \omega_o^3 s^2 + (1 + k_r^2) \omega_o^4} \quad (5.25)$$

A variable time-delay block has been used to generate the perfect quadrature signal from the DC-offset free signal of the SOGI. Hence, no DC-offset in input of the ROGI block. The algorithm generates perfect sinusoidal in-phase and quadrature phase signal of the load current. The gain values of SOGI -ROGI has already discussed in Section 4.1.5 and its values have been selected as  $k_o = 1.414$  and  $k_r = 1.414$ . The magnitude of the fundamental load current is estimated as-

$$I_f = \sqrt{i_{\alpha}^2 + i_{\beta}^2} \quad (5.26)$$

#### 5.2.2.1 Estimation of Reference Current and Switching Signals

There are some switching losses in the VSC and this switching loss is estimated in the form of  $I_{loss}$  using the equation 5.27. It is estimated by calculating the DC-link voltage error ( $V_{dce}(n)$ ) and regulating it to zero using a PI controller. The DC link voltage error ( $V_{dce}(n)$ ) is calculated by subtracting sensed DC-link voltage

to reference DC-link voltage. As  $V_{dce}(n) = V_{dc}^*(n) - V_{dc}(n)$ , where  $V_{dc}^*(n)$  is the reference DC-link Voltage and  $V_{dc}(n)$  is the measured DC link voltage nth instant. The output of the Proportional-Integral controller is given as 5.27.

$$I_{loss}(n) = I_{loss}(n-1) + k_p\{V_{dce}(n) - V_{dce}(n-1)\} + k_i V_{dce}(n) \quad (5.27)$$

where  $k_p$  and  $k_i$  denote the proportional and integral gains of the PI controller. The gains are appropriately selected to obtain a good steady-state and dynamic response. After calculating the synchronization signal ( $u_g$ ), fundamental load current component ( $I_f$ ) and the DC loss component ( $I_{loss}$ ), the reference current ( $i_{ref}$ ) can be estimated. The reference grid current is estimated by multiplying the synchronizing signal to the estimated net current. The net current ( $I_{net}$ ) has been calculated by adding the fundamental load current component ( $I_f$ ) and the loss component ( $I_{loss}$ ) as given in 5.28.

$$I_{net} = I_f + I_{loss} \quad (5.28)$$

The reference current is estimated using 5.29,

$$i_{ref} = I_{net}u_g \quad (5.29)$$

The hysteresis current controller (HCC) generates the switching pulses. The input of the HCC is the error signal, which is computed by subtracting the sensed and the reference supply currents.

#### 5.2.2.2 Simulation Results

The complete block diagram representation of the proposed controller for the single-phase system is shown in Fig. 5.25. Synchronizing signal has been estimated by the SOGI-FLL-ROGI and the fundamental component has been estimated by the SOGI-ROGI block. PI controller has been used for regulating the DC-link voltage.

Open-loop simulation performance has been shown in Fig. 5.25(a) and the comparison with ROGI, SOGI-FLL and SOGI -ROGI has been shown in Fig. 5.25(b).

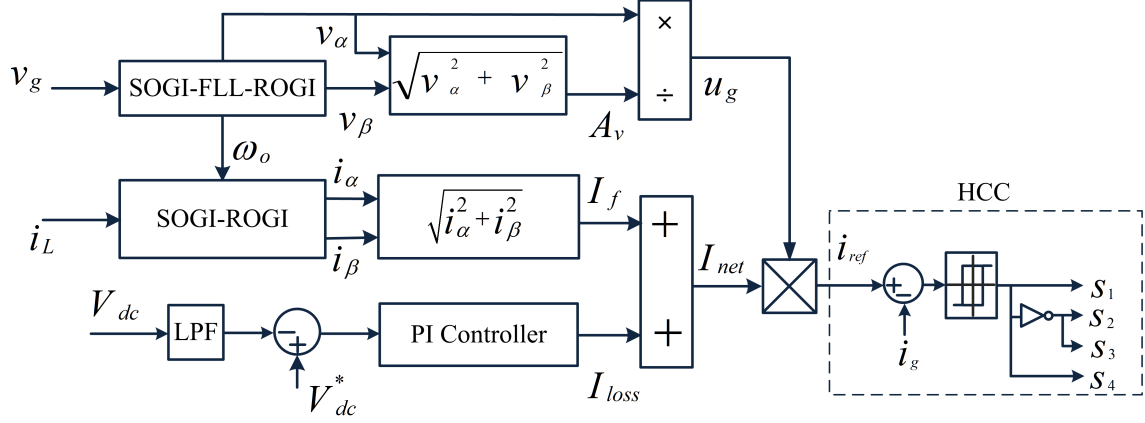


Figure 5.24: Control structure for single-phase SAPF for SOGI-ROGI

In-phase load component extracted by SOGI-ROGI algorithm shows very low distort-

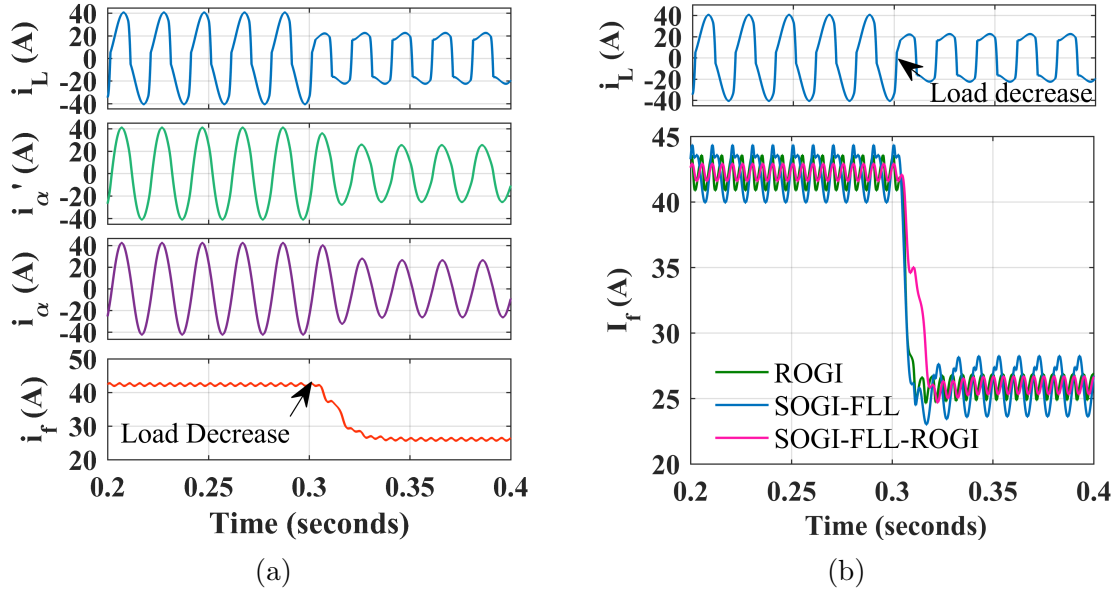


Figure 5.25: Simulation results (a) SOGI-ROGI performance (b) Comparison of ROGI, SOGI and SOGI-ROGI

tion. Load has been decreased at  $t=0.3$ s, accordingly the fundamental component has been changed from 42A to 26A. Figure 5.25(b) shows the comparison performance of ROGI, SOGI-FLL and SOGI-ROGI. The convergence time is 11.54ms, 12.43ms and 17.78ms taken by ROGI, SOGI-FLL and SOGI-ROGI respectively i.e. convergence is achieved by SOGI-ROGI technique is within 1 cycle. Ripple in the estimated fundamental component observed to be 2.73A, 4.43A and 1.3A by ROGI, SOGI-FLL and SOGI-ROGI respectively. Hence, the SOGI-ROGI algorithm gives

very low ripple and it gives better performance in steady-state.

Now, the proposed SOGI-ROGI algorithm has been used for the harmonic mitigation and the reactive power compensation. Closed-loop simulation results have been shown in Fig. 5.26-5.28. Figure 5.26 shows the waveform for grid voltage ( $v_g$ ), grid current ( $i_g$ ), load current ( $i_L$ ), compensator current ( $i_c$ ) and DC-link voltage ( $V_{dc}$ ) respectively. SAPF has been tested under both ideal grid and polluted grid voltage under non-linear load current.

The proposed SOGI-ROGI algorithm has been tested under both normal grid and

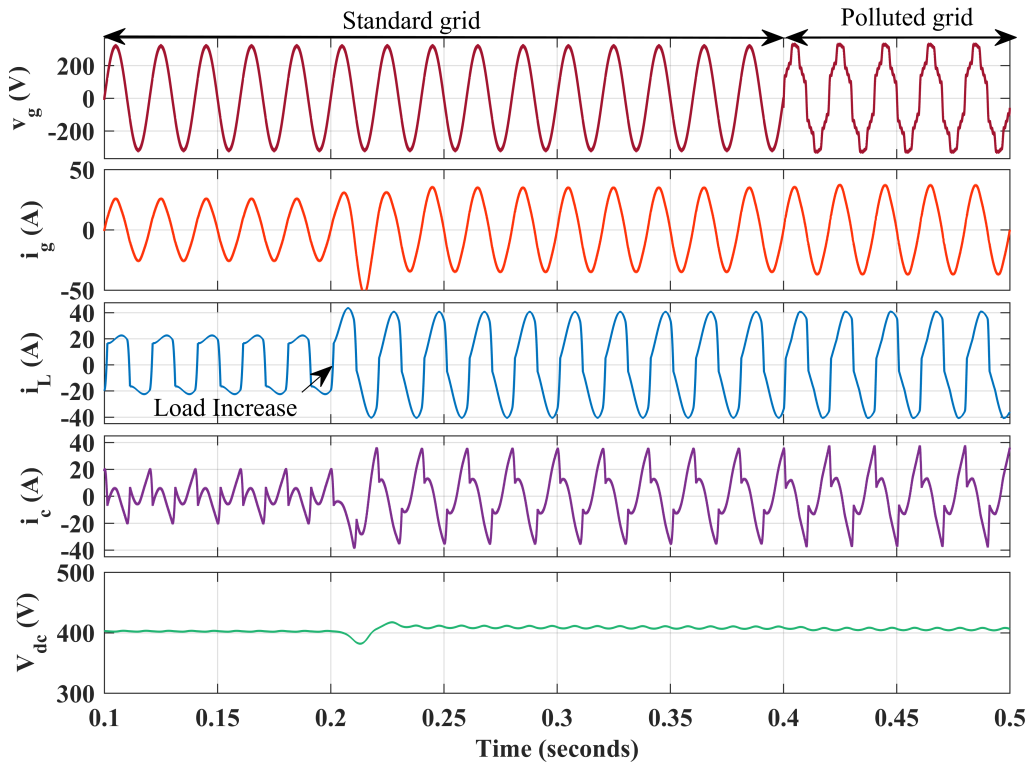


Figure 5.26: Simulation performance of single-phase SAPF with SOGI-ROGI control and SOGI-FLL-ROGI synchronization

under polluted grid voltage conditions which feed non-linear load. Initially the grid voltage is normal and at  $t=0.4s$  it is polluted with harmonics (THD 14.33%). The proposed technique works as per standard in both the case. Load has been increased at  $t=0.2s$ , and the DC-link settles to reference value of 400V after a small deviation from the DC-link voltage. Here, under all the cases the SOGI-ROGI algorithm improved the quality of grid-current.



Figure 5.27 shows the variation of complex power at load, grid and compensator. The load demand measured at  $t=0.1s$  is 3932W, 1504Var and the active power sup-

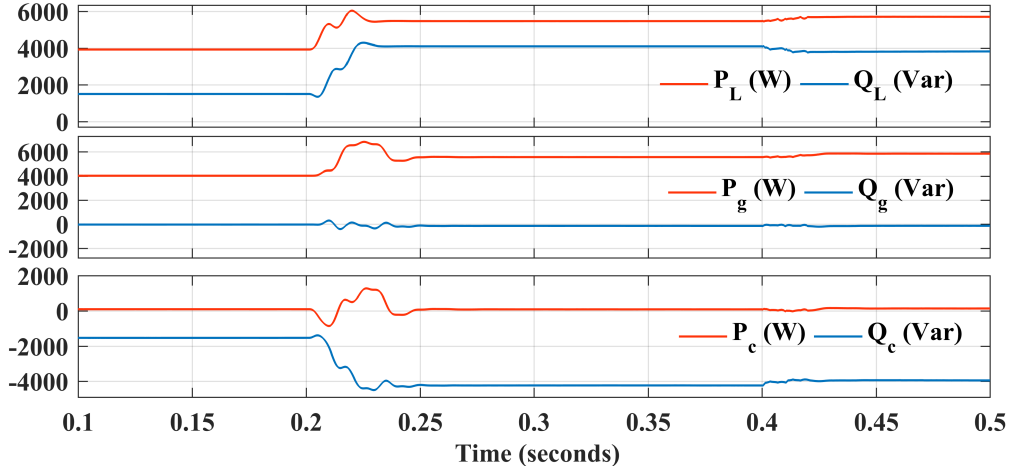


Figure 5.27: Simulation performance for power of single-phase SAPF with SOGI-ROGI control and SOGI-FLL-ROGI synchronization

plied by the grid is 4037W and the reactive power compensated by the compensator is 1528Var. Linear load is added at the PCC and the new load demand measured at  $t=0.3s$  is 5469W, 4106Var. Here, also the active power is of 5560W supplied by the grid and the reactive power of 4130Var is compensated by the SAPF.

THD analysis of the different grid parameters has been performed under both normal grid and the polluted grid and the obtained results are shown in Fig. 5.28. In case I, under normal grid condition, THD of the grid voltage is 2.00% and the THD of the load current is 32.95%. After the power quality improvement THD of the grid current is only 3.74% which follows IEEE Std-519. In case II, under polluted grid condition THD of the grid voltage is 14.33% which contains 5<sup>th</sup>, 7<sup>th</sup>, 11<sup>th</sup> and some higher order harmonics. THD of the load current is 22.12% and after SAPF operation THD of the grid current achieved is 3.28%.

After detailed simulation analysis, it is observed that the SOGI-ROGI control algorithm can be used for the power quality improvement under different grid voltage and loading conditions. The experimental results are discussed next.

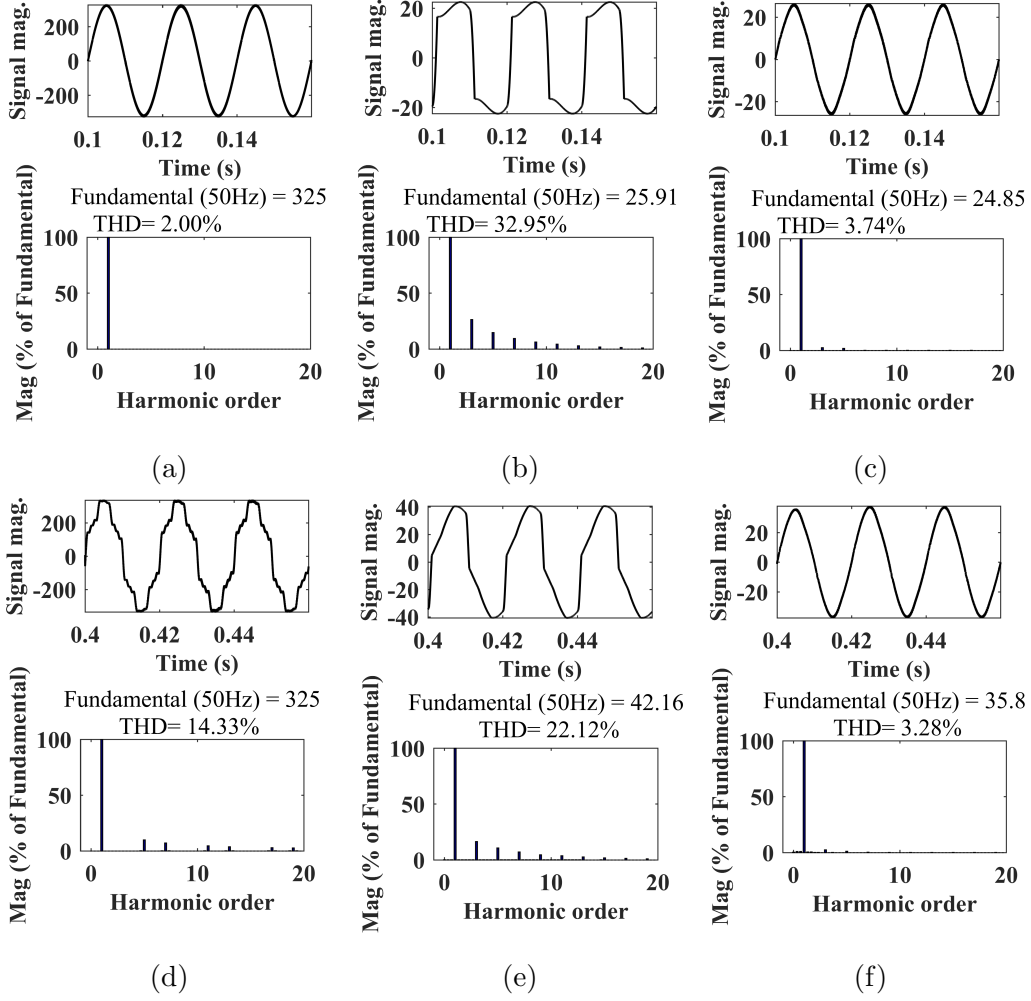


Figure 5.28: THD analysis for SAPF with SOGI-ROGI and SOGI-FLL-ROGI synchronization, Case I: Standard/Normal grid (a) THD of  $v_g$  (b) THD of  $i_L$  (c) THD of  $i_g$   
Case II: Polluted grid (d) THD of polluted grid ( $v_g$ ) (e) THD of  $i_L$  (f) THD of  $i_g$

### 5.2.2.3 Experimental Results

Experimental configuration for single-phase system with non-linear load has been shown in Figure 5.2. Figure 5.29 shows the open loop experimental results for fundamental load compensation by SOGI-ROGI and the comparison of with ROGI and SOGI-FLL under load change condition. Figure 5.29(a) shows the filtered response of SOGI-FLL and the SOGI-ROGI and the fundamental component of load current estimated by the SOGI-ROGI. The waveform of  $i_\alpha$  is more to sinusoidal than  $i'_\alpha$ . Figure 5.29(b) and 5.29(c) shows the dynamic performance of ROGI, SOGI-FLL and SOGI-ROGI. The fundamental ( $I_f$ ) estimated by proposed having almost no

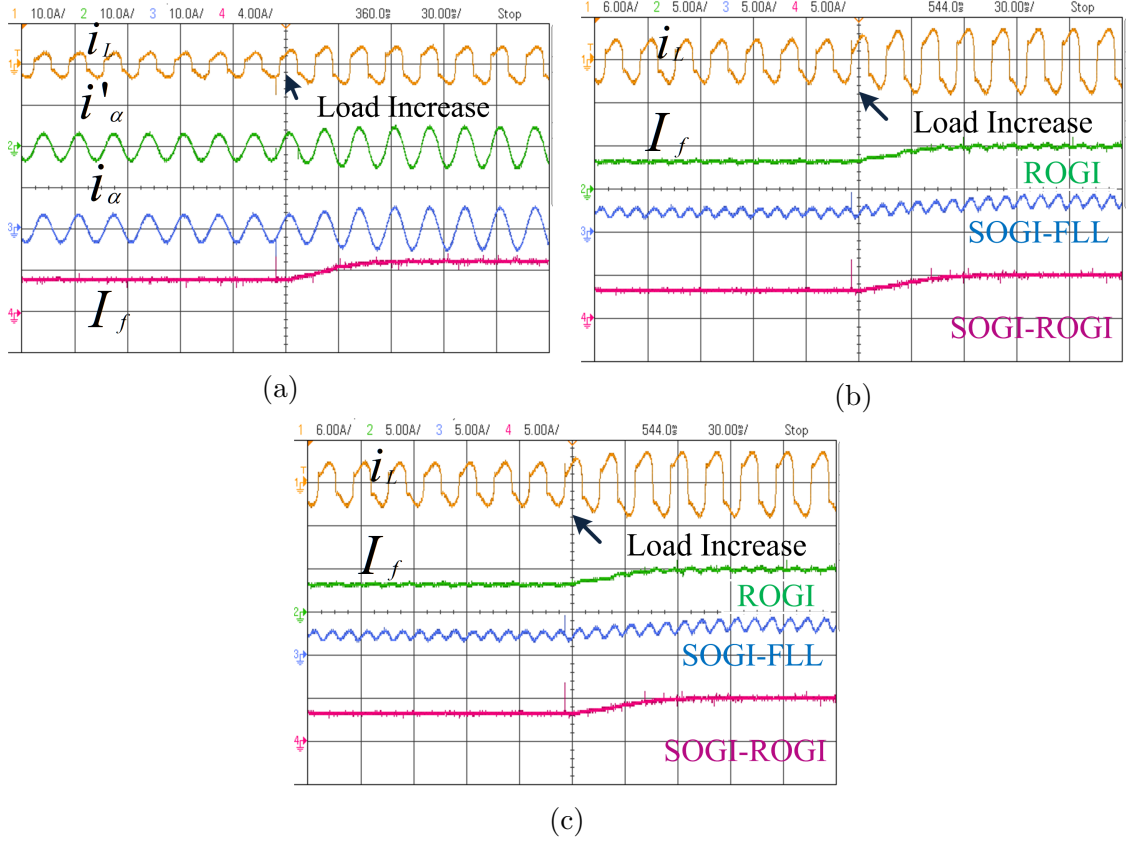


Figure 5.29: Experimental results for fundamental load component and intermediates (a) Load increase ( $i_L$ ,  $i'_\alpha$ ,  $i_\alpha$ ,  $I_f$ ) (b) Load increase ( $i_L$ ,  $I_f$  by ROGI, SOGI-FLL and SOGI-FLL-ROGI) (C) Load decrease ( $i_L$ ,  $I_f$  by ROGI, SOGI-FLL and SOGI-FLL-ROGI)

ripples while ROGI and SOGI-FLL under non-linear load conditions. Also, it shows the convergence is little slower than ROGI and SOGI-FLL but it converges within 1 cycle.

Figure 5.30 shows the closed-loop steady-state performance of the SOGI-ROGI control algorithm. A non-linear variable load has been connected to the system for conducting experiments. These test have been performed under two cases. In the first case, the undistorted supply is considered and in the second case; the grid supply had a distortion level of 10%. The algorithm is designed for achieving active compensation under both conditions. The inverter is controlled to work as a single-phase shunt compensator and mitigate several power quality issues as well. A non-linear load has been connected to the system in both cases so that load current is non-sinusoidal. Perfect sinusoidal synchronization signals obtained using the

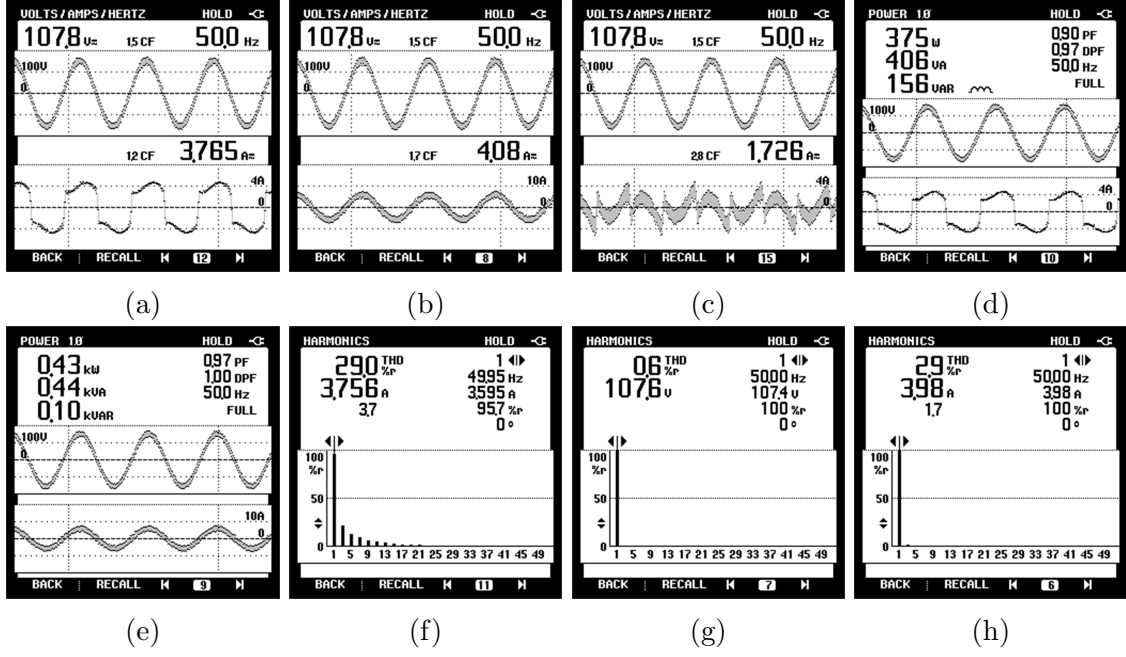


Figure 5.30: Steady-state experimental performance of single-phase SAPF with non-linear load and normal grid condition by SOGI-FLL-ROGI algorithm (a)  $v_g$  and  $i_L$  (b)  $v_g$  and  $i_g$  (c)  $v_g$  and  $i_c$  (d) load power (e) grid power (f) load current THD (g) grid voltage THD (h) grid current THD

proposed SOGI-ROGI algorithm and it helps generate sinusoidal reference supply currents. Using the indirect current controller designed in Fig. 5.24 achieves reactive power compensation and harmonic reduction in supply current. Results obtained with SOGI-ROGI are first discussed.

Figure 5.30(a-c) shows the waveform of  $i_g, i_L, i_c$  respectively with undistorted grid voltage ( $v_g$ ). It is observed that, when no harmonics are injected in the grid voltage (110V, 50Hz), the THD of the grid voltage is only 0.6% as observed in Fig. 5.30(g). Load power demand and grid power are shown in Fig. 5.30(d) and 5.30(e) respectively. The load power demand is 375W and 156Var and the grid power is 430W and 100Var. The displacement power factor (DPF) of the grid has improved to 1.00, while the DPF of the load is 0.97. The load currents have a high THD of 29.0%, which is reduced to 2.9% with active compensation using the proposed controller.

Figure 5.31 shows the waveform of  $i_g, i_L, i_c$  respectively under distorted grid voltage. The tests are performed under distorted grid conditions when the grid voltage has THD of 9.8% as shown in Fig. 5.31(g). The load current has a distortion level of

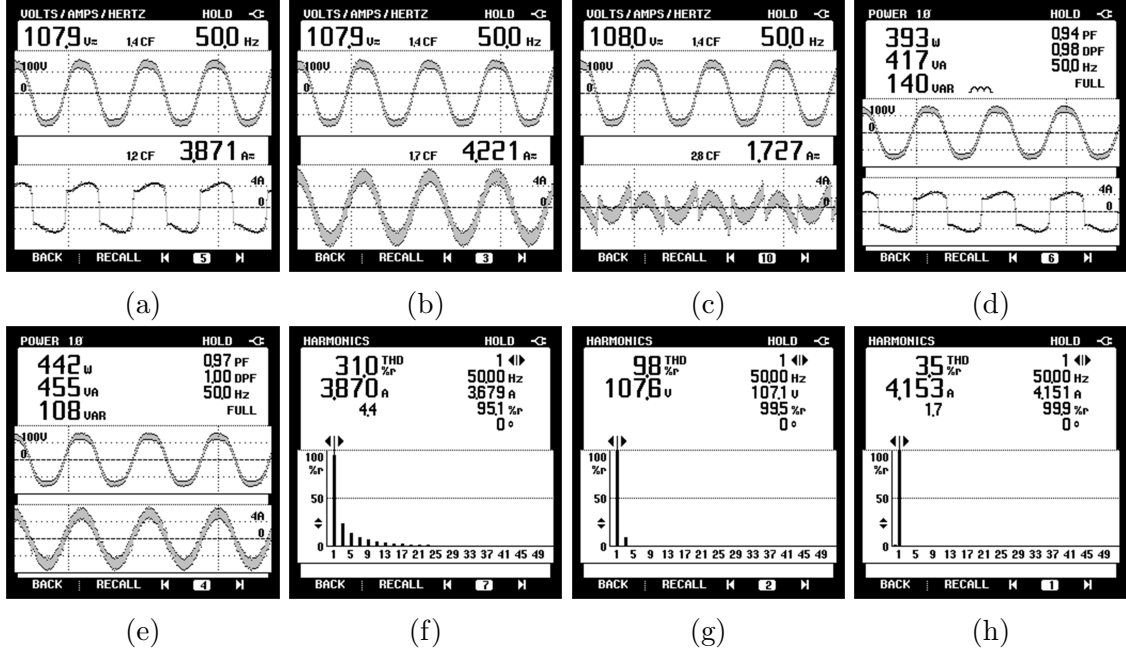


Figure 5.31: Steady-state experimental performance of single-phase SAPF with non-linear load and polluted grid condition by SOGI-ROGI algorithm (a)  $v_g$  and  $i_L$  (b)  $v_g$  and  $i_g$  (c)  $v_g$  and  $i_c$  (d) load power (e) grid power (f) load current THD (g) grid voltage THD (h) grid current THD

31.0%. Thus, both distorted grid and distorted load conditions are investigated here. The proposed SOGI-ROGI controller is used to obtain sinusoidal voltage templates for synchronization. These are used later to develop a controller for PQ mitigation. Figure 5.31(h) shows grid current THD is reduced to 3.5%. Load power demand and grid power are shown in Fig. 5.31(d) and 5.31(e) respectively. The load power demand is 393W and 140Var and the grid power is 442W and 108Var. The DPF of the grid is observed to be 1.00 while the DPF of the load is 0.98. Results show that the proposed controller is very effective under undistorted as well as distorted grid conditions. Improved power quality is achieved using SAPF controlled using the proposed controller.

The dynamic performance in closed-loop is shown in Fig. 5.32 for sudden load change. Figure 5.32(a) and 5.32(b) show the grid voltage, grid current, load current and the DC-link voltage for sudden load decrease and increase respectively. In both the cases stability of DC-link voltage has been maintained and the grid current is sinusoidal.

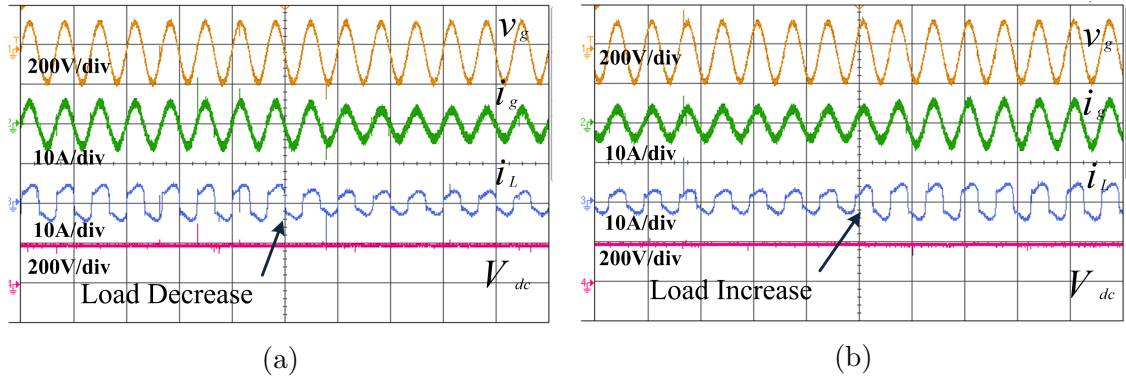


Figure 5.32: Closed-loop dynamic performance of SOGI-ROGI with sudden load change (a) load decrease ( $v_g, i_g, i_L$  and  $V_{dc}$ ) (b) load increase ( $v_g, i_g, i_L$  and  $V_{dc}$ )

Performance of control and synchronization techniques discussed for single-phase SAPF have been summarized in Table 5.4 for ideal and polluted grid condition. During the normal grid condition unit-template synchronization works good. But, Table 5.4: Performance comparison of control and synchronization technique for single-phase SAPF

		SOGI with unit template synchronization			SOGI with AZCD synchronization			SOGI-ROGI		
		$v_g$	$i_L$	$i_g$	$v_g$	$i_L$	$i_g$	$v_g$	$i_L$	$i_g$
Normal grid	Simulation (THD%)	1.98	37.28	4.45	2.01	38.5	4.27	2.0	32.95	3.74
	Experimental (THD%)	0.6	27.3	4.8	0.6	27.5	4.3	0.6	29.0	2.9
Polluted grid	Simulation (THD%)	14.12	22.13	12.66	14.20	38.5	4.26	14.33	22.12	3.28
	Experimental (THD%)	NA	NA	NA	9.1	29.8	4.4	9.8	31.0	3.5

during the polluted grid condition advanced synchronization algorithm are required which estimates synchronizing signals even under polluted grid condition. It has been observed that SOGI control with AZCD and SOGI-FLL-ROGI performed as per IEEE Std.519 under both the normal and polluted grid condition. The trends observed in simulation results and observed in experimental results almost similar. Synchronization by SOGI-FLL-ROGI with SOGI-ROGI shows better performance in simulation and experimental results under both normal and distorted grid conditions.

### 5.3 Three-Phase SAPF under Ideal and Polluted Grid

Three-phase systems comprise three-phase AC power circuit with each phase displaced by  $120^\circ$ . Single-phase supply is given to homes while commercial and industrial loads are fed by three-phase power supply. Different type of loads are connected to three-phase supply system viz linear/non-linear loads/mixed loads. The quality of power may be improved by compensating the reactive power demanded by the load and this requires a three-phase SAPF. System configuration for three-phase SAPF is been shown in Fig. 5.33.

In Fig. 5.33, a non-linear load is connected at PCC and for shunt compensation

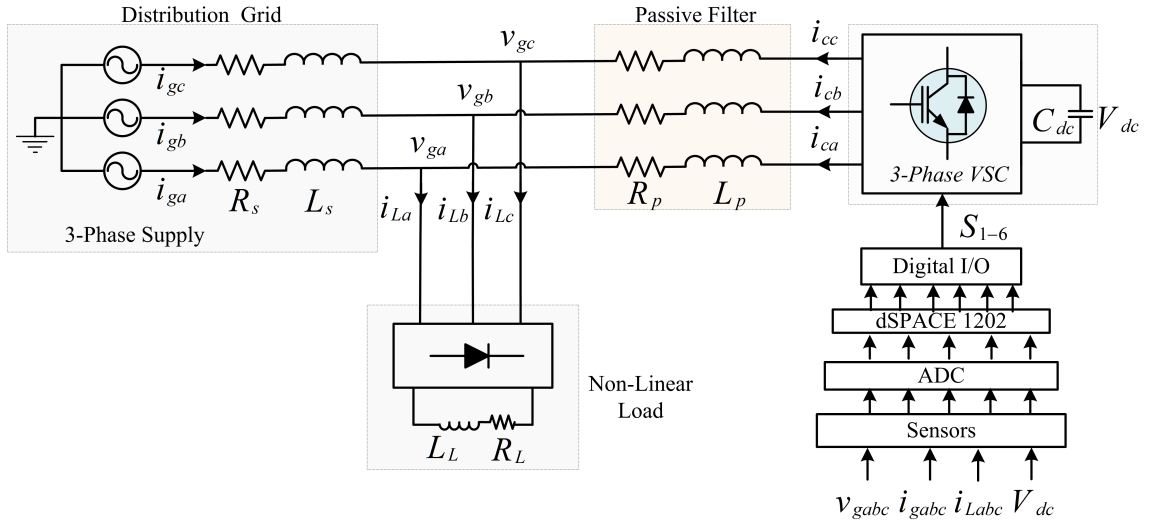


Figure 5.33: Structure of three-phase system with three phase 3-leg SAPF

three-phase VSC is also connected at PCC via interfacing inductors. Voltage and current sensors has been used in the developed experimental prototype system to measure the different parameters of the system and given to the dSpace1202 for signal processing via ADC ports. After processing the required algorithm, six pulses have been generated and given to the switches of VSC. Unit template, SRF-PLL and Spline-PLL based synchronization techniques with SRFT control technique have been designed, applied and discussed for three-phase SAPF system.

### 5.3.1 Three-Phase SRF Control with Unit-Template Synchronization

A three-phase SAPF controller requires the estimation of fundamental component of the load current of all the phases, synchronizing templates and the DC-link voltage regulator. SRFT is a conventional technique to estimate the fundamental component and for achieving the synchronization unit template method is the conventional and simplest technique.

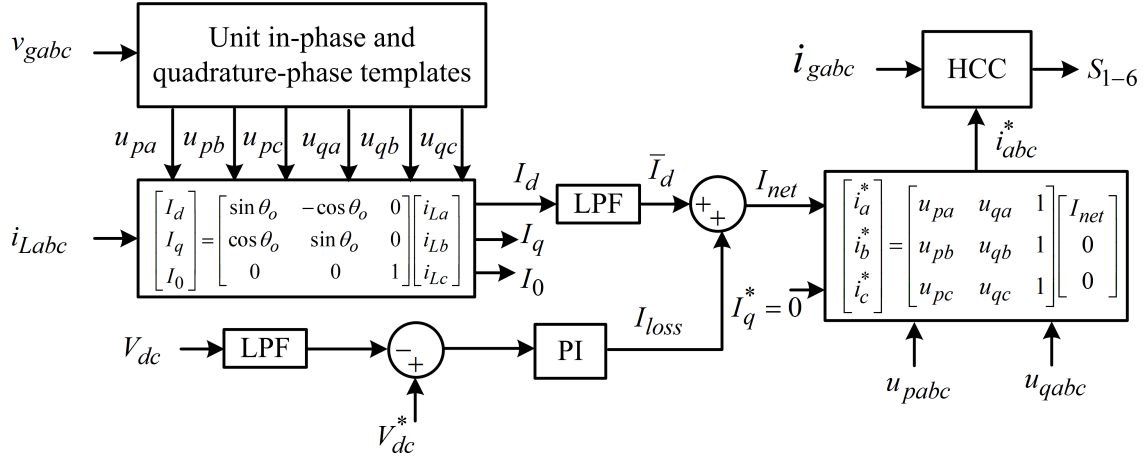


Figure 5.34: Control structure of three-phase SAPF control with unit template synchronization

The control structure to generate the switching signals for VSC has been shown in Fig. 5.34.

#### 5.3.1.1 Fundamental Component Estimation by SRFT Algorithm

The three-phase balanced non-linear load contains harmonics and the respective equations are-

$$i_{La}(t) = I_{fa} \sin(\omega_i t) + H_n(t) \quad (5.30)$$

$$i_{Lb}(t) = I_{fb} \sin(\omega_i t - \frac{2\pi}{3}) + H_n(t) \quad (5.31)$$

$$i_{Lc}(t) = I_{fc} \sin(\omega_i t + \frac{2\pi}{3}) + H_n(t) \quad (5.32)$$



In above equations,  $I_{fa}$ ,  $I_{fb}$  and  $I_{fc}$  represent the fundamental components of the load current and  $H_n(t)$  denotes the harmonic component in the load current. The active ( $I_d$ ) and reactive component ( $I_q$ ) can be estimated with the help of  $abc$  to  $dq0$  Park transformation. When the rotating frame is aligned behind  $90^\circ$  the  $\alpha$ -axis, Park transformation can be depicted in 5.33.

$$\begin{bmatrix} I_d \\ I_q \\ I_0 \end{bmatrix} = \begin{bmatrix} \sin \theta_o & -\cos \theta_o & 0 \\ \cos \theta_o & \sin \theta_o & 0 \\ 0 & 0 & 1 \end{bmatrix} \begin{bmatrix} i_{La} \\ i_{Lb} \\ i_{Lc} \end{bmatrix} \quad (5.33)$$

The d-component or active component of the load current contains the AC components also. Hence, it requires additional LPF to get the filtered active load component ( $\bar{I}_d$ ) as shown in Fig. 5.34.

### 5.3.1.2 Estimation of Loss Component

DC-link voltage is regulated by the PI controller. Hence, the loss component ( $I_{loss}(n)$ ) for the discrete implementation of the VSC at the  $n^{th}$  sampling is estimated from the output of the PI controller and it is calculated by 5.34.

$$I_{loss}(n) = I_{loss}(n-1) + k_p \{V_{dce}(n) - V_{dce}(n-1)\} + k_i V_{dce}(n) \quad (5.34)$$

In 5.34,  $k_p$  and  $k_i$  are the proportional and integral gains of PI controller.  $V_{dce}(n)$  is the DC-link voltage error at  $n^{th}$  sampling instant and it is calculated as-

$$V_{dce}(n) = V_{dc}^*(n) - V_{dc}(n) \quad (5.35)$$

In 5.35,  $V_{dc}(n)$  is the measured DC-link voltage and  $V_{dc}^*(n)$  is the reference DC-link voltage. The net active component ( $I_{net}$ ) is calculated by adding the fundamental active load component ( $\bar{I}_d$ ) and the losses ( $I_{loss}$ ) in the VSC.

$$I_{net} = \bar{I}_d + I_{loss} \quad (5.36)$$

### 5.3.1.3 Generation of Switching Pulses

The reference grid currents are now generated by using the inverse  $dq0$  to  $abc$  inverse park transformation. The reference reactive component ( $I_q^*$ ) is taken as zero so that total reactive power support to the grid is provided by SAPF. The controller is designed and developed such that the active power demand of the load and the switching losses of the VSC are fed from the grid and the SAPF meets the reactive power demand of the load.

The reference currents ( $i_{abc}^*$ ) are expressed as-

$$\begin{bmatrix} i_a^* \\ i_b^* \\ i_c^* \end{bmatrix} = \begin{bmatrix} \sin \theta_{ao} & \cos \theta_{ao} & 1 \\ \sin \theta_{bo} & \cos \theta_{bo} & 1 \\ \sin \theta_{co} & \cos \theta_{co} & 1 \end{bmatrix} \begin{bmatrix} I_{net} \\ 0 \\ 0 \end{bmatrix} = \begin{bmatrix} u_{pa} & u_{qa} & 1 \\ u_{pb} & u_{qb} & 1 \\ u_{pc} & u_{qc} & 1 \end{bmatrix} \begin{bmatrix} I_{net} \\ 0 \\ 0 \end{bmatrix} \quad (5.37)$$

In above equation ??, estimation of  $u_{pa}$ ,  $u_{qa}$ ,  $u_{pb}$ ,  $u_{qb}$ ,  $u_{pc}$  and  $u_{qc}$  are the in-phase and quadrature phase templates of three-phase voltages. Three-phase voltages have been measured at PCC named as  $v_{ga}$ ,  $v_{gb}$  and  $v_{gc}$ . Unit templates have been obtained by simply dividing the individual phase voltages by  $A_v$ . The in-phase unit templates of each phases have been given by 5.38.

$$u_{pa} = \frac{v_{ga}}{A_v}, u_{pb} = \frac{v_{gb}}{A_v} \text{ and } u_{pc} = \frac{v_{gc}}{A_v} \quad (5.38)$$

where,  $A_v$  is the magnitude of three-phase grid voltage and is calculated by 5.39,

$$A_v = \sqrt{\frac{2}{3}(v_{ga}^2 + v_{gb}^2 + v_{gc}^2)} \quad (5.39)$$

Quadrature-phase templates of three-phase can also be evaluated by (5.40).

$$\begin{aligned} u_{qa} &= \frac{-u_{pb}}{\sqrt{3}} + \frac{u_{pc}}{\sqrt{3}} \\ u_{qb} &= \frac{\sqrt{3}}{2}u_{pa} + \frac{1}{2\sqrt{3}}(u_{pb} - u_{pc}) \\ u_{qc} &= \frac{-\sqrt{3}}{2}u_{pa} + \frac{1}{2\sqrt{3}}(u_{pb} - u_{pc}) \end{aligned} \quad (5.40)$$

The reference currents ( $i_{abc}^*$ ) and the sensed supply currents ( $i_{gabc}$ ) have been given to the hysteresis current controller (HCC), which generates the required six pulses to the driver circuit of the VSC. Now, the developed algorithm can be used for the control of SAPF in three-phase system under different loading conditions for power quality improvement.

#### 5.3.1.4 Simulation Results

SRF control theory along with the unit-template synchronization has been simulated for three-phase SAPF under linear/non-linear load and combination loads. The estimation of fundamental component of the load current has been shown in Fig. 5.35 under different loading conditions.

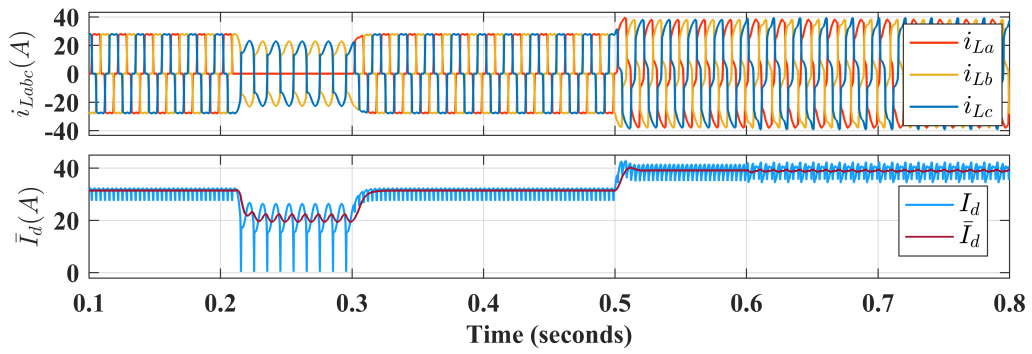


Figure 5.35: Fundamental current component by SRF technique

It also shows the filtered value of the fundamental load component ( $\bar{I}_d$ ). During  $t=0.2$  s to  $t=0.3$  s, one phase of the load has been removed and the unfiltered fundamental component shows high oscillations while the filtered component shows low oscillations. At  $t=0.5$  s, linear lagging load has been connected at PCC, the fundamental has been estimated. During  $t=0.6$  s to  $t=0.8$  s, the grid voltage feeding the load is also polluted with harmonics (THD 18.03%) and the fundamental load component is estimated with oscillations and even after filtering, reduced oscillations are observed in the fundamental component. This estimated fundamental component is used to improve the power quality in three-phase system.

The closed-loop simulation results for three-phase SAPF are shown in Fig. 5.36 and

Fig. 5.37. In Figure 5.36, phase-a of the load has been removed from  $t=0.2s$  to

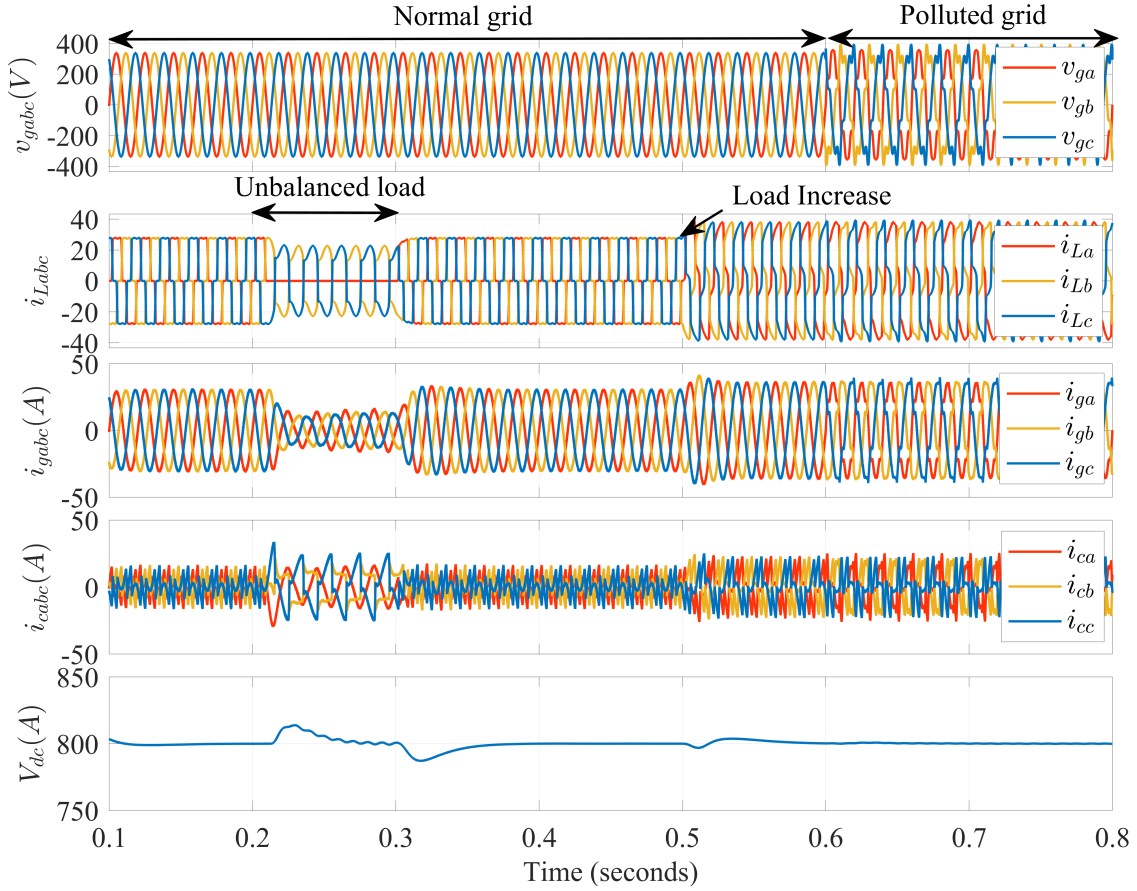


Figure 5.36: Three-phase simulation performance under SRF control and unit-template synchronization

$t=0.3s$ . During this condition, the DC-link voltage becomes regulated after some initial deviation from the reference voltage and the grid current is sinusoidal. At  $t=0.5s$ , the load has been increased, the DC-link voltage is regulated to reference voltage. The control technique has been also tested under polluted grid voltage condition ( $t=0.6s$  to  $t=0.8s$ ). The DC-link voltage shows fluctuations and the grid current is sinusoidal. Hence, this control technique doesn't improve power quality under polluted grid condition.

Figure 5.37 shows the performance of power of with SRFT technique with unit template synchronization under different loading conditions. Initially the system feeds balanced non-linear load and compensator is compensating the reactive power to PCC. The load demand is  $1.52 \times 10^4 W$  and  $2.5 \times 10^3 Var$ . Active power demanded

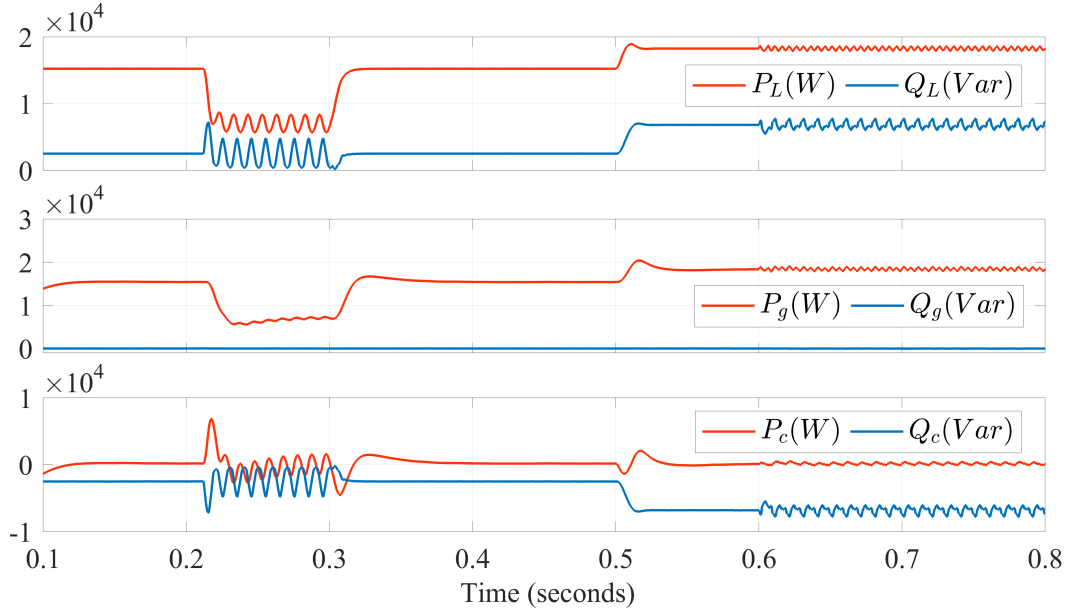


Figure 5.37: Three-phase power performance under SRF control and unit-template synchronization

by the load is supplied by the grid and the reactive power is compensated by the three-phase SAPF. Now, the inductive load has been added at  $t=0.5s$ , and now the power demanded by the load is  $1.82 \times 10^4 W$  and  $6.8 \times 10^3 Var$ . Here also, active power demanded by the load is supplied by the grid and reactive power is compensated by the grid.

THD analysis of different parameters viz  $v_{ga}$ ,  $i_{La}$  &  $i_{ga}$  have been shown in Fig. 5.38. SRF algorithm with unit template synchronization has been tested under both normal and polluted grid conditions and the non-linear load has been connected at PCC. In Case I, normal grid voltage has been applied and the THD of the non-linear load current is 25.75%. Before the compensation the THD of the grid current equals the THD of the load current. After applying the three-phase SAPF the THD of grid current is reduced to 1.72%. In Case II, the THD of the polluted grid voltage is 18.03% and THD of the load current is 18.77%. After applying the SAPF, the THD of the grid current is improved to 15.57%. Hence it proves that the SRF control algorithm works according to IEEE Std.519 during normal grid voltage and non-linear load current condition but it doesn't work well as per IEEE Std.519 during polluted grid voltage. Advanced synchronization techniques are required to the polluted grid

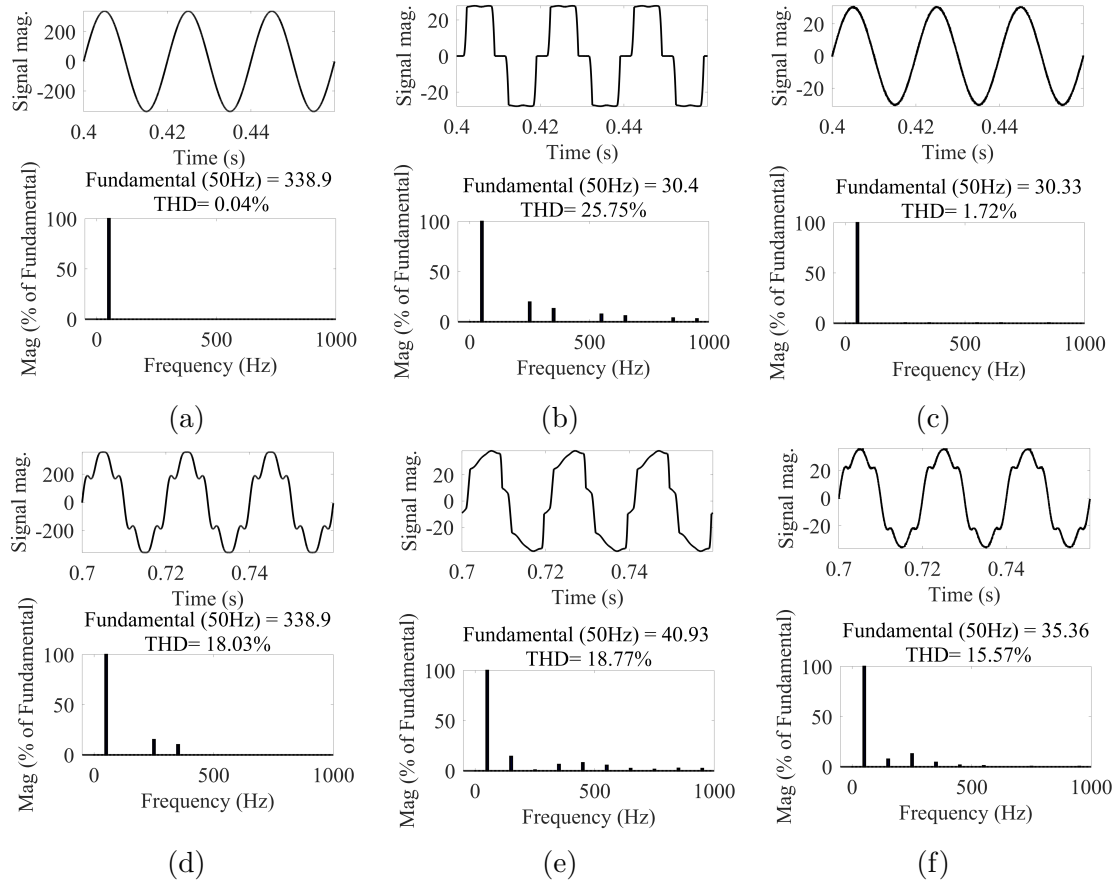


Figure 5.38: THD analysis for three-phase SAPF with SRF and unit-template synchronization, Case I: Normal grid (a) THD of  $v_{ga}$  (b) THD of  $i_{La}$  (c) THD of  $i_{ga}$  Case II: Polluted grid (d) THD of polluted grid  $v_{ga}$  (e) THD of  $i_{La}$  (f) THD of  $i_{ga}$

voltage condition. These are designed and discussed in the next section.

### 5.3.2 Three-Phase SRF control with SRF-PLL Synchronization Technique

Unit template synchronization can not be used under distorted or polluted grid condition. In this Section, implementation of SRF-PLL has been done for the power quality improvement under normal and distorted grid condition feeding non-linear load. Fundamental estimation by SRF-PLL has been explained in Section 5.3.1.1 and the SRF-PLL based synchronization technique has been explained in Section 4.2.2. Overall control structure for the SRF technique with the SRF-PLL has been shown in Fig. 5.39. System configuration for hardware implementation has been shown in Fig. 5.33.

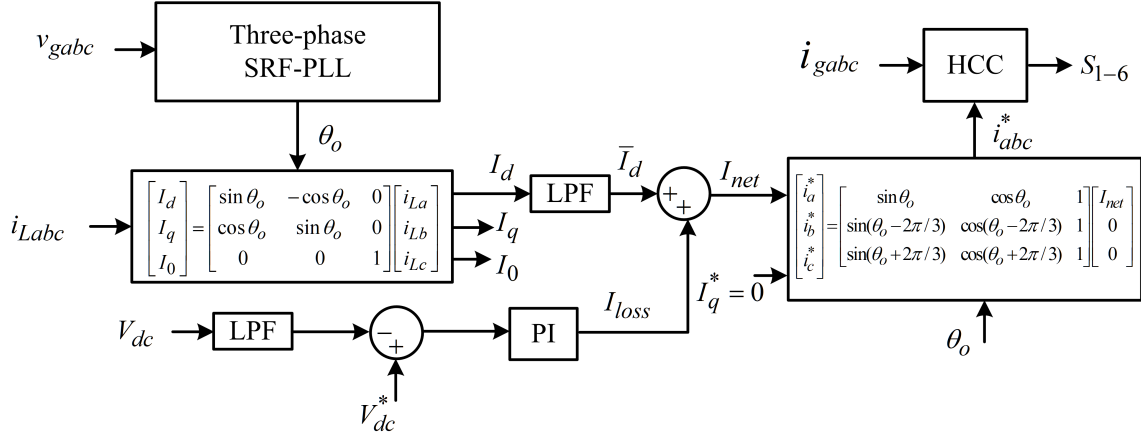


Figure 5.39: Control structure of three-phase SAPF control with SRF-PLL based synchronization

#### 5.3.2.1 Simulation Results

Detailed simulation has been performed for different loading conditions and different grid voltage conditions with the SRF-PLL based synchronization and shown in Fig. 5.40-5.42. SRF-PLL has been employed for generating sinusoidal unit synchronization signals for improving the power quality under both normal and polluted grid conditions. Figure 5.40 shows the grid voltage, non-linear load current, fundamental component of the load current, grid current, compensator current and the DC-link voltage. Initially normal grid voltage has been supplied and at  $t=0.6s$  the

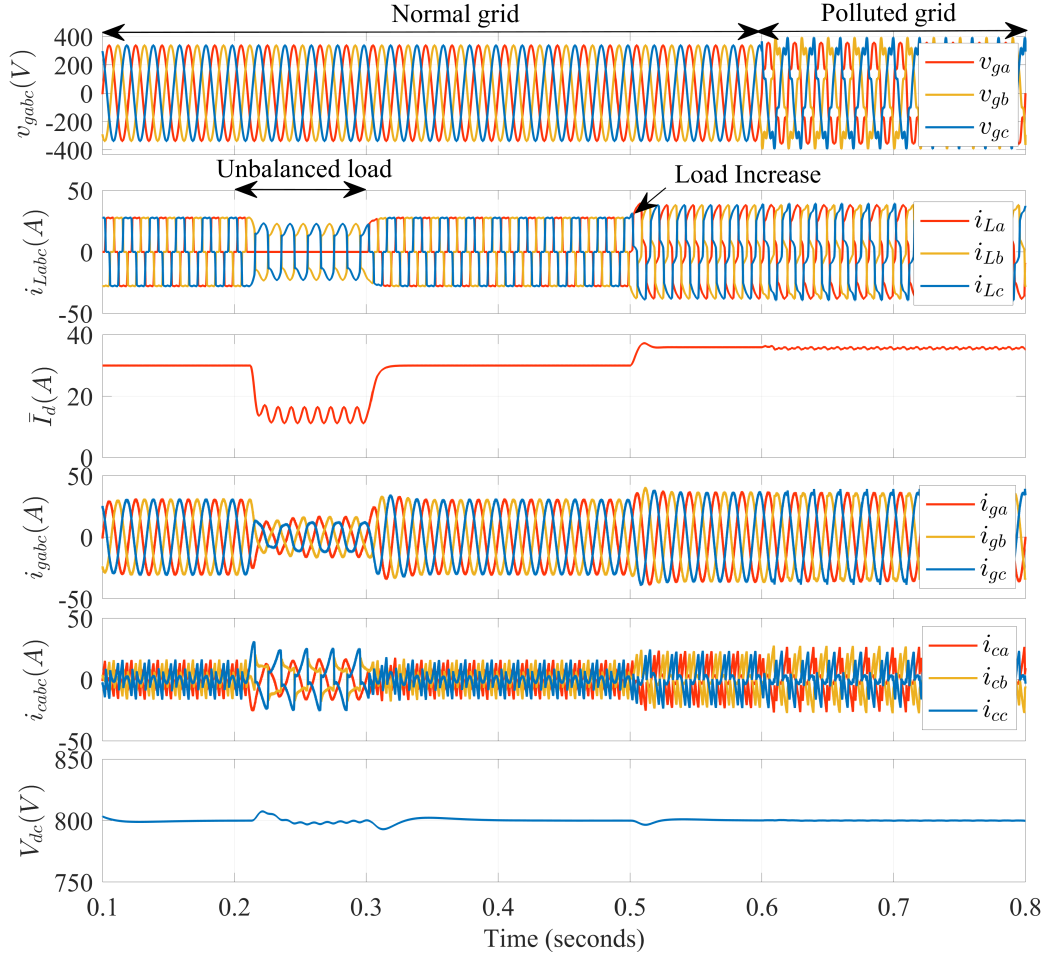


Figure 5.40: Three-phase simulation performance under SRF control and SRF-PLL based synchronization

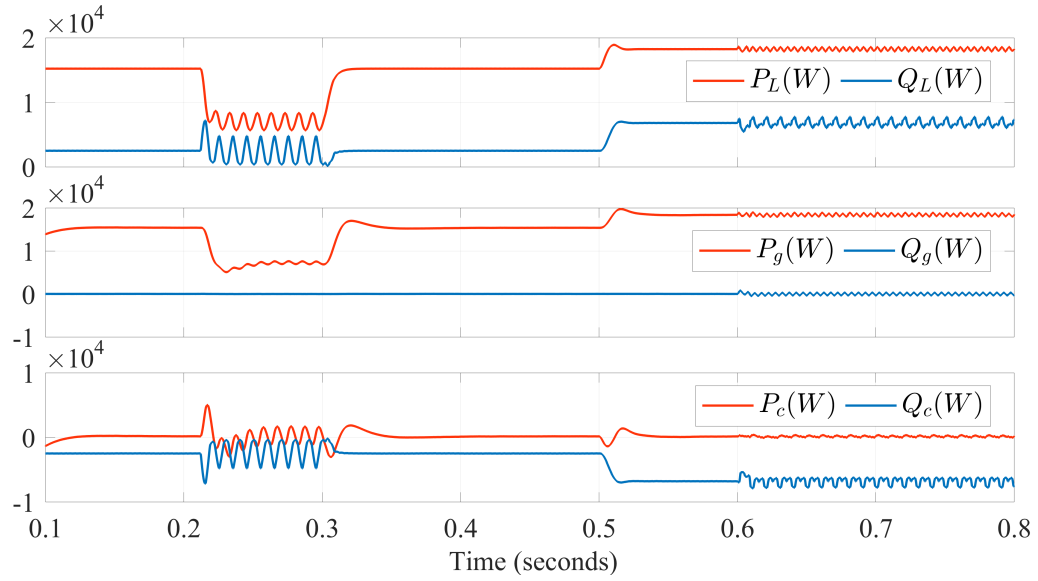


Figure 5.41: Three-phase power performance under SRF-PLL based synchronization



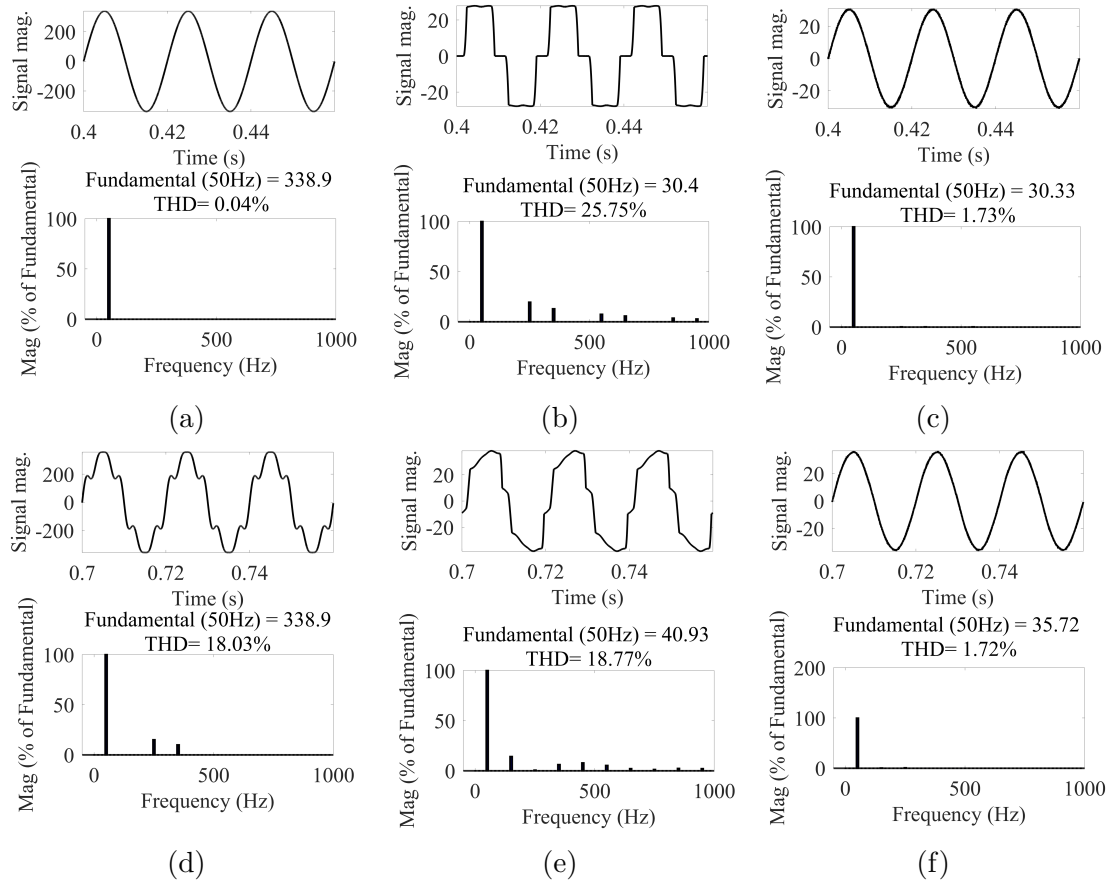


Figure 5.42: THD analysis for three-phase SAPF with SRF-PLL based synchronization, Case I: Normal grid (a) THD of  $v_{ga}$  (b) THD of  $i_{La}$  (c) THD of  $i_{ga}$   
Case II: Polluted grid (d) THD of polluted grid  $v_{ga}$  (e) THD of  $i_{La}$  (f) THD of  $i_{ga}$

grid is polluted with harmonics (THD 18.03%). Unbalancing has been simulated from  $t=0.2s$  to  $t=0.3s$  and then load has been increased at  $t=0.5s$ . The fundamental component of load current has been estimated correctly as per variation in the load current. During all these conditions, the grid-current is close to sinusoidal. Compensator current is provided by the SAPF such that it compensates the load harmonics and reactive power.

Figure 5.41 shows the performance of the three-phase SAPF under SRF-PLL based grid synchronization. Power demanded by the load at  $t=0.4s$  is  $1.523 \times 10^4 W$  and  $2.517 \times 10^3 Var$  and the power supplied by the grid is  $1.535 \times 10^4 W$  and  $3.132 \times 10^1 Var$ . The reactive power compensated by SAPF is  $2.486 \times 10^3 Var$ , while the switching losses occurring in compensator amount to 114.7W. A linear inductive load has been connected to PCC at  $t=0.55s$ , now the load demand is

$1.826 \times 10^4 W$  and  $6.822 \times 10^3 Var$ . The active power demanded by the load is supplied by the grid is  $1.834 \times 10^4 W$  and the reactive power is compensated by SAPF is  $6.794 \times 10^3 Var$ . Here, it validates the compensation of reactive power by SAPF. Figure 5.42 shows the THD analysis of the different parameters. Case I shows the power quality improvement under normal grid voltage condition. In this case, THD of the grid voltage is 0.04% and THD of the non-linear load current is 25.75% and after applying SAPF, THD of the grid current is reduced to 1.73%. In case II, the grid voltage is polluted with harmonics and its THD is 18.03%. The THD of the grid current is improved to 1.72% from 18.77%. In both the cases, the quality gets improved and IEEE Std.519 is met.

Simulation result analysis of the SRF-PLL validates that the algorithm improves the quality the grid current and is able to compensate the reactive power demanded by the load connected at PCC.

### 5.3.3 Three-Phase SRF Control with Spline-PLL Synchronization Technique

The Spline based adaptive PLL has been explained in Section 4.2.4. It has been observed that Adaptive Spline based synchronization technique gives distortion free synchronizing signals under distorted grid voltage condition. In this Section, Spline-PLL has been implemented for the three-phase shunt active filter under both normal and distorted grid condition feeding non-linear load. Overall control structure has been shown in Fig. 5.43. System configuration for hardware implementation has been shown in Fig. 5.33.

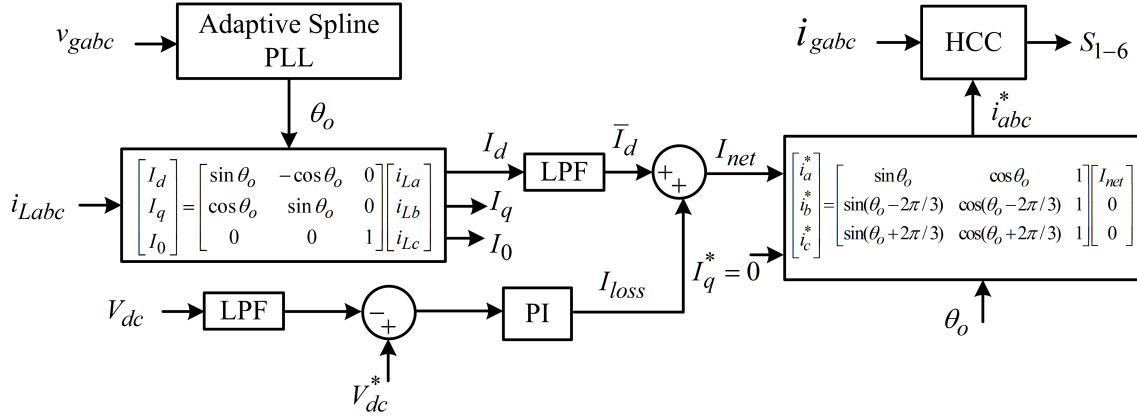


Figure 5.43: Control structure of three-phase SAPF control with adaptive spline based synchronization

#### 5.3.3.1 Simulation results

Detailed simulation has been done under normal and distorted grid condition feeding non-linear load and shown in Fig. 5.44-5.46. Figure 5.44 shows simulation performance of Spline based synchronization and shows the grid voltage, load current, fundamental extracted from the load current, compensated grid current, compensator current and the DC-link voltage. The grid voltage is considered normal from  $t=0.2s$  to  $t=0.6s$  with negligible harmonic content and then it is made polluted till  $t=0.8s$ . Load current is unbalanced during  $t=0.2s$  to  $t=0.3s$  and it is increased at

$t=0.5s$  and maintained till  $t=0.8s$ . The fundamental component ( $\bar{I}_d$ ) is extracted using SRFT and varies as the load current is increased or decreased. The DC-link voltage maintains the reference DC-link voltage during the unbalanced load and the sudden load increase. The grid current maintains sinusoidal waveform despite the non-linear load connected at PCC. Compensator current is injected due to controller action which is designed to be able to improve the quality of the grid power.

Figure 5.45 shows the performance with the proposed grid synchronization tech-

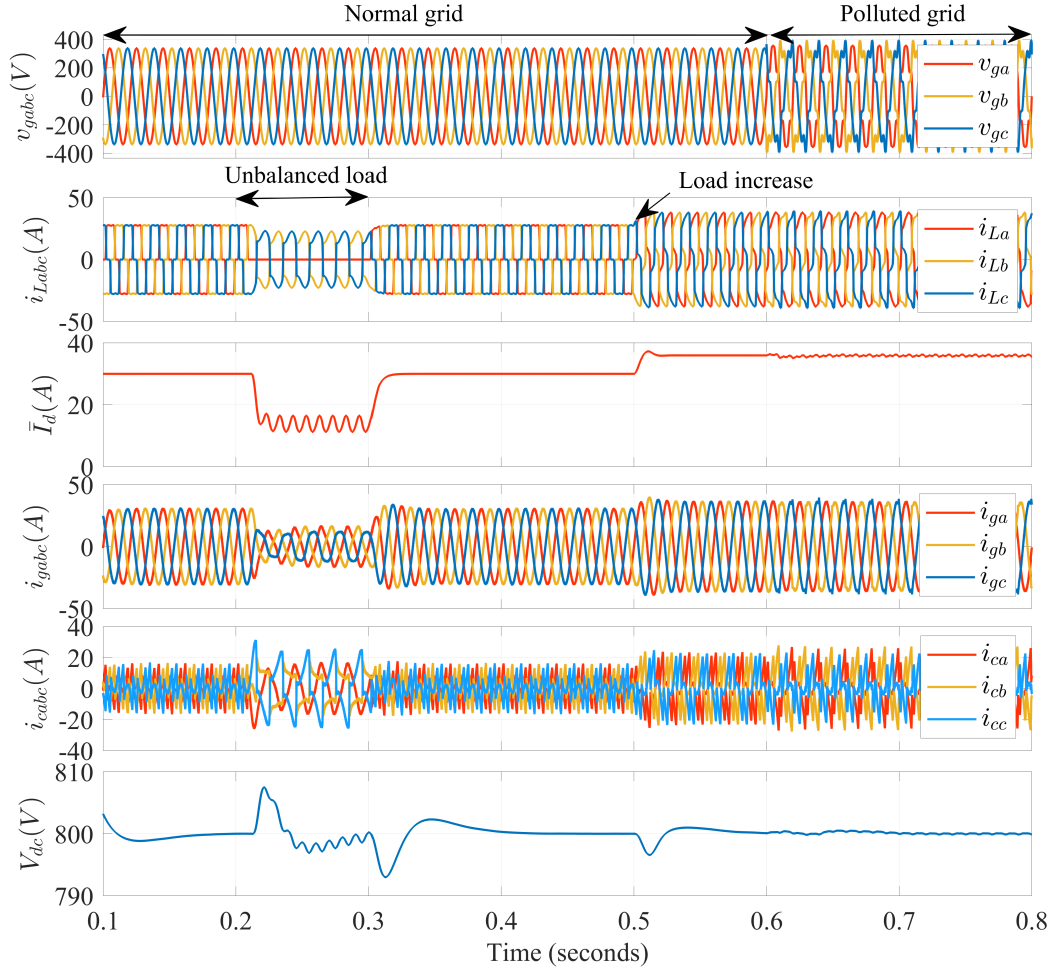


Figure 5.44: Three-phase simulation performance under SRF control and adaptive spline based synchronization

nique. The power is measured at  $t=0.4s$  for initial load and at  $t=0.55s$  at increased load. At  $t=0.4s$  power demanded by the load is  $1.523 \times 10^4 W$  and  $2.515 \times 10^3 Var$  and active power of  $1.535 \times 10^4 W$  is supplied by the grid and the reactive power compensated by the VSC is  $2.495 \times 10^3 Var$ . Some loss of  $116.7 W$  occurs in the VSC

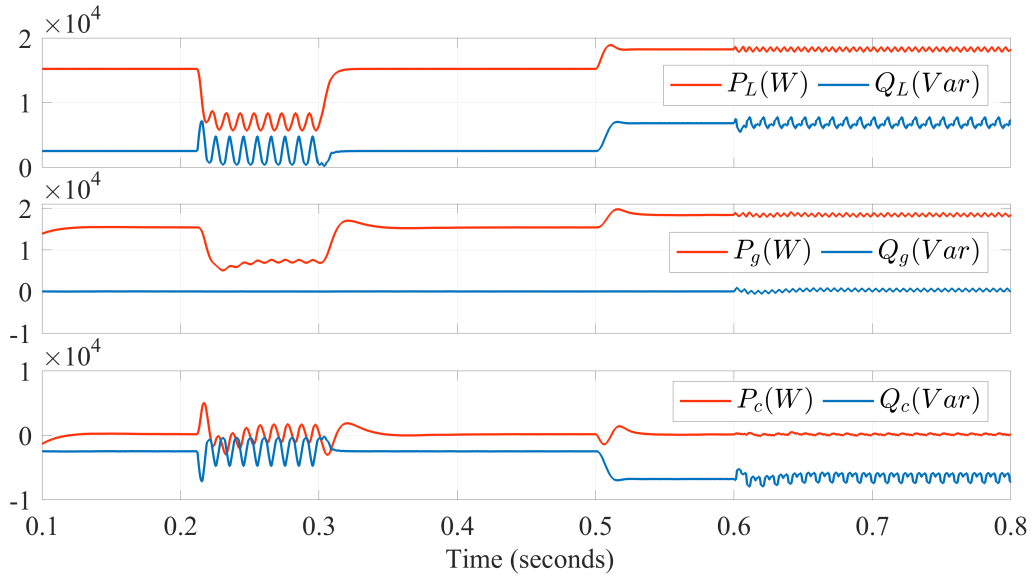


Figure 5.45: Three-phase power performance under SRF-PLL based synchronization

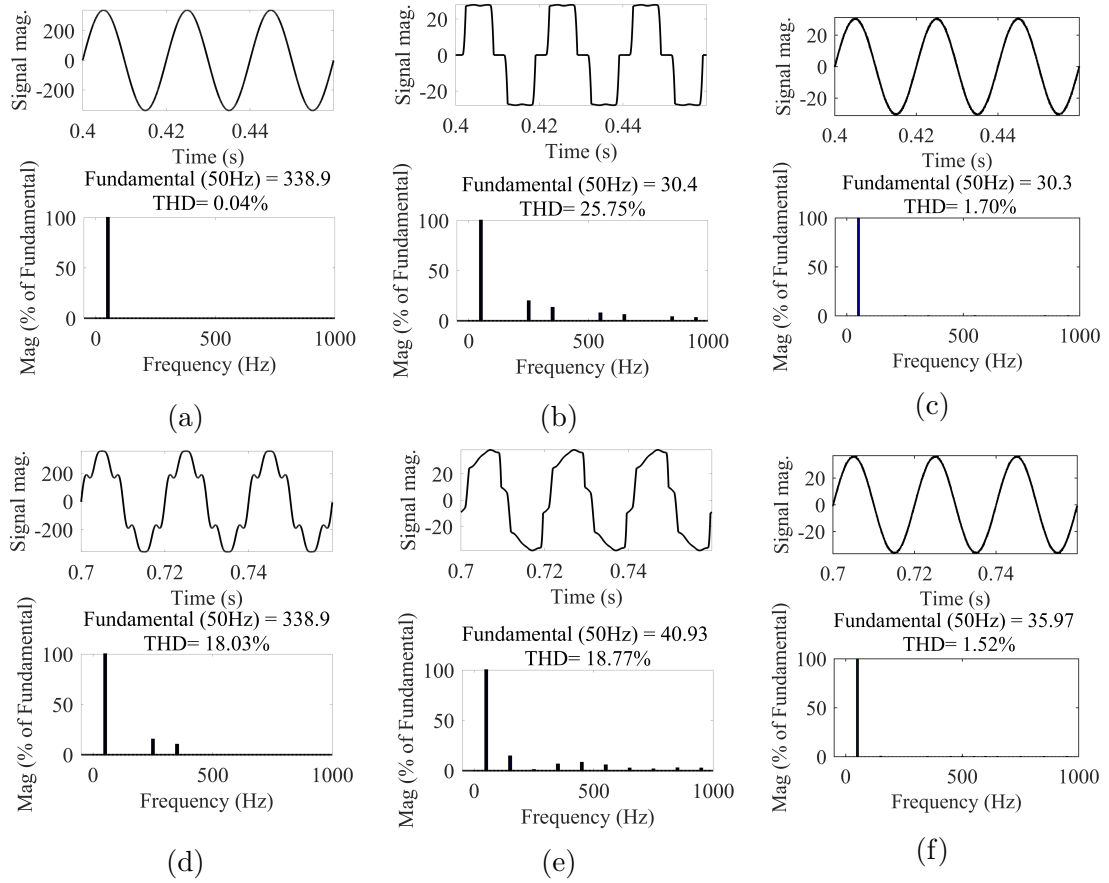


Figure 5.46: THD analysis for three-phase SAPF with spline based synchronization, Case I: Normal grid (a) THD of  $v_{ga}$  (b) THD of  $i_{La}$  (c) THD of  $i_{ga}$  Case II: Polluted grid (d) THD of polluted grid  $v_{ga}$  (e) THD of  $i_{La}$  (f) THD of  $i_{ga}$

as switching loss. An inductive load is added at  $t=0.5s$  and the power demanded by the load is  $1.826 \times 10^4 W$  and  $6.822 \times 10^3 Var$ . Here also, the active power demanded by the load is supplied by the grid and the reactive power is compensated by the three-phase SAPF system.

Figure 5.46 shows the THD analysis of the different parameters of the three-phase SAPF system. In Case I (5.46(a)-5.46(c)), the grid voltage is undistorted and the load connected to PCC is non-linear (THD=25.75%) and after applying the SAPF the THD of the grid current is 1.70%. In Case II, under distorted grid voltage condition the THD of the grid voltage and the current is 18.03% and 18.77% respectively. The THD of the compensated grid current is 1.52%. In both cases, the quality of power has been improved and it follows IEEE Std.519.

Simulation performance of SRFT control algorithm with unit-template, SRF-PLL and Spline-PLL synchronization techniques have been summarized in Table 5.5.

The Spline-PLL based synchronization shows better performance than SRF-PLL

Table 5.5: Performance comparison of synchronization techniques for three-phase SAPF

Synchronization techniques	unit template			SRF-PLL			Spline-PLL		
	$v_{ga}$	$i_{La}$	$i_{ga}$	$v_{ga}$	$i_{La}$	$i_{ga}$	$v_{ga}$	$i_{La}$	$i_{ga}$
<b>Parameters (THD)</b>									
<b>Normal grid</b>	0.04%	25.75%	1.72%	0.04%	25.75%	1.73%	0.04%	25.75%	1.70%
<b>Polluted grid</b>	18.03%	18.77%	15.57%	18.03%	18.77%	1.72%	18.03%	18.77%	1.52%

and unit-template method for the three-phase SAPF system. The lowest THD obtained in grid current during undistorted grid voltage of 1.7% and 1.52% during polluted grid condition are both observed with Spline-PLL and SRFT control. It is also clearly observed that unit template scheme fails during polluted grid condition.

### 5.3.3.2 Experimental Results

Spline-PLL shows better performance in simulation. hence, it is also tested on experimental setup developed in the laboratory. The experimental closed-loop steady-state and dynamic performance have been shown in Fig. 5.47 and 5.48. Figure 5.47(a)

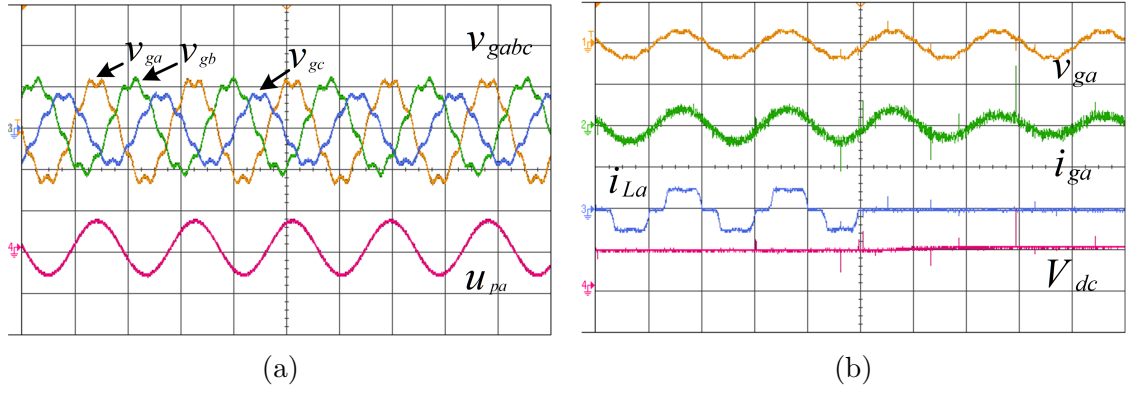


Figure 5.47: Experimental results for Spline based synchronization for polluted grid condition (a) Three-phase polluted grid ( $v_{gabc}$ ) and extracted synchronizing signal ( $u_{pa}$ ) (b) SAPF operation during load unbalancing ( $v_{ga}$ ,  $i_{ga}$ ,  $i_{La}$  and  $V_{dc}$ )

shows the extraction of synchronization templates from the grid voltage under distorted grid condition. The proposed algorithm generates distortion free synchronizing signal ( $u_{pa}$ ) under polluted grid condition. Figure 5.47(b) shows the closed loop dynamic result under load unbalancing during the distorted grid condition. The grid current is sinusoidal under balanced load and unbalanced load. DC-link is stable at reference voltage.

Figure 5.48 shows the steady-state performance of three-phase SAPF. The polluted grid voltage (L-L) of 109V with THD of 10.0% has been supplied to the non-linear having a THD of 21.8% and the magnitude of current is 3.964A. The grid current THD improves to 3.9% which follows IEEE Std-519. The experimental results also proves that the proposed algorithm works as per standard even under distorted grid condition.

## 5.4 Conclusions

In this chapter, SAPF operation for single-phase and three-phase system have been presented under both ideal and polluted grid condition. In single-phase SAPF, SOGI, cascaded SOGI and SOGI-ROGI have been used for fundamental load component estimation. These control algorithms have been applied with different synchronization techniques under both normal and polluted grid conditions. The unit-

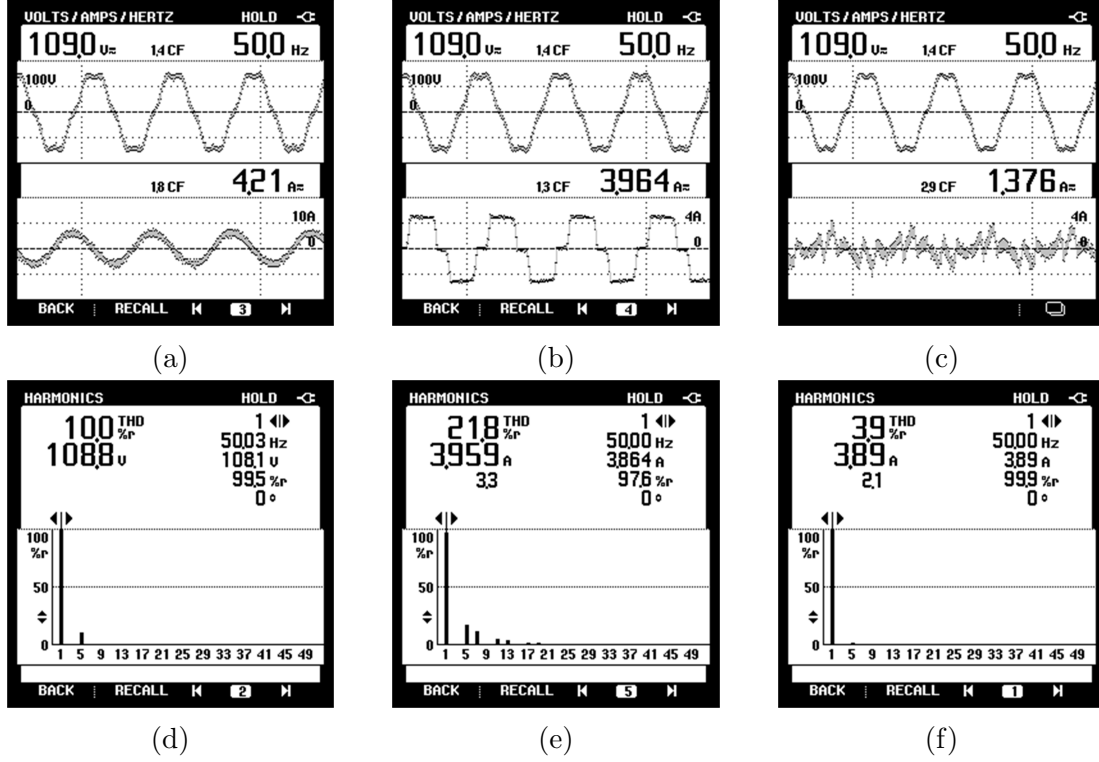


Figure 5.48: Experimental steady-state performance with Spline based synchronization under distorted grid voltage (a)  $v_{LL}$  and  $i_{ga}$  (b)  $v_{LL}$  and  $i_{La}$  (d) THD of polluted grid voltage (e) THD of load current (f) THD of grid current

template synchronization doesn't work as per IEEE Std. 519 during polluted grid condition. The performance of SOGI-ROGI with SOGI-FLL-ROGI perform better than SOGI control with AZCD under both normal and polluted grid conditions. In three-phase system SRFT control algorithm with unit-template, SRF-PLL and Spline based PLL have been applied for PQ improvement and reactive power compensation. Extensive simulation has been done and summarized. The simulation results results of SRFT control algorithm with Spline-PLL show the best performance under both normal and distorted grid condition. The experimental results with SRFT and Spline PLL are in agreement with the simulation results.



## Chapter 6

# Power Quality Improvement in Single-Phase Grid-Connected PV System

In previous chapter, single-phase and three-phase SAPF and their control algorithms have been discussed. In this chapter, PV has been integrated to single-phase grid via VSC which also adds capability of active power injection to the grid. Both active and reactive power compensation along with power quality improvement requires to design an appropriate control algorithm. The designed control algorithm needs to estimate the fundamental current component estimation of non-linear load current, obtain synchronization signal from the grid voltage signal, MPPT algorithm, DC-voltage regulator and estimation of feed-forward current from the PV array.

## 6.1 Single-Stage and Double-stage Grid-Connected PV System

Active power injection from the PV to grid require different such as single-stage and double-stage grid-connected PV system which are shown in Fig. 6.1 and 6.2 respectively. In single-stage grid-connected PV system DC-DC boost converter is not employed and the MPPT technique is used to achieve maximum power from the PV by generating the reference voltage and is maintained at DC-link. In double-stage grid-connected PV system an additional DC-DC boost converter is employed

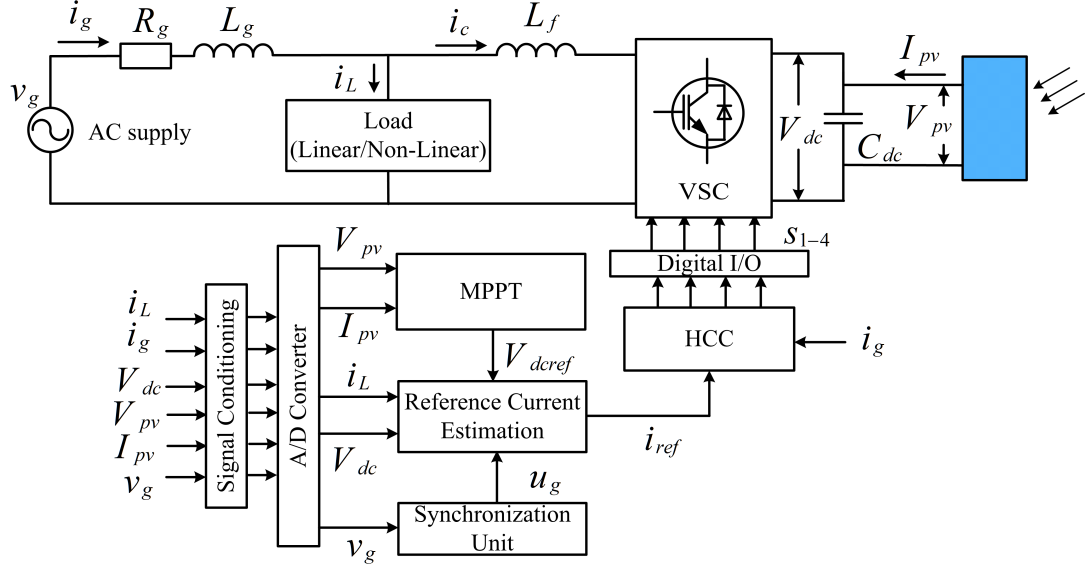


Figure 6.1: Single-phase single-stage grid connected PV system

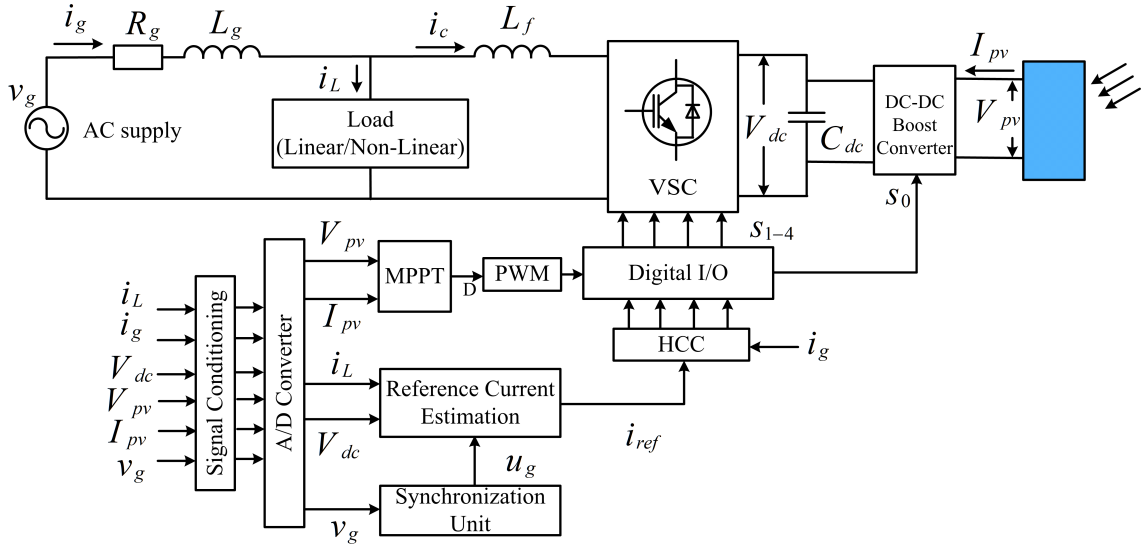


Figure 6.2: Single-phase double-stage grid connected PV system

and the MPPT technique gives the duty cycle which helps to achieve maximum power from the PV array.

### 6.1.1 Fundamental Load Component Estimation

SOGI-ROGI control technique has been designed, applied and discussed for the single-phase grid connected PV system as its performance is superior than other algorithms. The conventional SRFT control technique has also been discussed and

compared with the SOGI-ROGI controller for the single-phase grid-connected PV system in both single-stage and double-stage configuration.

#### 6.1.1.1 Single-Phase SRFT Technique

SRFT is the conventional control technique to estimate the fundamental component of the load current. Fundamental component estimation requires the in-phase component and the quadrature-phase component. Load current is considered as the in-phase component ( $i_\alpha$ ) and to generate quadrature-phase component delay of  $90^\circ$  has been applied. The Park-Transformation to get the fundamental load component is given by 6.1:

$$\begin{bmatrix} I_d(t) \\ I_q(t) \end{bmatrix} = \begin{bmatrix} \sin \theta_o & -\cos \theta_o \\ \cos \theta_o & \sin \theta_o \end{bmatrix} \begin{bmatrix} i_\alpha(t) \\ i_\beta(t) \end{bmatrix} \quad (6.1)$$

Fundamental load current estimated by the SRFT technique shows high amount of ripples and requires additional LPF. Fundamental load current estimated by the SRFT technique with and without filter is shown in Fig. 6.3. The unfiltered

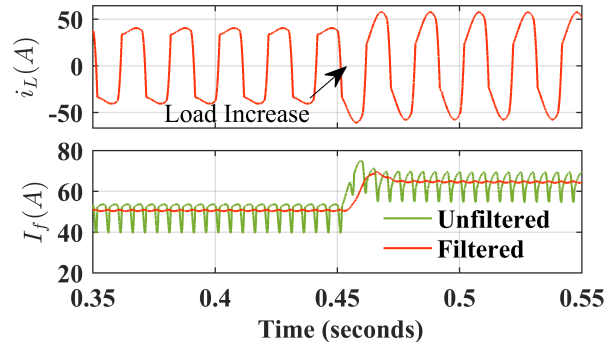


Figure 6.3: Fundamental load current component by SRFT

component has the oscillations of 14.1A and oscillations in the filtered component is 0.65A. High oscillations in the fundamental load component is not recommended as it could not improve the PQ significantly.

### 6.1.1.2 SOGI-ROGI Technique

Estimation of fundamental component by combination of SOGI and ROGI has been explained here. This algorithm has been explained earlier in Section 5.2.2 for the fundamental component estimation of the load current. The block diagram representation for calculating the fundamental component of the load current is shown in Fig. 6.4. In Fig. 6.4,  $i_L$  denotes the input signal and  $(i'_\alpha, i''_\beta)$  are the filtered

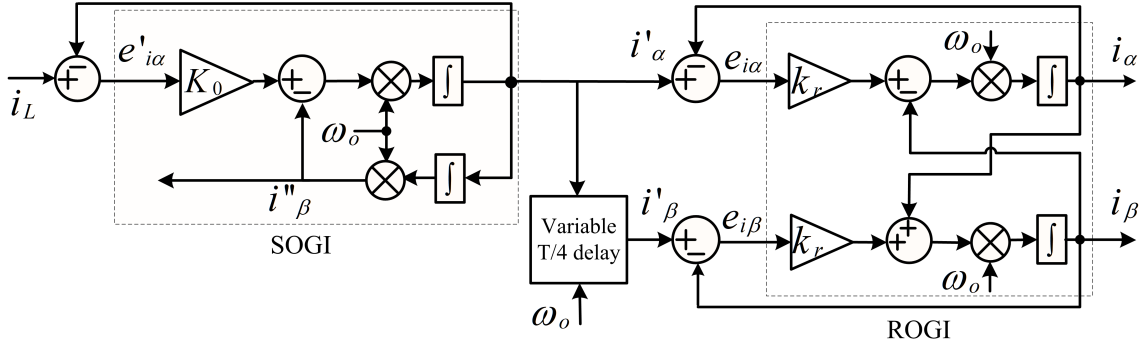


Figure 6.4: Structure of SOGI-ROGI for fundamental current component estimation

outputs of SOGI.  $(i_\alpha, i_\beta)$  are the final outputs obtained after the cascaded operation for SOGI and ROGI technique.  $\omega_o$  is the estimated frequency obtained from grid-voltage by SOGI-FLL-ROGI. The proposed algorithm has also the capability of removing DC-offset along with removing harmonics and find out ripple free fundamental load component.  $k_0$  and  $k_r$  are the gains of SOGI and ROGI respectively. Open-loop transfer function of SOGI is given as-

$$SOGI(s) = \frac{k_o \omega_o s}{s^2 + \omega_o^2} \quad (6.2)$$

The closed-loop transfer functions of  $(i'_\alpha, i''_\beta)$  of the SOGI block considering error signal  $(e'_{i\alpha})$  are given as in 6.3 and 6.4.

$$\frac{i'_\alpha(s)}{i_L(s)} = \frac{k_o \omega_o s}{s^2 + k_o \omega_o s + \omega_o^2} \quad (6.3)$$

$$\frac{i''_\beta(s)}{i_L(s)} = \frac{k_o \omega_o^2}{s^2 + k_o \omega_o s + \omega_o^2} \quad (6.4)$$

As discussed in [95], ROGI is an algorithm with single complex pole. The transfer function of ROGI is represented as-

$$\frac{i_{\alpha,\beta}(s)}{e_{i\alpha,i\beta}(s)} = \frac{k_r}{s - j\omega_o} \quad (6.5)$$

where,  $e_{i\alpha,i\beta} = i'_{\alpha\beta} - i_{\alpha\beta}$  is the error signal for the ROGI. Now, the closed-loop transfer function with the ROGI for in-phase and quadrature signals are given as in 6.6-6.8.

$$\frac{i_{\alpha}(s)}{i'_{\alpha}(s)} = \frac{i_{\beta}(s)}{i'_{\beta}(s)} = \frac{k_r\omega_o s}{s^2 + 2k_r\omega_o s + (1 + k_r^2)\omega_o^2} \quad (6.6)$$

$$Q(s) = \frac{i_{\beta}(s)}{i_L(s)} = \frac{k_0 k_r \omega_o^2 (2\omega_o s + k_0 \omega_o^2)}{s^4 + (k_o + 2k_r)\omega_o s^3 + (2 + 2k_o k_r + k_r^2)\omega_o^3 s^2 + (1 + k_r^2)\omega_o^4} \quad (6.7)$$

$$D(s) = \frac{i_{\alpha}(s)}{i_L(s)} = \frac{k_0 k_r \omega_o^2 (s^2 + k_r \omega_o s - \omega_o^2)}{s^4 + (k_o + 2k_r)\omega_o s^3 + (2 + 2k_o k_r + k_r^2)\omega_o^3 s^2 + (1 + k_r^2)\omega_o^4} \quad (6.8)$$

A variable time-delay block has been used to generate the perfect quadrature signal from the DC-offset free signal of the SOGI. Hence, no DC-offset in input of the ROGI block. The algorithm generates perfect sinusoidal in-phase and quadrature phase signal of the load current. The gain values of SOGI -ROGI has already discussed in Section 4.1.5 and its values have been selected as  $k_o = 1.414$  and  $k_r = 1.414$ . The magnitude of the fundamental load current is estimated as-

$$I_f = \sqrt{i_{\alpha}^2 + i_{\beta}^2} \quad (6.9)$$

The estimated magnitude of the load current has almost no oscillations; hence, there is no requirement of additional filter. All the conventional algorithms normally employ an additional filter after fundamental component estimation of load current.

### 6.1.2 Maximum Power Point Tracking (MPPT)

The performance of PV is largely dependent on the environmental parameters specially the irradiance and the temperature. P-V and I-V curve of a module are shown in Fig. 6.5. From Fig. 6.5(a) as the irradiance changes it is observed that

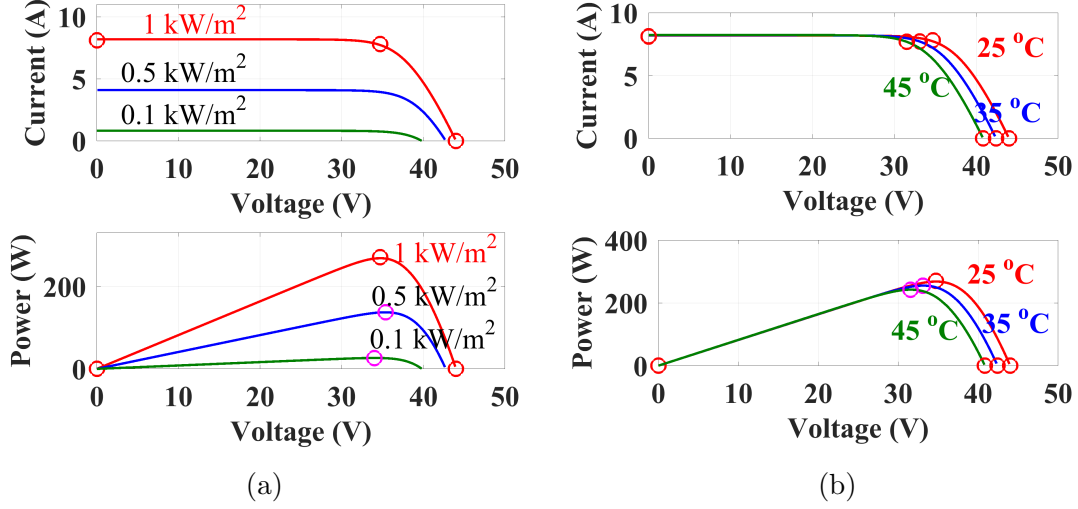


Figure 6.5: P-V and I-V curve of PV module (a) 25°C and at specified irradiance (b) 1000W/m<sup>2</sup> and at specified temperatures

the PV current and the power changes varies widely. While during the temperature changes of the PV module the variation of PV power output is smaller. For higher temperature power output is lesser and for lower temperature output power of PV array is higher. From P-V and I-V curves there is only one point at which power is maximum at specified irradiance and temperature and that point is called maximum power point. Power at maximum power point is called maximum power point ( $P_{mp}$ ) and voltage and current at maximum power point is called maximum power point voltage ( $V_{mpp}$ ) and maximum power point current ( $I_{mpp}$ ) respectively. MPPT algorithm is required to achieve maximum power from the PV module, string or array. There are number of MPPT algorithms developed and implemented in literature, namely, P&O, Incremental Conductance (INC) and soft computing based techniques such as fuzzy logic and artificial neural network (ANN) based algorithms. Out of all the algorithms discussed in literature, P&O is one of the simplest and easy to implement and also provides a good tracking performance. The flow-chart of the P&O algorithm for sing-stage grid-connected PV system is shown in Fig. 6.6. It is based on obtaining the voltage and current samples at every sampling cycles and uses these to calculate the power and compare the previous obtained value of power and estimates maximum power voltage ( $V_{mpp}$ ). The mathematical expression

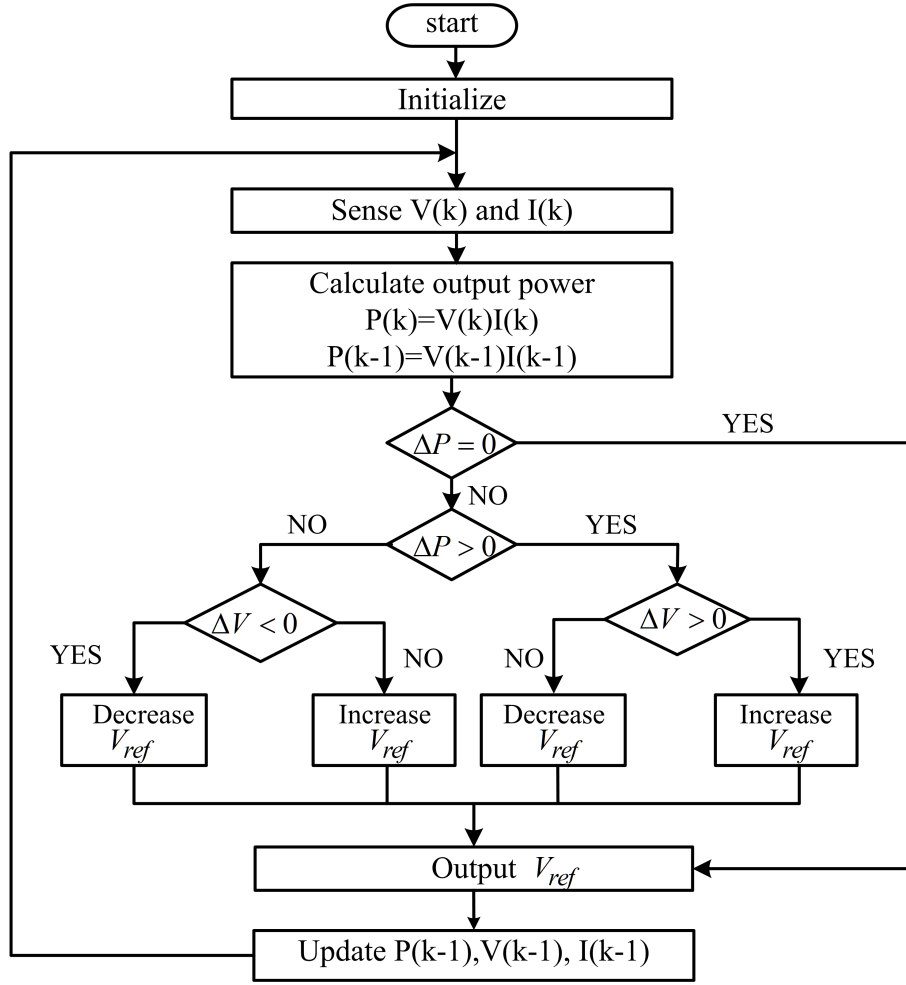


Figure 6.6: Flow chart of P&O MPPT

for the P& O algorithm for single-stage grid-connected PV system is given in 6.10, which generates  $V_{mpp}$  and further it is used as  $V_{dcref}$ .

$$\begin{aligned}
 &\text{if } \Delta P \times \Delta V > 0 \implies V_{new} = V_{old} + \Delta V \\
 &\text{and if } \Delta P \times \Delta V < 0 \implies V_{new} = V_{old} - \Delta V \\
 &\text{at MPPT } \Delta P \times \Delta V = 0 \implies V_{new} = V_{old}, \Delta V = 0
 \end{aligned} \tag{6.10}$$

In 6.10,  $\Delta V$  is the step-size of voltage to update to reference maximum power voltage at each step. The mathematical expression for the P& O algorithm for double-stage grid-connected PV system is given in 6.11, which generates duty-cycle and further

it is given to the DC-DC boost converter.

$$\begin{aligned}
& \text{if } \Delta P \times \Delta V > 0 \implies D_{new} = D_{old} - \Delta D \\
& \text{and if } \Delta P \times \Delta V < 0 \implies D_{new} = D_{old} + \Delta D \\
& \text{at MPPT } \Delta P \times \Delta V = 0 \implies D_{new} = D_{old}, \Delta D = 0
\end{aligned} \tag{6.11}$$

Here,  $D$  denotes the duty cycle of the inverter and the  $\Delta D$  is the step-size to update value of  $D$ . Higher value of step-size gives the faster response but at the same time the oscillations is higher and higher oscillations are not preferable as it changes the output voltage continuously. Hence an optimized value of  $\Delta V = 0.1$  has been chosen for single-stage system and  $\Delta D = 0.001$  for double-stage grid-connected PV system.

### 6.1.3 Feed-Forward Current Estimation

The PV array transfers active power to the grid as per its capability and rating via VSC. Under ideal conditions, the power generated by PV is delivered to the grid equals to active power measured at output of VSC ( $P_{pv}=P_c$ ) such that the inverter has negligible loss. Here,  $P_{pv}$  is the power generated by the PV and  $P_c$  represents the AC side power of the VSC. Power calculated at DC link is given as

$$P_{pv} = V_{pv} I_{pv} \tag{6.12}$$

Active power calculated at single phase ac side of the inverter is given as

$$P_c = V_{rms} I_{rms} = \frac{A_v}{\sqrt{2}} \frac{I_{ff}}{\sqrt{2}} \tag{6.13}$$

Here,  $A_v$  is the magnitude of the voltage signal and  $I_{ff}$  is the feed forward current or peak current magnitude of the VSC current which is injected to the grid. Ideally,

$$P_{pv} = P_{VSC} \implies P_{pv} = \frac{A_v}{\sqrt{2}} \frac{I_{ff}}{\sqrt{2}} \tag{6.14}$$



$$I_{ff} = \frac{2P_{pv}}{A_v} \quad (6.15)$$

#### 6.1.4 Loss Component Estimation

For shunt active compensation, DC-link voltage of the H-bridge inverter is controlled by the PI controller. The active compensation is performed by appropriate switching of IGBT switches. Some losses occurs during switching operation of VSC. Estimation of such losses is obtained with the help of following equation.

$$I_{loss}(n) = I_{loss}(n-1) + k_p[V_{dce}(n) - V_{dce}(n-1)] + k_i V_{dce}(n) \quad (6.16)$$

Here,  $V_{dce}(n) = V_{dc}^*(n) - V_{dc}(n)$  is the evaluated voltage error at DC-link inverter,  $k_p$  and  $k_i$  are the proportional and integral gains of the PI controller.

#### 6.1.5 Generation of Switching Pulses

The grid reference current ( $i_{ref}$ ) is generated by the multiplying the synchronizing signal ( $u_g$ ) and the net current ( $I_{net}$ ) for compensation. The net current and the reference current estimated is expressed by 6.17 and 6.18 respectively .

$$I_{net} = I_f + I_{loss} - I_{ff} \quad (6.17)$$

$$i_{ref} = I_{net} u_g \quad (6.18)$$

Hysteresis current controller (HCC) is used for its simplicity and robust working for generation of switching signals.

## 6.2 Performance of SRFT Control in a Single-Phase Grid-Connected PV System

The complete control structure with SRFT control technique for single-stage and double-stage grid-connected are presented in Fig. 6.7 and 6.8 respectively. The

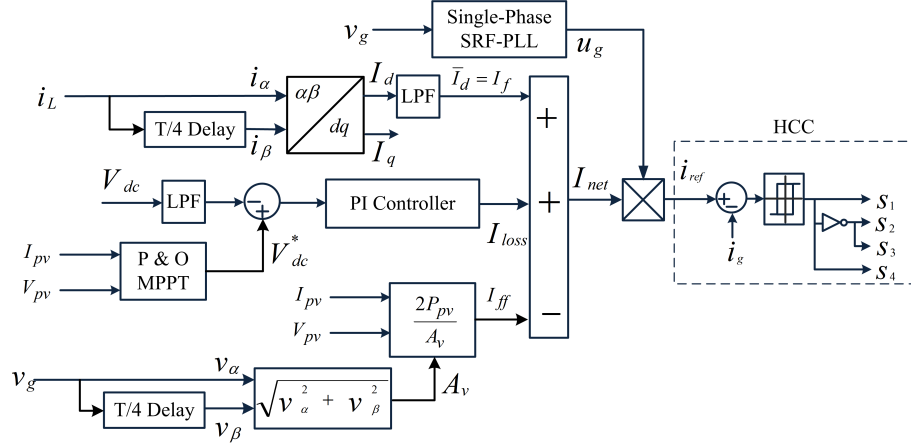


Figure 6.7: Single-phase single-stage SRFT control structure for grid-connected PV system

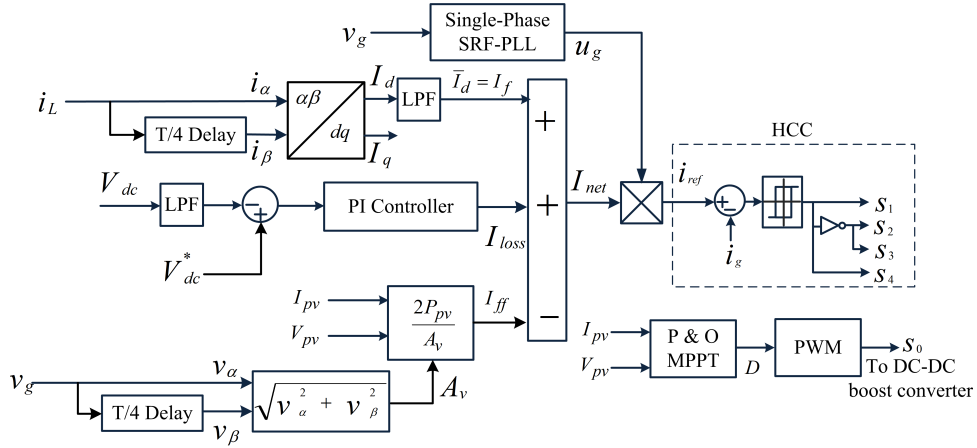


Figure 6.8: Single-phase double-stage SRFT control structure for grid-connected PV system

main difference between the control technique for single-stage and the double-stage system is that, the MPPT technique used in single-stage is used to generate reference voltage to achieve maximum power from PV and in double-stage PV system MPPT technique is used to generate duty cycle for the PWM block to generate switching

pulses for IGBT switch of the DC-DC boost converter.

### 6.2.1 Simulation Performance for Single-Stage Grid-Connected PV System

Single-phase single-stage grid-connected PV system has been simulated under MATLAB/Simulink environment. A combination of linear and non-linear load has been connected at PCC, where the VSC has been connected via the interfacing inductor. A PV string of 12 modules connected in series is connected to DC-link of the VSC for power injection. MPPT technique has been used to estimate reference DC-link voltage, which is also the maximum power point voltage. This system is tested under normal and polluted grid conditions for power quality improvement.

Simulation performance of PV string consist 12 panels in series is shown in Fig. 6.9. Here, output of PV string is directly connected to the DC-link of the H-bridge VSC.

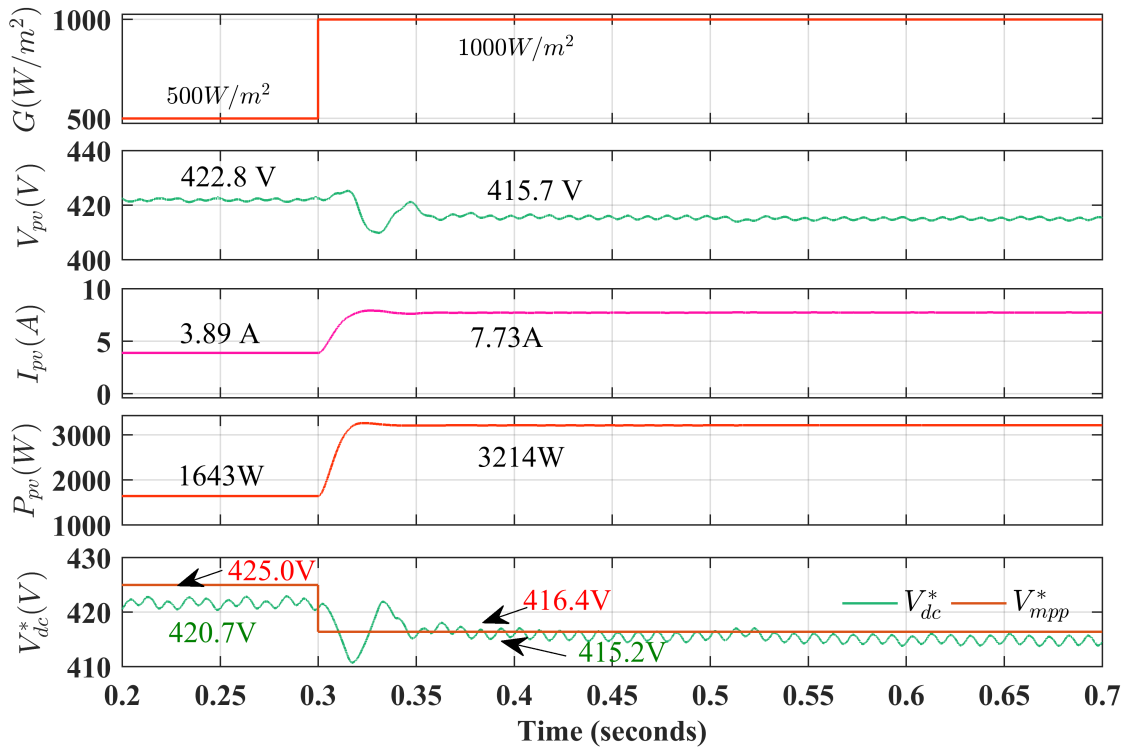


Figure 6.9: Simulation performance of PV string under single-stage grid-connected PV system

Initially, the irradiance is  $500W/m^2$  and it is changed to  $1000W/m^2$  at  $t=0.3s$ .

PV output voltage during the lower irradiance of  $500W/m^2$  is 422.8 V and during irradiance level of  $1000W/m^2$  is 415.7 V. Current and power achieved during  $500W/m^2$  are 3.89A and 1643W respectively. After  $t=0.3s$  during irradiance level of  $1000W/m^2$  current and power achieved are 7.73A and 3214W respectively. Efficiency achieved during irradiance level of  $1000W/m^2$  is 98.95%. The reference DC-link voltage estimated during the irradiance level of  $500W/m^2$  is 420.7V and during irradiance level of  $1000W/m^2$  is 415.2 V.

Fig. 6.10 shows the simulation performance for single-stage grid-connected SAPF showing  $v_g, i_g, i_L, i_c$  and  $V_{dc}$  respectively. This shows the performance for the normal

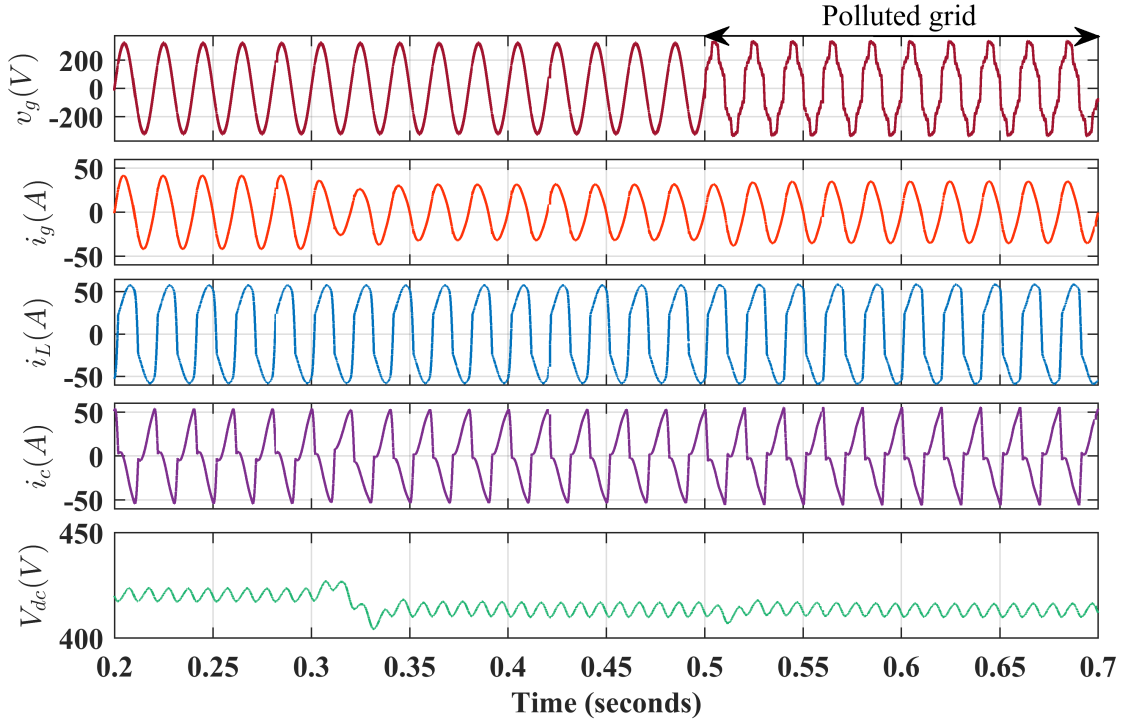


Figure 6.10: Simulation performance for grid parameters of single-phase single-stage grid-connected PV system

and distorted grid voltage conditions feeding the non-linear load. During both the conditions the grid-current has been improved. As the irradiance has been increased at  $t=0.3s$  the grid current has been decreased as the PV current has been increased and feeding to the load. The DC-link has been regulated by the PI controller to the reference DC-link voltage which is estimated by the MPPT.

THD analysis of the grid-parameters of AC signals have been shown in Fig. 6.11. In

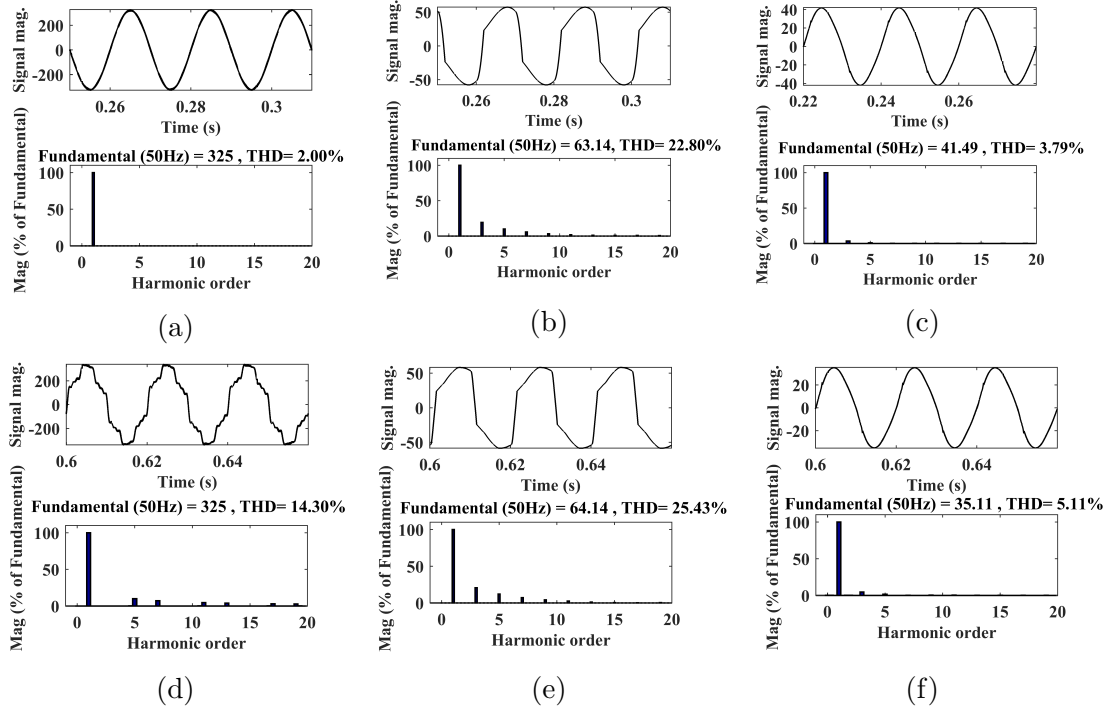


Figure 6.11: THD analysis for single-phase single-stage grid-connected PV system with SRFT technique with additional LPF, Case I: Standard/Normal grid (a) THD of  $v_g$  (b) THD of  $i_L$  (c) THD of  $i_g$   
Case II: Polluted grid (d) THD of polluted grid ( $v_g$ ) (e) THD of  $i_L$  (f) THD of  $i_g$

Case I, normal grid condition has been considered and simulated. The THD of the grid voltage is 2.00% (6.11(a)) and the THD of the non-linear load current (6.11(b)) is 22.80%. The quality of current has been improved to 3.79% as per IEEE Std.519 is shown in Fig. 6.11(c). In Case II, polluted grid condition has been considered and simulated. The THD of the grid voltage is 14.30% (6.11(d)) and the THD of the non-linear load current (6.11(e)) is 25.43%. The quality of current has been improved to 5.11% (6.11(f)) which is above the IEEE Std.519 and it is not permissible. Fig. 6.11 shows the performance of SRFT control technique when an additional LPF block has been employed. The THD analysis of the grid current for normal and polluted grid condition with SRFT control technique without additional LPF has been shown in Fig. 6.12. THD of the grid current obtained for normal grid condition is 13.44% (6.12(a)) and for polluted grid is 12.12% (6.12(b)). The performance of SRFT without additional LPF is not good and not permissible as per IEEE Std.519. Hence, an LPF is must required to achieve the good quality of power

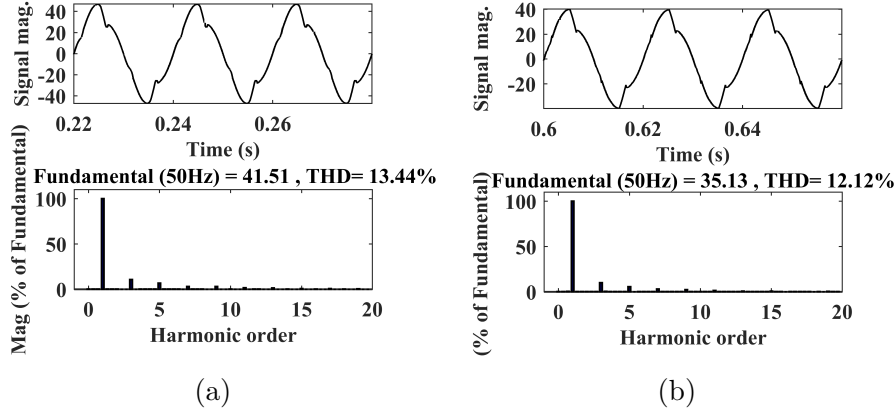


Figure 6.12: THD analysis for single-phase single-stage grid-connected PV system with SRFT technique without additional LPF, Case I: Standard/Normal grid (a) THD of  $i_g$ , Case II: Polluted grid (b) THD of  $i_g$

as per standard.

Figure 6.13 shows the simulation results for power measured at PCC. At  $t=0.25s$

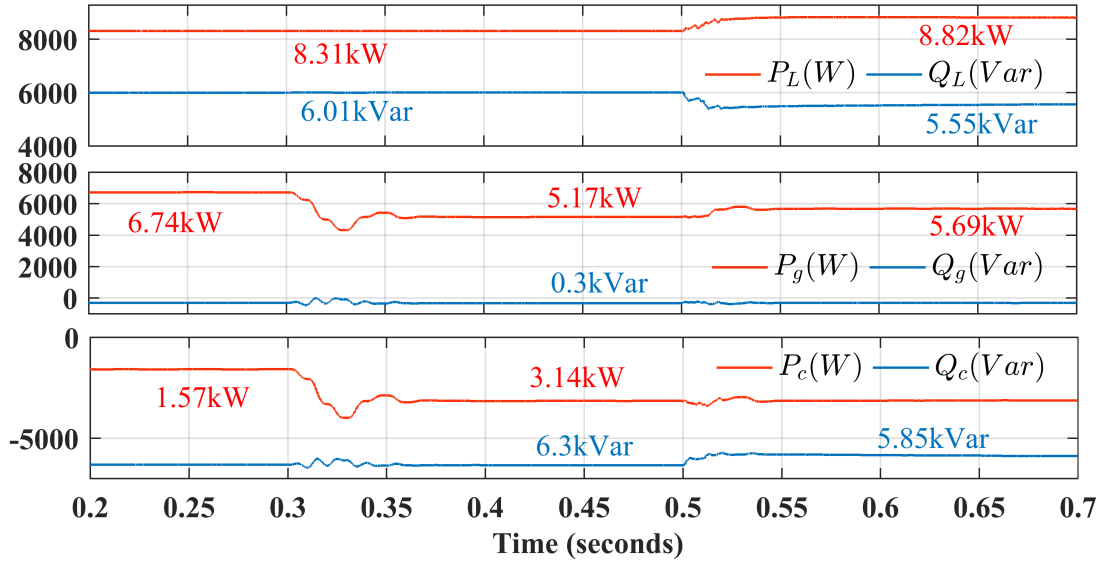


Figure 6.13: Simulation performance for power transfer under single-phase single-stage grid-connected PV system

the active and reactive load demand is 8.31kW and 6.01kVar respectively. Power supplied by the grid is 6.74kW and the reactive power demanded by the load is compensated by the VSC. At  $t=0.3s$ , irradiance level has been increased from  $500W/m^2$  to  $1000W/m^2$  and in this condition the load demand has not been changed. The VSC power has been increased to 3.14kW and the active power supplied by the grid

is decreased to 5.17kW. During the polluted grid condition ( $t=0.5s$  to  $t=0.7s$ ), the load demand has been changed to (8.82kW, 5.55kVar). At this situation, the active power of 5.69kW is supplied by the grid and active power of 3.14kW is supplied by the PV via single-phase VSC.

## 6.2.2 Simulation Performance for Double-Stage Grid-Connected PV System

In this section simulation performance of single-phase double-stage grid-connected PV system with SRFT control technique has been shown and discussed. Here, in double-stage configuration the PV output is first connected to DC-DC boost converter and the output of DC-DC boost converter is connected to single-phase VSC. Simulation performance of PV array has been shown in Fig. 6.14. Number of panels

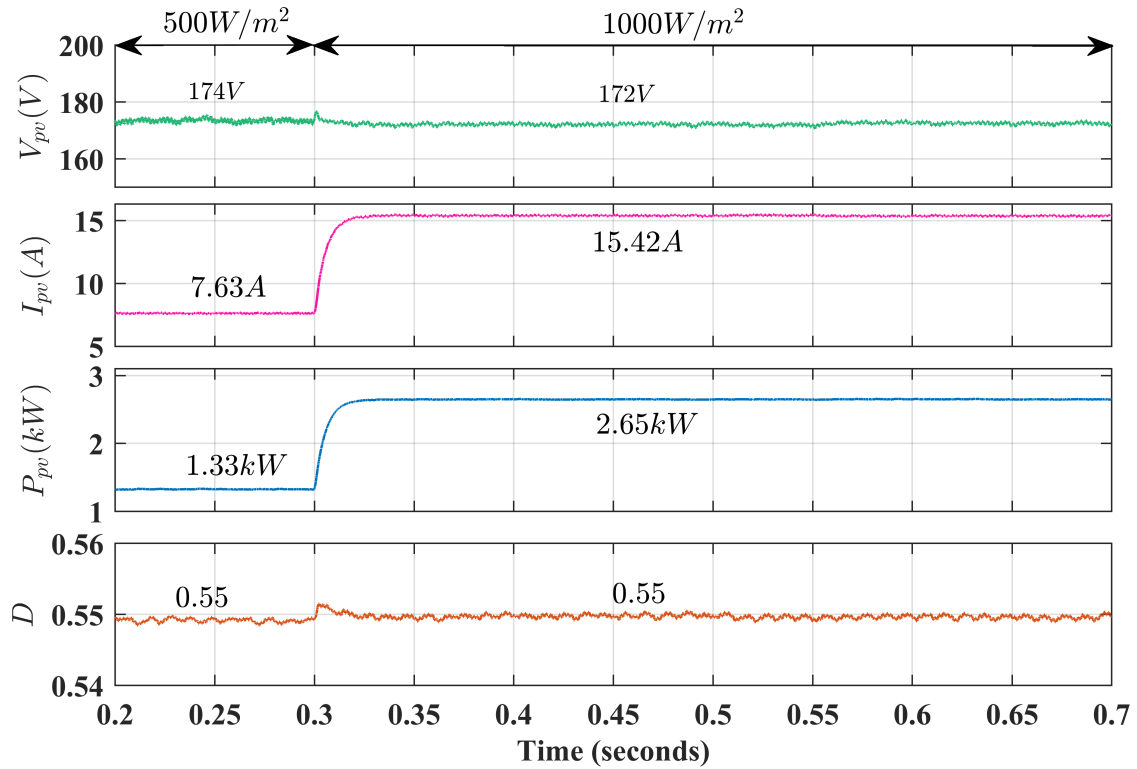


Figure 6.14: Simulation performance of PV string under double-stage grid-connected PV system

in this array is 10 in which 2 strings with 5 panels each string has been connected

in parallel. Initially, the irradiance level is  $500W/m^2$  and it is increased at  $t=0.3s$  to  $1000W/m^2$ . PV voltage, current and power measured at  $t=0.25s$  are 174V, 7.63A and 1.33kW respectively. At  $t=0.45s$ , when the irradiance is  $1000W/m^2$  the measured PV parameters are 172V, 15.42A and 2.65kW. At this condition the efficiency of the PV array calculated is 97.93%. The duty cycle for the IGBT switch of DC-DC boost converter is estimated by P & O technique is also shown.

Figure 6.15 shows the simulation performance for single-stage grid-connected SAPF showing  $v_g, i_g, i_L, i_c$  and  $V_{dc}$  respectively. During both the normal and polluted grid

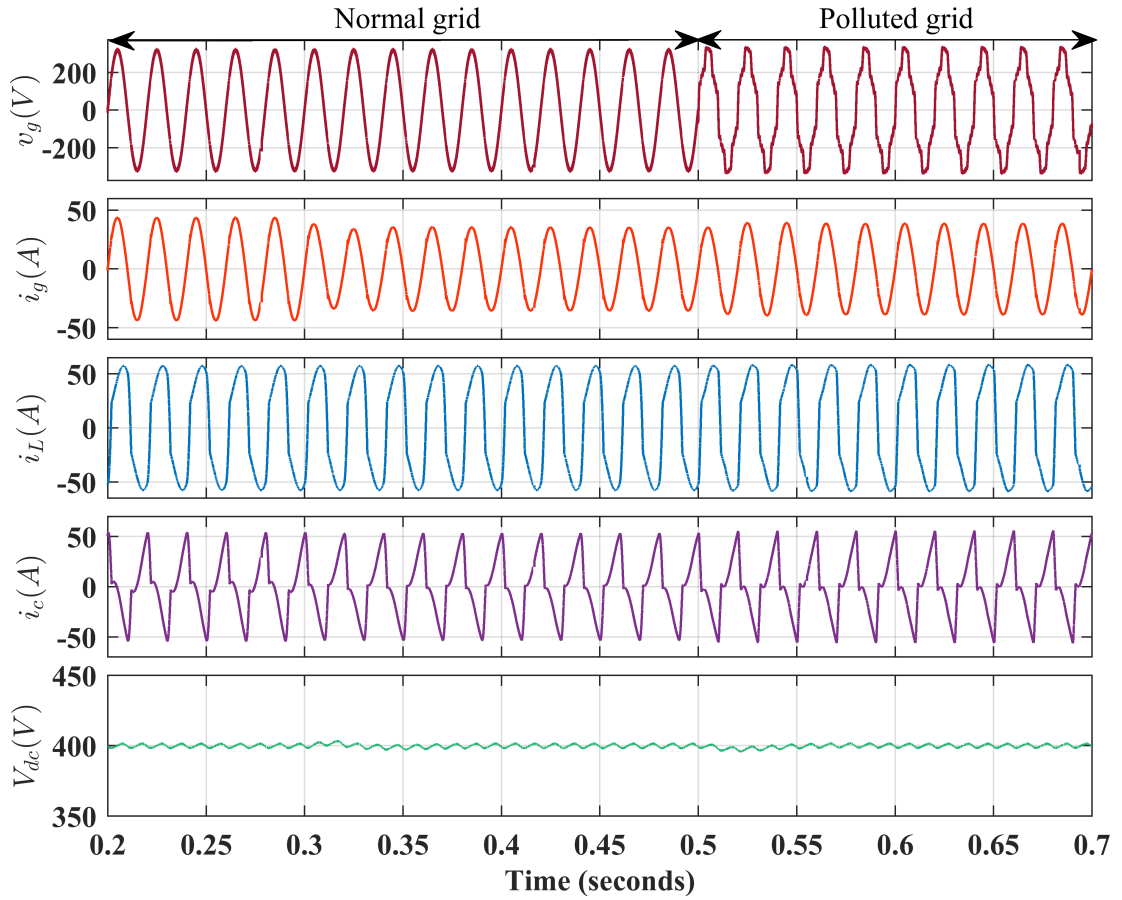


Figure 6.15: Simulation performance for grid parameters of single-phase double-stage grid-connected PV system

condition feeding non-linear load current, the grid current is sinusoidal. The DC-link voltage is maintained to 400V by the PI controller. The irradiance level has been increased to  $1000W/m^2$  at  $t=0.3s$ . During this condition, as the PV current increases the compensator started giving more power hence, the grid current is de-



creased at  $t=0.3s$ .

THD analysis of the grid-parameters of AC signals have been shown in Fig. 6.16. In

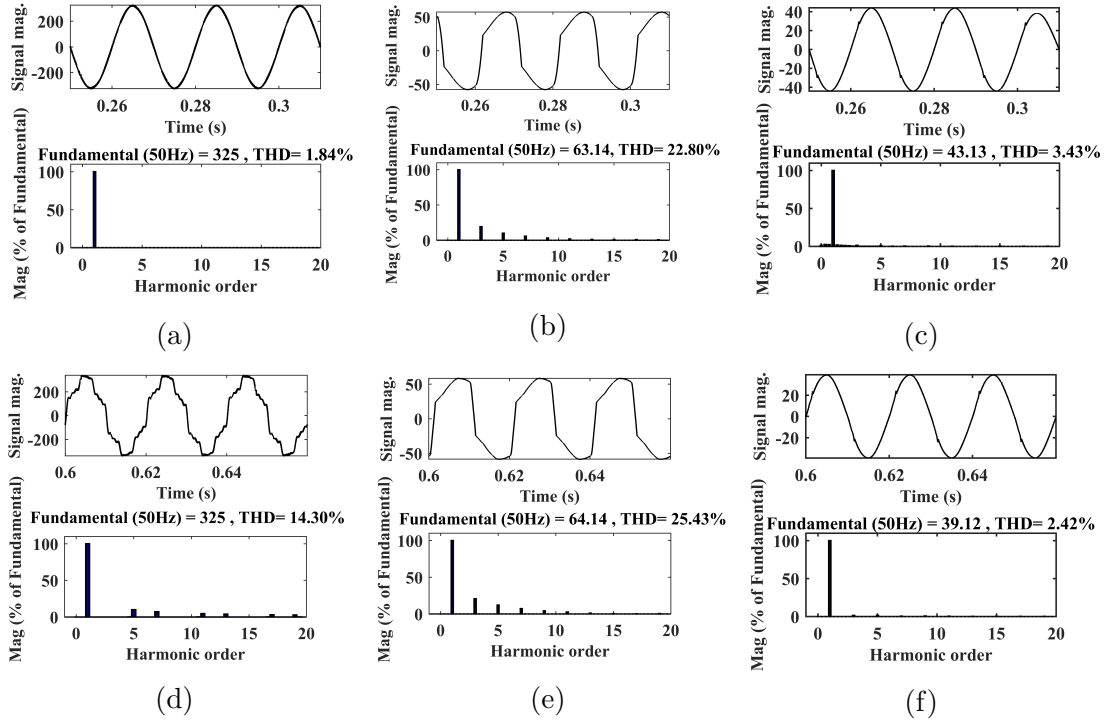


Figure 6.16: THD analysis for single-phase double-stage grid-connected PV system with SRFT technique with additional LPF, Case I: Standard/Normal grid (a) THD of  $v_g$  (b) THD of  $i_L$  (c) THD of  $i_g$   
Case II: Polluted grid (d) THD of polluted grid ( $v_g$ ) (e) THD of  $i_L$  (f) THD of  $i_g$

Case I, normal grid condition has been considered and simulated. The THD of the grid voltage is 1.84% (6.16(a)) and the THD of the non-linear load current (6.16(b)) is 22.80%. The quality of current has been improved to 3.43% as per IEEE Std.519 is shown in Fig. 6.16(c). In Case II, polluted grid condition has been considered and simulated. The THD of the grid voltage is 14.30% (6.16(d)) and the THD of the non-linear load current (6.16(e)) is 25.43%. The quality of current has been improved to 2.42% (6.16(f)), which follows IEEE Std.519.

Figure 6.17 shows the simulation results for power measured at PCC. At  $t=0.25s$  the active and reactive load demand is 8.32kW and 6.00kVar respectively. Power supplied by the grid is 7.14kW and the reactive power demanded by the load is compensated by the VSC. At  $t=0.3s$ , irradiance level has been increased from  $500W/m^2$  to  $1000W/m^2$  and in this condition the load demand has not been changed. The

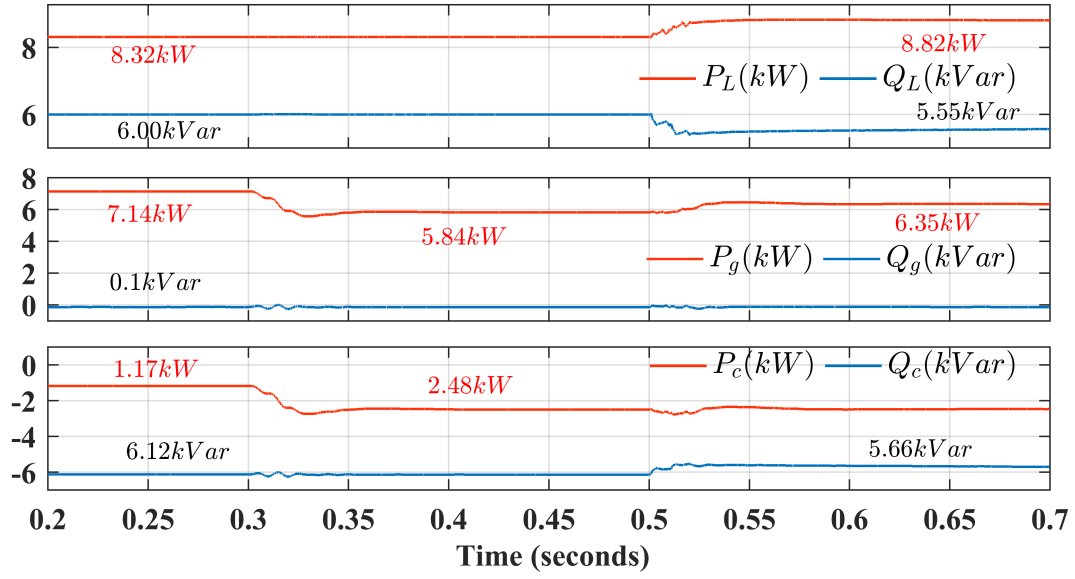


Figure 6.17: Simulation performance for power transfer under single-phase double-stage grid-connected PV system

VSC power has been increased to 2.48kW and the active power supplied by the grid is decreased to 5.84kW. During the polluted grid condition ( $t=0.5$ s to  $t=0.7$ s), the load demand has been changed to (8.82kW, 5.55kVar). At this situation, the active power of 6.35kW is supplied by the grid and active power of 2.48kW is supplied by the PV via single-phase VSC.

### 6.3 Performance of SOGI-ROGI Control in a Single-Phase Grid-Connected PV System

The complete control structure with SOGI-ROGI control for single-stage and double-stage grid-connected are presented in Fig. 6.18 and 6.19 respectively.

Simulation for both single-phase single-stage and double-stage has been done in

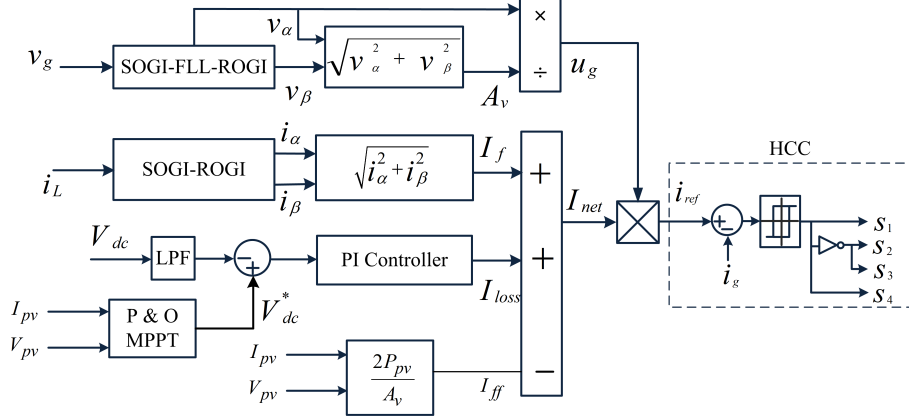


Figure 6.18: Single-phase single-stage SOGI-ROGI control structure for grid-connected PV system

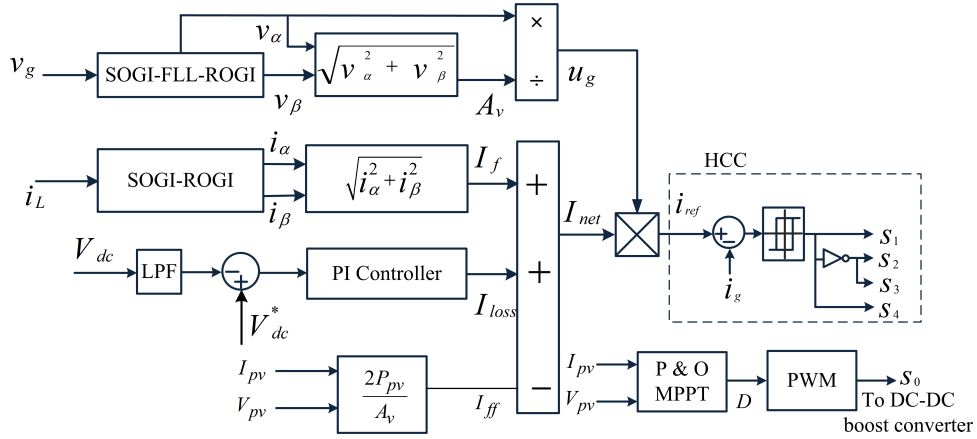


Figure 6.19: Single-phase double-stage SOGI-ROGI control structure for grid-connected PV system

MATLAB/Simulink environment. In both the configuration, the simulation has been done for normal grid conditions as well as polluted grid conditions. Dynamics performance of PV has also been analysed by changing the irradiance level for PV

array under non-linear load condition. Experimental results has also been added for the single-stage grid-connected PV system.

### 6.3.1 Simulation Performance for Single-Stage Grid-Connected PV System

Figure 6.20 shows the performance of the PV under steady-state and dynamic conditions. Initially, the irradiance is  $500\text{W}/\text{m}^2$  and later at it changed to  $1000\text{W}/\text{m}^2$

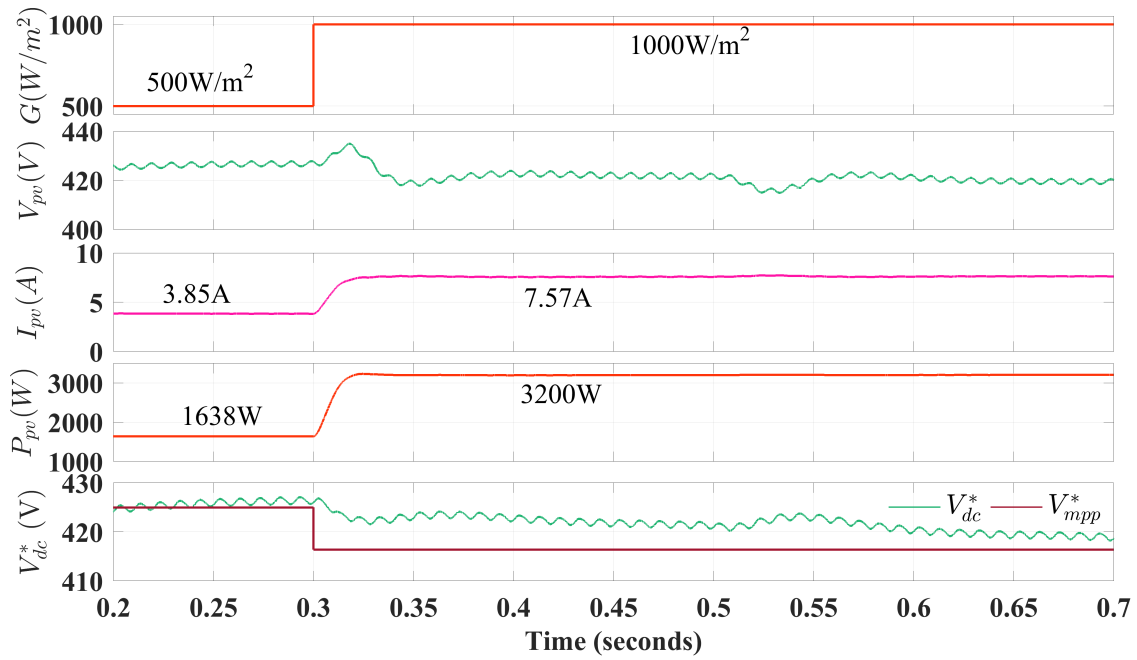


Figure 6.20: Simulation performance of PV string under single-stage grid-connected PV system

at  $t=0.3\text{s}$ . When the solar irradiance is  $500\text{W}/\text{m}^2$ , then the PV current and power are 3.85A and 1638W respectively. And at  $t=0.3\text{s}$  the irradiance has increased to  $1000\text{W}/\text{m}^2$  then the current doubles to 7.57A and power achieved from PV panel is 3200W. The efficiency of the PV string achieved is 98.52%. The reference DC-link voltage ( $V_{dc}^*$ ) has changed according to the MPPT technique to achieve maximum power from PV.

Figure 6.21 shows the grid parameters such as grid voltage, grid current, load current, compensator current and the DC-link voltage (top to bottom) for the single-

phase grid connected PV system. The DC-link voltage is regulated to the DC-

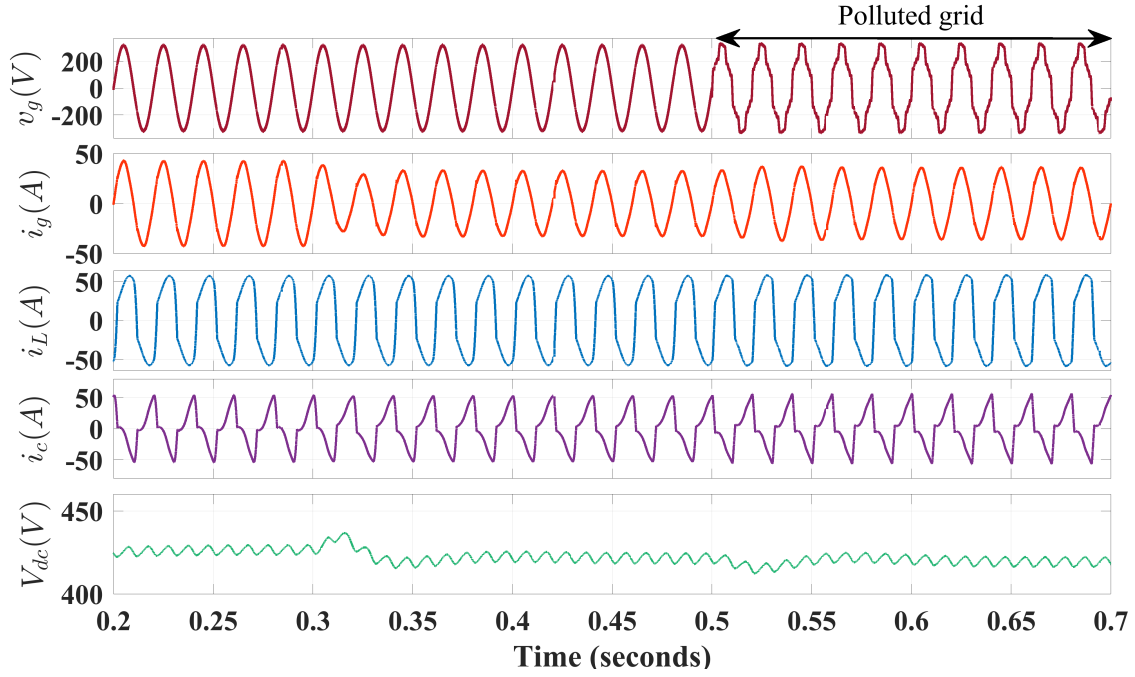


Figure 6.21: Simulation performance for grid parameters of single-phase single-stage grid-connected PV system

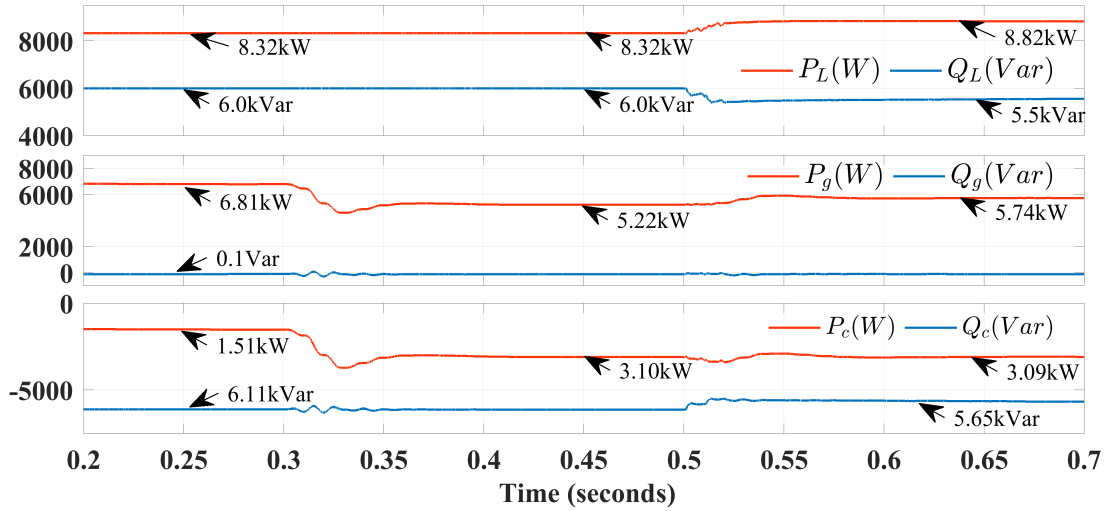


Figure 6.22: Simulation performance for power transfer under single-phase single-stage grid-connected PV system

link reference voltage which is estimated by the P&O MPPT technique. Also, the grid current reduces at  $t=0.3s$  as the PV irradiance increases from  $500W/m^2$  to  $100W/m^2$ . During  $t=0.5s$  to  $t=0.7s$ , the grid becomes polluted with harmonics

(THD 14.32%) and even under this worst case the grid current is sinusoidal and in phase with the grid.

Figure 6.22, shows the power performance of the supply, load and the compensator under irradiance change and the change in grid voltage condition. Initially, before  $t=0.3s$ , the grid voltage has normal waveform and the irradiance is  $500W/m^2$ , during this case power demanded by the load (8.32kW,6.0kVar). The reactive power is supplied by the VSC (6.11kVar) and the active power is supplied by both the PV and the grid. Same has been followed during at higher irradiance and at polluted grid condition.

Figure 6.23, shows the THD analysis of the different grid parameters under both normal grid and the polluted grid under non-linear load current. In first case, irradiance is  $500w/m^2$  and grid voltage is normal (THD=2.03%) and the load current THD is 22.81%. By applying the SAPF operation the grid current THD is 3.79% which is under the IEEE Std. 519. In case II, the irradiance has been increased to  $1000W/m^2$  and the grid is polluted and its THD is 14.32% the THD of the non-linear load current is 25.45%. In this scenario, THD of the grid current obtained is 3.20%.

Hence, these simulation results shows that the single-stage single-phase grid-connected PV system, the active and reactive power injection and the mitigation of harmonics effectively under simulation environment.

### **6.3.2 Experimental Performance for Single-Phase Single-Stage Grid-Connected PV System**

A prototype of single-phase single-stage grid-connected system has been made in the laboratory. The experimental steady-state performance has been shown in Fig. 6.24. A non-linear load has been connected to the grid consuming power of 379W and the THD of the load current is 27.6% and shown in Figure 6.24(a)-(c). PV simulator is feeding 1kW to grid at DC side of the VSC. Here, after losses in the VSC is delivering power of 0.87kW (Fig. 6.24(e)). Normal grid voltage has been applied

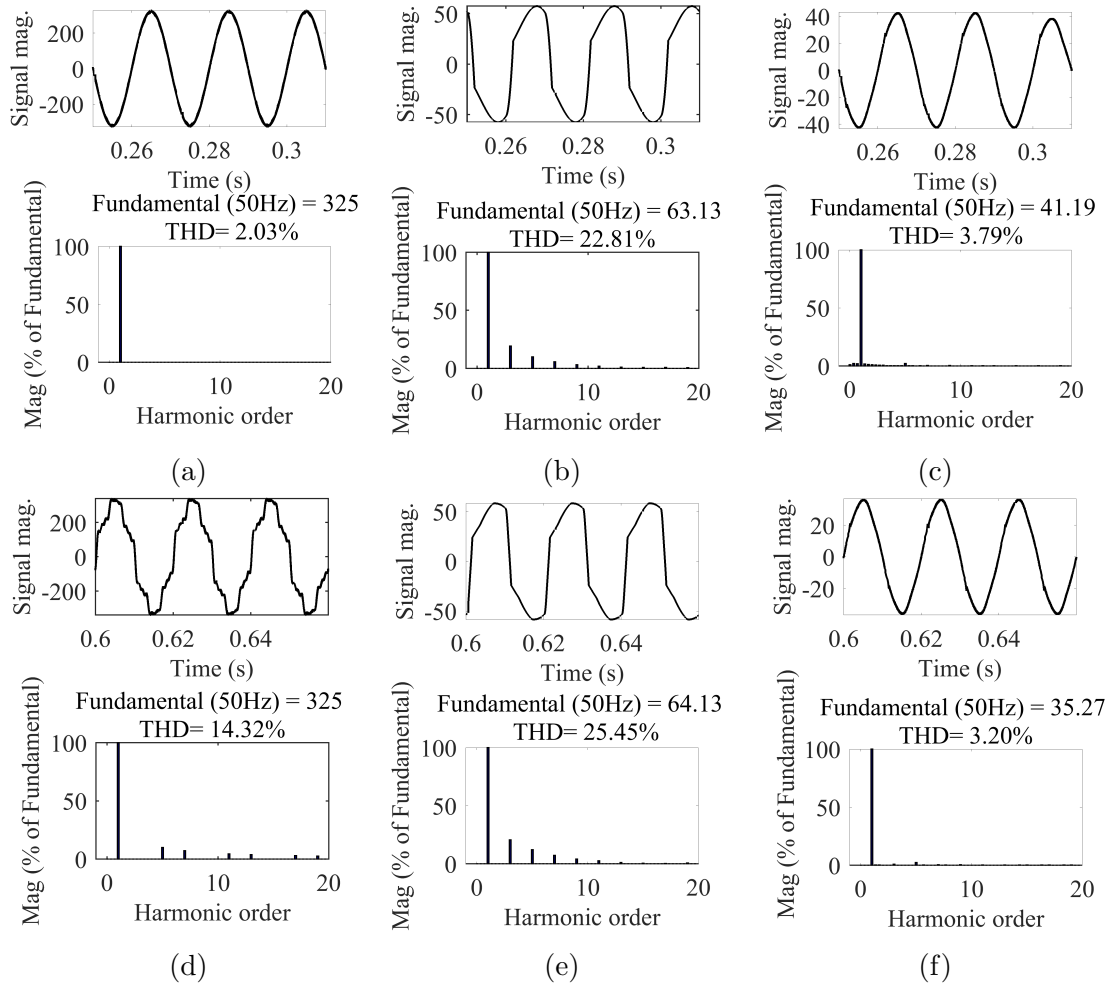


Figure 6.23: THD analysis for single-phase single-stage grid-connected PV system with SOGI-ROGI technique, Case I: Standard/Normal grid (a) THD of  $v_g$  (b) THD of  $i_L$  (c) THD of  $i_g$  Case II: Polluted grid (d) THD of polluted grid ( $v_g$ ) (e) THD of  $i_L$  (f) THD of  $i_g$

and its THD is 2.4% as shown in Fig. 6.24(f). The quality of grid current has been improved to 4.7% (Fig. 6.24(g)), which follows the IEEE Std. 519. The extra power of 498W (Fig. 6.24(i)) has been transferred to the grid.

### 6.3.3 Simulation Performance for Double-Stage Grid Connected PV System

Figure 6.25, 6.26, 6.27 and 6.28 shows the simulation performance of single-phase double-stage grid-connected PV system under normal and polluted grid connected system feeding combination of non-linear load. DC-DC boost converter has been

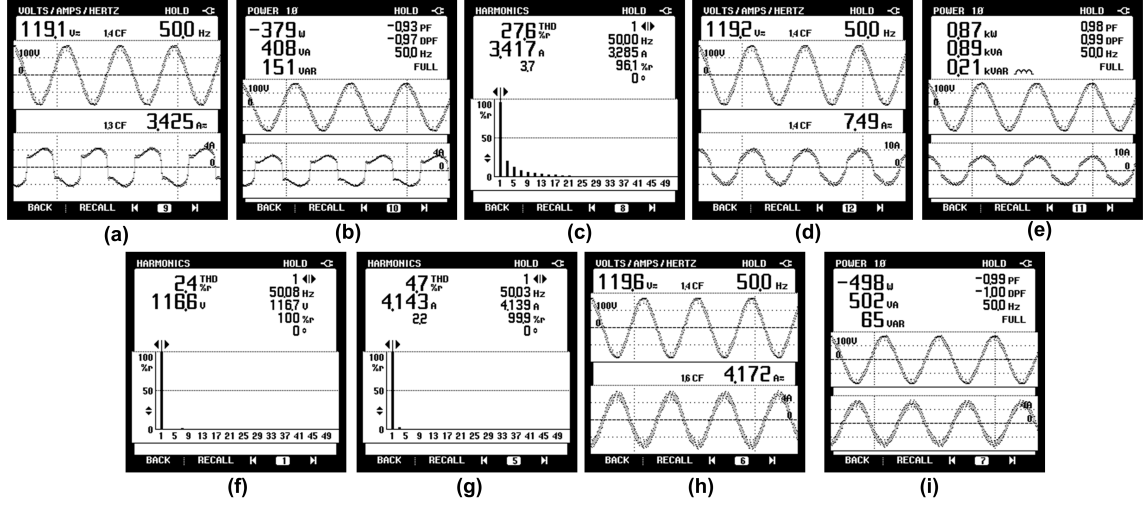


Figure 6.24: Experimental closed-loop steady-state performance of PV array under single-stage grid-connected PV system

used to implement MPPT technique. MPPT technique estimates the duty ratio for the DC-DC boost converter to achieve maximum power from the PV. A PV array has been consist of two string and each string has 6 PV modules with the capacity of 2706.6W under STC.

Figure 6.25, shows the performance of PV array under irradiance of  $500W/m^2$  and  $1000W/m^2$  under double-stage mode. The calculated voltage for maximum power at STC is 173V while the achieved voltage at STC is 176V nearer to maximum power voltage. Power achieved by PV array at  $t=0.23$  s is 1280W and at  $t=0.5$ s is 2623W. The current is 7.10A when the irradiance is  $500W/m^2$  and 14.91A at  $1000W/m^2$  as the PV is the current source and varies according to the irradiance level. The efficiency of PV array achieved is 96.93%. Duty cycle has been estimated by the MPPT to achieve maximum power and given to boost converter.

Figure 6.26, shows the main grid parameters for the SAPF. The grid current ( $I_g$ ) reduces as the irradiance increased to  $100W/m^2$  from  $500W/m^2$  at  $t=0.3$ s. The DC-link has been maintained all the time at DC-link reference voltage at 400V. The waveform of grid current is sinusoidal and in-phase with the grid voltage during both normal and polluted grid condition.

Figure 6.27, shows the analysis of power of single-phase double-stage grid-connected



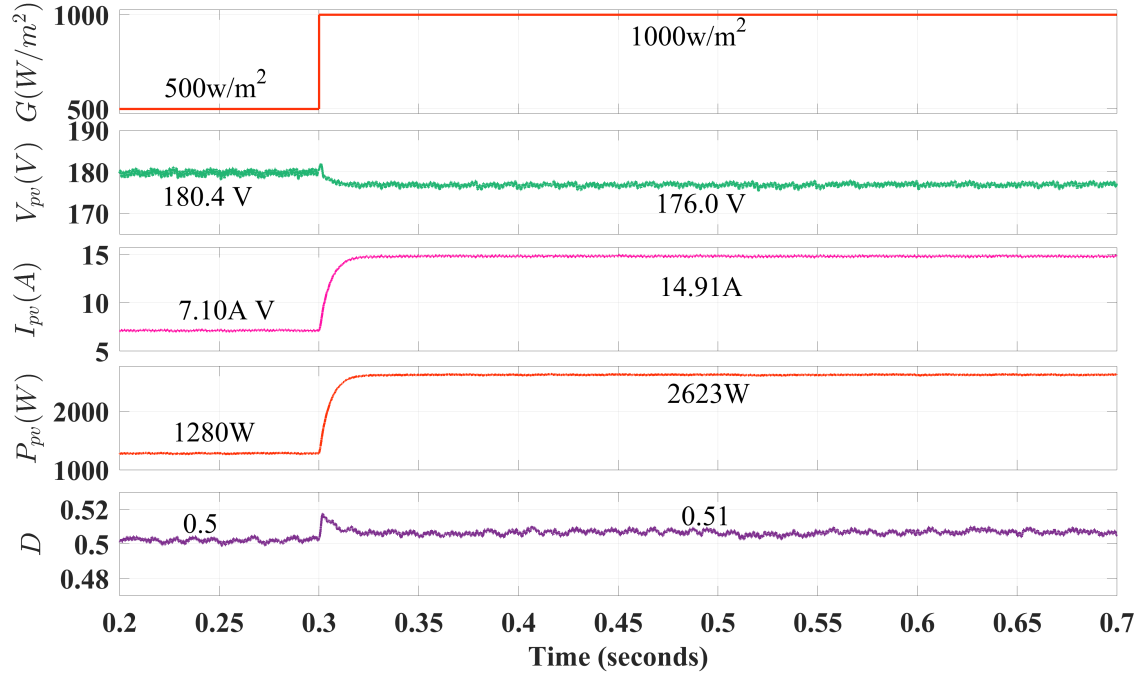


Figure 6.25: Simulation performance of PV array for double-stage grid-connected PV system with varying irradiance level

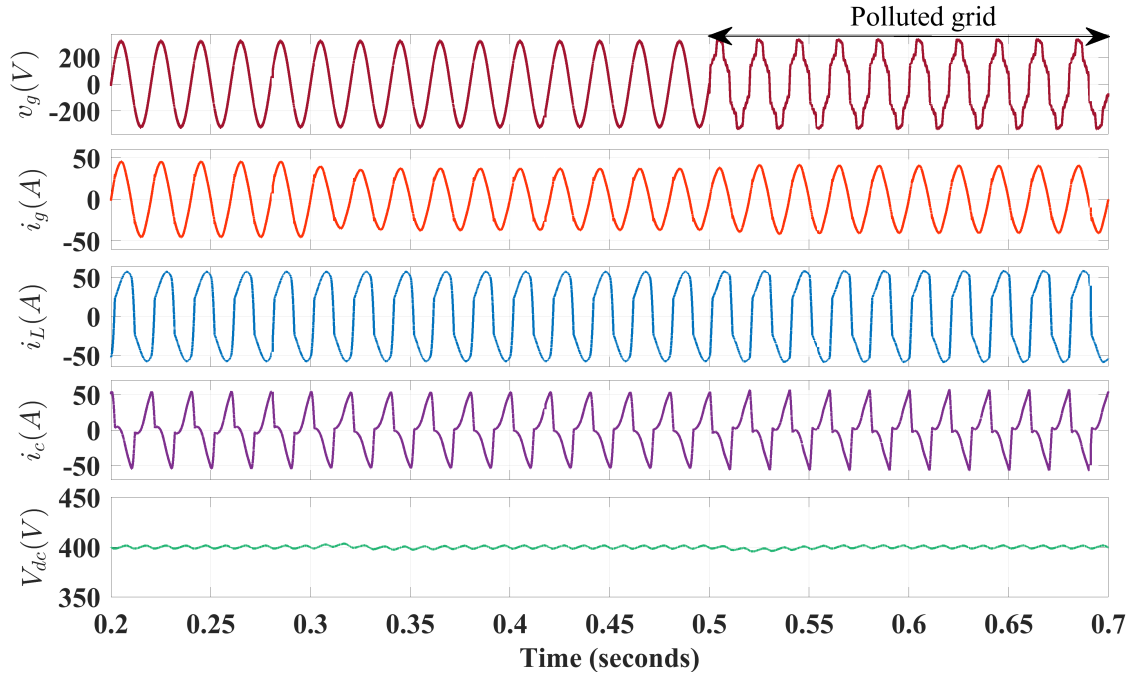


Figure 6.26: Simulation performance for grid parameters of single-phase double-stage grid-connected PV system

PV system at different grid voltage and irradiance conditions. At  $t=0.25s$ , irradiance is  $500W/m^2$  and grid is normal, the power of load, supply and the compensator

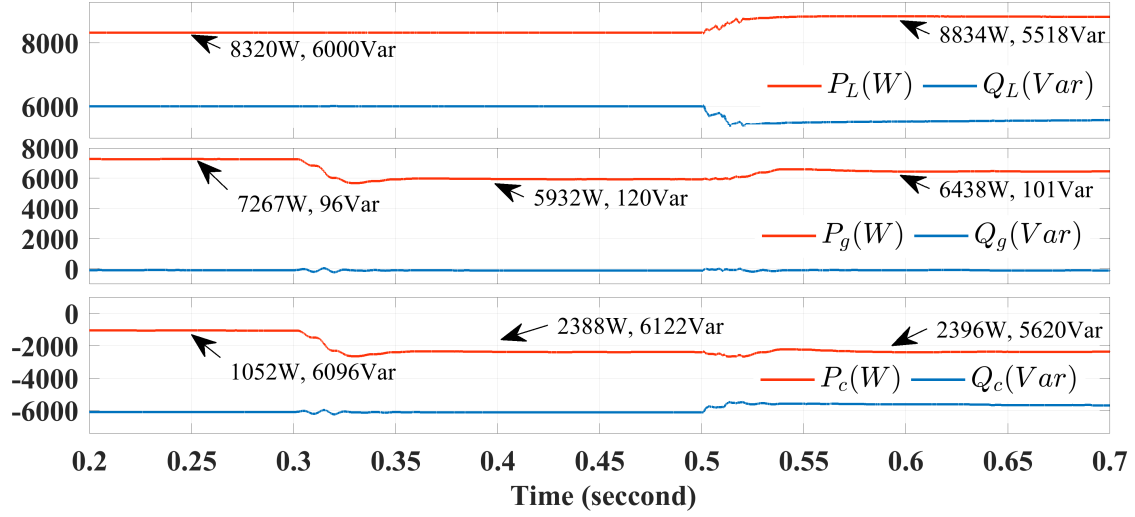


Figure 6.27: Simulation performance for power transfer under single-phase double-stage grid-connected PV system

are (8320W, 6000Var), (7267W, 96Var) and (1052W, 6096Var) respectively. Here, it is clearly observed that the reactive power demanded by the load is supplied by the compensator and the active power demanded by the load is supplied by both grid and the compensator. 228W of PV power is lost in boost converter and VSC. Similarly, the performance of the system has been followed and shown in Fig. 6.27 during the solar irradiance of  $1000W/m^2$  and under polluted grid voltage condition. Figure 6.28, shows the THD analysis of the different grid parameters under both normal grid and the polluted grid under non-linear load current. In first case, irradiance is  $500W/m^2$  and grid voltage is normal (THD=1.82%) and the load current THD is 22.81%. By applying the SAPF operation the grid current THD is 3.96% which follows the IEEE std. 519. In case II, the irradiance has been increased to  $1000W/m^2$  and the grid is polluted and its THD is 14.32% and the THD of the non-linear load current is 25.45%. In this scenario, THD of the grid current obtained is 3.29%.

A comparison table has been drawn on the basis of simulation performances of SRFT with additional LPF and SOGI-ROGI control algorithm in single-stage and double-stage system under normal and polluted grid condition feeding non-linear load. The summary of the simulation performance has been shown in Table 6.1. The THD of

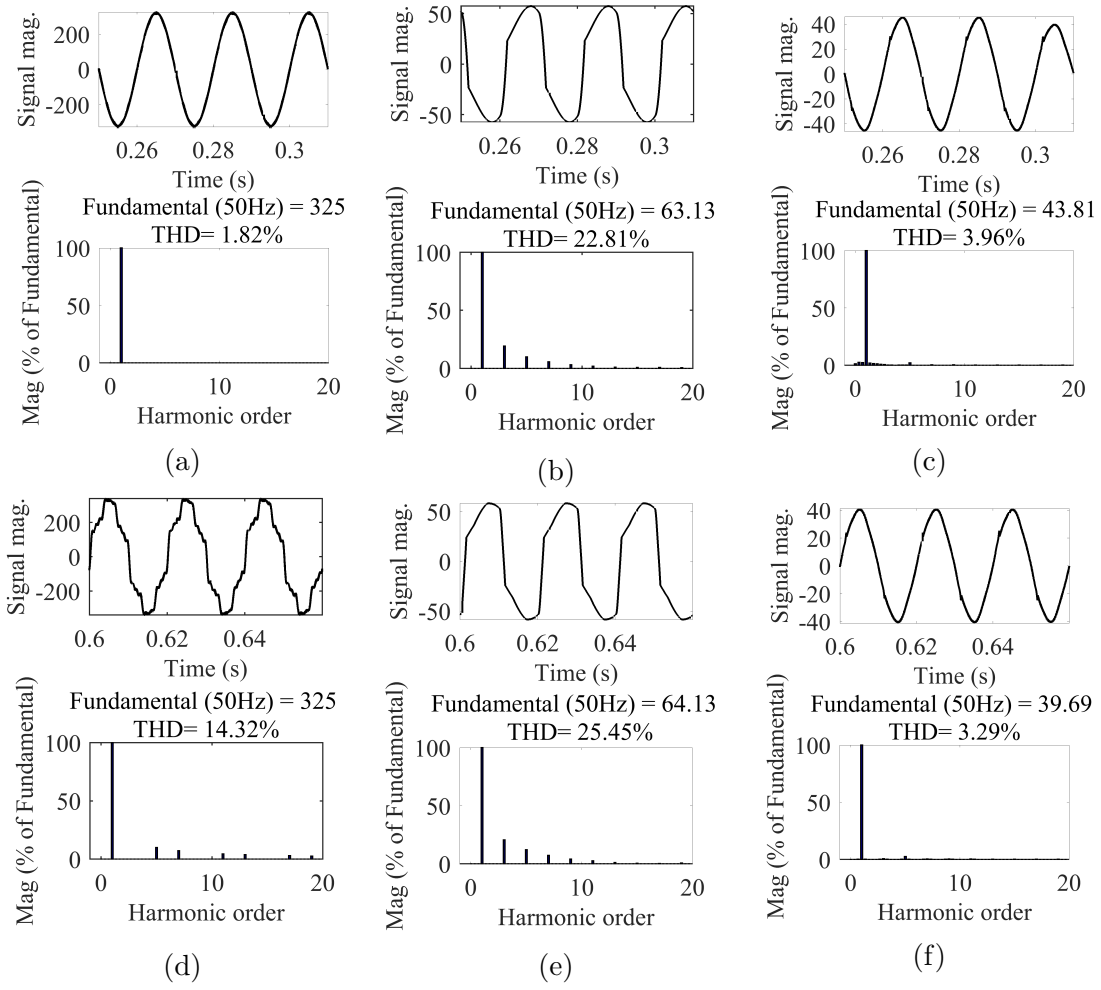


Figure 6.28: THD analysis for single-phase double-stage grid-connected PV system with SOGI-ROGI technique, Case I: Standard/Normal grid (a) THD of  $v_g$  (b) THD of  $i_L$  (c) THD of  $i_g$   
Case II: Polluted grid (d) THD of polluted grid ( $v_g$ ) (e) THD of  $i_L$  (f) THD of  $i_g$

Table 6.1: Performance summary of SRFT and SOGI-ROGI control algorithm for single-stage and double-stage grid-connected PV system

Parameters		Double-stage		Single-stage	
		SRFT	SOGI-ROGI	SRFT	SOGI-ROGI
Normal grid (THD)	$v_g$	2.0%	2.03%	1.84%	1.82%
	$i_L$	22.8%	22.81%	22.8%	22.81%
	$i_g$	3.79%	3.79%	3.43%	3.96%
Polluted grid (THD)	$v_g$	14.30%	14.32%	14.30%	14.32%
	$i_L$	25.43%	25.45%	25.43%	25.45%
	$i_g$	5.11%	3.2%	2.42%	3.29%
PV power(kW)	$P_{pv}$	3.21kW	3.20kW	2.65kW	2.62kW
PV efficiency(%)	$\eta$	98.95%	98.52%	97.93%	96.93%

the grid current is same in single-stage grid-connected PV system for both SRFT and SOGI-ROGI control algorithm. But during the polluted grid condition SRFT shows the THD of 5.11% while the SOGI-ROGI shows 3.2% in single-stage system. During the polluted grid condition the THD performance by SRFT is better than SOGI-ROGI control technique. Efficiency of the PV is higher in single-stage than double-stage grid-connected PV system.

## 6.4 Conclusions

In this chapter SRFT and SOGI-ROGI control algorithms have been designed and applied for the single-phase single-stage and single-phase double-stage system for active power injection and reactive power compensation. Extensive simulation has been done for single-phase single-stage and double-stage grid-connected PV system. performance of SRFT control is not as per standard it requires additional LPF to improve the performance SRFT control algorithm. Even after using the additional LPF its performance is not satisfactory during polluted grid condition. SOGI-ROGI performs consistently in single-stage and double-stage grid condition under both normal and polluted grid condition. Efficiency of PV is better in the single-stage system than the double-stage grid-connected PV system. Experimental performance of SOGI-ROGI has also been added in this section for single-stage grid-connected PV system. The performance clearly approves the active and reactive power injection to the grid efficiently as per load demand and PV power generation. The power quality has been improved in both the cases under non-linear load and polluted grid voltage.

## Chapter 7

# Power Quality Improvement in Three-Phase Grid-Connected PV System

In this Chapter, three-phase single-stage and double-stage grid-connected PV system has been developed for power quality improvement under non-linear load condition. Both the proposed systems have been analysed under normal grid and polluted grid condition. Conventional SRFT control technique has been applied for the three-phase single-stage and double-stage grid-connected PV system. Modelling of proposed Improved Adaline (IAdaline) has been done and used for estimation of synchronization signals and estimation of fundamental component. The performance of IAdaline technique has been compared with three-phase SRFT technique. Extensive simulation and experimental analysis has been done under different conditions, which justifies the suitability for the active and reactive power injection along with the capability of harmonic mitigation.

### 7.1 Three-Phase Single-Stage and Double-Stage SAPF for Grid-Connected PV System

Figure 7.1 and Fig. 7.2 show the system configuration for three-phase single-stage and double-stage grid-connected PV system respectively. In Fig. 7.1, PV string or array is connected to DC-link voltage of the three-phase VSC. In this type of system,

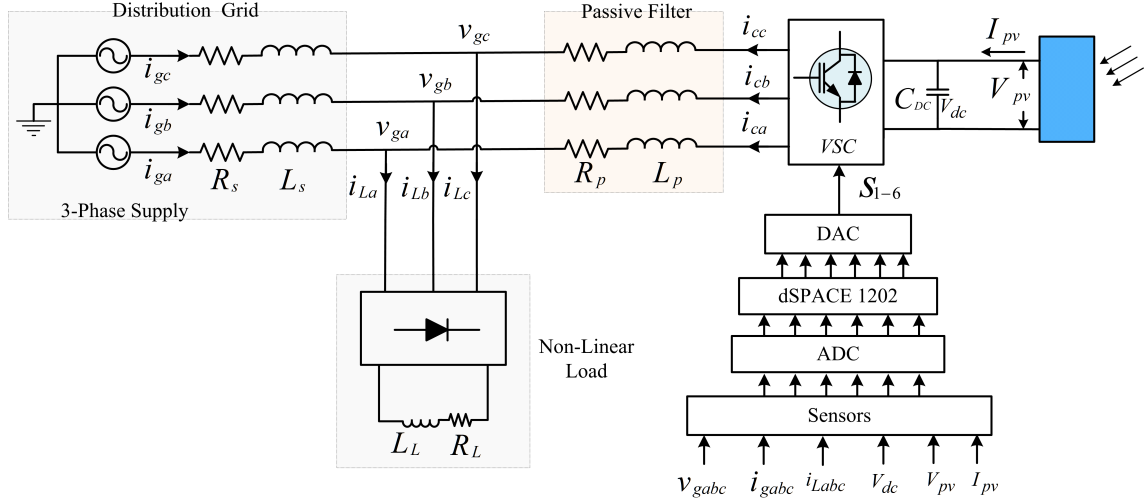


Figure 7.1: Three-phase single-stage grid-connected PV system

no DC-DC converter is required. The output of MPPT technique is used to generate the reference DC-link voltage ( $V_{dcref}$ ). This system can be used for both active and reactive power compensation along with harmonic mitigation of grid current under linear/non-linear load condition.

Figure 7.2 shows the system configuration of three-phase three-wire double-stage grid-connected PV system. In this configuration, a DC-DC boost converter has

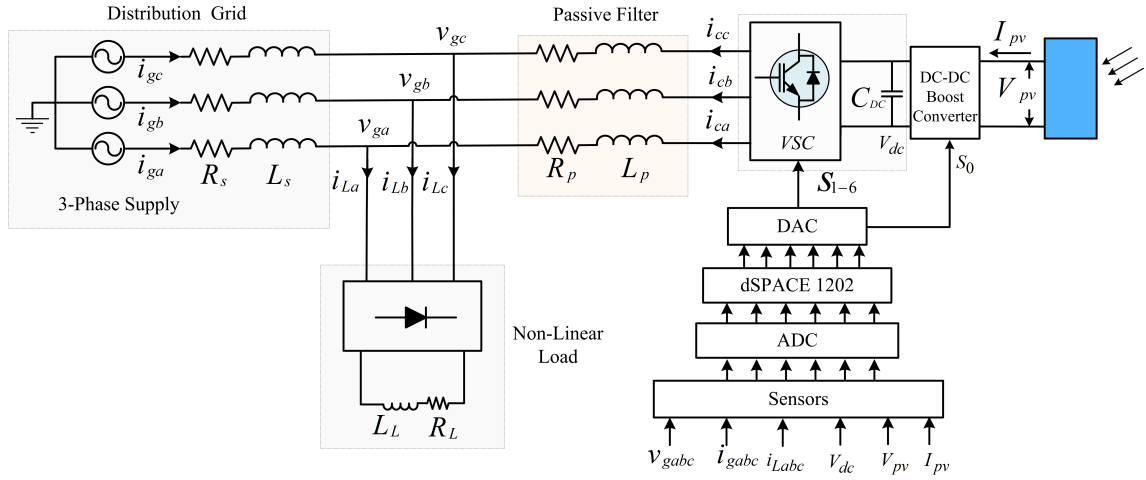


Figure 7.2: Three-phase double-stage grid-connected PV system

been used to level up the PV output voltage. The output of the MPPT technique is duty cycle which is used to control the DC-DC boost converter. In this configuration, lower number of PV module can be used than single-stage grid-connected

PV system.

To ensure the proper working of three-phase grid-connected PV system it require control algorithm. The control algorithm require fundamental load current component, DC-voltage controller, estimation of feed-forward current, an MPPT technique and uni-templates form the three-voltage signal. MPPT technique for the single-stage and double-stage grid-connected PV system has been discussed in previous chapter.

### 7.1.1 Fundamental Load Current Component Estimation

For the estimation of fundamental load current component conventional SRFT control technique and the proposed IAdaline technique has been designed and discussed.

#### 7.1.1.1 Three-Phase SRFT Control Technique

The three-phase balanced non-linear load contains harmonics and the respective equations are-

$$i_{La}(t) = I_{fa} \sin(\omega_i t) + H_n(t) \quad (7.1)$$

$$i_{Lb}(t) = I_{fb} \sin(\omega_i t - \frac{2\pi}{3}) + H_n(t) \quad (7.2)$$

$$i_{Lc}(t) = I_{fc} \sin(\omega_i t + \frac{2\pi}{3}) + H_n(t) \quad (7.3)$$

In above equations,  $I_{fa}$ ,  $I_{fb}$  and  $I_{fc}$  represent the fundamental components of the load current and  $H_n(t)$  denotes the harmonic component in the load current.

$$\begin{bmatrix} I_d \\ I_q \\ I_0 \end{bmatrix} = \begin{bmatrix} \sin \theta_o & -\cos \theta_o & 0 \\ \cos \theta_o & \sin \theta_o & 0 \\ 0 & 0 & 1 \end{bmatrix} \begin{bmatrix} i_{La} \\ i_{Lb} \\ i_{Lc} \end{bmatrix} \quad (7.4)$$

The active ( $I_d$ ) and reactive component ( $I_q$ ) can be estimated with the help of  $abc$  to  $dq0$  Park transformation. When the rotating frame is aligned behind  $90^\circ$  the  $\alpha$ -axis, Park transformation can be depicted in equation 7.4. The d-component or active

component of the load current contains the AC components also. Hence, it requires additional LPF to get the filtered active load component ( $\bar{I}_d$ ).

#### 7.1.1.2 Improved Adaline Control Technique

Modelling of Adaline has been discussed in Section 4.2.3.1. As the conventional Adaline works with a fixed intelligent factor and thus its performance may not always optimum under steady-state and dynamics conditions. Hence, an Improved Adaline based algorithm has been designed for extraction of fundamental load component estimation from the non-linear load current. The proposed algorithm is applied to the voltage signal to extract the unit template for synchronization of the VSC to the grid and other parameters of the signal such as phase, frequency and amplitude and is already discussed in Section 4.2.3.2. Figure 7.3 shows the structure of the designed algorithm for the fundamental estimation of phase "a" non-linear load current.

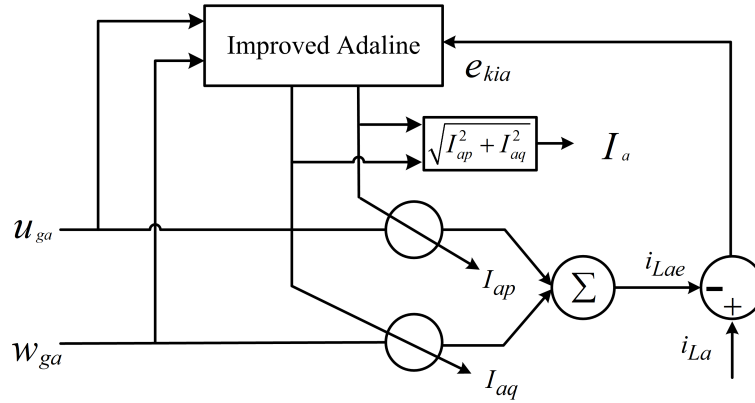


Figure 7.3: Structure of Improved Adaline control technique

Here, the error between the estimated and actual current signal in a-phase is expressed as-

$$e_{kia} = i_{La} - i_{Lae} \quad (7.5)$$

$e_{kia}$  is the error in the load current signal of phase "a",  $i_{La}$  and  $i_{Lae}$  denote the actual and estimated load current signal. The estimated load current is given as in (7.6).

$$i_{gae} = i_{ap1}u_{ga} + i_{aq1}w_{ga} \quad (7.6)$$



Here,  $i_{ap1}$  and  $i_{aq1}$  are the active and reactive fundamental weights of the a-phase load current.  $u_{ga}(\sin \theta_{ao})$  and  $w_{ga}(\cos \theta_{ao})$  denote the in-phase and quadrature phase unit templates of the grid voltage. The weights are updated using 7.7 and 7.8.

$$I_{ap}(k+1) = I_{ap}(k) + \alpha_{ia} e_{kia} u_{ga} \quad (7.7)$$

$$I_{aq}(k+1) = I_{aq}(k) + \alpha_{ia} e_{kia} w_{ga} \quad (7.8)$$

Where,  $\alpha_{ia}$  is the learning rate to update the weights. The conventional Adaline uses a fixed learning rate. The performance of conventional Adaline algorithm for training and convergence speed can be update further. One simple yet effective way for improving the performance of Adaline algorithm is by making the learning rate ( $\alpha_{ia}$ ) variable instead of a constant value. This is achieved by incorporating an additional term as shown in (7.9) below;

$$\alpha_{ia} = \alpha_{i0} + \alpha_{i1} |\bar{e}_{kia}| \quad (7.9)$$

Above,  $\alpha_{i0}$  and  $\alpha_{i1}$  are both fixed values and  $\alpha_{ia}$  is the improved learning rate. The first term of the learning rate is fixed but the second term is designed to depend on the absolute value of the mean of the error signals. This makes the learning rate inherently adaptive and variable. Under steady state-state conditions, the absolute value of mean error is negligible and at that time learning rate will be constant ( $\alpha_{ia} = \alpha_{i0}$ ). However, during dynamics the value of  $|\bar{e}_{kia}|$  is non-zero and the learning rate will be higher for higher error. Thus ensures faster convergence under both steady-state as well as dynamic conditions. The proposed simple modification helps to automatically achieve the benefits of low learning rate under steady-state conditions and higher learning rate during dynamic conditions. Fig. 7.3 shows the weights  $I_{ap}$  and  $I_{aq}$  obtained using Improved Adaline technique. For a three-phase system, load currents may/may not be equal i.e. unbalanced load may present. The algorithm is designed to work well under any such condition also, so the amplitude of the load current of all the three-phases computed separately. The amplitude of

the a-phase load current is calculated as-

$$I_a = \sqrt{I_{ap}^2 + I_{aq}^2} \quad (7.10)$$

Similarly, for phases b and c, the fundamental load component can be computed by 7.11 and 7.12.

$$I_b = \sqrt{I_{bp}^2 + I_{bq}^2} \quad (7.11)$$

$$I_c = \sqrt{I_{cp}^2 + I_{cq}^2} \quad (7.12)$$

The fundamental component of three-phase current is computed by averaging the fundamental component of the individual phases.

$$I_f = \frac{I_a + I_b + I_c}{3} \quad (7.13)$$

Simulation analysis for differing learning rates using the Improved Adaline technique has been shown in Fig. 7.4. A non-linear load is increased at  $t=0.5s$  and decreased

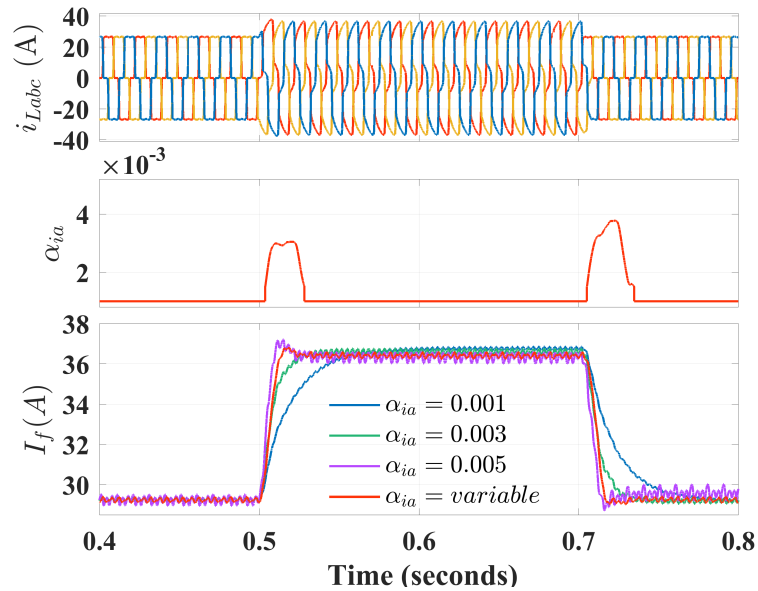


Figure 7.4: Performance comparison of Improved Adaline versus conventional Adaline

back to previous condition at  $t=0.7s$ . For lower learning rate ( $\alpha_{ia} = 0.001$ ) the response is slower but the oscillations are very low. At higher learning rates ( $\alpha_{ia} =$

0.005) the response is faster but the oscillations during steady-state is higher. Here, the proposed Improved Adaline shows lower oscillations during steady-state and faster response during dynamics. The learning rate automatically becomes higher during dynamics as per the absolute mean value of error increases. The maximum value of learning rate has also been selected as 0.005, so that the response does not become unstable during worst case scenerio.

### 7.1.2 Feed-Forward Current Estimation

The PV array transfers active power to the grid as per its capability and rating via VSC. Under ideal conditions, the power generated by PV is delivered to the grid such that  $P_{pv}=P_c$  such that the inverter has negligible loss. Here,  $P_{pv}$  is the power generated by the PV and  $P_c$  represents the AC side power of the VSC. Power calculated at DC link is given as -

$$P_{pv} = V_{pv} I_{pv} \quad (7.14)$$

Active power calculated at three phase ac side of the inverter is given as

$$P_c = 3V_{rms}I_{rms} = \frac{3A_v}{\sqrt{2}} \frac{I_{ff}}{\sqrt{2}} \quad (7.15)$$

Here,  $A_v$  is the magnitude of the voltage signal and  $I_{ff}$  is the feed forward current or peak current magnitude of the VSC current which is injected to the grid. Ideally,

$$P_{pv} = P_{VSC} \implies P_{pv} = \frac{3A_v}{\sqrt{2}} \frac{I_{ff}}{\sqrt{2}} \quad (7.16)$$

$$I_{ff} = \frac{2P_{pv}}{3A_v} \quad (7.17)$$

### 7.1.3 Estimation of Switching Pulses for Three-Phase VSC

Estimation of the switching pulses require the fundamental load component, loss component and the feed forward current for the contribution of PV. The loss com-

ponent is estimated by the output of the PI controller which can be estimated by 7.18. switching of IGBT switches. Some losses occur during switching operation of VSC. Estimation of such losses is obtained with the help of following equation.

$$I_{loss}(n) = I_{loss}(n-1) + k_p[V_{dce}(n) - V_{dce}(n-1)] + k_i V_{dce}(n) \quad (7.18)$$

Here,  $V_{dce}(n) = V_{dc}^*(n) - V_{dc}(n)$  is the evaluated voltage error at DC-link inverter,  $k_p$  and  $k_i$  are the proportional and integral gains of the PI controller. Here,  $V_{dc}^*$  is fixed to 800V for double-stage and it varies as per  $V_{mpp}$  in single-stage grid integrated PV system. Once, the all the three current component estimated the reference currents are generated by multiplying the synchronizing signal to net current. The net current is estimated by adding the load component and subtracting the feed-forward current and is given by 7.19.

$$I_{net} = I_f + I_{loss} - I_{ff} \quad (7.19)$$

The synchronizing signals have been estimated by the IAdaline and was discussed earlier in Section 4.2.3.2. The reference current is estimated by 7.20.

$$\begin{bmatrix} i_a^* \\ i_b^* \\ i_c^* \end{bmatrix} = \begin{bmatrix} u_{pa} & u_{qa} & 1 \\ u_{pb} & u_{qb} & 1 \\ u_{pc} & u_{qc} & 1 \end{bmatrix} \begin{bmatrix} I_{net} \\ 0 \\ 0 \end{bmatrix} \quad (7.20)$$

The reference currents ( $i_{abc}^*$ ) and the sensed grid currents ( $i_{gabc}$ ) have been given to the HCC, which generates the required six pulses to the driver circuit of the VSC. Now, the developed algorithm can be used for the SAPF in three-phase system in single-stage and double-stage grid-connected PV system.

## 7.2 Performance of SRFT Control Algorithm for Three-Phase Grid-Connected PV System

Figure 7.5 shows the control structure for three-phase single-stage grid-connected PV system with SRFT control technique. In this configuration P & O MPPT is

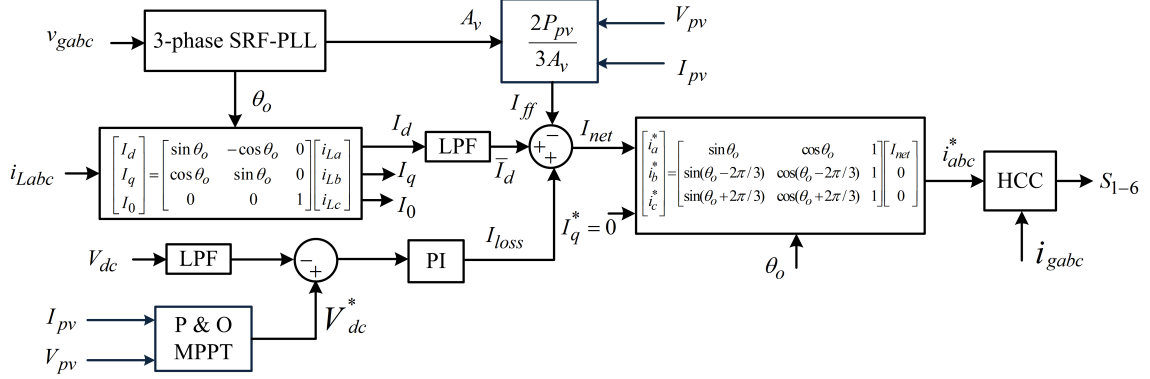


Figure 7.5: Structure of SRFT control technique for three-phase single-stage grid-connected PV system

used to estimate the reference DC-link voltage to achieve maximum power from the PV. Here, in this case the reference DC-link voltage is the MPP voltage of the PV. Three-phase SRF-PLL has been employed to estimate phase angle and the amplitude of the grid-voltage signal. An additional LPF has been employed to filter the fundamental load component. A PV string of 22 panels is used to inject active power to the grid with the maximum power capacity of 5.95kW

Figure 7.6 shows the control structure for three-phase double-stage grid-connected PV system with SRFT control technique. Here, PV array is connected to the DC-DC boost converter and its output is connected to the DC terminal of the three-phase VSC. In this configuration P & O MPPT is used to estimate the duty cycle for the DC-DC boost converter. A PV array of 20 panels consist 2 strings and each having 10 panels is used to inject active power to the grid with the maximum power capacity of 5.41kW.

In next sections, these control structure has been employed to improve PQ and reactive power compensation under different conditions such as irradiance change,

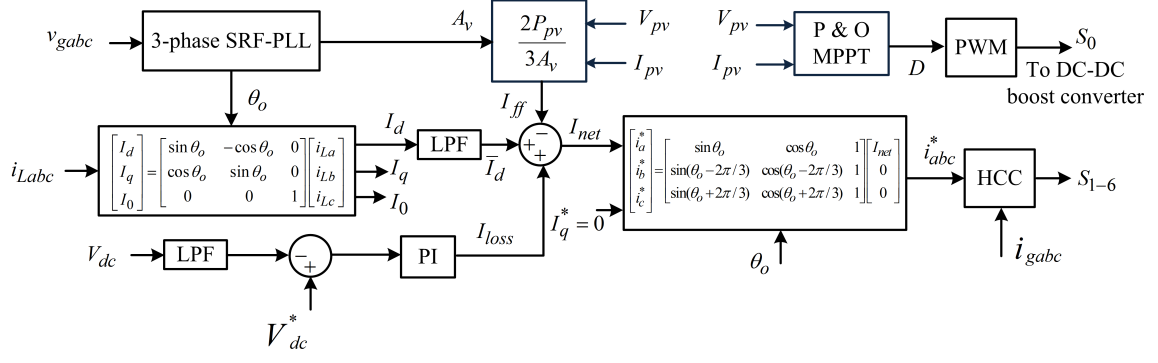


Figure 7.6: Structure of SRFT control technique for three-phase double-stage grid-connected PV system

load unbalance and polluted grid condition.

## 7.2.1 Simulation Results for Single-Stage Grid-Connected PV System

Figure 7.7 shows the simulation performance in a three-phase single-stage grid-connected system with SRFT control technique. Initially, the irradiance level is

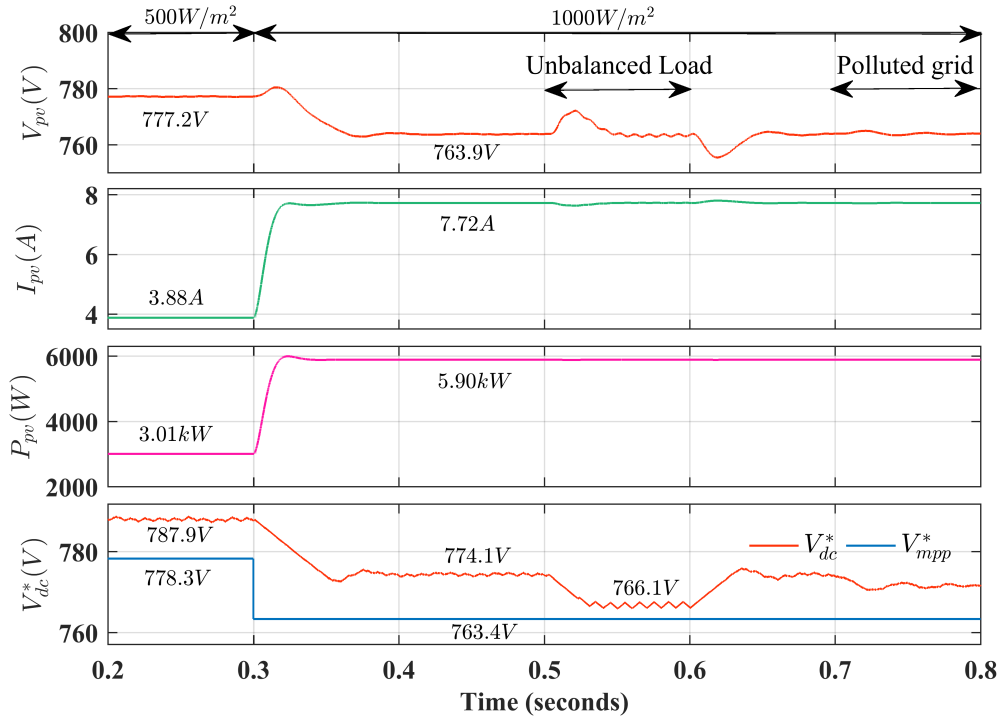


Figure 7.7: Simulation performance of PV string under single-stage grid-connected PV system

$500W/m^2$  and is increased to  $1000W/m^2$  at  $t=0.3s$ . At  $t=0.25s$ , measured value of PV voltage, current and power are 777.2, 3.88A and 3.01kW respectively. The estimated reference MPP voltage is 787.9V while the rated MPP voltage is 778.3V. At  $t=0.45s$ , when the irradiance level is  $1000W/m^2$  the measured PV voltage, current and power are 763.9V, 7.72A and 5.90kW. The estimated reference MPP voltage is 774.1V while the rated MPP voltage is 763.4V. The efficiency achieved from the PV string is 99.09%. PV parameters also vary during the load unbalancing at PCC.

Figure 7.8 shows the SAPF simulation performance showing grid voltages ( $v_{gabc}(V)$ ), load currents ( $i_{Labc}(A)$ ), grid currents ( $i_{gabc}(A)$ ), compensator currents  $i_{cabc}(A)$  and the DC-link voltage  $V_{dc}(V)$ . The grid voltage is normal from  $t=0.2s$  to  $t=0.7s$  and its

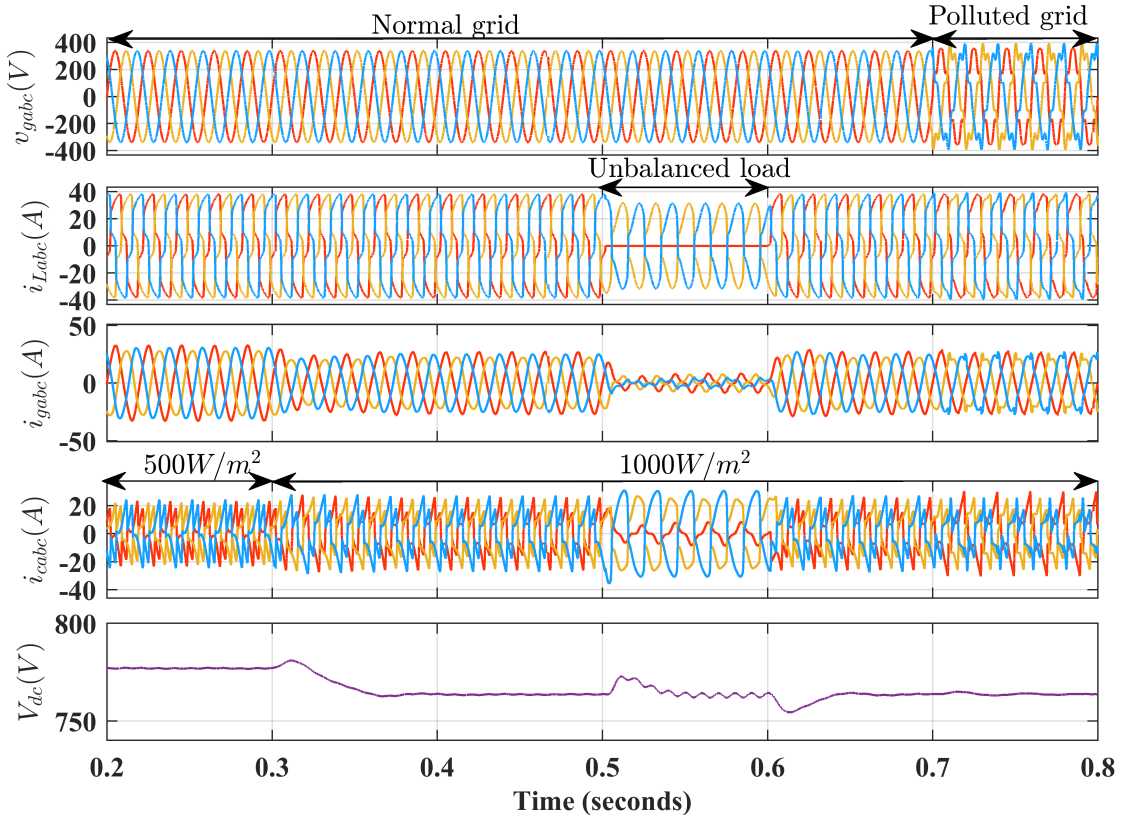


Figure 7.8: Simulation performance for grid parameters of single-stage grid-connected PV system

polluted after  $t=0.7s$ . The load is unbalanced from  $t=0.5s$  to  $t=0.6s$ , in this condition the grid currents are balanced. Irradiance has been increased to  $1000W/m^2$  from  $500W/m^2$  at  $t=0.3s$ . At this condition the compensator current increases and

grid current decreases. DC-link voltage is regulated by the PI controller to estimated reference voltage by P & O MPPT technique.

THD analysis of different grid AC parameters have been shown in Fig. 7.9. In

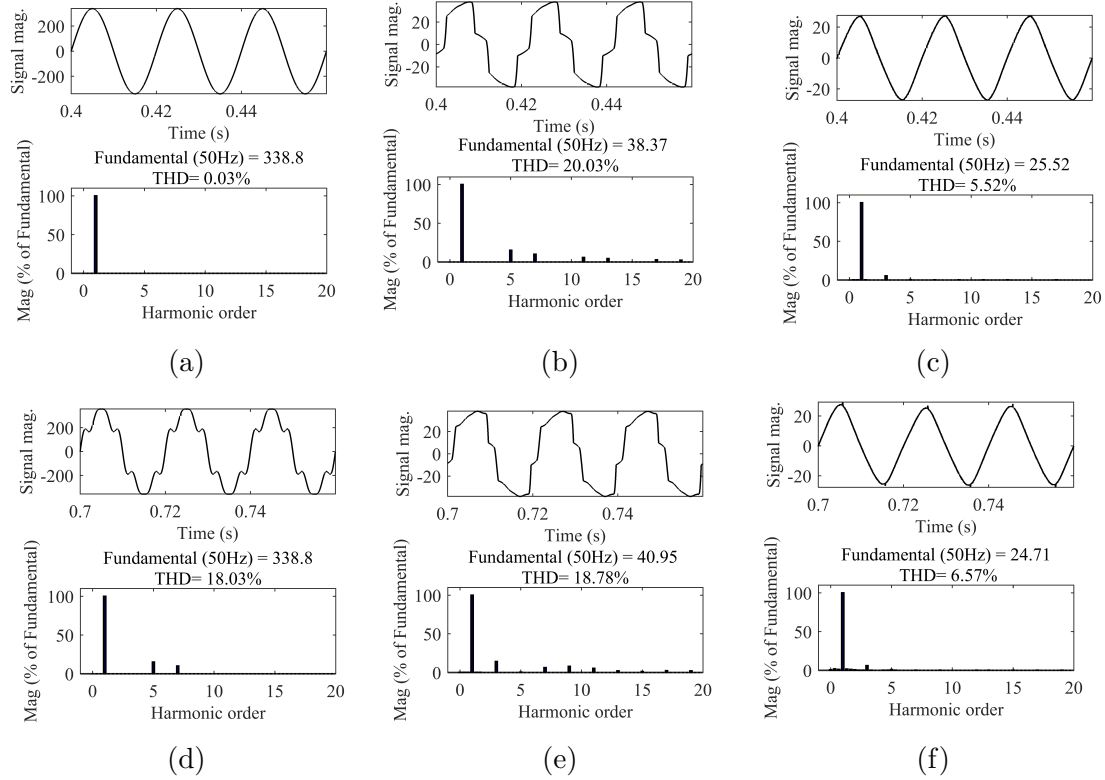


Figure 7.9: THD analysis for single-stage grid-connected PV system with SRFT technique Case I Normal grid (a) THD of  $v_{ga}$  (b) THD of  $i_{Lb}$  (c) THD of  $i_{ga}$  Case II Polluted grid (d) THD of  $v_{ga}$  (e) THD of  $i_{La}$  (f) THD of  $i_{ga}$

case I, when the grid voltage is free from distortion (THD 0.03%) and the THD of the load current of phase-a is 20.03%. THD of the improved grid current is 5.52% as shown in Fig. 7.9(c). In case II when the grid is polluted with the harmonics and its THD is 18.03%. The THD of the non-linear load current is 18.78% and the improved THD of the grid current is 6.57%. SRFT improves the quality of power but it do not follow the IEEE Std.1547.

Power transfer at PCC by the load, grid and compensator are shown in Fig. 7.10. At  $t=0.25s$  during the irradiance level of  $500W/m^2$  active and reactive power demanded by the load are 18.26kW and 6.83kVar. At this condition active power of 2.75kVar is supplied by the PV via compensator and 15.51kW is supplied by the



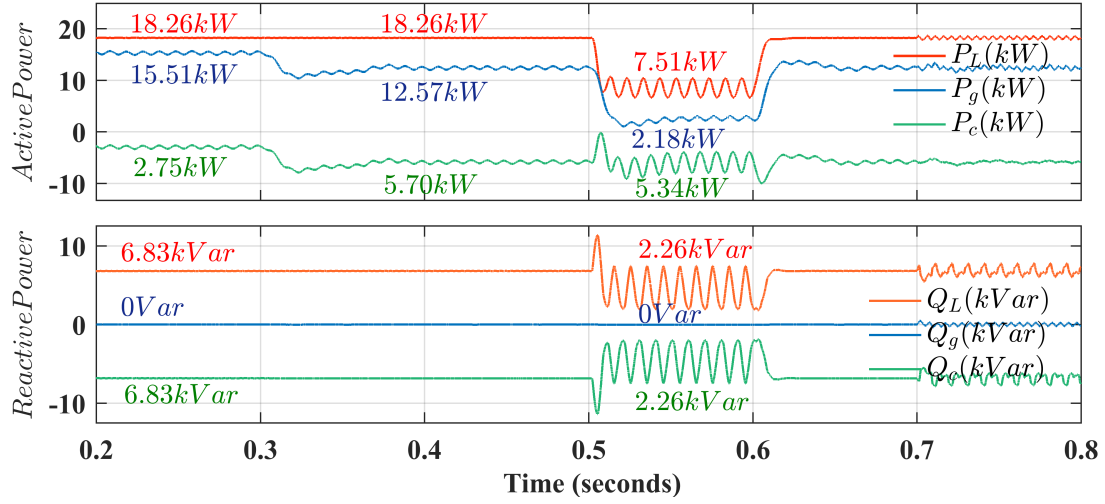


Figure 7.10: Simulation performance for power transfer in single-stage grid-connected PV system

grid. The reactive power of 6.83kW demanded by the load is supplied by compensator. At  $t=0.3s$ , the irradiance level has been increased to  $1000W/m^2$  the PV power contribution increases to 5.70kW and the grid power reduces to 12.57kW. During the unbalanced condition the instantaneous active and reactive power demanded by load are 7.51kW and 2.26kVar. Active power supplied by the compensator is 5.34kW and 2.18kW power is supplied by the grid.

## 7.2.2 Simulation Results for Double-Stage Grid-Connected PV System

Figure 7.11 shows the simulation performance in a three-phase single-stage grid-connected system with SRFT control technique. Initially, the irradiance level is

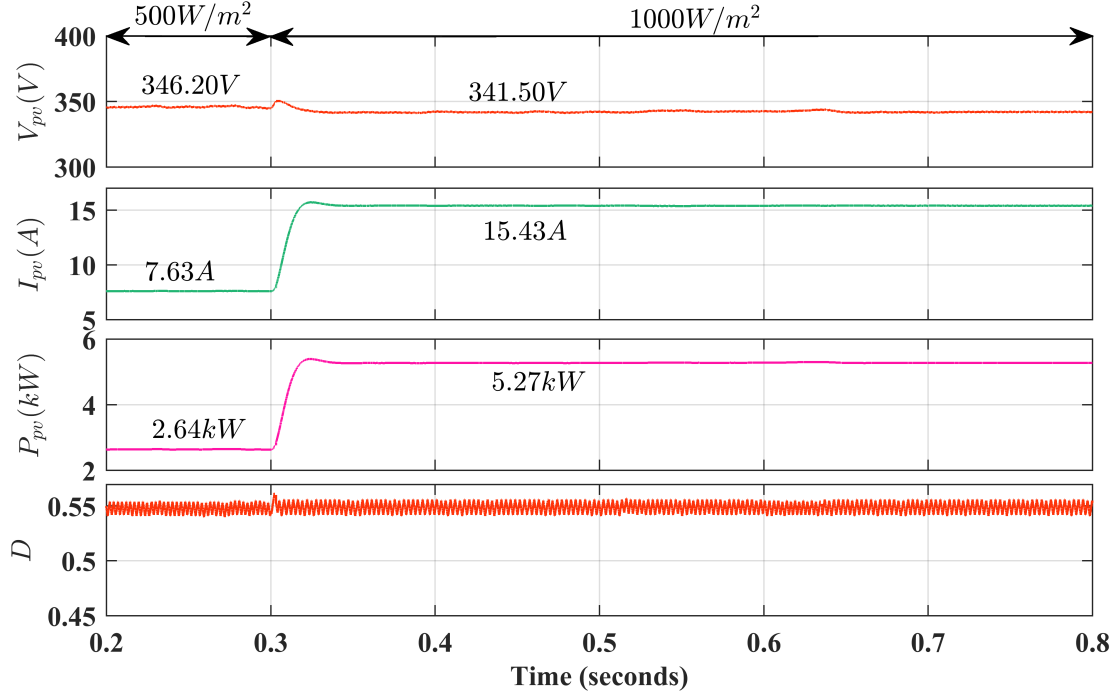


Figure 7.11: Simulation performance of PV string under double-stage grid-connected PV system

$500W/m^2$  and is increased to  $1000W/m^2$  at  $t=0.3s$ . At  $t=0.25s$ , measured value of PV voltage, current and power are 346.2, 7.66A and 2.64kW respectively. The estimated duty cycle for the DC-DC boost converter is 0.55. At  $t=0.45s$ , when the irradiance level is  $1000W/m^2$  the measured PV voltage, current and power are 341.5V, 15.43A and 5.27kW. The efficiency achieved from the PV string is 97.35%. Here, the PV parameters do not vary during the load unbalancing at PCC.

Figure 7.12 shows the SAPF simulation performance showing grid voltages ( $v_{gabc}(V)$ ), load currents ( $i_{Labc}(A)$ ), grid currents ( $i_{gabc}(A)$ ), compensator currents  $i_{cabc}(A)$  and the DC-link voltage  $V_{dc}(V)$ . The grid voltage is normal from  $t=0.2s$  to  $t=0.7s$  and its polluted after  $t=0.7s$ . The load is unbalanced from  $t=0.5s$  to  $t=0.6s$ , in this condition the grid currents are balanced. Irradiance has been increased to  $1000W/m^2$

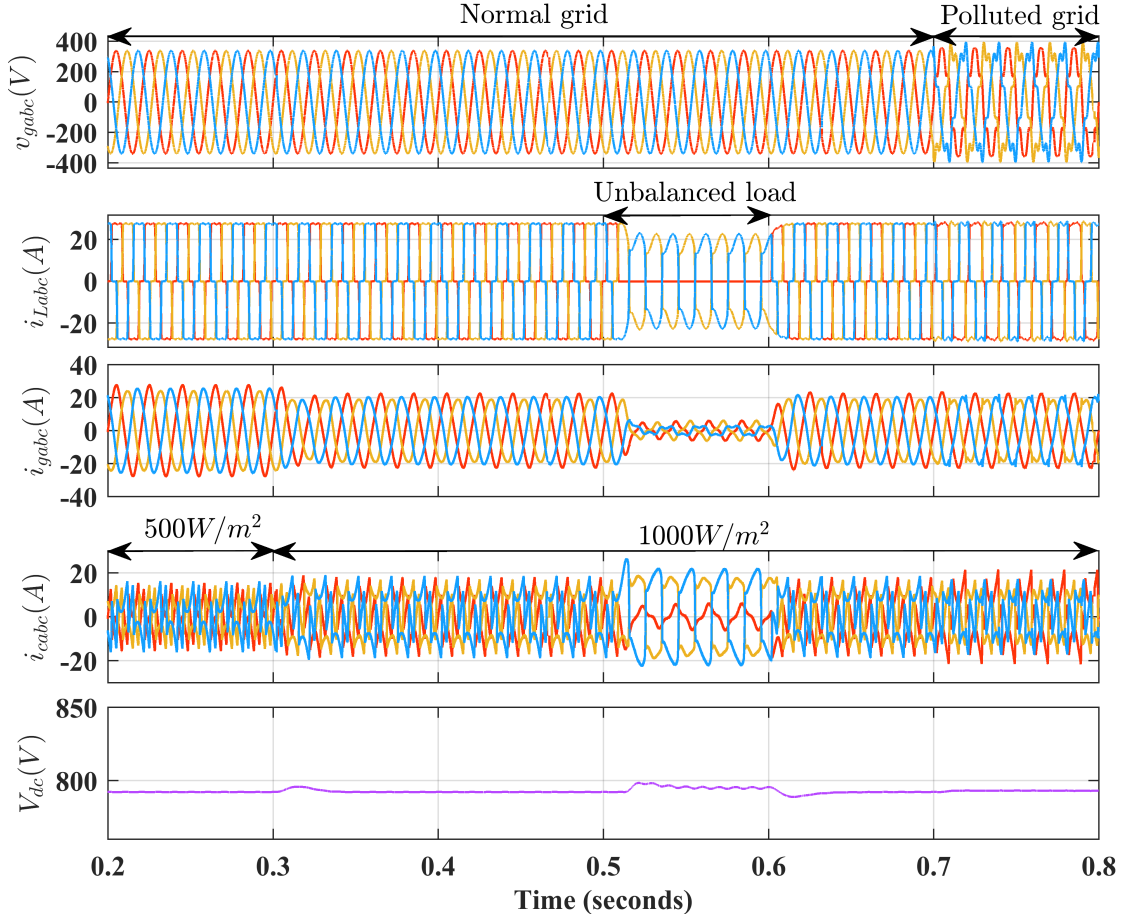


Figure 7.12: Simulation performance for grid parameters of double-stage grid-connected PV system

from  $500W/m^2$  at  $t=0.3s$ . At this condition the compensator current increases and grid current decreases. DC-link voltage is regulated by the PI controller to 800V.

THD analysis of different grid AC parameters have been shown in Fig. 7.13. In case I, when the grid voltage is free from distortion (THD 0.03%) and the THD of the load current of phase-a is 25.75%. THD of the improved grid current is 5.14% as shown in Fig. 7.9(c). In case II when the grid is polluted with the harmonics and its THD is 18.03%. The THD of the non-linear load current is 24.06% and the improved THD of the grid current is 5.79%. SRFT improves the performance of grid current but it could not follow the IEEE Std.1547.

Power transfer at PCC by the load, grid and compensator are shown in Fig. 7.14. At  $t=0.25s$  during the irradiance level of  $500W/m^2$  active and reactive power demanded by the load are 15.24kW and 2.52kVar. At this condition active power of

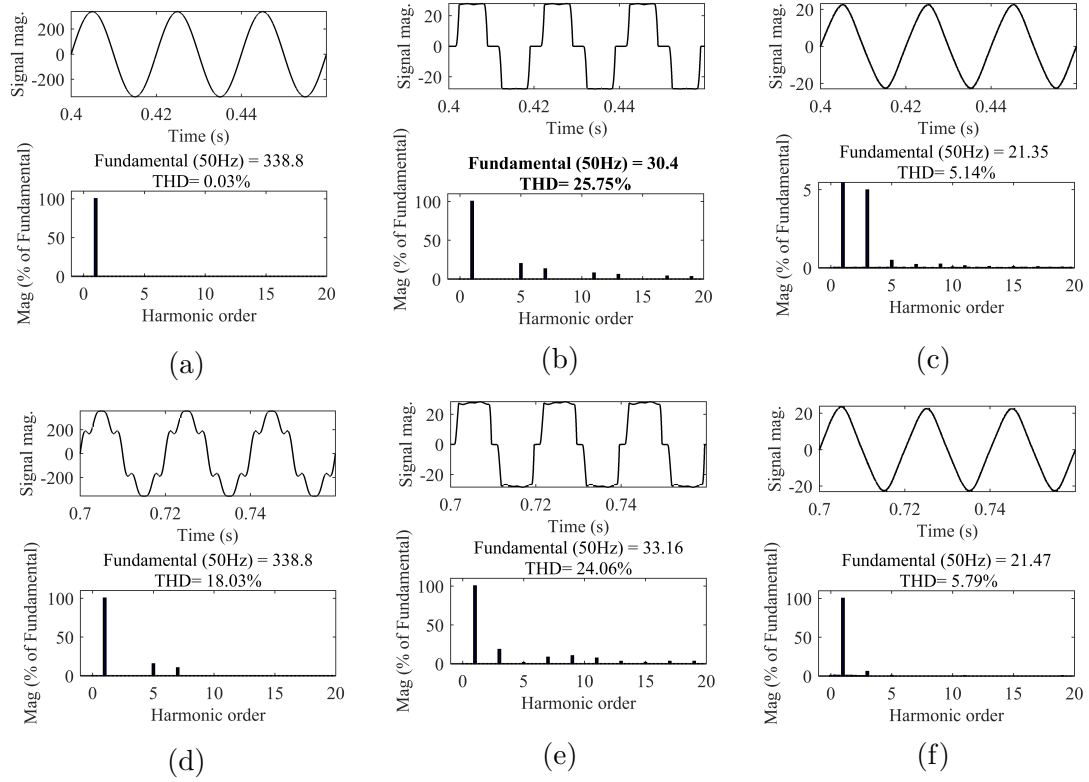


Figure 7.13: THD analysis for double-stage grid-connected PV system with SRFT technique Case I Normal grid (a) THD of  $v_g$  (b) THD of  $i_L$  (c) THD of  $i_g$  Case II Polluted grid (d) THD of  $v_g$  (e) THD of  $i_L$  (f) THD of  $i_g$

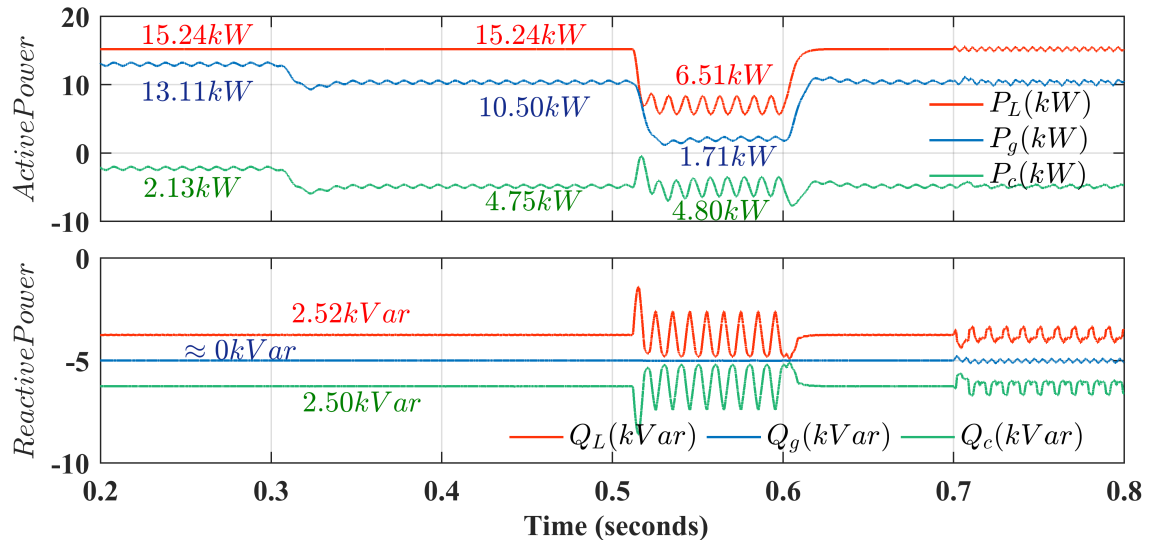


Figure 7.14: Simulation performance for power transfer in double-stage grid-connected PV system

2.13kW is supplied by the PV via compensator and 13.11kW is supplied by the grid.

At  $t=0.3s$ , the irradiance level has been increased to  $1000W/m^2$  the PV power con-

tribution increases to 4.75kW and the grid power reduces to 10.50kW. During the unbalanced condition the instantaneous active power demanded by load are 6.51kW. Active power supplied by the compensator is 4.80kW and 1.71kW power is supplied by the grid.

### 7.3 Performance of Improved Adaline Control Algorithm for Three-Phase Grid-Connected PV System

Figure 7.1 shows the control structure for three-phase single-stage grid-connected PV system with Improved Adaline control technique. In this configuration P & O

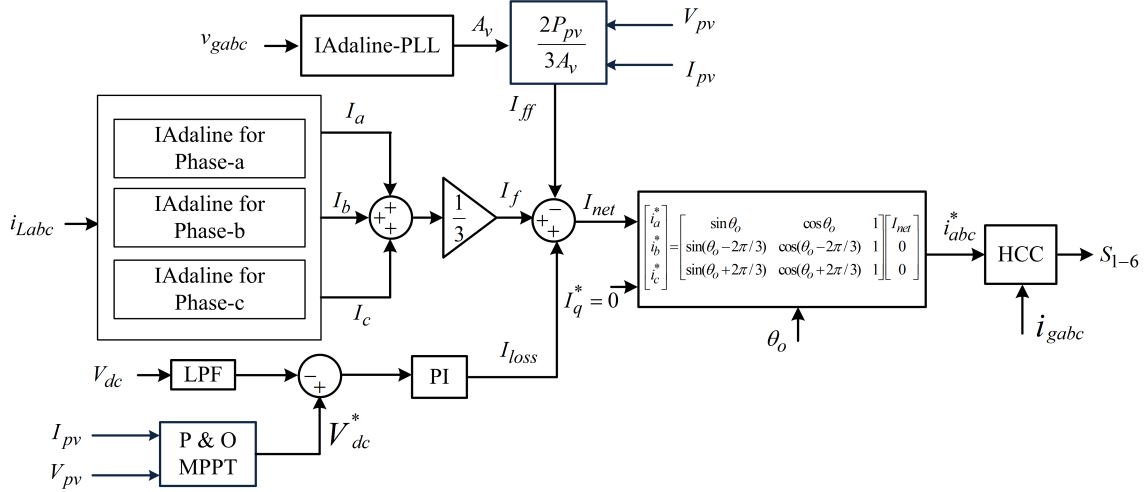


Figure 7.15: Structure of IAdaline control technique for three-phase single-stage grid-connected PV system

MPPT is used to estimate the reference DC-link voltage to achieve maximum power from the PV. Here, in this case the reference DC-link voltage is the MPP voltage of the PV. Three-phase Improved Adaline based PLL has been employed to estimate phase angle and the amplitude of the grid-voltage signal. No any additional LPF has been employed to filter the fundamental load component. A PV string of 22 panels is used to inject active power to the grid with the maximum power capacity of 5.95kW

Figure 7.16 shows the control structure for three-phase double-stage grid-connected PV system with Improved Adaline control technique. Here, PV array is connected to the DC-DC boost converter and its output is connected to the DC terminal of the three-phase VSC. In this configuration P & O MPPT is used to estimate the duty cycle for the DC-DC boost converter. A PV array of 20 panels consist 2 strings and

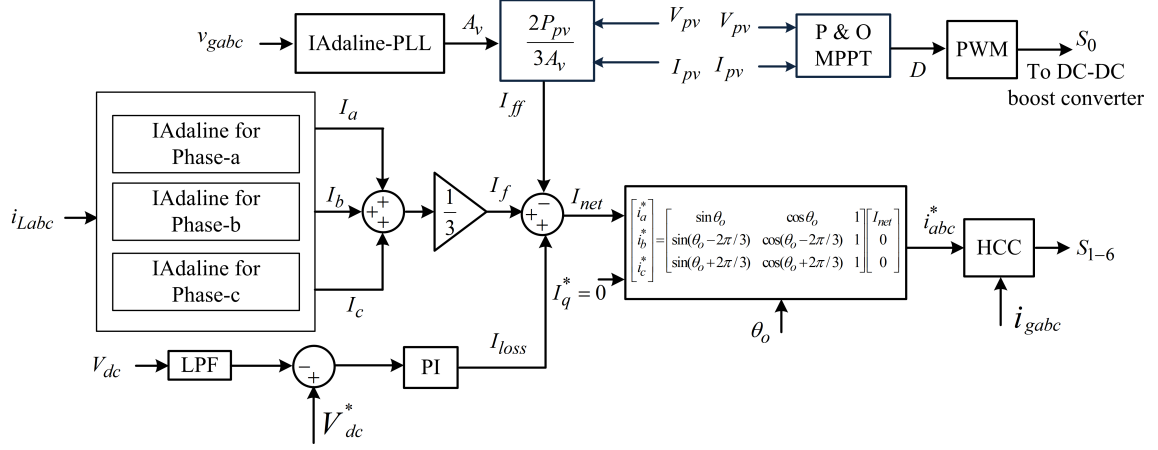


Figure 7.16: Structure of IAdaline control technique for three-phase double-stage grid-connected PV system

each having 10 panels is used to inject active power to the grid with the maximum power capacity of 5.41kW.

These control structures has been processed and generates switching signals for the 3-phase VSC and DC-DC boost converter. The detailed simulation and experimental results have been shown and discussed in next section.

### 7.3.1 Simulation Results for Single-Stage Grid-Connected PV System

Extensive simulation has been done for the effectiveness of the proposed system. The structure for the simulation studies has been shown in Fig. 7.1 for the single-stage grid-connected PV system.

A PV string consists of 22 PV module of maximum power rating of 5.95kW has been connected at DC-link of the VSC. Initially the irradiance level is  $500W/m^2$  and increased to  $1000W/m^2$  at  $t=0.3s$ . A combination of linear and non-linear load have been connected to PCC. The load unbalancing has been done at  $t=0.5s$  and removed at  $t=0.6s$ . Figure 7.17 shows the performance of PV string and the estimation of DC-link reference voltage by P & O MPPT technique. During the lower irradiance ( $500W/m^2$ ), PV current is 3.88A and the power delivered by PV is 3.01kW and the reference DC-link estimated voltage ( $V_{dc}^*$ ) is 778.3V. At higher

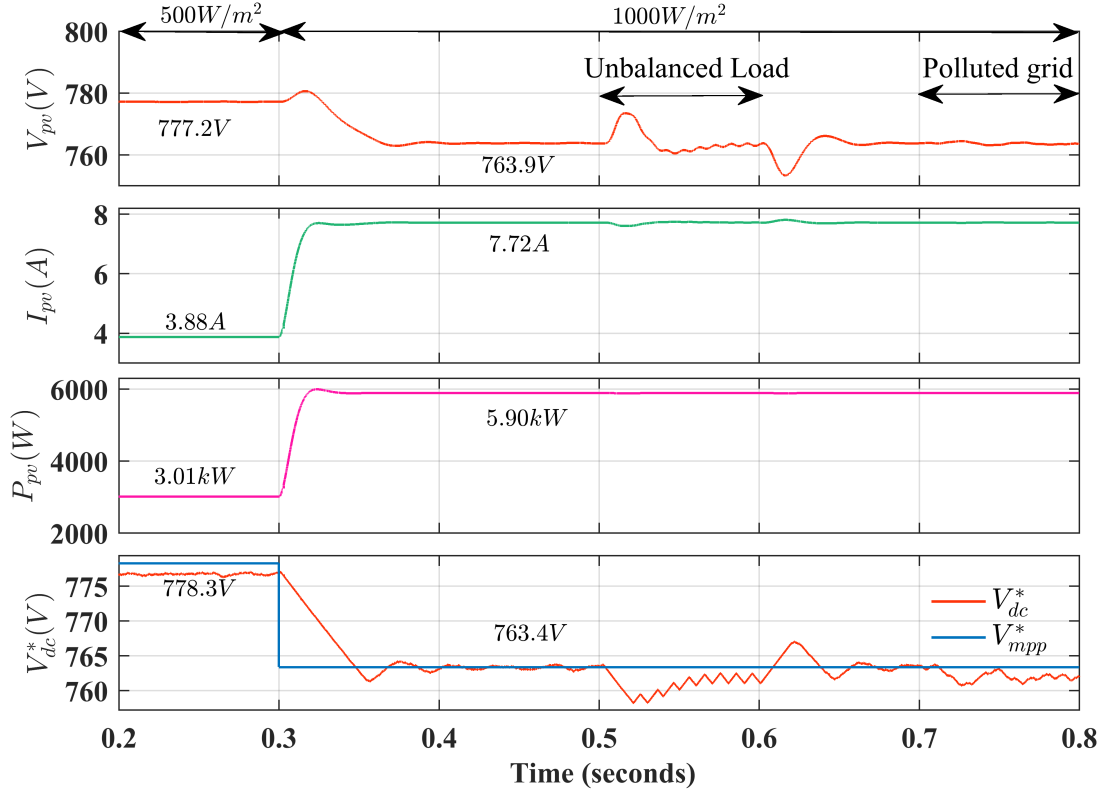


Figure 7.17: Simulation performance of PV string under single-stage grid-connected PV system

irradiance of  $1000W/m^2$ , the PV current is 7.72A and the power delivered by PV is 5.9kW. Efficiency of the PV string achieved is 99.09%. The reference DC-link voltage is 763.4V, which is obtained by P & O MPPT technique. During the unbalanced load condition introduced from  $t=0.5s$  to  $t=0.6s$ , a variation in DC-link has been observed but settles back to MPP voltage.

Fig. 7.18 shows the simulation results of grid parameters under irradiance change and load unbalancing. During  $t=0.2s$  to  $t=0.3s$ , irradiance is  $500W/m^2$ , the grid current is high as the VSC current is lower due to the lower irradiance. Once the irradiance is increased the VSC current increases and the grid current decreases. This happens as the PV injects higher power at  $1000W/m^2$  as compared to  $500W/m^2$ . During the load unbalancing, DC-link voltage settles to the reference DC-link voltage of 763.3V after a little variation due to PI controller action. The grid current is sinusoidal and in-phase with the grid voltage. At  $t=0.7s$  the grid voltage is polluted with harmonics at this condition the grid current is sinusoidal and DC-voltage is also regulated.



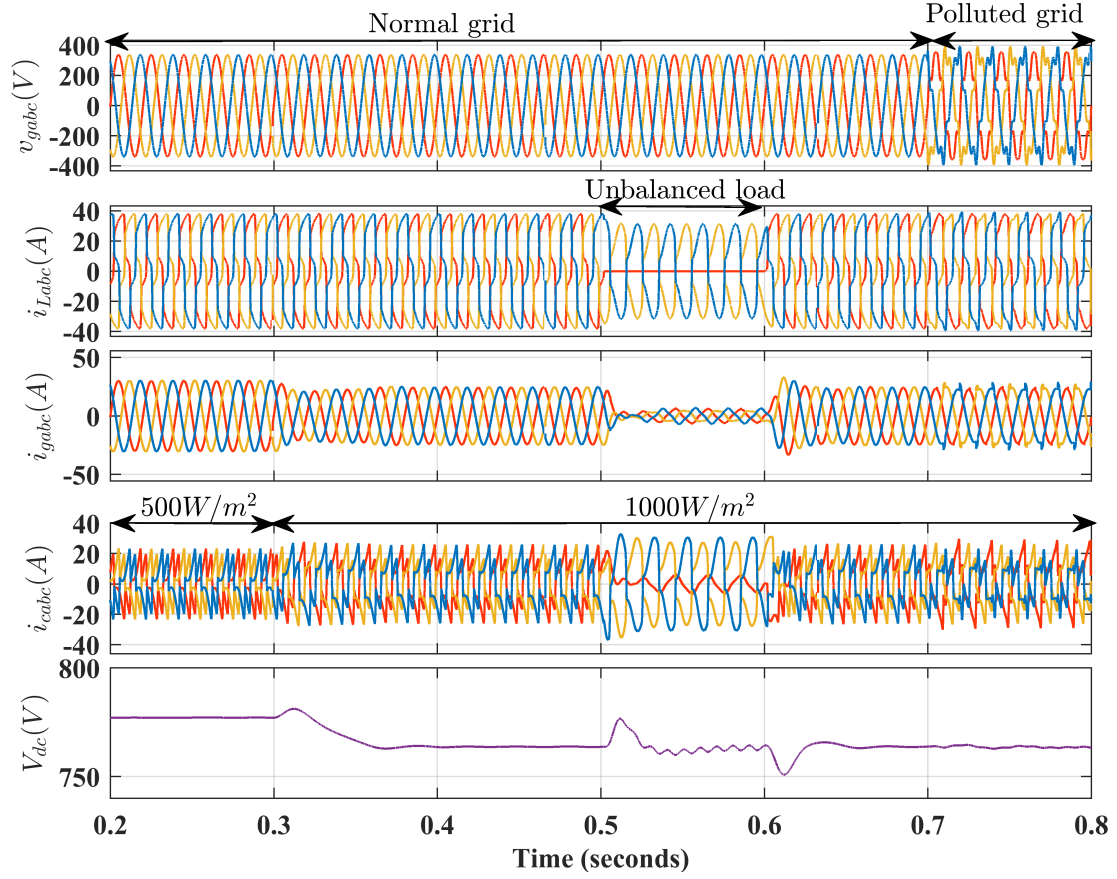


Figure 7.18: Simulation performance for grid parameters of single-stage grid-connected PV system

Figure 7.19 show the THD analysis of different grid parameters. In case I, the grid is in normal condition and shows the THD of 0.02%. THD of the non-linear load current is 20.03% (7.19(b)). After applying the SAPF it improves to 2.26% which is below the maximum standard value. In case II, the grid voltage is polluted with harmonics of the THD of 18.03% and the THD of the non-linear load current is 18.78%. After the application of SAPF the THD of the grid current improves to 3.06% which follows the IEEE Std.1547.

Figure 7.20 show the simulation results for power transfer in three-phase single-stage grid-connected PV system. Initially up to  $t=0.3s$ , the active and reactive power demand by load are 18.26kW and 6.83kVar. Active power supplied by the grid is 15.341kW and the active power supplied by the OV via compensator is 2.93kW. There is losses of 0.15kW has been occurred in the VSC. Reactive power demand of 6.83kVar is fulfilled by the three-phase SAPF. Irradiance level on PV array is

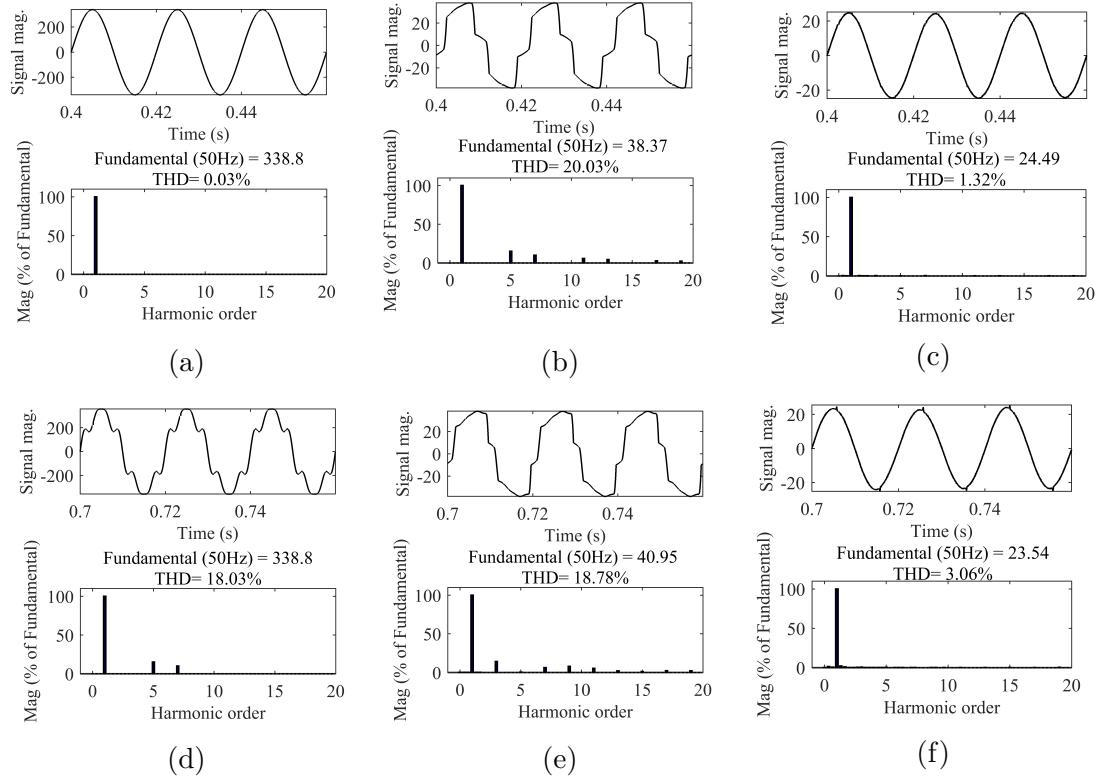


Figure 7.19: THD analysis for single-stage grid-connected PV system with Improved Adaline technique Case I Normal grid (a) THD of  $v_{ga}$  (b) THD of  $i_{La}$  (c) THD of  $i_{ga}$   
Case II Polluted grid (d) THD of  $v_{ga}$  (e) THD of  $i_{La}$  (f) THD of  $i_{ga}$

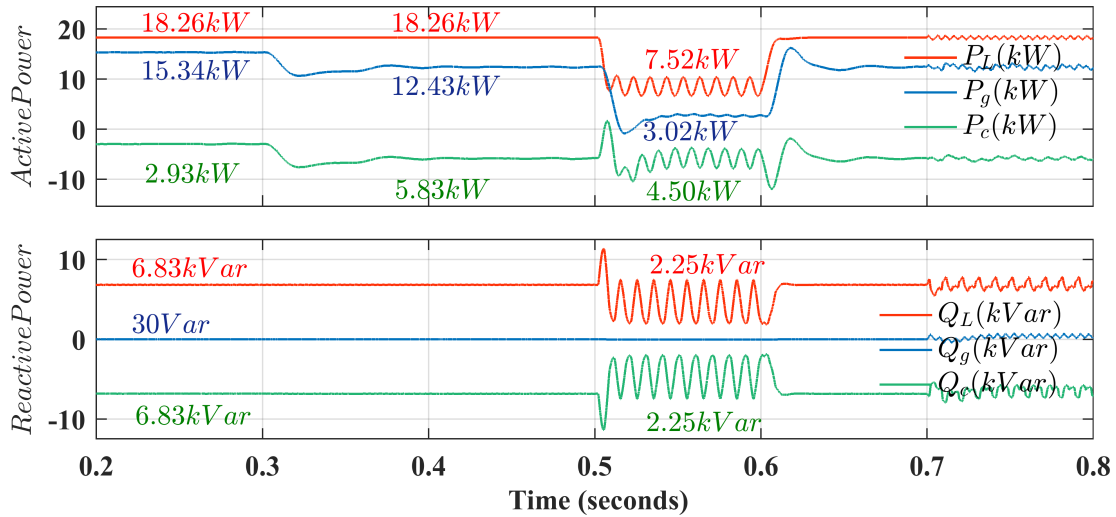


Figure 7.20: Simulation performance for power transfer in single-stage grid-connected PV system

increased to  $1000 \text{ W/m}^2$  at  $t = 0.3$  s. At this condition the load demand is constant and the compensator power is increased to  $5.83 \text{ kW}$  and rest of the active power of

12.43kW is supplied by the grid to the load. During the unbalance condition, the instantaneous active power demand by the load measured at  $t=0.55s$  is 7.52kW. The instantaneous power injected by the PV via compensator is 4.50kW and active power of 3.02kW is supplied by the grid. The instantaneous reactive power demand of 2.25kVar is supplied by the compensator at  $t=0.55s$ .

### 7.3.2 Experimental Results for Single-Stage SAPF Grid-Connected PV System

Experimental performance has been shown in Fig. 7.21 for the three-phase single-stage grid-connected PV system. 110V (RMS L-L) has been applied at PCC and the load demand is 0.931A. The VSC current is 4.645A and the extra current of

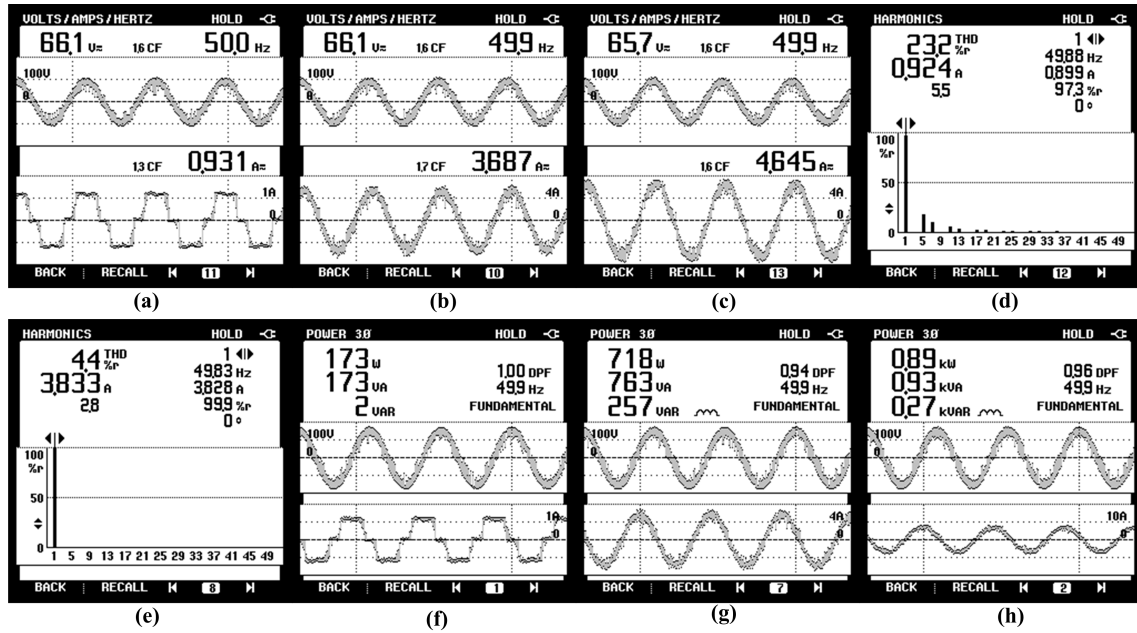


Figure 7.21: Experimental performance of single-stage SAPF grid-connected PV system (a)  $v_{ga}$  and  $i_{La}$  (b)  $v_{ga}$  and  $i_{ga}$  (c)  $v_{ga}$  and  $i_{ca}$  (d) THD of  $i_{La}$  (e) THD of  $i_{ga}$  (f) Load power (g) Grid power (h) Compensator power

3.687A is feed to the grid. The THD of the load current is 23.2% and the corrected THD is 4.4%. The load power demand is 173W and the PV power feeding through VSC is 0.89kW and hence extra power of 0.718kW has been given back to the grid. Here, the simulation and experimental performance shows the successful power

transfer from PV to the grid with the feature of power quality improvement in the three-phase single-stage grid-connected PV system.

### 7.3.3 Simulation Results for Double-Stage SAPF Grid Connected PV System

The structure for the simulation studies has been shown in Fig. 7.2 for the double-stage grid integrated PV system. Simulation parameters of PV array has been shown in Fig. 7.22 for the  $500W/m^2$  and the  $1000W/m^2$  condition under double-stage mode. PV array consists of 10 modules in series and 2 strings in parallel which

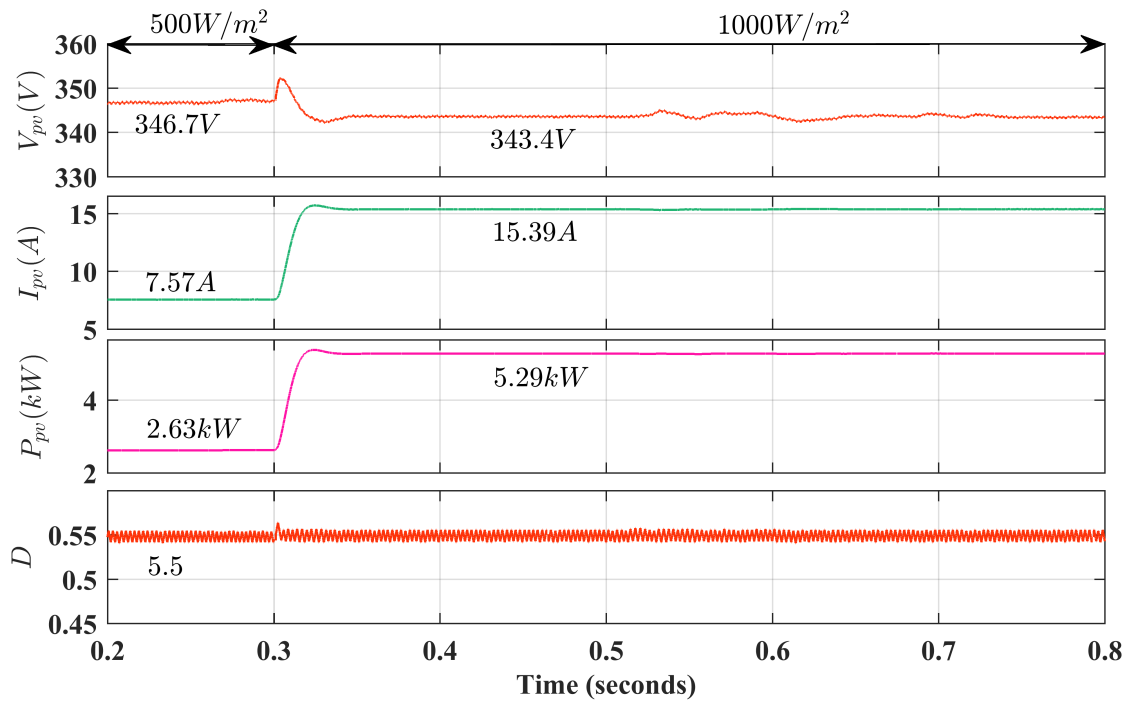


Figure 7.22: Simulation performance of PV array under double-stage grid-connected PV system

having the maximum power of 5.41kW. The DC-link reference voltage is fixed to 800V. P&O technique has been used for estimate the duty-cycle for the boost converter. Initially the irradiance is  $500W/m^2$  and the PV voltage, current, and power are 346.7V, 7.57A and 2.63kW respectively. The irradiance has been changed to  $1000W/m^2$  at  $t=0.3s$ . PV voltage, current and PV power are 343.4V, 15.39A and the 5.29kW respectively. The efficiency of the PV array achieved in this case is

97.72%.

Figure 7.23 show the performance of grid parameters for feeding non-linear condition and the load unbalancing. At  $t=0.3s$  the irradiance has been increased from

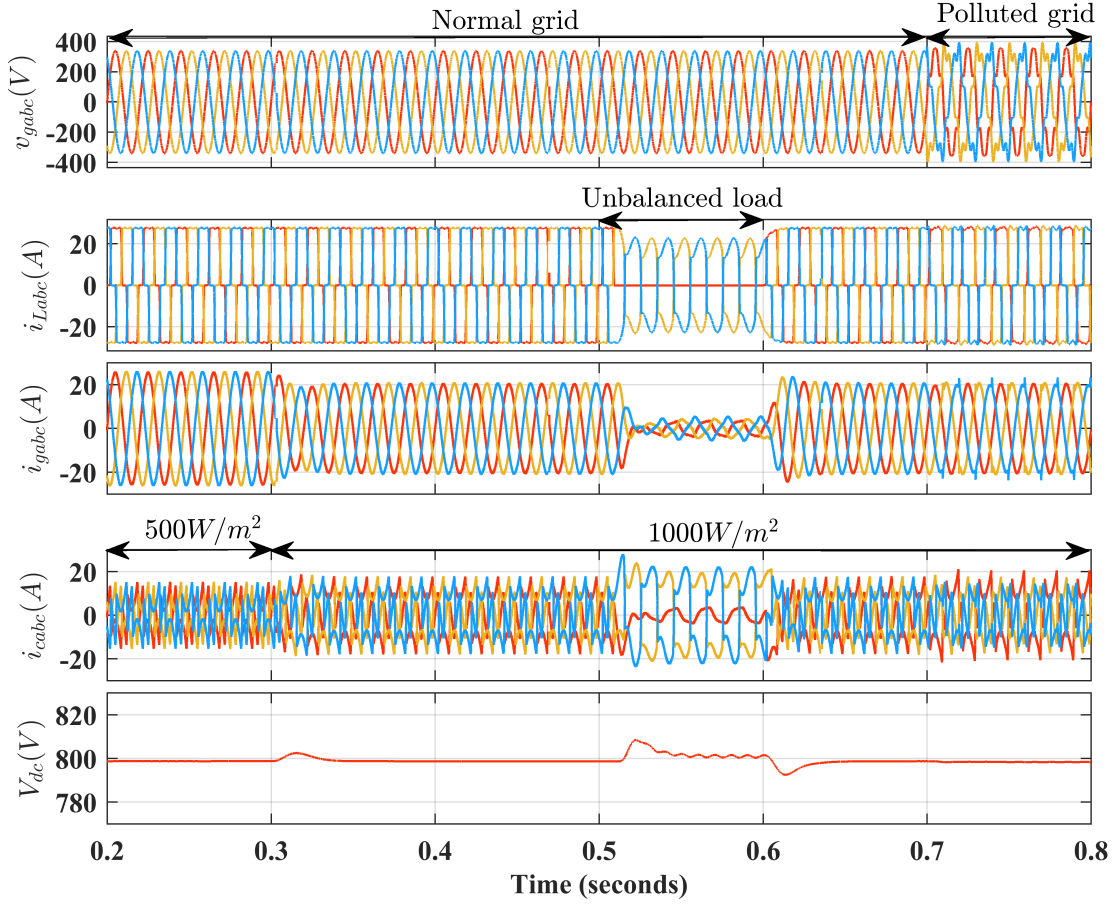


Figure 7.23: Simulation performance for grid parameters of double-stage grid-tied PV system

$500W/m^2$  to  $1000W/m^2$  and the load current is fixed. As the irradiance increases the compensator current increases and the grid current decreases. The measured DC-link voltage has been fixed at 800V under both balanced and unbalanced load condition. The grid current is sinusoidal and in-phase with the grid voltage. The grid voltage is polluted from  $t=0.7s$  to  $t=0.8s$ . During this condition the grid current is sinusoidal and the DC-link voltage is regulated.

THD of the different grid parameters has been shown in Fig. 7.24. In case I, THD of the considered ideal grid voltage is 0.04%. The THD of the load current is 25.76% and without SAPF the THD of the grid current will be same to the load current.

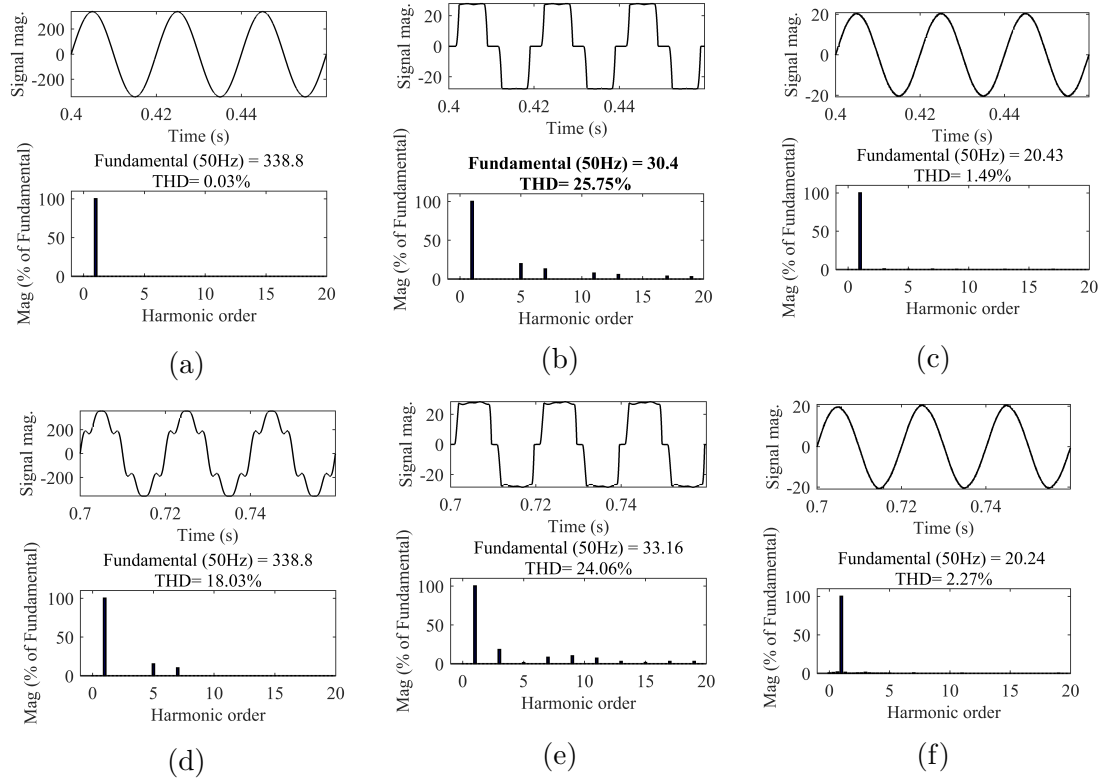


Figure 7.24: THD analysis for double-stage grid-connected PV system with Improved Adaline technique Case I: Normal grid (a) THD of  $v_{ga}$  (b) THD of  $i_{La}$  (c) THD of  $i_{ga}$   
Case II: Polluted grid (d) THD of  $v_{ga}$  (e) THD of  $i_{La}$  (f) THD of  $i_{ga}$

The improved THD of the grid current is 2.71%, which follows the IEEE Std.1547. In case II, the THD of the considered polluted grid voltage is 18.03% and the THD of the non-linear load current is 24.06%. After the SAPF operation the THD of the grid current improves to 2.27%.

Figure 7.25 show the performance for power transfer at PCC. The active load demand is 15.24kW and the active power given by the PV via VSC is 2.20kW and active power of 13.04kW is supplied by the grid. At  $t=0.45s$ , during irradiance of  $1000W/m^2$ , the contribution of PV power is 4.86kW and the active power of 10.38kW is provided by the grid. All the reactive power of 2.52kVar demanded by the load is compensated by the VSC. During the unbalanced load condition, the instantaneous power at PCC demanded by the load is 6.51kW where 4.57kW is supplied by the PV and 1.95kW is supplied by the 1.95kW.

Performance of SRFT and IAdaline control algorithm for three-phase single-stage

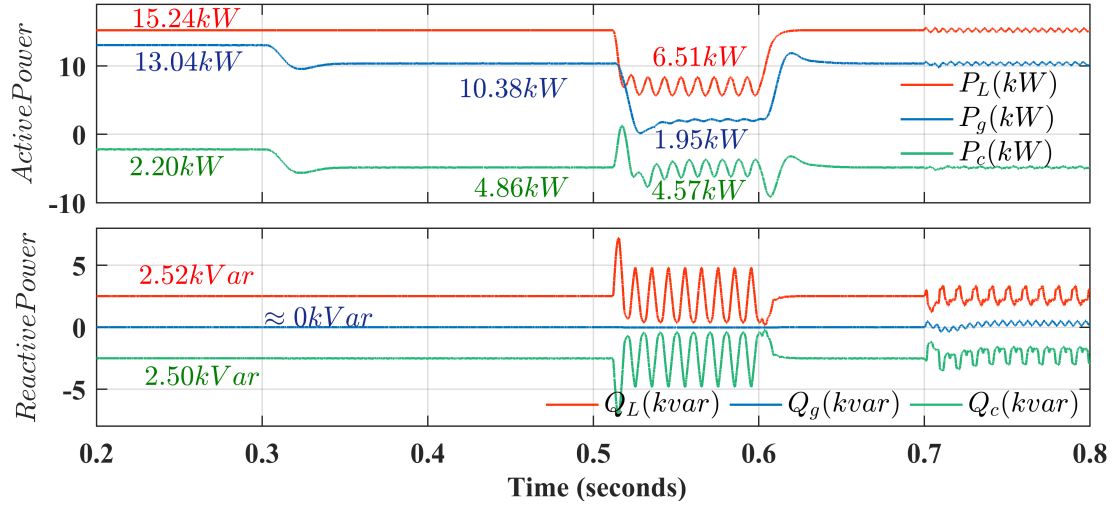


Figure 7.25: Simulation performance for power transfer in double-stage grid-connected PV system

and double-stage grid-connected PV system under normal and polluted grid condition are have been summarized in Table 7.1. THD performance of SRFT in single-

Table 7.1: Performance summary of SRFT and IAdaline control algorithm for three-phase single-stage and double-stage grid-connected PV system

Parameters		Double-stage		Single-stage	
		SRFT	IAdaline	SRFT	IAdaline
Normal grid (THD)	$v_{ga}$	0.03%	0.03%	0.03%	0.03%
	$i_{La}$	20.03%	20.03%	25.75%	25.75%
	$i_{ga}$	5.52%	1.32%	5.14%	1.49%
Polluted grid (THD)	$v_{ga}$	18.03%	18.03%	18.03%	18.03%
	$i_{La}$	18.78%	18.78%	18.78%	18.78%
	$i_{ga}$	6.57%	3.06%	5.79%	2.27%
PV power(kW)	$P_{pv}$	5.90kW	5.90kW	5.27kW	5.29kW
PV efficiency(%)	$\eta$	99.09%	99.09%	97.35%	97.72%

stage and double-stage system improve the power quality but not as per IEEE Std.1547. The IAdaline control algorithm shows consistence performance in both the single-stage and double-stage grid-connected PV system under normal and polluted grid condition and follow IEEE Std. 1547. In single-stage system the efficiency of PV string is 99.09% but in double-stage system the efficiency of PV array is 97.72%.

## 7.4 Conclusions

In this chapter, SRFT and IAdaline control algorithms have been employed for the SAPF in three-phase single-stage and double-stage grid connected PV system under normal and polluted grid. Performance of IAdaline in single-stage and double-stage under both the normal and polluted grid condition show better performance than SRFT control algorithm and follows standard. Experimental performance of IAdaline control algorithm has also added for the single-stage grid-connected PV system. Hence, from the extensive simulation analysis for the three-phase single-stage and double-stage grid-tied PV system show the effectiveness the proposed system and the proposed algorithm. Both the active and reactive power compensation has been achieved along with the power quality improvement.



# Chapter 8

## Conclusions and Future Scope

The main aim of thesis work is the application of power electronics for the improvement of power quality in single-phase and three-phase grid-connected PV systems feeding non-linear loads. These goals can be achieved by the designing the system components with implementation of control algorithms for the power quality improvement. The control algorithms requires the synchronization techniques, control algorithms to estimate fundamental component, DC-link voltage controllers and the feed form term. Simulation and experimental work have been performed to find out the effectiveness of the system and the control algorithms. The main conclusions of the thesis work have been discussed in next section.

### 8.1 Conclusions

Introduction of this thesis work has been presented first which discusses power quality, its reason, effect and the state of art to solve these problems. Chapter 2 presented the literature review on PV modelling, MPPT techniques, PQ problems, impacts and their solutions. The effective solution for both active power injection and the power quality improvement in single-phase and three-phase grid-connected PV system require synchronization and control techniques and are discussed here.

Chapter 3 discusses the design and development of single-phase and three-phase grid-connected PV system have been discussed in detail. Design equations, sys-

tem configuration and the figures of experimental prototype setup have also been presented. Rating of PV string/array has been designed for single-stage and double-stage manner in single-phase and three-phase grid-connected PV system.

In Chapter 4, grid-synchronization techniques have been presented for both single-phase and three-phase grid voltage. In single-phase synchronization techniques PLL and non-PLL type techniques have been presented. For the variation in grid voltage, the AZCD shows best performance for both the amplitude estimation and frequency estimation. Frequency estimated by AZCD shows zero error and faster convergence. During the polluted grid condition SOGI-FLL-ROGI shows best performance as it filter out harmonic effectively and estimates amplitude and frequency without minimal or zero oscillations. SOGI-FLL and SOGI-FLL-ROGI has inherent frequency-locked loop hence it estimates frequency precisely. During the phase shift condition, the AZCD shows faster response than other PLLs. Noisy signals have wide range of frequency hence SOGI-PLL shows low oscillations for frequency estimation. In this case, SOGI-FLL-ROGI and AZCD show best results. During the DC-offset in grid voltage, the performance of EPLL and AZCD is not satisfactory, while the performance of SOGI-FLL-ROGI is observed to be the best.

For estimation of three-phase synchronizing signals and other voltage parameters unit-template method, SRF-PLL, IAdaline-PLL and Spline based PLLs have been designed and presented. Its performance of unit-template method is best under normal grid condition but during the polluted grid condition its performance is very poor and not acceptable. During the voltage variation, SRF-PLL shows better performance than other techniques. Moreover, during polluted grid condition, SRF-PLL show oscillations in both the tracked amplitude and frequency. IAdaline-PLL shows best performance under polluted grid condition. During the phase change or the frequency change the IAdaline-PLL shows best performance as it has faster response during dynamic condition and minimal error during steady-state condition. The SRF-PLL show best performance under DC-offset condition in the grid-voltage.

Spline-PLL has the capability of smoothening the output waveform hence its performance is best during the noisy grid voltage condition. For other grid voltage conditions the performance of Spline-PLL is of moderate level.

In Chapter 5, SOGI, cascaded SOGI and SOGI-ROGI control algorithms have been used for power quality improvement in single phase SAPF. These control algorithms have been applied with different synchronization techniques under both normal and polluted grid conditions. The performance of SOGI-ROGI with SOGI-FLL-ROGI perform better than SOGI control with AZCD under both normal and polluted grid conditions in steady-state conditions.

In three-phase system SRFT control algorithm with unit-template, SRF-PLL and Spline based PLL have been applied for PQ improvement and reactive power compensation. The performance of SRFT control algorithm with Spline-PLL show the best performance under both normal and distorted grid condition.

In Chapter 6, SRFT and SOGI-ROGI control algorithms have been designed and applied for the single-phase single-stage and single-phase double-stage system for active power injection and reactive power compensation. Performance of SRFT control is not as per standard it requires additional LPF to improve the performance SRFT control algorithm. Even after using the additional LPF its performance is not satisfactory during polluted grid condition. SOGI-ROGI performs consistently in single-stage and double-stage grid condition under both normal and polluted grid condition. Efficiency of PV is better in the single-stage system than the double-stage grid-connected PV system. The performance of SOGI-ROGI clearly approves the active and reactive power compensation to the grid effectively as per load demand and PV power generation. The power quality has been improved in both the cases under non-linear load and polluted grid voltage.

In Chapter 7, SRFT and IAdaline based control algorithms have been employed for the SAPF in three-phase single-stage and double-stage grid connected PV sys-

tem under normal and polluted grid. Performance of IAdaline in single-stage and double-stage under both the normal and polluted grid condition show better performance than SRFT control algorithm and follows IEEE std.1547. The performance of single-stage and double-stage grid connected PV system has been compared. In the single-stage grid-connected PV system the efficiency of PV is better than the single-stage. In double-stage grid-connected PV system the stability DC-link voltage of VSCs is better.

## 8.2 Future Scope

In this thesis work, design, control and analysis the single-phase and three-phase grid-connected PV system has been demonstrated. Some conventional and new synchronization algorithm has been designed to work in adverse grid-voltage conditions. More work is still required to develop new synchronization techniques specially under DC-offset conditions. Mathematical stability analysis could also been done for the stable operation of the synchronization techniques under various grid voltage conditions.

Conventional P & O MPPT technique has been employed to achieve maximum power form the PV in single-stage and double-stage grid-connected PV system for the fixed or changing irradiance condition. New techniques should be developed for the varying irradiance and partial shading conditions.

These days PV is widely used for the electricity generation. Hence, impact of the larger number of PV integration to the distribution grid should be analyzed. It may further enhances the reliability of the system. In this thesis work inter-harmonic component has not been analyzed and if available should be mitigated.

Economical DSP kit should be employed for the economic application for the power quality enhancement.

# Publications

## List of publications in SCI/SCIE journals

1. **H. Saxena**, A. Singh, J. N. Rai and M. Badoni, "PV integrated grid synchronization technique using modified SOGI-FLL and zero-crossing detector" Electr Eng (2021). <https://doi.org/10.1007/s00202-021-01394-3> (IF 1.836)
2. **H. Saxena**, A. Singh and J. N. Rai, "Enhanced Third-Order Generalized Integrator-Based Grid Synchronization Technique for DC-Offset Rejection and Precise Frequency Estimation." 1-10, Arabian Journal for Science and Engineering (2021): (IF 2.334).
3. **H. Saxena**, A. Singh and J. N. Rai, "Analysis of SOGI-ROGI for synchronization and shunt active filtering under distorted grid condition", ISA Transactions, 2020, ISSN 0019-578,<https://doi.org/10.1016/j.isatra.2020.10.025> (IF 5.468)
4. **H. Saxena**, A. Singh and J. N. Rai, "Design and performance analysis of improved Adaline technique for synchronization and load compensation of grid-tied photovoltaic system." International Transactions on Electrical Energy System. 2020; 30:e12388. <https://doi.org/10.1002/2050-7038.12388> (IF 2.860)
5. **H. Saxena**, A. Singh and J. N. Rai, "Adaptive spline-based PLL for synchronization and power quality improvement in distribution system," in IET Generation, Transmission & Distribution, vol. 14, no. 7, pp. 1311-1319, 14 4 2020, doi: 10.1049/iet-gtd.2019.0662. (IF 2.995 )
6. **H. Saxena**, A. Singh and J. N. Rai, "Design and analysis of different PLLs as load compensation techniques in 1- $\phi$  grid-tied PV system," International Journal of Electronics, 106:11, 1632-1659, 2019, DOI: 10.1080/00207217.2019.1600745. (IF 1.336)
7. **H. Saxena**, A. Singh and J. N. Rai, "Design and performance analysis of generalized integrator-based controller for grid connected PV system," International Journal of Electronics, 105:7, 1079-1096, 2018, DOI: 10.1080/00207217.2018.1426117. (IF 1.336)

## List of Publications in National and International Conferences

1. **H. Saxena**, A. Singh and J. N. Rai, "Design and Testing of Frequency Adaptive Zero- Crossing Detector as a Synchronizing Technique," 2020 IEEE 9<sup>th</sup> Power India International Conference (PIICON), SONEPAT, India, 2020, pp. 1-6, doi: 10.1109/PIICON49524.2020.9113009.
2. **H. Saxena**, A. Singh and J. N. Rai, "Application of Time Delay Recurrent Neural Network for Shunt Active Power Filter in 3-Phase Grid-tied PV System," 2019 National Power Electronics Conference (NPEC), Tiruchirappalli, India, 2019, pp. 1-6, doi: 10.1109/NPEC47332.2019.9034769.
3. **H. Saxena**, A. Singh and J. N. Rai, "Design and Analysis of Cascaded Generalized Integrators for Mitigation of Power Quality Problems," 2019 International Symposium on Advanced Electrical and Communication Technologies (ISAECT), Rome, Italy, 2019, pp. 1-6, doi: 10.1109/ISAECT47714.2019.9069704.

# Bibliography

- [1] H. Bellia, Y. Ramdani, and M. Fatima, “A detailed modeling of photovoltaic module using matlab,” *NRIAG Journal of Astronomy and Geophysics*, vol. 3, no. 1, pp. 53–61, 2014.
- [2] A. Trivedi, *Micro-grid Operation and Control*. PhD dissertation, Delhi Technological University, 2018.
- [3] P. I. B. Govt. of India, “Revision of cumulative targets under national solar mission from 20,000 mw by 2021-22 to 1,00,000 mw,” 17 June 2015.
- [4] B. Singh, C. Ambrish, and K. Al-Haddad, *Power Quality: Problems and Mitigation Techniques*. John Wiley & Sons, 2014.
- [5] M. H. Bollen, “What is power quality ?,” *Electric power systems research*, vol. 66, no. 1, pp. 5–14, 2003.
- [6] C. Sankaran, *Power quality*. CRC Press, 2017.
- [7] M. B. Latran, T. Ahmet, and Y. Yoldaş, “Mitigation of power quality problems using distribution static synchronous compensator: a comprehensive review,” *IET power electronics*, vol. 8, no. 7, pp. 1312–1328, 2015.
- [8] S. Devassy and B. Singh, “Design and performance analysis of three-phase solar pv integrated upqc,” *IEEE Transactions on Industry Applications*, vol. 54, no. 1, pp. 73–81, 2017.

- [9] M. Yamaguchi and A. Luque, “High efficiency and high concentration in photovoltaics,” *IEEE Transactions on Electron Devices*, vol. 46, no. 10, pp. 2139–2144, 1999.
- [10] R. Har-Lavan and D. Cahen, “40 years of inversion layer solar cells: From mos to conducting polymer/inorganic hybrids,” *IEEE Journal of Photovoltaics*, vol. 3, no. 4, pp. 1443–1459, 2013.
- [11] P. Reinhard, C. Adrian, P. Blösch, F. Pianezzi, S. Nishiwaki, B. Stephan, and A. N. Tiwari, “Review of progress toward 20% efficiency flexible cigs solar cells and manufacturing issues of solar modules,” *IEEE Journal of Photovoltaics*, vol. 3, no. 1, pp. 572–580, 2013.
- [12] Y. Chen, P. P. Altermatt, D. Chen, X. Zhang, G. Xu, Y. Yang, Y. Wang, Z. Feng, H. Shen, and P. J. Verlinden, “From laboratory to production: Learning models of efficiency and manufacturing cost of industrial crystalline silicon and thin-film photovoltaic technologies,” *IEEE Journal of Photovoltaics*, vol. 8, no. 6, pp. 1531–1538, 2018.
- [13] M. Gloeckler, I. Sankin, and Z. Zhao, “Cdte solar cells at the threshold to 20% efficiency,” *IEEE Journal of Photovoltaics*, vol. 3, no. 4, pp. 1389–1393, 2013.
- [14] A. Pavan Kumar, A. M. Parimi, and K. Uma Rao, “Performance analysis of a two-diode model of pv cell for pv based generation in matlab,” in *2014 IEEE International Conference on Advanced Communications, Control and Computing Technologies*, pp. 68–72, 2014.
- [15] T. Le, H. Colin, F. A. Shakarchi, and T. T. Quoc, “Improved matlab simulink two-diode model of pv module and method of fast large-scale pv system simulation,” in *2018 7th International Conference on Renewable Energy Research and Applications (ICRERA)*, pp. 982–985, 2018.
- [16] T. Wei, F. Yu, G. Huang, and C. Xu, “A particle-swarm-optimization-based parameter extraction routine for three-diode lumped parameter model of or-



- ganic solar cells,” *IEEE Electron Device Letters*, vol. 40, no. 9, pp. 1511–1514, 2019.
- [17] N. M. A. Alrahim Shannan, N. Z. Yahaya, and B. Singh, “Single-diode model and two-diode model of pv modules: A comparison,” in *2013 IEEE International Conference on Control System, Computing and Engineering*, pp. 210–214, 2013.
- [18] C. S. Solanki, *Solar Photovoltaics: Fundamentals, Technologies and Applications*. PHI learning pvt. Ltd., 2015.
- [19] S. H. Hanzaei, S. A. Gorji, and M. Ektesabi, “A scheme-based review of mppt techniques with respect to input variables including solar irradiance and pv arrays’ temperature,” *IEEE Access*, vol. 8, pp. 182229–182239, 2020.
- [20] A. K. Gupta and R. Saxena, “Review on widely-used mppt techniques for pv applications,” in *2016 International Conference on Innovation and Challenges in Cyber Security (ICICCS-INBUSH)*, pp. 270–273, 2016.
- [21] D. Singh and H. Singh, “Technical survey and review on mppt techniques to attain maximum power of photovoltaic system,” in *2019 5th International Conference on Signal Processing, Computing and Control (ISPCC)*, pp. 265–268, 2019.
- [22] R. B. Bollipo, S. Mikkili, and B. P. Kumar, “Hybrid, optimal, intelligent and classical pv mppt techniques: A review,” *CSEE Journal of Power and Energy Systems*, vol. 7, no. 1, pp. 9–33, 2021.
- [23] N. Femia, G. Petrone, G. Spagnuolo, and M. Vitelli, “Optimization of perturb and observe maximum power point tracking method,” *IEEE Transactions on Power Electronics*, vol. 20, no. 4, pp. 963–973, 2005.
- [24] D. Sera, L. Mathe, T. Kerekes, S. V. Spataru, and R. Teodorescu, “On the perturb-and-observe and incremental conductance mppt methods for PV systems,” *IEEE Journal of Photovoltaics*, vol. 3, no. 3, pp. 1070–1078, 2013.

- [25] I. V. Banu, R. Beniugă, and M. Istrate, “Comparative analysis of the perturb-and-observe and incremental conductance mppt methods,” in *2013 8TH INTERNATIONAL SYMPOSIUM ON ADVANCED TOPICS IN ELECTRICAL ENGINEERING (ATEE)*, pp. 1–4, 2013.
- [26] S. S. Satapathy and N. Kumar, “Modulated perturb and observe maximum power point tracking algorithm for solar pv energy conversion system,” in *2019 3rd International Conference on Recent Developments in Control, Automation Power Engineering (RDCAPE)*, pp. 345–350, 2019.
- [27] V. Kavitha and K. Subramanian, “Investigation of power quality issues and its solution for distributed power system,” in *2017 International Conference on Circuit ,Power and Computing Technologies (ICCPCT)*, pp. 1–6, 2017.
- [28] S. Kaur and B. Dwivedi, “Power quality issues and their mitigation techniques in microgrid system-a review,” in *2016 7th India International Conference on Power Electronics (IICPE)*, pp. 1–4, 2016.
- [29] S. Elphick, P. Ciufo, V. Smith, and S. Perera, “Summary of the economic impacts of power quality on consumers,” in *2015 Australasian Universities Power Engineering Conference (AUPEC)*, pp. 1–6, 2015.
- [30] R. G. Suryavanshi and I. Korachagaon, “A review on power quality issues due to high penetration level of solar generated power on the grid,” in *2019 2nd International Conference on Power and Embedded Drive Control (ICPEDC)*, pp. 464–467, 2019.
- [31] A. K. Karmaker, S. Roy, and M. R. Ahmed, “Analysis of the impact of electric vehicle charging station on power quality issues,” in *2019 International Conference on Electrical, Computer and Communication Engineering (ECCE)*, pp. 1–6, 2019.
- [32] M. H. Bollen, “Understanding power quality problems,” in *Voltage sags and Interruptions*, IEEE press, 2000.

- [33] A. Ghosh and G. Ledwich, *Power quality enhancement using custom power devices*. Springer science & business media, 2012.
- [34] “IEEE recommended practice for monitoring electric power quality,” *IEEE Std 1159-1995*, pp. 1–80, 1995.
- [35] “IEEE recommended practice for monitoring electric power quality,” *IEEE Std 1159-2009 (Revision of IEEE Std 1159-1995)*, pp. 1–94, 2009.
- [36] “IEEE recommended practice and requirements for harmonic control in electric power systems,” *IEEE Std 519-2014 (Revision of IEEE Std 519-1992)*, pp. 1–29, 2014.
- [37] “IEEE standard for interconnection and interoperability of distributed energy resources with associated electric power systems interfaces,” *IEEE Std 1547-2018 (Revision of IEEE Std 1547-2003)*, pp. 1–138, 2018.
- [38] “IEEE standard for interconnecting distributed resources with electric power systems,” *IEEE Std 1547-2003*, pp. 1–28, 2003.
- [39] P. Ribeiro, “Power electronics conditioners: configurations, performance, power quality and cost issues,” in *10th International Conference on Harmonics and Quality of Power. Proceedings (Cat. No.02EX630)*, vol. 2, pp. 587–589 vol.2, 2002.
- [40] J. Liu, S. Choi, and S. Chen, “Design of step dynamic voltage regulator for power quality enhancement,” *IEEE Transactions on Power Delivery*, vol. 18, no. 4, pp. 1403–1409, 2003.
- [41] J. G. Nielsen, M. Newman, H. Nielsen, and F. Blaabjerg, “Control and testing of a dynamic voltage restorer (dvr) at medium voltage level,” *IEEE Transactions on power electronics*, vol. 19, no. 3, pp. 806–813, 2004.

- [42] L. F. J. Meloni, F. L. Tofoli, n. J. J. Rezek, and E. R. Ribeiro, “Modeling and experimental validation of a single-phase series active power filter for harmonic voltage reduction,” *IEEE Access*, vol. 7, pp. 151971–151984, 2019.
- [43] M. Badoni, *Analysis, Design and Control of DSTATCOM and its Applications*. PhD dissertation, Delhi Technological University, 2015.
- [44] A. Ghosh and G. Ledwich, “Load compensating dstatcom in weak ac systems,” *IEEE transactions on Power Delivery*, vol. 18, no. 4, pp. 1302–1309, 2003.
- [45] M. K. Mishra, A. Ghosh, and A. Joshi, “Operation of a dstatcom in voltage control mode,” *IEEE transactions on power delivery*, vol. 18, no. 1, pp. 258–264, 2003.
- [46] P. Chittora, *Analysis and Control of Shunt Compensator in Distribution System*. PhD dissertation, Delhi Technological University, 2018.
- [47] S. R. Arya, B. Singh, R. Niwas, C. Ambrish, and K. Al-Haddad, “Power quality enhancement using dstatcom in distributed power generation system,” *IEEE Transactions on Industry Applications*, vol. 52, no. 6, pp. 5203–5212, 2016.
- [48] V. Khadkikar, “Enhancing electric power quality using upqc: A comprehensive overview,” *IEEE transactions on Power Electronics*, vol. 27, no. 5, pp. 2284–2297, 2011.
- [49] A. Ghosh and G. Ledwich, “A unified power quality conditioner (upqc) for simultaneous voltage and current compensation,” *Electric power systems research*, vol. 59, no. 1, pp. 55–63, 2001.
- [50] M. Kesler and E. Ozdemir, “Synchronous-reference-frame-based control method for upqc under unbalanced and distorted load conditions,” *IEEE transactions on industrial electronics*, vol. 58, no. 9, pp. 3967–3975, 2010.

- [51] G. Jianjun, X. Dianguo, L. Hankui, and G. Maozhong, “Unified power quality conditioner (upqc): the principle, control and application,” in *Proceedings of the Power Conversion Conference-Osaka 2002 (Cat. No. 02TH8579)*, vol. 1, pp. 80–85, IEEE, 2002.
- [52] P. Chittora, S. Alka, and M. Singh, “Simple and efficient control of dstatcom in three-phase four-wire polluted grid system using mccf-sogi based controller,” *IET Generation, Transmission & Distribution*, vol. 12, no. 5, pp. 1213–1222, 2017.
- [53] J. Bangarraju, V. Rajagopal, and A. Jayalaxmi, “Unit template synchronous reference frame theory based control algorithm for dstatcom,” *Journal of the Institution of Engineers (India): Series B*, vol. 95, no. 2, pp. 135–141, 2014.
- [54] S. Golestan and J. M. Guerrero, “Conventional synchronous reference frame phase-locked loop is an adaptive complex filter,” *IEEE Transactions on Industrial Electronics*, vol. 62, no. 3, pp. 1679–1682, 2014.
- [55] A. Ghoshal and J. Vinod, “Performance evaluation of three phase srf-pll and maf-srf-pll,” *Turkish Journal of Electrical Engineering and Computer Science*, vol. 23, no. 6, pp. 1781–1804, 2015.
- [56] F. Sevilmiş and H. Karaca, “Performance analysis of srf-pll and ddsrf-pll algorithms for grid interactive inverters,” *International Advanced Researches and Engineering Journal*, vol. 3, no. 2, pp. 116–122, 2019.
- [57] Y. Singh, I. Hussain, S. Bhim, and S. Mishra, “Real time implementation of EPLL with generalized filtering in single phase grid interfaced spv system,” in *2016 IEEE International Conference on Electrical, Computer and Electronics Engineering (UPCON)*, pp. 50–54, IEEE, 2016.
- [58] P. Rodriguez, A. Luna, M. Ciobotaru, R. Teodorescu, and F. Blaabjerg, “Advanced grid synchronization system for power converters under unbalanced

- and distorted operating conditions,” in *IECON 2006-32nd Annual Conference on IEEE Industrial Electronics*, pp. 5173–5178, IEEE, 2006.
- [59] M. Karimi-Ghartemani and M. R. Iravani, “A method for synchronization of power electronic converters in polluted and variable-frequency environments,” *IEEE Transactions on Power Systems*, vol. 19, no. 3, pp. 1263–1270, 2004.
- [60] S. Golestan, J. M. Guerrero, J. C. Vasquez, A. M. Abusorrah, and Y. Al-Turki, “Modeling, tuning, and performance comparison of second-order-generalized-integrator-based FLLs,” *IEEE Transactions on Power Electronics*, vol. 33, no. 12, pp. 10229–10239, 2018.
- [61] F. Xiao, L. Dong, L. Li, and X. Liao, “A frequency-fixed sogi-based pll for single-phase grid-connected converters,” *IEEE Transactions on Power Electronics*, vol. 32, no. 3, pp. 1713–1719, 2016.
- [62] S. Golestan, J. M. Guerrero, J. C. Vasquez, A. M. Abusorrah, and Y. Al-Turki, “Single-phase FLLs based on linear kalman filter, limit-cycle oscillator, and complex bandpass filter: Analysis and comparison with a standard FLL in grid applications,” *IEEE Transactions on Power Electronics*, vol. 34, no. 12, pp. 11774–11790, 2019.
- [63] C. Zhang, X. Zhao, X. Wang, X. Chai, Z. Zhang, and X. Guo, “A grid synchronization pll method based on mixed second-and third-order generalized integrator for dc offset elimination and frequency adaptability,” *IEEE Journal of Emerging and Selected Topics in Power Electronics*, vol. 6, no. 3, pp. 1517–1526, 2018.
- [64] P. Rodríguez, A. Luna, I. Candela, R. Mújal, R. Teodorescu, and F. Blaabjerg, “Multiresonant frequency-locked loop for grid synchronization of power converters under distorted grid conditions,” *IEEE Transactions on Industrial Electronics*, vol. 58, no. 1, pp. 127–138, 2010.

- [65] Y. F. Wang and Y. W. Li, “Grid synchronization pll based on cascaded delayed signal cancellation,” *IEEE Transactions on Power Electronics*, vol. 26, no. 7, pp. 1987–1997, 2010.
- [66] H. A. Hamed, A. F. Abdou, E. H. Bayoumi, and E. El-Kholy, “Frequency adaptive cdsc-pll using axis drift control under adverse grid condition,” *IEEE Transactions on Industrial Electronics*, vol. 64, no. 4, pp. 2671–2682, 2016.
- [67] Z. Dai, M. Fan, H. Nie, J. Zhang, and J. Li, “A robust frequency estimation method for aircraft grids under distorted conditions,” *IEEE Transactions on Industrial Electronics*, vol. 67, no. 5, pp. 4254–4258, 2019.
- [68] A. A. Vedyakov, A. O. VEDIKOVA, A. A. Bobtsov, A. A. Pyrkin, and S. V. Aranovskiy, “Frequency estimation of a sinusoidal signal with time-varying amplitude,” *IFAC*, vol. 50, no. 1, pp. 12880–12885, 2017.
- [69] Z. Dai, P. Zhao, X. Chen, M. Fan, and J. Zhang, “An enhanced transfer delay-based frequency locked loop for three-phase systems with dc offsets,” *IEEE Access*, vol. 7, pp. 40380–40387, 2019.
- [70] M. Qasim, P. Kanjiya, and V. Khadkikar, “Artificial-neural-network-based phase-locking scheme for active power filters,” *IEEE Transactions on Industrial Electronics*, vol. 61, no. 8, pp. 3857–3866, 2014.
- [71] B. Widrow and M. E. Hoff, “Adaptive switching circuits,” tech. rep., Stanford Univ Ca Stanford Electronics Labs, 1960.
- [72] J. Mazumdar and R. G. Harley, “Recurrent neural networks trained with back-propagation through time algorithm to estimate nonlinear load harmonic currents,” *IEEE Transactions on Industrial Electronics*, vol. 55, no. 9, pp. 3484–3491, 2008.
- [73] F. Alcantara and P. Salmeron, “A new technique for unbalance current and voltage estimation with neural networks,” *IEEE Transactions on Power Systems*, vol. 20, no. 2, pp. 852–858, 2005.

- [74] B. Singh, V. Verma, and J. Solanki, "Neural network-based selective compensation of current quality problems in distribution system," *IEEE Transactions on Industrial Electronics*, vol. 54, no. 1, pp. 53–60, 2007.
- [75] H. Akagi, A. Nabae, and S. Atoh, "Control strategy of active power filters using multiple voltage-source pwm converters," *IEEE Transactions on Industry Applications*, vol. IA-22, no. 3, pp. 460–465, 1986.
- [76] F. Z. Peng and J.-S. Lai, "Generalized instantaneous reactive power theory for three-phase power systems," *IEEE Transactions on Instrumentation and Measurement*, vol. 45, no. 1, pp. 293–297, 1996.
- [77] F. Z. Peng, G. Ott, and D. Adams, "Harmonic and reactive power compensation based on the generalized instantaneous reactive power theory for three-phase four-wire systems," *IEEE Transactions on Power Electronics*, vol. 13, no. 6, pp. 1174–1181, 1998.
- [78] B. Singh and J. Solanki, "A comparison of control algorithms for dstatcom," *IEEE Transactions on Industrial Electronics*, vol. 56, no. 7, pp. 2738–2745, 2009.
- [79] K. Bhattacharjee, "Design and simulation of synchronous reference frame based shunt active power filter using simulink," in *National Conference on Challenges in Research Technology in the Coming Decades (CRT 2013)*, pp. 1–7, 2013.
- [80] A. R. K P and J. P, "Comparison of srft and isogi-qsg control algorithm for grid integrated spv system," in *2019 2nd International Conference on Intelligent Computing, Instrumentation and Control Technologies (ICICICT)*, vol. 1, pp. 119–124, 2019.
- [81] M. Monfared, S. Golestan, and J. M. Guerrero, "Analysis, design, and experimental verification of a synchronous reference frame voltage control for



- single-phase inverters,” *IEEE Transactions on Industrial Electronics*, vol. 61, no. 1, pp. 258–269, 2014.
- [82] B. Singh, D. T. Shahani, and A. K. Verma, “Power balance theory based control of grid interfaced solar photovoltaic power generating system with improved power quality,” in *2012 IEEE International Conference on Power Electronics, Drives and Energy Systems (PEDES)*, pp. 1–7, 2012.
- [83] B. Singh, B. Singh, A. Chandra, and K. Al-Haddad, “Design and digital implementation of active filter with power balance theory,” *IEE Proceedings-Electric Power Applications*, vol. 152, no. 5, pp. 1149–1160, 2005.
- [84] R. R. Pereira, C. H. da Silva, L. E. B. da Silva, and G. Lambert-Torres, “Application of adaptive filters in active power filters,” in *2009 Brazilian Power Electronics Conference*, pp. 770–774, 2009.
- [85] M. Badoni, A. Singh, and B. Singh, “Comparative performance of wiener filter and adaptive least mean square-based control for power quality improvement,” *IEEE Transactions on Industrial Electronics*, vol. 63, no. 5, pp. 3028–3037, 2016.
- [86] B. Singh and J. Solanki, “An implementation of an adaptive control algorithm for a three-phase shunt active filter,” *IEEE Transactions on Industrial Electronics*, vol. 56, no. 8, pp. 2811–2820, 2009.
- [87] P. Karuppanan and K. K. Mahapatra, “Active harmonic current compensation to enhance power quality,” *International Journal of Electrical Power & Energy Systems*, vol. 62, pp. 144–151, 2014.
- [88] L. Merabet, S. Saad, D. O. Abdeslam, and J. Merckle, “Direct neural method for harmonic currents estimation using adaptive linear element,” *Electric Power Systems Research*, vol. 152, pp. 61–70, 2017.

- [89] G. Fedele, “Non-adaptive second-order generalized integrator for sinusoidal parameters estimation,” *International Journal of Electrical Power & Energy Systems*, vol. 42, no. 1, pp. 314–320, 2012.
- [90] C. Zhang, X. Zhao, X. Wang, X. Chai, Z. Zhang, and X. Guo, “A grid synchronization pll method based on mixed second- and third-order generalized integrator for dc offset elimination and frequency adaptability,” *IEEE Journal of Emerging and Selected Topics in Power Electronics*, vol. 6, no. 3, pp. 1517–1526, 2018.
- [91] P. Shah, I. Hussain, and B. Singh, “Fuzzy logic based fogi-fll algorithm for optimal operation of single-stage three-phase grid interfaced multifunctional secs,” *IEEE Transactions on Industrial Informatics*, vol. 14, no. 8, pp. 3334–3346, 2018.
- [92] B. Singh, S. Kumar, and C. Jain, “Damped-sogi-based control algorithm for solar pv power generating system,” *IEEE Transactions on Industry Applications*, vol. 53, no. 3, pp. 1780–1788, 2017.
- [93] F. U. Nazir, N. Kumar, B. C. Pal, B. Singh, and B. K. Panigrahi, “Enhanced sogi controller for weak grid integrated solar pv system,” *IEEE Transactions on Energy Conversion*, vol. 35, no. 3, pp. 1208–1217, 2020.
- [94] M. Kashif, S. Murshid, and B. Singh, “Solar pv array fed self-sensing control of pmsm drive with robust adaptive hybrid sogi based flux observer for water pumping,” *IEEE Transactions on Industrial Electronics*, vol. 68, no. 8, pp. 6962–6972, 2021.
- [95] C. A. Busada, S. Gomez Jorge, A. E. Leon, and J. A. Solsona, “Current controller based on reduced order generalized integrators for distributed generation systems,” *IEEE Transactions on Industrial Electronics*, vol. 59, no. 7, pp. 2898–2909, 2012.

- [96] S. Gomez Jorge, C. A. Busada, and J. Solsona, “Low computational burden grid voltage sensorless current controller,” *IET Power Electronics*, vol. 6, no. 8, pp. 1592–1599, 2013.
- [97] C. Xie, X. Zhao, K. Ki, D. Liu, J. M. Guerrero, and J. C. Vasquez, “Phase compensated reduced order generalized integrators for grid-tied vses with harmonics compensation capability,” *IEEE Transactions on Industry Applications*, vol. 54, no. 3, pp. 2568–2578, 2018.
- [98] S. Jiao, K. Rajashekara, R. K. Potti, L. Ben-Brahim, and A. Gastli, “A double reduced order generalized integrator based algorithm for control of four-leg converter to enhance power quality,” in *2019 IEEE Energy Conversion Congress and Exposition (ECCE)*, pp. 4293–4298, 2019.
- [99] S. Benhalima, A. Chandra, and M. Rezkallah, “Real-time experimental implementation of an lms-adaline-based anfis controller to drive pv interfacing power system,” *IET Renewable Power Generation*, vol. 13, no. 7, pp. 1142–1152, 2019.
- [100] S. R. Arya and B. Singh, “Performance of dstatcom using leaky lms control algorithm,” *IEEE Journal of Emerging and Selected Topics in Power Electronics*, vol. 1, no. 2, pp. 104–113, 2013.
- [101] M. Badoni, A. Singh, and B. Singh, “Adaptive neurofuzzy inference system least-mean-square-based control algorithm for dstatcom,” *IEEE Transactions on Industrial Informatics*, vol. 12, no. 2, pp. 483–492, 2016.
- [102] M. Cirrincione, M. Pucci, G. Vitale, and A. Miraoui, “Current harmonic compensation by a single-phase shunt active power filter controlled by adaptive neural filtering,” *IEEE Transactions on Industrial Electronics*, vol. 56, no. 8, pp. 3128–3143, 2009.
- [103] Z. Zhang, L. Zheng, J. Weng, Y. Mao, W. Lu, and L. Xiao, “A new varying-parameter recurrent neural-network for online solution of time-varying

- sylvester equation,” *IEEE Transactions on Cybernetics*, vol. 48, no. 11, pp. 3135–3148, 2018.
- [104] D. Molina, J. Liang, R. Harley, and G. K. Venayagamoorthy, “Comparison of tdnn and rnn performances for neuro-identification on small to medium-sized power systems,” in *2011 IEEE Symposium on Computational Intelligence Applications In Smart Grid (CIASG)*, pp. 1–8, 2011.
- [105] D. Molina, G. K. Venayagamoorthy, J. Liang, and R. G. Harley, “Intelligent local area signals based damping of power system oscillations using virtual generators and approximate dynamic programming,” *IEEE Transactions on Smart Grid*, vol. 4, no. 1, pp. 498–508, 2013.
- [106] M. Badoni, A. Singh, and B. Singh, “Real time recurrent learning based algorithm for control of dstatcom,” in *2015 Annual IEEE India Conference (INDICON)*, pp. 1–6, 2015.
- [107] R. Majumder, “Reactive power compensation in single-phase operation of microgrid,” *IEEE Transactions on Industrial Electronics*, vol. 60, no. 4, pp. 1403–1416, 2013.
- [108] J. Rocabert, A. Luna, F. Blaabjerg, and P. Rodríguez, “Control of power converters in ac microgrids,” *IEEE Transactions on Power Electronics*, vol. 27, no. 11, pp. 4734–4749, 2012.
- [109] Y. Yang, K. Zhou, and F. Blaabjerg, “Current harmonics from single-phase grid-connected inverters—examination and suppression,” *IEEE Journal of Emerging and Selected Topics in Power Electronics*, vol. 4, no. 1, pp. 221–233, 2016.
- [110] F. Blaabjerg, R. Teodorescu, M. Liserre, and A. Timbus, “Overview of control and grid synchronization for distributed power generation systems,” *IEEE Transactions on Industrial Electronics*, vol. 53, no. 5, pp. 1398–1409, 2006.

- [111] J. Selvaraj and N. A. Rahim, "Multilevel inverter for grid-connected pv system employing digital pi controller," *IEEE Transactions on Industrial Electronics*, vol. 56, no. 1, pp. 149–158, 2009.
- [112] A. Kumar and V. Verma, "Performance enhancement of single-phase grid-connected pv system under partial shading using cascaded multilevel converter," *IEEE Transactions on Industry Applications*, vol. 54, no. 3, pp. 2665–2676, 2018.
- [113] W. Libo, Z. Zhengming, and L. Jianzheng, "A single-stage three-phase grid-connected photovoltaic system with modified mppt method and reactive power compensation," *IEEE Transactions on Energy Conversion*, vol. 22, no. 4, pp. 881–886, 2007.
- [114] H. Patel and V. Agarwal, "Mppt scheme for a pv-fed single-phase single-stage grid-connected inverter operating in ccm with only one current sensor," *IEEE Transactions on Energy Conversion*, vol. 24, no. 1, pp. 256–263, 2009.
- [115] E. Sreeraj, K. Chatterjee, and S. Bandyopadhyay, "One-cycle-controlled single-stage single-phase voltage-sensorless grid-connected pv system," *IEEE Transactions on Industrial Electronics*, vol. 60, no. 3, pp. 1216–1224, 2013.
- [116] A. Datta, R. Sarker, and I. Hazarika, "An efficient technique using modified p–q theory for controlling power flow in a single-stage single-phase grid-connected pv system," *IEEE Transactions on Industrial Informatics*, vol. 15, no. 8, pp. 4635–4645, 2019.
- [117] B. N. Alajmi, K. H. Ahmed, G. P. Adam, and B. W. Williams, "Single-phase single-stage transformer less grid-connected pv system," *IEEE Transactions on Power Electronics*, vol. 28, no. 6, pp. 2664–2676, 2013.
- [118] A. Kumar, Seema, B. Singh, and R. Jain, "Double stage grid-tied solar pv system using hc-lms control," in *2020 IEEE 9th Power India International Conference (PIICON)*, pp. 1–6, 2020.

- [119] H. S. Sahu and S. K. Nayak, "Extraction of maximum power from a pv array under nonuniform irradiation conditions," *IEEE Transactions on Electron Devices*, vol. 63, no. 12, pp. 4825–4831, 2016.
- [120] M. S. ElNozahy and M. M. A. Salama, "Uncertainty-based design of a bilayer distribution system for improved integration of phevs and pv arrays," *IEEE Transactions on Sustainable Energy*, vol. 6, no. 3, pp. 659–674, 2015.
- [121] B. Lu and M. Shahidehpour, "Short-term scheduling of battery in a grid-connected pv/battery system," *IEEE Transactions on Power Systems*, vol. 20, no. 2, pp. 1053–1061, 2005.
- [122] V. Rallabandi, O. M. Akeyo, N. Jewell, and D. M. Ionel, "Incorporating battery energy storage systems into multi-mw grid connected pv systems," *IEEE Transactions on Industry Applications*, vol. 55, no. 1, pp. 638–647, 2019.
- [123] T.-F. Wu, C.-H. Chang, L.-C. Lin, and C.-L. Kuo, "Power loss comparison of single- and two-stage grid-connected photovoltaic systems," *IEEE Transactions on Energy Conversion*, vol. 26, no. 2, pp. 707–715, 2011.
- [124] S. Jain and V. Agarwal, "A single-stage grid connected inverter topology for solar pv systems with maximum power point tracking," *IEEE Transactions on Power Electronics*, vol. 22, no. 5, pp. 1928–1940, 2007.
- [125] T. Sreekanth, N. Lakshminarasamma, and M. K. Mishra, "A single-stage grid-connected high gain buck–boost inverter with maximum power point tracking," *IEEE Transactions on Energy Conversion*, vol. 32, no. 1, pp. 330–339, 2017.
- [126] A. K. Singh, I. Hussain, and B. Singh, "Double-stage three-phase grid-integrated solar pv system with fast zero attracting normalized least mean fourth based adaptive control," *IEEE Transactions on Industrial Electronics*, vol. 65, no. 5, pp. 3921–3931, 2018.

- [127] N. Femia, G. Petrone, S. Giovanni, and M. Vitelli, “A technique for improving p o mppt performances of double-stage grid-connected photovoltaic systems,” *IEEE Transactions on Industrial Electronics*, vol. 56, no. 11, pp. 4473–4482, 2009.
- [128] S. A. Taher, M. H. Alaee, and Z. Dehghani Arani, “Model predictive control of pv-based shunt active power filter in single phase low voltage grid using conservative power theory,” in *2017 8th Power Electronics, Drive Systems Technologies Conference (PEDSTC)*, pp. 253–258, 2017.
- [129] A. Chouder, S. Silvestre, N. Sadaoui, and L. Rahmani, “Modeling and simulation of a grid connected pv system based on the evaluation of main pv module parameters,” *Simulation Modelling Practice and Theory*, vol. 20, no. 1, pp. 46–58, 2012.
- [130] A. Pradhan and B. Panda, “Design of dc-dc converter for load matching in case of pv system,” in *2017 International Conference on Energy, Communication, Data Analytics and Soft Computing (ICECDS)*, pp. 1002–1007, 2017.
- [131] B. M. Hasaneen and A. A. Elbaset Mohammed, “Design and simulation of dc/dc boost converter,” in *2008 12th International Middle-East Power System Conference*, pp. 335–340, 2008.
- [132] S. Masri and P. W. Chan, “Design and development of a dc-dc boost converter with constant output voltage,” in *2010 International Conference on Intelligent and Advanced Systems*, pp. 1–4, 2010.
- [133] M. Rahman, T. Radwan, A. Osheiba, and A. Lashine, “Analysis of current controllers for voltage-source inverter,” *IEEE Transactions on Industrial Electronics*, vol. 44, no. 4, pp. 477–485, 1997.
- [134] A. Blorfan, P. Wira, D. Flieller, G. Sturtzer, and J. Mercklé, “A three-phase hybrid active power filter with photovoltaic generation and hysteresis current

- control,” in *IECON 2011 - 37th Annual Conference of the IEEE Industrial Electronics Society*, pp. 4316–4321, 2011.
- [135] “Chapter 2 - basic control principles in power electronics: Analog and digital control design,” in *Control of Power Electronic Converters and Systems* (F. Blaabjerg, ed.), pp. 31–68, Academic Press, 2018.
- [136] D. Wenjin and H. Taiyang, “Design of single-phase shunt active power filter based on ann,” in *2007 IEEE International Symposium on Industrial Electronics*, pp. 770–774, 2007.
- [137] Krismadinata, N. A. Rahim, and J. Selvaraj, “Implementation of hysteresis current control for single-phase grid connected inverter,” in *2007 7th International Conference on Power Electronics and Drive Systems*, pp. 1097–1101, 2007.
- [138] P. Karuppanan, S. K. Ram, and K. Mahapatra, “Three level hysteresis current controller based active power filter for harmonic compensation,” in *2011 International Conference on Emerging Trends in Electrical and Computer Technology*, pp. 407–412, 2011.
- [139] B. Singh, S. Dwivedi, I. Hussain, and A. K. Verma, “Grid integration of solar pv power generating system using qp ll based control algorithm,” in *2014 6th IEEE Power India International Conference (PIICON)*, pp. 1–6, 2014.
- [140] M. Karimi-Ghartema, *Enhanced phase-locked loop structures for power and energy applications*. John Wiley & Sons, 2014.
- [141] M. Karimi-Ghartemani, “Linear and pseudolinear enhanced phased-locked loop (ep ll) structures,” *IEEE transactions on industrial electronics*, vol. 61, no. 3, pp. 1464–1474, 2013.
- [142] S. B. Q. Naqvi, S. Kumar, and B. Singh, “Three-phase four-wire pv system for grid interconnection at weak grid conditions,” *IEEE Transactions on Industry Applications*, vol. 56, no. 6, pp. 7077–7087, 2020.



- [143] S. K. Pandey, B. Singh, and G. Modi, “Frequency-adaptive complex-coefficient filter-based control for grid-integrated pv system,” *IET Generation, Transmission Distribution*, vol. 14, no. 19, pp. 4141–4151, 2020.
- [144] M. Karimi-Ghartema, *Synchronous Reference Frame PLL*, pp. 133–145. 2014.
- [145] S. Ali, I. Setiawan, and S. Handoko, “Design and performance test of three phased synchronous reference frame-phase locked loop (srf-pll) using dspic30f4011,” in *2018 5th International Conference on Information Technology, Computer, and Electrical Engineering (ICITACEE)*, pp. 51–56, 2018.
- [146] M. Rasheduzzaman, S. Khorbotly, and J. W. Kimball, “A modified srf-pll for phase and frequency measurement of single-phase systems,” in *2016 IEEE Energy Conversion Congress and Exposition (ECCE)*, pp. 1–7, 2016.
- [147] A. Singhal and A. singh, “Design and performance analysis of synchronization techniques under non-ideal conditions,” in *2019 International Conference on Power Electronics, Control and Automation (ICPECA)*, pp. 1–6, 2019.
- [148] S. Golestan and J. M. Guerrero, “Conventional synchronous reference frame phase-locked loop is an adaptive complex filter,” *IEEE Transactions on Industrial Electronics*, vol. 62, no. 3, pp. 1679–1682, 2015.
- [149] A. K. Verma, R. K. Jarial, and U. M. Rao, “An improved pre-filtered three-phase srf-pll for rapid detection of grid voltage attributes,” in *2019 National Power Electronics Conference (NPEC)*, pp. 1–4, 2019.
- [150] M. Qasim, P. Kanjiya, and V. Khadkikar, “Optimal current harmonic extractor based on unified adalines for shunt active power filters,” *IEEE Transactions on Power Electronics*, vol. 29, no. 12, pp. 6383–6393, 2014.
- [151] G. W. Chang, C.-I. Chen, and Q.-W. Liang, “A two-stage adaline for harmonics and interharmonics measurement,” *IEEE Transactions on Industrial Electronics*, vol. 56, no. 6, pp. 2220–2228, 2009.

- [152] M. Rathod, V. Patel, and N. V. George, “Generalized spline nonlinear adaptive filters,” *Expert Systems with Applications*, vol. 83, pp. 122–130, 2017.
- [153] T. Yu, W. Li, Y. Yu, and R. C. de Lamare, “Robust spline adaptive filtering based on accelerated gradient learning: Design and performance analysis,” *Signal Processing*, vol. 183, p. 107965, 2021.

# Appendix

Table 8.1: Parameters for single-phase and three-phase grid-connected PV system

Simulation Parameters			Experimental Parameters
Single-Phase Grid-Connected PV System			
Grid Voltage ( $v_g$ )	230V, 50Hz		110V, 50Hz
DC-link Reference Voltage ( $V_{dcref}$ )	400V		200V
Dc-link capacitance ( $C_{dc}$ )	2000 $\mu F$		4700 $\mu F$
Interfacing Inductor ( $L_f$ )	3.20mH		1.60mH
	Single-stage	Double-stage	Single-stage
PV Rating	$N_{ss}=12$	$N_{ss}=5$	
	$N_{pp}=1$	$N_{pp}=2$	$P_{mp}=1000W$
	$P_{mp}=3247.92W$	$P_{mp}=2706.6W$	$V_{oc}=250.75$
	$V_{oc}=528.0V$	$V_{oc}=220.0V$	$V_{mp}=200V$
	$V_{mp}=416.4V$	$V_{mp}=173.5V$	$I_{sc}=5.53A$
	$I_{sc}=8.1A$	$I_{sc}=16.2A$	$I_{mp}=5.0A$
	$I_{mp}=7.8A$	$I_{mp}=15.6V$	
Three-Phase Grid-Connected PV System			
Grid Voltage ( $V_{ll}$ )	415V, 50Hz		110V, 50Hz
DC-link Reference Voltage ( $V_{dcref}$ )	800V		200V
DC-link capacitance ( $C_{dc}$ )	4000 $\mu F$		1640 $\mu F$
Interfacing Inductor ( $L_f$ )	6.4mH		3.2mH
	Single-stage	Double-stage	Single-stage
PV Rating	$N_{ss}=22$	$N_{ss}=10$	
	$N_{pp}=1$	$N_{pp}=2$	$P_{mp}=1000W$
	$P_{mp}=5954.52W$	$P_{mp}=5413.2W$	$V_{oc}=250.75$
	$V_{oc}=968.0V$	$V_{oc}=440.0V$	$V_{mp}=200V$
	$V_{mp}=763.4V$	$V_{mp}=347.0V$	$I_{sc}=5.53A$
	$I_{sc}=8.1A$	$I_{sc}=16.2A$	$I_{mp}=5.0A$
	$I_{mp}=7.8A$	$I_{mp}=15.6V$	